Imperial College London

Additive manufacturing of Inconel 718 using solid-state bonding

A Thesis submitted to Imperial College London

For the Degree of Doctor of Philosophy

Yaping Wang

March 2022

Mechanics of Materials Division

Department of Mechanical Engineering Imperial College London

Certificate of Authorship

I certify that this thesis has not already been submitted for any degree and is not being submitted as part of candidature for any other degree.

I also certify that the thesis has been written by me and that any assistance that I have received in preparing this thesis and all sources used have been acknowledged in this thesis.

Yaping Wang

Copyright Declaration

The copyright of this thesis rests with the author and is made available under a Creative Commons Attribution Non-Commercial No Derivatives licence. Researchers are free to copy, distribute or transmit the thesis on the condition that they attribute it, that they do not use it for commercial purposes and that they do not alter, transform or build upon it. For any reuse or redistribution, researchers must make clear to others the licence terms of this work.

Acknowledgements

I would like to thank people involved in the completion of my Ph.D. and first and foremost, express my deepest gratitude to my research supervisor Dr. Jun Jiang from Imperial College London. His guidance, attention to all the aspects of the work, as well as critique and assessment, have led this research to its successful and fruitful results. I could not imagine any progress Conceptualization and Optimization without your oversight.

My acknowledgement also goes to my co-supervisor Professor Jian-Guo Lin. Thank you for providing such productive research platform and valuable critics that led to the completion of this project. Thank my co-supervisor Jing-Hua Zheng for her advice both in work and life when I just started my PhD study at Imperial.

I would also like to thank other people who have contributed in various ways.

I would like to thank Dr. Ruth Brooker, Mr. Alex Toth and Dr. Zhusheng Shi for their timely technical consultations, without which it is impossible to conduct the experiments. I am immensely grateful for insights and knowledge Dr. Christopher Hopper, Miss Yuehan Liu, Mr. Wei Wang shared with on the subject matter. I must commemorate Dr. Kailun Zheng, Dr. Yong Li and Dr. Yibo Li for their assistance with various aspects of the research.

I must send my gratitude to Mr. Bo Lan for his help in both experiment conduction and data gathering, as well as Dr. Hui Xing from Shanghai JiaoTong University for the material supply.

Last but not least, I would also like to recognize the biggest support and love that came from my family and my friends throughout the completion of my PhD.

Abstract

The capability for manufacturing large scale metallic components is a sign of a country's productive capacity. Further capability improvement is limited by factors such as quality control during the casting (solidification defects), the high tonnage requirement on equipment and the high energy consumption of the processes. In this thesis, a new manufacturing method has been proposed for the construction of large or extra-large components, based on a layer-by-layer solid-state bonding method. The advantages of the newly proposed method lie in improved quality control and a lower tonnage capacity requirement for the equipment.

For this novel method, the bonding quality between each layer is the key to the final product achieving high performance in service. In this thesis, the bonding has been conducted at different scales: at a small-scale using bar samples and a Gleeble testing machine, and at a larger scale using three-layer plates under forging conditions to first demonstrate the construction concept. At the Gleeble scale, the bonded samples, as well as reference samples without a bonding interface, have been tested to evaluate bonding interface quality, while excluding the microstructural effects. From microstructure characterization, the bonding mechanisms have been revealed as being a mix of oxide film fracture, metal extrusion and microstructure-evolution-induced interface grain boundary migration processes. Based on these, a four-stage model has been developed to quantitatively describe the bonding process and predict the bonding quality. At the larger plate scale, the bonding was conducted under practical industrial conditions. The effects of vacuum, ageing heat treatment, and location have been evaluated through tensile tests at both room and high temperatures. Based on the proposed bonding mechanism and model, the results from the larger plate forging trial show agreement between model and practice.

Due to the complexity of the various mechanisms dominating the bonding process, it is important to understand the role of grain boundaries at the bonding interface. To identify this role, bi-crystalline samples, as well as polycrystalline samples showing typical grain boundary migrated and non-migrated behaviour across the bonding interfaces were manufactured and tested so that the role of interface grain boundary could be unambiguously determined.

Table of Contents

Certificate of Authorship 2
Copyright Declaration 3
Acknowledgements 4
Abstract 5
List of Figures 10
List of Tables 15
Nomenclature 16
Chapter 1 Introduction 22
1.1 The challenges in heavy manufacturing 22
1.2 Aim of the work and research approach 23
1.2.1 The challenges in manufacturing large IN718 parts 23
1.2.2 The strategy 24
1.2.3 Objectives of the research 25
1.3 Structure of thesis 26
Chapter 2 Literature review 28
2.1 The manufacturing of Inconel 718 28
2.1.1 The casting ingots of IN718 28
2.1.2 The Powder Metallurgy (PM) of IN718 29
2.1.3 The hot deforming of IN718 30
2.1.4 The additive manufacturing of IN718 35
2.2 Understanding the solid-state bonding mechanism of metals 37
2.2.1 Cold Pressure Welding and Roll Bonding 38
2.2.2 Diffusion Bonding 43
2.2.3 Extrusion Bonding 47
2.2.4 Hot Compression Bonding 50
2.2.5 Solid-State Bonding of IN718 54
2.3 The additive forming methods based on solid-state bonding 56
Chapter 3 Methodology 57
3.1 Introduction 57
3.2 The solid-state bonding of IN718 using Gleeble under different conditions 57

3.2.1 Materials – IN718 bar samples 57
3.2.2 Gleeble bonding test with bar sample 58
3.2.3 Bar sample tensile tests 61
3.2.4 Microstructure characterization 61
3.3 The multi-layer construction of IN718 plate in forging practice 62
3.3.1 Materials -IN718 plate samples 62
3.3.2 Isothermal forging bonding process 63
3.3.3 Bonded plate microstructure and tensile test 64
3.4 Bonding mechanism investigation with pure Ni and Al 65
3.4.1 Materials – Ni and Al small cylinder samples 65
3.4.2 Gleeble bonding with small cylinder samples 66
3.4.3 Small sample tensile evaluation and in-situ observation 69
3.4.4 Small sample microstructure characterization 69
Chapter 4 The solid-state bonding of IN718 using Gleeble under different conditions 71
4.1 Introduction 71
4.2 Strain effect results 72
4.2.1 The interface microstructure evolution during at different strain levels 72
4.2.2 The tensile results for samples bonded at different strain levels 79
4.3 Strain rate effect results 83
4.3.1 Effect of strain rate on the interface bonding microstructure 83
4.3.2 Effect of strain rate on tensile results 86
4.4 Temperature effect results 90
4.4.1 Effect of temperature on the interface bonding microstructure 90
4.4.2 Effect of temperature on tensile results 94
4.5 Discussion 96
4.5.1 The bonding mechanism - strain effect 97
4.5.2 The interaction between GB migration and oxide barrier during bonding 98
4.5.3 The effect of strain rate on the interface bonding behaviour 101
4.5.4 The effect of deformation temperature on the interface bonding behaviour 102
4.6 Conclusions 103
Chapter 5 The simulation of the bonding process and model for bond quality prediction 105
5.1 Introduction 105
5.2 The simulation of the bonding process with bar samples 106
5.3 Model description for bond quality 111

5.4 The implementation of the bonding model for bar sample bonding simulation 119
5.5 The implementation of the bonding model and predicted bond quality 122
5.5.1 The interpretation of bonding at different strains with calculated results 122
5.5.2 The calculated bond behaviour and quality at different strain rates 124
5.5.3 The calculated bond behaviour and quality at different deformation temperatures 126
5.6 The evaluation of the now bond model for bonding at hot deformation 128
5.7 Conclusions 130
Chapter 6 The multi-layered forging of IN718 132
6.1 Introduction 132
6.2 Results 132
6.2.1 The microstructure near bonding interfaces 132
6.2.2 The room-temperature tensile test 135
6.2.3 The bond interface microstructure 139
6.3 Discussion 144
6.3.1 The δ phase microstructure evolution at 950 ˚C 144
6.3.2 The bonding uniformity over forging bonded plates 146
6.3.3 Comparison with Gleeble bonding and Optimization of properties 147
6.4 Conclusions 148
Chapter 7 Role investigation of interface GB migration in the bonding with typical interfaces 150
7.1 Introduction 150
7.2 The tensile properties of Al samples 151
7.2.1 The grain structures 151
7.2.2 The tensile results for Al samples 152
7.3 The tensile properties of bonded polycrystalline pure nickel joints 155
7.3.1 The microstructure of nickel joints 155
7.3.2 The tensile test results for nickel joints 160
7.4 Discussion 166
7.4.1 The role of interface grain boundary migration 166
7.5 Conclusions 169
Chapter 8 Summary and Future Work 171
8.1 Summary 171
8.2 Suggestions for further research work 174
8.2.1 Distinguish the role of a single process in the complex bonding mechanism 175

8.2.2 Model further modification with more detailed research 176
8.2.3 Suggestions for the practical manufacturing application 176
References 177
Appendices 195
Appendix A 195
Different heating scheme to simulate the hot compression of bar samples in QForm 195
Appendix B 198
Appendix C 205
The evaluation of high-temperature mechanical properties of the multi-layer forging bonded plate in Chapter 6 205
Appendix D 207
Publications during Ph. D. 207

List of Figures

Figure 1-1 Two ways to achieve the new proposed forming concept based on solid-state bonding for manufacturing large-scale components. (a) additive forging; (b) solid-state AM. 25

Figure 2-1 a) Schematic of the Electro-Slag Remelting (ESR) and b) Vacuum Arc Remelting (VAR); c) the microstructure by unstable melting; d) macro-etched transverse Section of as-cast IN718. [21] 29

Figure 2-2 a) Schematic of a HIP set-up[22]; b) typical as-received microstructure with prior particle boundaries (PPB) after HIP[23]. 30

Figure 2-3 Grain-size comparison between metallographic analysis and microstructure simulation for IN718 forging.[60] 34

Figure 2-4 Grain size distribution of SLM (Selective Lase Melting), forged and cast microstructure[29].....36

Figure 2-5 The review on yielding strength of AM-IN718 in a) as-built state; b) after heat-treated; c) fatigue properties ; d) creep properties of SLM IN718 at room temperature[73]. .37

Figure 2-6 The assumptions on the film behaviour for cold pressure welding/roll bonding film theory: (a) Schematic illustration of the welding process in [116]; (b) Schematic outline of coalescence mechanisms in [119]; (c) Aluminium surface of original length L_0 stretched to length $L_0(1+\varepsilon)$ in [121]. 43

Figure 2-7 The different void geometric assumption in different models: (a) Hill's model[86]; (b) Orhan's model[158]; (c) [162]'s model; (d) Derby's model[143]; (e) Guo and Ridley's model[163]; (d) Routes of material transfer described in Hill's model[86]. 46

Figure 2-8 Schematic diagram of solid-state bonding mechanism in porthole die extrusion process.[172].....48

Figure 3-1 The microstructure of (a) as-received wrought IN718; and after being heated up and soaked for 3 min at the designated temperature of (b) 1150 ˚C; (c) 1050 ˚C; (d) 950 ˚C. 58

Figure 3-2 a) Compressive bonding set-up on Gleeble 3800; b) the heating scheme; c) half cylinder sample to be bonded and whole cylinder sample for reference test; d) bonded samples after compression (the reference samples are with the same shape, and the marked area taken for microstructure characterization); e) the dimension of tensile sample and fractured samples 60

Figure 3-3 The temperature distribution of the bar samples in Gleeble after heating and soaking at different designated temperatures of a)950 ˚C; b)1050 ˚C; c)1150 ˚C; length unit, mm. ...61

Figure 3-4 The configuration of the piled-up three-layered preform within the container, a) before compression and b) after compression. 63

Figure 3-5 a) The forged samples at different conditions, b) The sampling scheme from the forged plate for microstructure characterization and mechanical tests. 65

Figure 3-6 The geometry of samples for tensile test.....65

Figure 3-7 The pure aluminium samples from a casting ingot. (a) the ingot; (b) the schematic for sampling strategy.....66

Figure 3-8 The Gleeble set-up for nickel bonding test 67

Figure 3-9 The (a) diffusion bonding test and (b) compression bonding test for pure nickel and sampling strategy for the micro tensile test; (c) the dimension for micro tensile sample. 68

Figure 3-10 The (a) DEBEN micro-test machine and (b) set-up for in-situ observation using optical microscopy during tensile. 69

Figure 4-1 The bond line evolution of bonded samples at the height reduction of a) 0; b) 0.05; c) 0.1; d) 0.3; e) 0.5 at 1150 ˚C and strain rate of 0.1 s^{-1}. 73

Figure 4-2 The microstructure of the bonding zone of IN718 samples compressed at strain of a) 0; b) 0.05; c) 0.1; d) 0.3 e) 0.5; (0, 5%, 10%, 30%, 50% height reduction, respectively) at 1150 ˚C and strain rate of 0.1 s^{-1}.....75

Figure 4-3 The EBSD orientation map, recrystallized grains and grain size distribution of the bonding zone of IN718 samples compressed at engineering strain of a) 0; b) 0.05; c) 0.1; d) 0.3 e) 0.5; (0, 5%, 10%, 30%, 50% height reduction, respectively) at 1150 ˚C and strain rate of 0.1 s^{-1}.....77

Figure 4-4 The Rx fraction and grain size distribution of the bonding zone of IN718 samples compressed at different strain levels: 0, 5%, 10%, 30%, 50% height reduction, respectively, at 1150 ˚C and strain rate of 0.1 s^{-1}.....78

Figure 4-5 The EBSD maps and microscopic characterization of bonding zone of IN718 samples compressed at height reduction of a) 0.1, b) 0.3 at 1150 ˚C and strain rate of 0.1 s^{-1}. 79

Figure 4-6 The tensile test results: a) ultimate tensile strength (UTS); b) yielding strength (YS); c) elongation (EL) of IN718 samples bonded at 1150 ˚C/0.1 s^{-1}. 80

Figure 4-7 a) The tensile engineering stress-strain curves; b) the failure surfaces of IN718 samples bonded, bonded at 1150 ˚C/0.1 s^{-1}. 81

Figure 4-8 a) The tensile test results referred to the results of samples compressed at the same condition (reference test). b) The tensile engineering stress-strain curves referred to the results of samples compressed at the same condition (reference test) of 1150 ˚C/0.1 s^{-1} to different strains. 82

Figure 4-9 The microstructures and interfaces of IN718 samples bonded at 1150 ˚C under different conditions a) SR0.001 s^{-1}, HR 10%; b) SR0.01 s^{-1}, HR 10%; c) SR0.1 s^{-1}, HR 10%; d) SR0.001 s^{-1}, HR 30%; e) SR0.01 s^{-1}, HR 30%; f) SR0.1 s^{-1}, HR 30%; g) SR0.001 s^{-1}, HR 50%; h) SR0.01 s^{-1}, HR 50%; i) SR0.1 s^{-1}, HR 50%. 84

Figure 4-10 The IPF figures for samples bonded under different conditions at 1150 ˚C. 30% height reduction at a) 0.001 s^{-1}, b) 0.01 s^{-1}, c) 0.1 s^{-1}; 50% height reduction at d) 0.001 s^{-1}, e) 0.01 s^{-1}, f) 0.1 s^{-1}. 86

Figure 4-11 The tensile properties of bonds formed at different strain rates at 1150 ˚C a) 30% and b) 50%.The tensile curves of compress bonded samples at different conditions, c) 10%; d) 30%; e)50% height reduction.....87

Figure 4-12 The relative tensile properties of bonds formed under different strain rates 1150 ˚C and a) 30% and b) 50%. Comparison of tensile curves of compress bonded sample and references at different strain rates to 30% height reduction, c) 0.001 s^{-1}; d) 0. 01 s^{-1}; 50% height reduction e) 0.001 s^{-1}; f) 0.01 s^{-1}. 89

Figure 4-13 The fracture morphologies of samples bonded at HR 30% and a_1) 0.001 s^{-1}; a_2) 0.01 s^{-1}; a_3) 0.1 s^{-1}; HR 50% and b_1) 0.001 s^{-1}; b_2) 0.01 s^{-1}; a_3) 0.1 s^{-1}. 90

Figure 4-14 The microstructure of the interfaces bonded at different temperatures: 30% height reduction (a) 950 ˚C; (b) 1050 ˚C; (c) 1150 ˚C, 50% height reduction d_{1-3}) 1050 ˚C (e_{1-3}) 1050 ˚C; (f_{1-3}) 1150 ˚C. 92

Figure 4-15 The microstructure of the interface bonded to 30% at (a) 950 ˚C and (b) 1050 ˚C; to 50% (c) 950 ˚C and (d) 1050 ˚C. 93

Figure 4-16 The tensile properties of the samples bonded at different temperatures. (a) 30% and (b) 50% height reduction. 94

Figure 4-17 The relative tensile properties of the samples bonded at different temperatures. (a) 30% and (b) 50% height reduction. The tensile curves of samples bonded at different temperatures. (c-d) 950 ˚C; (e-f) 1050 ˚C. 96

Figure 4-18 The mechanism of microstructure evolution and grain boundary migration near the bonding interface over the strain with the existence of oxide film, a-c) high strain rate/low temperature, d-e) low strain rate/ high temperature. 101

Figure 5-1 The electrical upsetting model for simulating the Gleeble hot compression bonding process with bar samples 107

Figure 5-2 The flow stress-strain data comparison between Huang's JMAK model from the QForm library and Gleeble hot compression tests 108

Figure 5-3 The double-process simulated sample shape at different temperatures (1150 ˚C, 1050 ˚C, 950 ˚C) and different strain rates (0.001 s^{-1}, 0.01 s^{-1}, 0.1 s^{-1}) after compression deformation in comparison to the real samples. 109

Figure 5-4 The comparison between the simulated and recorded force for the hot compression bonding process under different conditions using double-process simulation. 110

Figure 5-5 The schematic graph of the oxide fragments remaining on the original bonding interface at large strain 116

Figure 5-6 The interface behaviour and bonding mechanism at different stages. 118

Figure 5-7 Flow chart of implementing the bond model with data from QForm simulation 120

Figure 5-8 The FE simulation results of the hot compression tests and contribution of different contacting pairs on the final bonding quality: a) oxide fragment gap; b) the normal pressure applied, and pressure needed for extrusion; c) the contribution of different contacting pairs on final bond; d) the calculated total bonding ratio and tested elongation ratio of joints 122

Figure 5-9 The calculated bond results for bonding at different strain rates, a) the radial strain; b) normal stress and extrusion stress; c) oxide gap; d) the contribution of different contacting pairs on bond ratio; e) the final bond ratio and obtained bond ratio. 124

Figure 5-10 The calculated bond results for bonding at different strain rates, a) the radial strain; b) normal stress and extrusion stress; c) oxide gap; d) the contribution of different contacting pairs on bond ratio; e) the final bond ratio and obtained bond ratio. 128

Figure 6-1 Optical morphologies of the interfaces of deformed plates at different conditions after heat treatment. a) 950 ˚C /10 mm·s^{-1}, b) 1050 ˚C /10 mm·s^{-1}, c) 1150 ˚C /0.1 mm·s^{-1}, c) 1150 ˚C /1 mm·s^{-1}, c) 1150 ˚C /10 mm·s^{-1} 135

Figure 6-2 The room-temperature tensile test results, including UTS, YS, EL for three-layer piled-up samples bonded at different conditions. a-c), different temperatures with a forging speed of 10 mm·s^{-1}; c-e), different strain rates at the temperature of 1150 ˚C. 136

Figure 6-3 The room-temperature tensile test results, including UTS, YS, EL for three-layer piled-up s bonded at different conditions. a-c), different temperatures with a forging speed of 10 mm·s^{-1}; c-e), different strain rates at the temperature of 1150 ˚C after heat treatment. ...138

Figure 6-4 The interface microstructure at the centre and edge zone of the plate bonded at 950 ˚C/10 mm·s^{-1}. a-b) as forged, c-d) after heat treatment. 140

Figure 6-5 The quantitative analysis of the δ phase in different locations of the multi-layer-built plate at the forging condition of 950 ˚C, 10 mm·s^{-1}. 140

Figure 6-6 The interface microstructure at the centre and edge zone of the plate bonded at 1150 ˚C/10 mm·s^{-1}. a-b) as forged, c-d) after heat treatment. 141

Figure 6-7 The interface microstructure at centre and edge zone of the plate bonded at 1150 ˚C/0.1 mm·s^{-1}. a-b) as forged, c-d) after heat treatment. 143

Figure 6-8 The interface microstructure and EDS mappings of the plate bonded at 1150 ˚C/0.1 mm·s^{-1} a) as forged, b) after heat treatment. 144

Figure 6-9 The simulated a) temperature, b) radial strain, c) bond ratio, results of the three-layer-built plate forged at 1150 ˚C, 10 mm·s^{-1}. 148

Figure 7-1 The EBSD IPF colouring maps showing the grain microstructure of pure aluminium samples, (a) Al-1, the single crystal sample with Grain G-1; (b) Al-2, the bi-crystal sample with vertical grain boundary; (c) Al-3, the bi-crystal sample with inclined grain boundary; (d) Al-4, the single crystal sample with Grain G-2.....152

Figure 7-2 The tensile curves of pure aluminium samples: a) Al-1; b) Al-2; c) Al-3; d) Al-4. 152

Figure 7-3 (a_1-d_1) The fracture aluminium samples and (a_2-d_2) the corresponding Schmid Factor calculation. (a) Al-1; (b) Al-2; (c) Al-3; (d) Al-4, note: blue line shows the slip plane and red arrow line in (a_2-d_2) indicates the sliding direction.....154

Figure 7-4 (a_1-d_1) The interrupted tensile pure aluminium samples, (a_2-d_2) SEM morphology images near the grain boundary and (a_3-d_3) corresponding GND maps from EBSD measurement. 155

Figure 7-5 The IPF colouring maps of polycrystalline pure nickel samples, (a) Ni-1, (b) Ni-2; and (c)the grain size distribution of Ni-1 and Ni-2. 156

Figure 7-6 (a-c) Enlarged view of the grain microstructure near the diffusion bonded interface in Ni-1 sample and (d) the SEM image. 158

Figure 7-7 The IPF colouring maps of polycrystalline pure nickel samples, (a) Ni-3, (b) Ni-4; and (c)the grain size distribution of Ni-3 and Ni-4. 159

Figure 7-8 The SEM image of Ni-4 near the bonded interface. 160

Figure 7-9 The tensile curves of polycrystalline pure nickel samples, a) diffusion bonded Ni, b) compress bonded Ni. 161

Figure 7-10 (a_1-d_1) The SEM images of Ni samples before the tensile test; (a_2-d_2) the OM images of fractured Ni samples after tensile test; (e) the OM image of diffusion bonded Ni

sample, Ni-1, white narrow marks the interface; (f) the OM image of the interface area of Ni-1 after tensile test and its corresponding EBSD IPF colouring map.....163

Figure 7-11 The in-situ observation (OM images) of the Ni-1 sample during the tensile test. 164

Figure 7-12 The OM images of interrupt Ni samples during the tensile test, (a) Ni-1; (b) Ni-2; (c) Ni-3 and (d) Ni-4; and the GNP maps for (e) the framed area in Ni-1 (a); (f) the framed area in Ni-3 (c).....166

Figure 7-13 The deformation mechanism of a) the bi-crystalline Al samples and b) bonded poly-crystalline Ni samples during tensile tests.....169

List of Tables

Table 3-1 The parameters for compression bonding tests of IN718 using Gleeble (B and R represent Bonding and Reference test, respectively) 59

Table 3-2 The forging/compression conditions 64

Table 3-3 The bonding conditions for pure nickel 68

Table 5-1 The temperature/strain rate-dependent model parameters for simulating the Gleeble bonding process 121

Table 5-2 The parameters relating to the oxide behaviour 121

Table 7-1 The tensile test results for pure aluminium samples 153

Nomenclature

Abbreviations			**Initials**	
IN718	Inconel 718		f	Nominal weld strength,
FE	Finite Element		R	Surface extension
HIP	Hot Isostatic Pressing		C	Constant
DB	Diffusion Bonding		σ_B	Shear strength of joint
VIM	Vacuum Induction Melting		σ_0	Shear strength of base
ESR	Electro-Slag Remelting		β	Film fraction
VAR	Vacuum Arc Remelting		Y	Surface expansion
PM	Powder Metallurgy		Y'	Critical surface expansion
PPB	Prior Particle Boundary		p_{nor}	Applied normal stress
Rx	Recrystallization		p_E	Extrusion pressure
DRx/DRX	Dynamic Recrystallization		r	Height reduction
DDRx	Discontinuous Dynamic Recrystallization		σ_m	Mean normal stress
CDRx	Continuous Dynamic Recrystallization		$\bar{\sigma}$	Effective stress
SRx	Static Recrystallization		$\bar{\varepsilon}$	Effective strain
GB	Grain Boundary		G_m	Welding criterion

HAB/HAGB	High-Angle Grain Boundary		G_D	Diffusion integration
LAB	Low-Angle Grain Boundary		t	Time
SFE	Stacking Fault Energy		T	Temperature
EBSD	Electron Backscatter Diffraction		R	Universal gas constant
bct	Body-Centred Tetragonal		Q_D	Diffusion activation energy
fcc	Face-centred cubic		k_0	Surface condition coefficient
DA	Direct Aging		K_{ad}	K criterion for extrusion bonding
DP	Delta-Processed		Q_{ad}	Q criterion for extrusion bonding
JMAK	Johnson-Mehl-Avrami-Kolmogorov model		p_{con}	Contact pressure
AM	Additive Manufacturing		$\bar{\sigma}$	Effective stress
SLM	Selective Laser Melting		v	Metal flow velocity
LENS	Laser Engineered Net Shaping		J	J criterion for extrusion bonding
DMD	Direct Metal Deposition		$\dot{\bar{\varepsilon}}$	Strain rate
DMLS	Direct Metal Laser Sintering		γ	Surface energy
EBM	Electron Beam Melting		γ_p	Energy for dislocation generation and movement
WAAM	Wire-Arc Additive Manufacturing		σ	Compressive stress

DEBD	Direct Electron Beam Deposition		a	Crack length
DED	Direct Energy Deposition		v	Poisson ratio
DLD	Direct Laser Deposition		E	Young's modulus
MC	Metal Carbide		U_T	Heating energy
STA	solution annealing + traditional aging		A	Section area
ARB	Accumulative Roll Bonding		p	Migration driving pressure
SPD	Severe Plastic Deformation		M	Temperature-dependent coefficient
TLP	Transient Liquid Phase		v	Migration rate
DAZ	Diffusion affected zone		D	Initial grain size
MD	Molecular Dynamics		p_D	Stored energy related driving pressure for migration
PPZ	Particle precipitation zone		p_Z	Zenger pinning pressure for migration
TEM	Transmission Electron Microscopy		γ_s	Boundary energy
SEM	Scanning Electron Microscopy		γ_b	High-angle boundary energy
OM	Optical Microscopy		F_v	Volume fraction of particles
IGB	Interface grain boundary		d	Diameter of particles

CSAM	Cold Spray Additive Manufacturing		R_a	Surface roughness
BJAM	Binder Jetting Additive Manufacturing		η	Critical strain
UAM	Ultrasonic Additive Manufacturing		ε	Surface strain
AFSD	Addictive Friction Stir Deposition		f_{o-o}	Area fraction of contacting oxide-oxide pair
FSAM	Friction Stir Additive Manufacturing		f_{o-m}	Area fraction of contacting oxide-metal pair
BIAM	Beijing Institute of Aeronautical Manufacturing		A_n	Nominal area
SR	Strain Rate		A_{o-o}	Actual contact area of oxide-oxide
Temp.	Temperature		A_{o-m}	Actual contact area of oxide-metal
B	Bonding		e	Oxide gap
R	Reference		K	Oxide-related linear coefficient
AC	Air cooling		λ	Length of the oxide fragment
C	Centre zone		p_{ex}	Extrusion pressure
E	Edge zone		t_c	Thickness of oxide film
RT-T	Room-temperature tensile test		Y_m/ Y_{m-m}	The yielding strength of metal

HT-T	High-temperature tensile test		f_{m-m}	The contacting metal-metal area fraction
OP-S	Oxide Polishing Suspension		A_{o-m}	Actual contact area of oxide-metal
EDS	Energy-dispersive X-ray spectroscopy		C_{m-m}	Achieved cohesion between contacting metal-metal pair
IPF	Inverse Pole Figure		C_{o-m}	Achieved cohesion between contacting oxide-metal pair
E/EL	Elongation		C_{o-o}	Achieved cohesion between contacting oxide-oxide pair
UTS	Ultimate Tensile Strength		α_{m-m}	Cohesion coefficient between contacting metal-metal pair
YS	Yielding Strength		α_{o-m}	Cohesion coefficient between contacting oxide-metal pair
HR	Height Reduction		α_{o-o}	Cohesion coefficient between contacting oxide-oxide pair
ODS	Oxide Dispersed Strengthened		σ_n	Normal pressure
PPT	Precipitation-Time-Temperature		p_{ex}	Extrusion pressure
GND	Geometrically Necessary Dislocation		σ_{Ni}	Tensile strength of bonded Ni
			$\sigma_{Al_2O_3}$	Tensile strength of bonded Al_2O_3
			$\sigma_{Al_2O_3/Ni}$	Tensile strength of bonded Al_2O_3-Ni

			Y_{o-m}	The yielding strength of contacting metal-oxide pair
			Y_{o-o}	The yielding strength of contacting oxide-oxide pair
			δ	Strain-amplifying factor

Chapter 1 Introduction

1.1 The challenges in heavy manufacturing

Large-scale metal-formed parts are widely used in various industries such as steel, power generation, quarrying, petrochemical and high-energy physics, and they play critical roles in ensuring the reliability and safety in such sectors [1-4]. These land-based plants usually serve under extreme loads and harsh environmental conditions and require reliable mechanical performance. For example, the typical large components in nuclear plants are normally heavily forged many times to ensure that the grain structure is homogeneous and fine with minimum voids and defects. This is to satisfy the high safety requirements for strength, fatigue resistance and corrosion resistance under the applied cyclic high pressure, high temperature and corrosive environment, which are particular safety considerations for the nuclear power industry [2]. The availability of heavy engineering plants is essential to the development of heavy industries and related industries required.

To improve plant efficiency, an increase in the size of these key large components is demanded. In the pursuit of meeting performance requirements, expanding the size and improving the approach of heavy manufacturing is the current challenge. As the size of the parts increases, defects in cast ingots get more serious. There are cases where larges ingots cannot be produced because of the severe chemical segregation and thermal cracking issues[5, 6]. The existing manufacturing method is smelting + forging. In the initial cast ingots, coarse grains and defects like voids, shrinkage, cracks and segregation are inevitable[7]. Hence, subsequent forging processes are necessary to refine the grain size and eliminate the defects[8].

In practice, successful heavy forging practice depends on the accurate design and detailed planning. To improve this practice, researchers have extensively studied material flow and microstructure evolution in various processes such as upsetting, stretching, etc. These studies turned to the Finite Element (FE) analysis as a way of reducing trial and error costs to a great degree[8, 9]. As well as the computer-aided design process, ultra-large component production also depends on equipment capacity, which includes both heavy presses and heavy operations. These main heavy facility constructions have only been seen in a few countries [9].

With the size of parts increasing, the requirements on the forging equipment become greater and this results in more difficulties for the overall operation and coordination[8, 10].

Optimization of the process not only brings huge invisible benefits by reducing the lead time, cost of equipment, labour, and transport, but also relieves the ecological stress imposed by increasing the equipment capacity. The ability to make the most use of existing equipment and yet further scale up the production capacity means a lot in the development of both economy and ecology.

1.2 Aim of the work and research approach

1.2.1 The challenges in manufacturing large IN718 parts

IN718 is (Cr-Ni-Fe)-based superalloy, which is extensively used due to its excellent strength and its resistance to oxidation and corrosion at elevated temperatures [3, 11-13]. Its application has been seen in areas such as gas turbines and land-based power plants under supercritical conditions [10, 13, 14]. For example, a typical GE heavy-duty gas turbine could be ranged from 6,000-15,000 kg, and it normally begins with an ingot of 685~915mm in diameter[10]. In oilfield industries, nickel superalloys are used for critical wellhead distribution components, which are machined from single ingots weighing as much as 9,000 kg[3].

Due to the size effect, transitioning the traditional IN718 forming process, e.g., casting and hot forging, is not straightforward. Common casting problems, including segregation, hot crack and dendritic structure, are especially difficult to deal with when manufacturing large IN718 ingots [10, 13]. Beyond that, the subsequent hot forging process for large ingots puts a high requirement on the tonnage of the equipment and its supporting environment[14]. Even though a lot of effort has been put into eliminating casting defects, e.g. improving the casting process by introducing electrical or magnetic fields[6], and also into developing advanced forging equipment with higher capabilities[9, 14], to control these large ingots free of defects, whilst also chasing low energy consumption is still a big challenge[5, 6, 13]. On the other side, Additive Manufacturing (AM) could potentially produce large parts through layer-by-layer deposition. Among all the developed AM technologies, Direct Energy Deposition (DED) offers a relatively high production rate and shows the potential to fabricate unconventional large-scale nickel superalloy structures. However, since solidification is involved, problems, like dendritic microstructure and thermal cracks still exist in these fusion based DED technologies[15, 16], and leads to inferior mechanical performance[17, 18]. Moreover, even though the use of wire feedstock material helps improve efficiency, the typical dimension for AM is at meter level and its use in land-based-scale application at has been barely reported.

1.2.2 The strategy

To avoid the large-size ingot preparation step, the bottom-up construction concept from additive manufacturing could be borrowed for large-size component manufacture[5]. The strategy is to develop a new incremental additive forming-bonding method without melting the materials. Instead of powder or wire, plates with high quality and larger dimensions would be used as feedstock to ensure a high production rate. As shown in Figure 1-1, this concept could be achieved in two ways: one, multilayer plates are to be piled up, followed by a sequence of hot deforming processes to achieve metallurgical bonding between every two layers, finally forming to get the desired shape (Figure 1-1a); or two, in which plates (or strips) are to be continuously fed on top of the previous layer, and deformed at elevated temperature by rolling/forging (which depends on the machine design with following roller or hammer installed) to achieve metallurgical bonding between layers. And a prototype with a rolling design is schematically shown in Figure 1-1b.

Compared with traditional ways of manufacturing large-size components, the advantages of the proposed technique mainly lie as follows:

a) As introduced, this forming process based on solid-state bonding could provide a solution to avoiding casting defects in a large ingot manufacturing process. Since solid-state bonding is achieved without melting material, and so enables a broad range of material candidates, including dissimilar materials and thermally sensitive materials with poor weldability (like high-strength aluminium).
b) As shown in Figure 1-1 a and b, the part is built by forging bonding or roll boning and the bonding zone can be controlled within the local deformed area. By scaling down the size of the bonding zone, the full-scale deforming can be adapted to an incremental deforming process, which makes the process less dependent on the tonnage of the equipment.
c) Each layer is to be joined in an inherently more controllable process, particularly from the processing parameter and microstructure perspectives. Thus, the component geometry and component quality would be more predictable, which endorse its potential of being adapted in digital manufacturing.

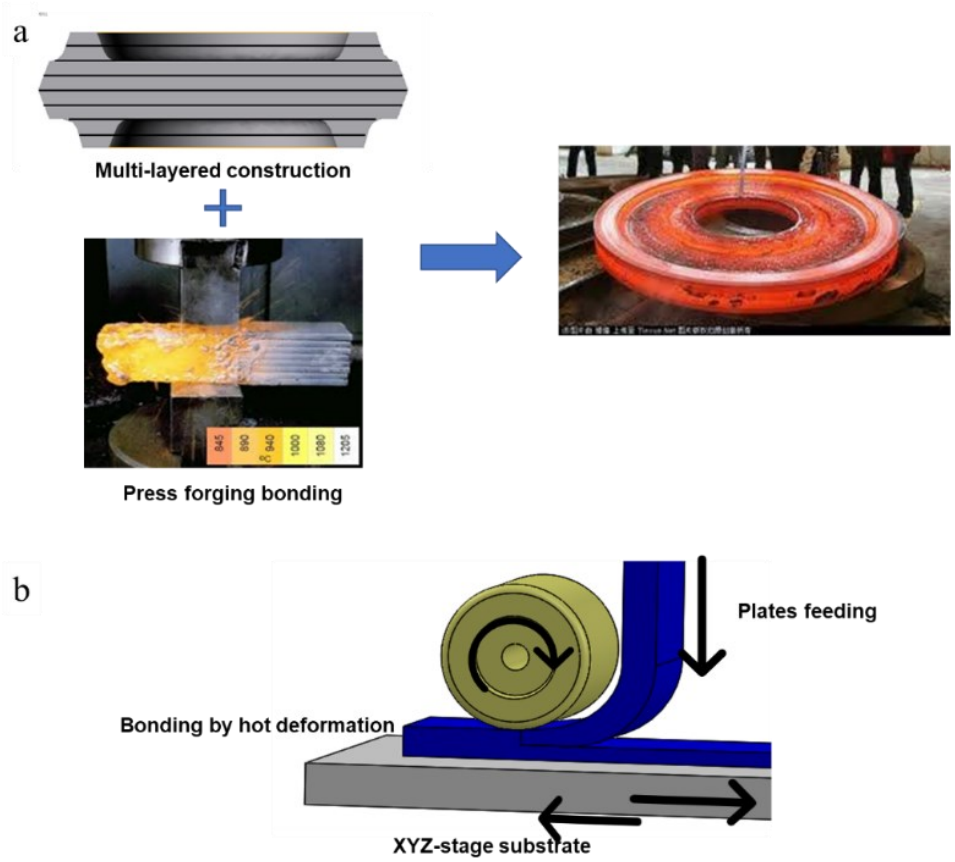


Figure 1-1 Two ways to achieve the new proposed forming concept based on solid-state bonding for manufacturing large-scale components. (a) additive forging; (b) solid-state AM.

1.2.3 Objectives of the research

The overall aim of this project is to determine the factors influencing the successful forging of multi-layered components and to investigate and predict the bond quality at the interface between every two layers. The first strategy mentioned in 1.3.2 is studied and a trial test is designed in this research, while the second strategy is documented in detail elsewhere.

To achieve this aim, the following objectives must be met:

1. Characterization of the interface bonding behaviour under various deformation conditions. Variables to be evaluated include Strain, Temperature, Strain rate, Surface condition and Vacuum condition.

2. Bonding mechanism and model development for bond quality prediction. Mechanical properties to be evaluated. Correlate these bond qualities with the characterised bonded

interfaces and embed these relationships into a model to be implemented in Finite Element Analysis software. Simulate the bonding process with bar samples to predict the bond quality of the interface.

3. Forging of prototype multi-layer plates. The forged plates were to be Sectioned to determine regions where metallurgical joining occurs and microstructure evolution near interfaces. Mechanical properties and their uniformity at the different locations over the plate are to be evaluated after standard ageing heat treatment. Prototype plates should be forged to determine the effect of billet temperature and strain rate.

4. Provide recommendations for future experimental forgings to improve the joining attained between different layers.

1.3 Structure of thesis

This thesis begins with Chapter 1 to give the background introduction of the heavy manufacturing processes and the fit of the new proposed forming method in the aforementioned field.

A literature review is followed in Chapter 2, presenting a state-of-art understanding of the key solid-state bonding process in the proposed forming method. A comprehensive review of the solid-state bonding technologies, bonding mechanisms, developed models is presented. Particular attention is given to the solid-state bonding of nickel-based IN718. A background to previous work conducted in the hot compression bonding of different materials is described, as well as previously investigated bonding mechanisms. Furthermore, a review of bonding by forming, and the barriers to successful bonding with potential solutions is presented.

The overall methodology is introduced in Chapter 3, presenting the test and simulation plans for (i) solid-state bonding test with bar sample; (ii) bar sample bonding simulation; (iii) multi-layer plate forgings and (iv) bonding mechanism investigation with typical interfaces.

In Chapter 4, the bonding behaviour under various hot deformation conditions is investigated with bar samples using Gleeble. The bonding mechanism is discussed based on the microstructure characterization near the bonding interface at different strain levels. Effects of deformation conditions, including temperature, strain, and strain rate are studied. The correlation between the microstructure and the mechanical properties of the joints are built.

Based on the bonding mechanism proposed in Chapter 4, a model to predict the interface bond quality is presented in Chapter 5. The bar-sample bonding process under the examined conditions is simulated. The predicted interface bond quality will be presented and compared with the test results from Chapter 4.

In Chapter 6, the new laminated construction concept is preliminarily realized with the prototype multi-layer-built plate forging trials. Compared to the bar sample bonding tests, the bonding is conducted under practical forging conditions. Parameters that are investigated include billet temperate and forging speed. The model stated in Chapter 5 is used to explain the bond results from the multi-layer plating forgings. The mechanical properties of the plate (including at room temperature and service temperature) and its uniformity are documented to provide a general impression of the potential of this technology in real applications.

An additional bonding mechanism study is conducted in Chapter 7, in which the role of interface grain boundary migration in determining the final bond quality is investigated with typical bonded interfaces. Excluding the affecting factors like oxide and micro-voids allows the in-depth understanding of the microstructure-bond quality evolution during bonding is given.

Finally, the conclusions drawn from this work are presented in Chapter 8, along with recommendations for future work, to overcome the challenges encountered in this research and drive the concept of multi-layer forging technology based on solid-state bonding toward a higher technology readiness level.

Chapter 2 Literature review

2.1 The manufacturing of Inconel 718

Nickle-based superalloy has been widely used in aeronautical, energy, chemical and nuclear industries due to its superior and stable performance at high temperatures. In the family of nickel-superalloy, Inconel 718 (IN718) has won especially extensive attention due to its high thermal and chemical resistance, preferable precipitation kinetics and good formability and weldability [12]. IN718 has presented half of their world tonnage and accounts for up to 50% of the weight of aircraft turbine engines, being the main component for discs, blades and casing of the high-pressure Section of the compressor and discs as well as some blades of the turbine Section. It also finds several applications in rocket engines and nuclear power plants as structural components[12, 16, 19].

IN718 is a γ'' precipitate hardened Cr-Fe-Ni superalloy. The addition of elements, e.g. Al, Cr, Ti, on one hand, endows the precipitation strengthening and the oxygen resistance; however, on the other hand, raises detrimental problems including solidification cracking and liquidation cracking problems in welding[16]. IN718 parts are manufactured through various processes such as the traditional melting and forming, casting, powder metallurgy (PM), powder metallurgy and subsequent forming [9][12], and the most recent studied additive manufacturing.

2.1.1 The casting ingots of IN718

Due to the high alloying degree and strengthening precipitation of IN718, it is designed to be used in a wrought state, rather than directly after casting solidification. The Induction Melting (VIM), and a remelting process including Electro-Slag Remelting (ESR) and Vacuum Arc Remelting (VAR) are used to convert the raw materials into ingots with accurate uniform composition[12]. Depending on the size of the obtained casting IN718 ingots, these ingots usually have macro- or micro-segregation, resulting in a non-uniform microstructure chemical composition distribution. For example, the Nb-rich Laves phase would be formed during IN718 solidification between dendritic structures presenting with island or blocky shapes[20], and these eutectic phases have been observed where the failure initiation sits in service at high temperature. The standard melting procedure and typically attained microstructure is presented in Figure 2-1. Thus, the IN718 ingot after casting would normally be subjected to various types

of homogenisation practices and hot deforming processes of various types to obtain the required homogeneous microstructure and uniformity.

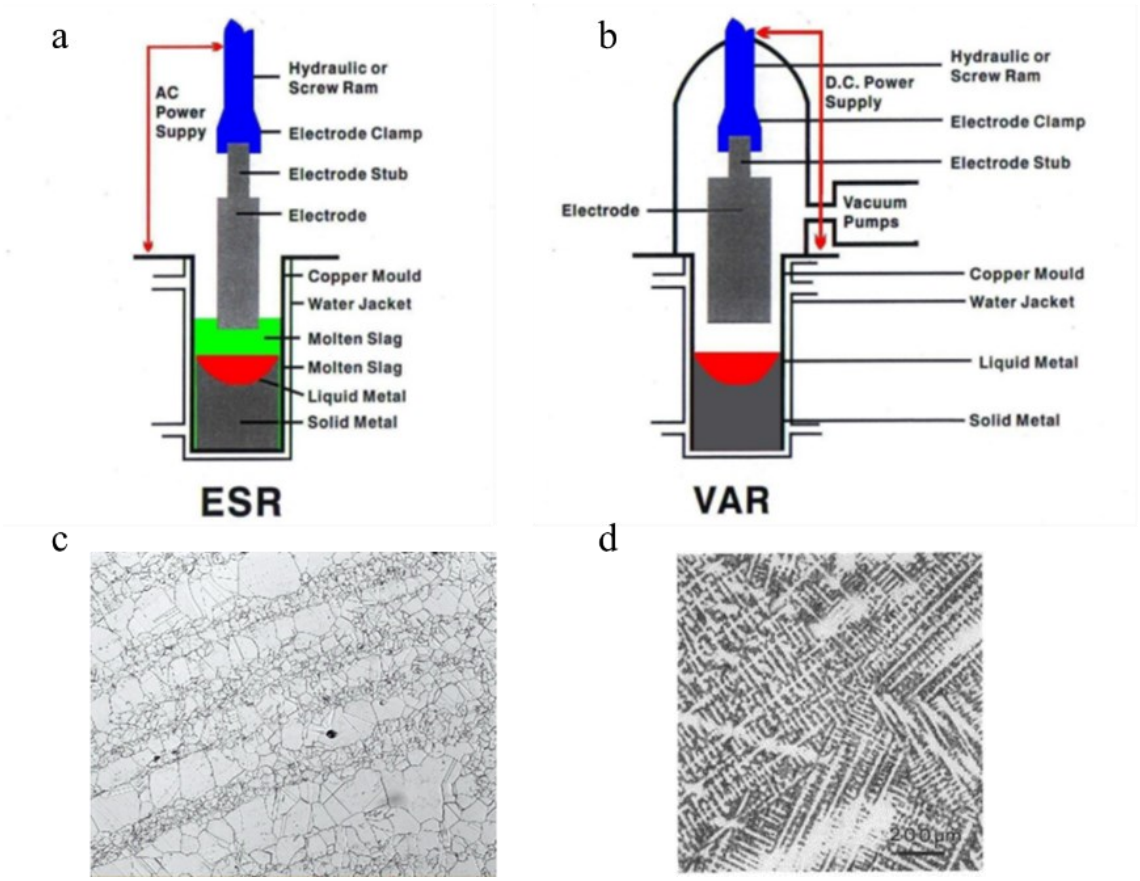


Figure 2-1 a) Schematic of the Electro-Slag Remelting (ESR) and b) Vacuum Arc Remelting (VAR); c) the microstructure by unstable melting; d) macro-etched transverse Section of as-cast IN718. [21]

2.1.2 The Powder Metallurgy (PM) of IN718

For IN718, the Powder-based metallurgy process is an effective routine to eliminate the segregation that existed in traditional casting, among which hot isostatic pressing (HIP) is the most commonly used near-net-shape forming technique. Starting from spherical pre-alloyed powder particles, HIP is undertaken by consolidation with capsule wrapped under hydrostatic pressure, and sintering processes at a combination of pressure, high temperature and long time. With the flexibility of the wrapping capsule, HIP has been used as a near-net-shape forming technology[22]. Isostatic pressure is passed from the gas, acting on the contacted power surfaces, however, the overall applied pressure is not high enough leading to severe

deformation for each powder. As a result, pores originated from the packing of power[22] and prior particle boundary (PPB) networks are often seen. The precipitates along the PPB in the as-HIPed specimen were mainly oxides and carbides, which come from the contamination on powder surfaces[23]. The set-up for HIP and obtained typical microstructure after HIP is seen in Figure 2-2. To assure the quality of the HIPed part, a long time is needed for the pores to be closed via diffusion-based bonding between particles. And the detrimental PPB network usually can be eliminated by strictly controlling the oxygen content[24] or surface contamination of powder[23]; moreover, the formation of PPB is also investigated to be related to HIP temperature[25].

Except for a few superalloys, e.g. Rene 95, MERL 76, which can be manufactured through simple HIP plus heat treatment, most PM nickel-based superalloys need to be processed with hot deforming processes to effectively break the PPB networks[25]. This hot-working routine includes subsequent upsetting, extrusion and following hot forging or rolling. Most recently, a new powder-based forming technique has been proposed by direct forging the capsuled and densified powder[26]. With the introduction of severe plastic deformation, the pore problem and PPB can be solved in the meantime with the powder sintering process.

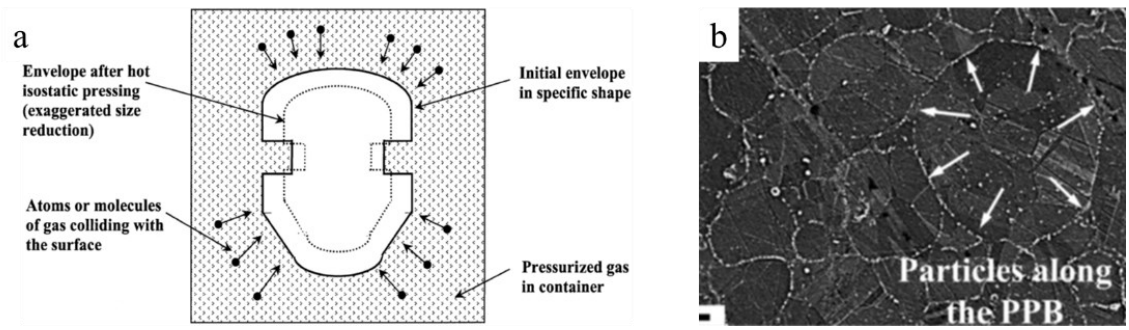


Figure 2-2 a) Schematic of a HIP set-up[22]; b) typical as-received microstructure with prior particle boundaries (PPB) after HIP[23].

2.1.3 The hot deforming of IN718

Due to the high strength and fatigue requirements for IN718 in applications, uniform and fine structures with small equiaxed grains have been favourable and the aim of the manufacturing process [14, 20, 27-29]. Because of the undesirable coarse dendritic microstructure for casting ingots and PPB problems for HIPed billets, hot deforming has been broadly adopted as a subsequent process to achieve the finely wrought microstructure. These hot deforming process

usually includes the preliminary repeated upset/draw processes and the following multi-step hot deforming to get the final shape. According to the shape of different components, the hot forming process includes extrusion for profiles[30], rolling for cylinders and rings[31], and the forging for most disk or blade parts[11, 14, 32, 33].

The grain refinement of IN718 is achieved by dynamic recrystallization (DRx) over the thermomechanical working. It is generally agreed that there are two mechanisms for DRx, namely discontinuous dynamic recrystallization (DDRx) and continuous dynamic recrystallization (CDRx). DDRx is characterized by clear nucleation and growth stages via grain boundary (GB) bulging, while CDRx is featured with progressive transformation and lattice rotation from the dislocation cell boundary to low angle boundary (LAB), and further to high angle boundary (HAB)[34-38]. In general, the DRx mechanism is related to the materials formability, like the crystal structure (CS) and stacking fault energy (SFE). CDRx has been observed in high SFE metals, such as aluminium, ferritic steel and beta-titanium as the major deformation mechanism and DDRx is more commonly seen in low SFE metals, like nickel and some steels[35-37, 39]. In hot deformation practice, IN718 presents a typical necklace microstructure over the DRx process[34, 40, 41] and the preferential nucleation near the grain boundaries (GB) is dominated by the boundary bulging according to the observation in studies [34, 37, 42-44]. The GB bulging is considered to be driven by the energy difference between adjacent grains, which also accounts for the strain-induced GB migration process and the grain growth[44]. Thus, at high temperature and low strain rate, DDRx is promoted and IN718 shows a high Rx fraction. However, recent studies show that both DDRx and CDRx are involved in the hot deformation of IN718. With the help of electron backscatter diffraction (EBSD) technology, the transformation from LABs to HABs have been captured in [34, 35, 44, 45]. It shows that CDRx is highly dependent on the deformation condition since it is directly related to the dislocation behaviour: Xie et al. [35] found that when the IN718 is forged at sub-solvus temperature, the CDRx became an important mechanism as the δ phase located along GBs prohibited its migration and helped the stacking of dislocations; Azarbarmas[34] showed the promoted CDRx in IN718 deformed at higher strain, larger strain rates and lower temperatures, which is preferential for dislocation accumulation. Thomas et al. [45] stated the DDRx/CDRx mechanism in the IN718 deformation is that the boundary bulging initiates the nucleation and forms the small grains along GBs (DDRx), while within the deformed grain, the dislocation

accumulates and are relocated near sub-grain boundaries, promoting the lattice rotation and forming newly Rxed grains in the original grains(CDRx).

Except for the grain size requirement for the hot deformation process, the enhancement of wrought IN718 also highly depends on the strengthening phase. As a precipitation hardening superalloy, the primary hardening phase for IN718 is *bct*-γ''(Ni_3Nb), and *fcc*-γ' (Ni_3(Al, Ti)) as the secondary in γ(*fcc*)-matrix. The obtainment of the expected strengthening phases is through appropriate double ageing [12, 46] or direct age (DA) [47]heat treatment after the thermomechanical working. Besides, δ (orthogonal, Ni_3Nb) has also been a common phase in wrought IN718 and the presence of the δ-phase affects the performance in a varying way, which depends on its shape and distribution[20]. A proper amount of δ-phase in rod shape improves its thermal strength. During hot deformation, the behaviour of the δ-phase shows a strong dependence on working conditions and an interaction effect with the microstructure. By intentionally controlling the amount, the existed δ-phase can effectively impede the grain growth and the corresponding technique, namely delta-processed (DP) forging[48, 49], has led to improved grain size control over the hot working of IN718.

The final performance of wrought IN718 is highly sensitive to the deforming condition and obtained microstructure, thus, simulating the hot deformation behaviour and its microstructure is of great importance for the process design and quality control in practical production. Over years, the hot formability of this alloy in a different state, e.g. as-cast[21], wrought[50] or as-PMed[51], has been studied over wide ranges of temperature and strain rate. To present, the constitutive relation modelling has mainly been classified into three categories: the phenomenological models, physical-based and neural artificial network models[39]and the most developed constitutive equations for IN718 are phenomenological and physical-based, or their combination. IN718 shows typical viscoplastic deformation behaviour (lower flow stress under higher temperature and lower strain rate) and presents work hardening, softening and steady stages on flow curves. This combined effect of temperature and strain rate is classically unified through the Zener-Hollomon(Z) parameter to formulate the experiment data phenomenologically and it has been associated with the flow stress in different ways. Sellar et al. [39, 52] proposed exponential, power or hyperbolic sine functions to associate strain and stress with the Z parameter, and Azarbamas[50] compared the stress predicted with three different functions in Sellars models and concluded that the power-law constitutive equation is the most easy-to-use for IN718. Based on the observation of Rx and its kinetics, Avrami

equations has widely been used to describe the phenomenological relation between Rx and stress/strain[39, 53] and constitutive equations in this type have also been successfully implemented into FE simulation for industrial production applications[54]. Johnson-Mehl-Avrami-Kolmogorov (JMAK) type model is relatively simple and stable, and it is implemented in commercial FE software and used to link processing parameters and microstructure in forging practice. A typical plate forging process simulation results and characterized microstructure is shown in Figure 2-3.

On a phenomenological basis, the mechanism at different stages has been taken into consideration in constitutive model development to better describe the hot deformation behaviour of IN718. Lin Y.C.[55] et al. introduced an isotropic internal variable, which is temperature/strain rate-dependent, to describe the dynamic strain hardening and recovery behaviour or Rx-related dynamic softening. Shen [56] and Reshetov [54] et al. incorporated Rx occurring at different stages, e.g. static recrystallization (SRx) or post-Rx grain growth to describe the obtained microstructure and predict stress. Lin [57] developed a physical-based constitutive model considering the dislocation behaviour in hardening, softening by Rx and recovery and damage effect of defects and Tang [58] has applied Lin's model on IN718 and showed flow behaviour and microstructure in good agreement with calculation. Zouari [59] adopted a mean-field approach to simulate the evolution of dislocation density in Rx nucleation and grain growth. Phenomenological models do not call for detailed understanding and are simple to use, however, cannot describe all deformation behaviours; while physical-based models can give a reasonable description but need complex material parameters to be determined.

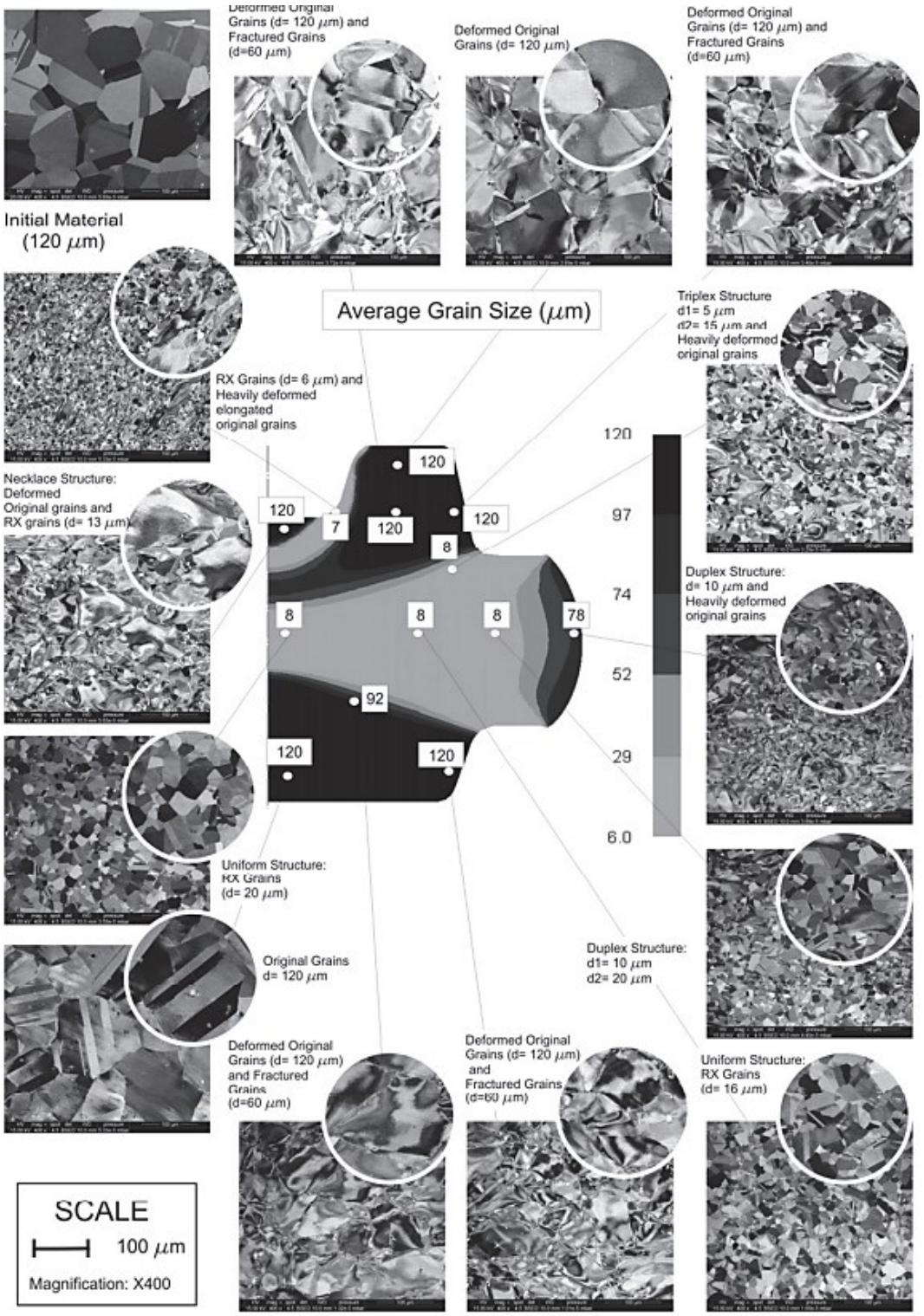


Figure 2-3 Grain-size comparison between metallographic analysis and microstructure simulation for IN718 forging.[60]

2.1.4 The additive manufacturing of IN718

Additive manufacturing (AM) is a merging manufacturing technique that builds parts layer upon layer from pre-designed 3D model data. Since it was first patented in the late 1980s, this bottom-up manufacturing technique has attracted extensive interest because of its irreplaceable advantages in producing complex geometry or complex multi-material compositions, laminating dissimilar internal structures (lattice structures) and fully integrated functional components[61, 62]. For IN718, its good formability has enabled the applicability of most metal AM methods to this alloy. Most common AM for IN718 includes the powder-based methods[63], like selective laser melting (SLM)[23, 29, 64-67], laser engineered net shaping (LENS)[68, 69] and direct metal deposition (DMD)[70], direct metal laser sintering (DMLS)[71, 72], electron beam melting (EBM)[72]; wire-based methods, like wire arc additive manufacturing (WAAM)[17], direct electron beam (wire) deposition (DEBD)[73], direct laser deposition (DLD)[74].

As melting is involved in most AM techniques, typical AM microstructure has column grains with MC-type carbide, δ-phase and eutectic Laves phase distributed between dendritic cells. Moreover, due to the rapid solidification rate in AM process, AM-IN718 usually presents smaller average grain sizes than cast and wrought IN718, as compared in Figure 2-4, and ends up with a supersaturated solid solution and absence of strengthening γ' and γ''[17, 61, 73]. The quality of the AM parts depends on the microstructure and the presence of defects, such as voids from contaminating evaporation or lack of fusion between layers, or cracking caused by thermal residual stress[17, 63, 73-75]. The AM quality control can be done by optimizing processing parameters, including the heat resource type, heat input, scanning strategy, scanning speed, powder size, wire feed speed etc[63]. Besides, as-built IN718 parts which were subjected to heat treatment would usually present better performance. Common heat treatment after AM process includes solution annealing + traditional ageing (STA), homogenization + STA, DA and the aim is to reduce the segregation, promote the precipitation of strengthening γ' and γ'' phases and modify the precipitation of δ-phase[63, 65, 76]. Through the effort on the AM process optimization and proper heat treatment, final static properties of AM IN718 comparable to wrought IN718 have been reported in many studies[63, 65, 68, 69, 73, 77]. As a superalloy, the application of IN718 under cyclic load and extreme conditions imposes high requirements upon its creep and fatigue endurance, however, the porosity problem, poor surface quality, unfavourable microstructure of AM parts deteriorate its dynamic service

performance[73]. Except for the optimization measure aforementioned, a hybrid AM process integrating other manufacturing methods, e.g. HIP[66, 73, 78] or hot forging[67, 79, 80], was proposed to eliminate the porosity, modify the microstructure, so as to improve the fatigue and creep response of AM IN718. Properties of as-built IN718 using various AM methods are reviewed and summarized[61, 73, 77] and typical comparison results are shown in Figure 2-4.

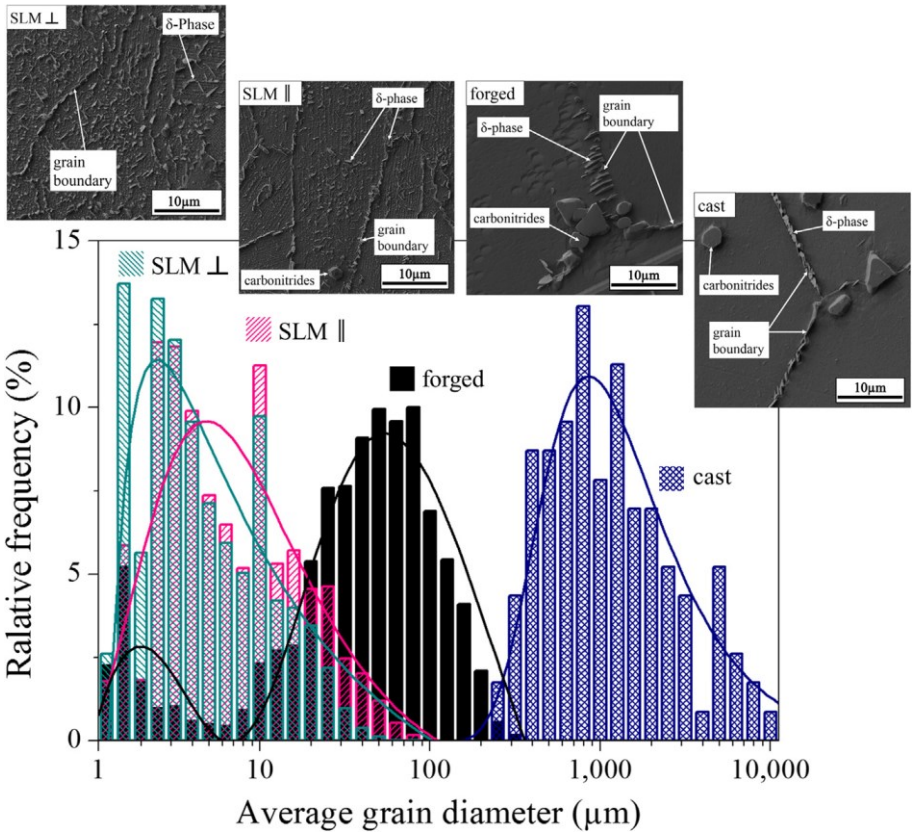


Figure 2-4 Grain size distribution of SLM (Selective Lase Melting), forged and cast microstructure[29].

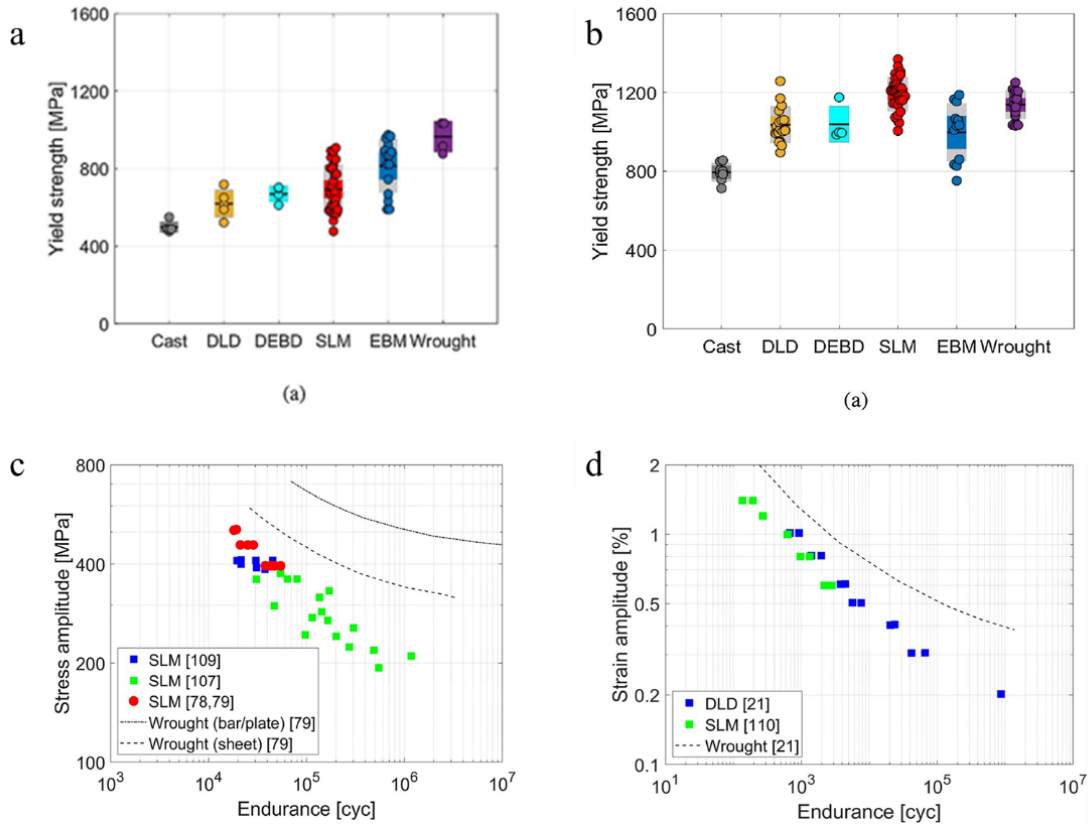


Figure 2-5 The review on yielding strength of AM-IN718 in a) as-built state; b) after heat-treated; c) fatigue properties ; d) creep properties of SLM IN718 at room temperature[73].

Despite the unique advantages of AM technology, the successful application of IN718 has been quite limited in practice[61, 81]. Lack of understanding of the sensitivity of the microstructure and properties to AM process parameters, unsatisfactory performance in practical service and under-developed qualifications have been the main reasons for this limitation[73].

2.2 Understanding the solid-state bonding mechanism of metals

Compared with fusion based welding methods, bonding in solid-state shows irreplaceable advantages and broad applicability in joining materials with poor weldability and dissimilar materials. As there is no melting and solidification involved, some defects such as thermal cracks and coarse dendritic microstructure[82, 83], and undesirable phase transformation[84, 85], could be avoided. To achieve metallurgical joining, fresh metals are brought into intimate contact and form a metallic bond by diffusion, creep[86] or plastic deformation[85], among which plastic deformation is the most efficient and rapid method. This has been implemented in varies joining processes, e.g. cold pressure welding[85, 87, 88], roll bonding[84, 89-92],

extrusion bonding[84, 85] and friction welding[85, 93, 94]. Also, it has been involved in some important manufacturing processes including the direction of power forging[26] or the crack healing in hot forging[95, 96] or rolling[97].

The mainstream mechanisms and models developed to describe the solid-state bonding process are reviewed. They mainly include (1) the oxide film theory for pressure welding and roll bonding; (2) the diffusion bonding theory dominated by micro-voids closure; (3) the energy barrier theory developed from extrusion bonding; (4) recrystallization mechanism.

2.2.1 Cold Pressure Welding and Roll Bonding

Cold Welding (or Cold Pressure Welding) is generally referred to as a method of using pressure to join two materials without heat[87]. Instead of liquifying material for the atom to diffuse, the joining is achieved through a solid-state diffusion process[98]. Since there is no external heating and solidification involved, the bonding process can be done quickly. According to the way of applying the joining force, the two most common cold welding techniques are butt jointing and lap jointing[87]. Butt joints are mostly adopted for welding wires with a diameter ranging from 0.5-10 mm, while lap joints are commonly used for joining metal sheets or sheets to rods.

Cold wire pressure welding can join wires, mainly with aluminium, copper, 70/30 brass, zinc, silver and silver alloys, nickel, and gold[98], given the good surface cleanliness (free from oxide layers or other contamination films), sufficient force or strain depending on the material, and enough ductility for at least one of the materials[85]. For the butt joining, the contact area is limited and deformation is large enough to break up the oxide layer on the surface, thus the requirement for surface preparation is lower than the lap joining, for which the contact area is much larger.

Roll Bonding is classified as pressure welding, in which the multi-layered metal sheets are passed through rollers and bonded under sufficient thickness reduction. Roll bonding has successfully been applied in joining similar and dissimilar materials including aluminium, copper, nickel, steel and titanium[91]. As an effective metal cladding technique, it has been successfully used in manufacturing large layered composite sheets and foils[91]. Normally, in order to achieve a sufficient deformation for sound bonding, two or even more layers of sheets are stacked to be rolled. In some cases, two layers can be repeatedly rolled and folded to achieve an accumulative strain as high as 4.0[99], and this technique is so named accumulative roll

bonding (ARB). Apart from being used to produce composite laminates, ARB, as a severe plastic deformation(SPD) technique, has been applied to prepare ultra-fined nano-structured grains[100]. The recrystallization and grain microstructure refinement have been studied in aluminium[101, 102], nickel[103, 104], ferrite-perlite steels[105], and et al. With the increase of stacking cycles, the bonding interfaces between layers are disappearing and the sound bonding is achieved with the refinement of grains.

Similar to lap joint, the roll bonding for strips involves a large bonding area, thus demanding careful surface cleaning and preparation[91]. Also, there are other two main groups of factors determining the final bond quality: rolling parameters, e.g., the rolling reduction, temperature and shape factors[102, 106, 107]; materials properties, including their strength ductility and crystal structures[91, 108, 109].

In most cases, roll bonding is conducted at room temperature; however under certain circumstances, rolling at warm temperatures is also favoured to achieve a good diffused bond, for example, materials like steel or nickel is not suitable for cold welding and usually requires pre-heating over 200 ˚C for a better joinability and workability[98, 110-112]. However, for ARB, the commonly adopted elevated temperature is lower than 0.3 of the melting point temperature, to avoid the occurrence of unexpected reduction of accumulated strain and grain growth[110].

Mechanisms

For both cold wire pressure welding and roll bonding, a perfect bond is hard to achieve due to the presence of oxide film and a contamination barrier at the interface. [91, 113, 114]. To explain the cold pressure welding behaviour, different mechanisms and theory have been proposed, among which the film theory has been the most accepted mechanism and it states that the bonding process involves the film fracture, metal extrusion and bonding.

In earlier studies, Milner[115] and Conard[114], et al. stated the significance of surface preparation in cold pressure bonding; Mohamed [116] and Vorm[117] studied the effects of surface roughness and metal properties on the weld strength, and revealed the dependence of weld strength on the fractional area of exposed clean metal, which was directly related to the deformation level; Later on, Bay[89, 118, 119] first confirmed the governing effect of normal pressure on the weld strength in addition to the surface expansion, and proposed the mechanism incorporating surface layer fracture and virgin metal being brought into contact; Le et al.[90]

observed the fracture of the coated oxide film on interfaces and metal extrusion processes during roll bonding and supported Bay's explanation of the bonding mechanism. In recent bonding mechanism studies, Bay's film theory has been developed and modifications have been made by[120-122] based on the discussion about the behaviour of the surface layer.

Except for the film theory, other mechanisms proposed for explaining cold pressure welding includes recrystallization theory, energy barriers theory and diffusion theory[121, 123]. In the welding study of aluminium, [124] stated that given the large deformation, the critical recrystallization temperature could be reduced and the recrystallization occurred. This recrystallization theory, proposed by [125], suggests that crystal growth minimize the effect of oxide film [121]. However, in most cold pressure welding or roll bonding studies, no obvious crystal growth is observed in joints and the bond line remains visible and straight[101, 121, 126], especially for bonding dissimilar materials[112, 127].

For the pressure welding of dissimilar materials, atom diffusion occurs and contribute to bond formation to some extent. In the welding practice of different combinations of metals, a solid-solution phase was observed for infinitely miscible Cu-Ni and the intermetallic compound formed for Al-Cu combinations; for Ag-Cu with limited miscibility, the crystal structure units for Ag and Cu were found distorted as the atoms were diffusion into each other[123]. The diffusion in cold pressure welding is believed to be through the plastic deformation on the surface rather than the temperature. The crystal defects and internal stress induced by deformation lower the diffusion activation energy and facilitate the atom diffusion, thus forming a thin diffusion layer[123, 128]. However, this diffusion theory could not explain the bond achieved for Ag-Ni, in which the two metals are not soluble and no diffusion layers are observed[123]. And also, even for the observed diffusion layer, it is difficult to distinguish it from the mechanical interlocking in practice [123, 129]. Moreover, for similar materials to be bonded (like Zn-Zn or Al-Al), the incomplete bond was obtained under low deformation, which could not be explained purely with this theory[119].

The energy barriers theory believes that the metallic bond formation requires the interface atoms to be activated with higher energy than a critical value. According to [116], this energy barrier may come from recrystallization[125], diffusion or the misorientation of the contacted crystals and the mismatch of the atoms[130]. In the studies of cold friction cohesion between different metal combinations [131], the mismatched orientation of copper showed less cohesion than matched atomic planes, which supported the statement [130]. These proposals were made

based on the observation of joints bonded under ultra-vacuum. In a review of the cold-welding mechanism, [132] believed this energy barrier was associated with the plastic deformation required to break the oxide film and build the contact between fresh metals when the bonding occurs in presence of the oxide layer. Although the energy barrier theory could explain most cold pressure welding results, however, in some cases, for example, some specially designed bonding experiments showed that the bonding is achievable once the clean surfaces get touched without deformation[114, 133], or in the study of [134], the single-crystalline gold nanowires were demonstrated to be cold-welded within seconds by mechanical contact alone, the energy barrier theory is not applicable.

In summary, for the aforementioned different cold pressure welding/roll bonding mechanisms, it is difficult to explain all the bonding behaviour in different cases using one theory, even though each one can make sense under certain circumstances. With the change of bonding conditions, e.g., temperature, deformation level, atmosphere environment or nature of materials, different mechanisms or theories can be dominating accordingly. When the pressure welding/roll bonding occurs at room temperature with the presence of surface oxide film, the film theory has been the most accepted mechanism to understand the bonding behaviour and develop a model predicting the bond quality. Therefore, the development of the model based on film theory will be reviewed here for pressure welding/roll bonding. The other theories would be discussed in detail in the following bonding method later in this chapter.

Model development

Theoretical models to predict the weld strength have been developed based on the film theory analysis and its dependence on the bonding parameters. For these film-theory-based models, the assumption of oxide film behaviour is decisive for predicting the final bond quality. At the earliest, Mohamed studied the oxide film and discussed the properties of an oxide film with different hardness and ductility[116]. However, to simplify, the film was assumed to be completely brittle and fracture simultaneously on both sides, as shown in Figure 2-6a, exposing the fresh metallic area, and the weld quality ratio was assumed to be equal to the amount of surface extension. Thus, the weldability was theoretically calculated based on the degree of oxide fragmentation[116]. The nominal weld strength, *f*, was roughly estimated in a squared relation of surface extension *R*,

$$f = C \cdot \left(\frac{R}{R+1}\right)^2 \qquad \textit{Equation 2-1}$$

where the parameter C here was considered to be associated with the surface preparation, whilst independent of the deformation. Mohamed's model successfully described the relationship between the deformation and resulting bond quality for different metals or alloys. However, the effects of other factors, like the strain rate or temperature or force needed further discussion.

Later in Bay's model[118, 119], two types of oxide film are assumed: the C-mechanism for the fragile thick type cover layer and the F-mechanism for thin films with certain ductility (Figure 2-6b). C-mechanism dominates at lower strain, which needs higher stress to extrude the metal through the gaps between the films. At the same time, F-mechanism describes the fracture of the ductile oxide film barrier, which would require higher plastic strain for metal parts to be in contact. Thus, a combination of high strain to stretch the ductile oxide film and high pressure to extrude the fresh metal would be needed. Bay incorporated both the oxide film fracture and the subsequent metal extrusion process into the model:

$$\frac{\sigma_B}{\sigma_0} = (1-\beta)Y\frac{p_{nor}-p_E}{\sigma_0} + \beta\frac{Y-Y\prime}{1-Y\prime}\frac{p_{nor}}{\sigma_0} \qquad \textit{Equation 2-2}$$

Here, the σ_B and σ_0 represents the tested shear strength for joint and the base metals, respectively. β is the estimated fraction of ductile film over the whole area. Y and Y' is the surface expansion and the critical value, over which the ductile film starts to fracture. The yield shear strength of the base metal is given as σ_0, while the p_{nor} and p_E are the applied normal pressure and the pressure needed for extruding the metal through the cracks, respectively. Bay's model was later applied to the roll bonding process[89] and the bond strength was adapted to be dependent on the height reduction *r*. In [135]'s work, the geometry and normal stress analysis in the rolling process were studied, and a more detailed calculation was given for cold roll bonding on similar and dissimilar materials with plating.

This oxide film fracture and metal extrusion process from the film theory has been the basis of the bonding model development in recent studies. With the help of finite element analysis, the model developed by [135] was modified to include the tangential interaction in [136]'s study and implemented into a framework to predict the bonding behaviour in roll bonding. Cooper et al.[121] also developed Bay's model and they assumed the oxide film to be brittle while oxidation occurs during the early stage of the bonding, as shown in Figure 2-6c, which explains no strength obtained until the critical strain is achieved. Cooper also included the effects of shear stress and more precise extrusion pressure calculation using more detailed oxide

dimension parameters, which helps predict a lower but more accurate bond strength for cold welding. Most recently, Kavan et al. [122] conducted a more accurate finite element analysis of the effect of the oxide behaviour at a micro-scale and found that the thickness/length ratio of the fractured oxide islands affects both the strength and the ductility of the joint. A final 50% bond strength compared to the substrate is estimated in Kavan's simulation. Since only metal-metal contact is assumed to contribute to the bonding in these film theory-based models, no bond strength was predicted to be achieved at a surface exposure ratio lower than 40%, and lower bond strength than the parent was achieved even at a considerable strain of 360%[118].

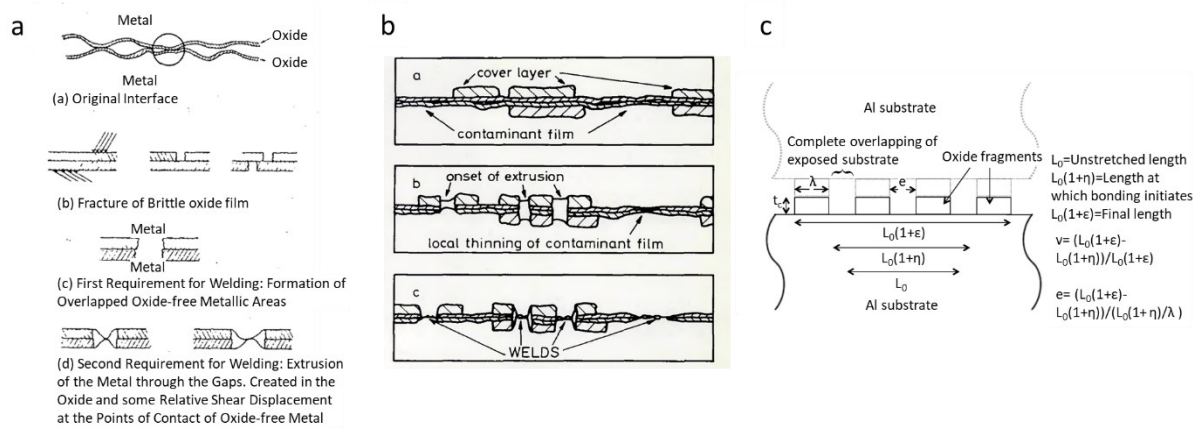


Figure 2-6 The assumptions on the film behaviour for cold pressure welding/roll bonding film theory: (a) Schematic illustration of the welding process in [116]; (b) Schematic outline of coalescence mechanisms in [119]; (c) Aluminium surface of original length L_0 stretched to length $L_0(1+\varepsilon)$ in [121].

2.2.2 Diffusion Bonding

Diffusion bonding (DB, also called diffusion welding) is one of the most widely used solid-state welding techniques in industrial applications. In the DB process, two surfaces are brought into contact within atomic distance under moderate pressure and elevated temperature for a prolonged period [87, 137]. Generally, DB is distinguished from other solid-state bonding techniques by the following features: temperature, duration, plastic deformation level and a high requirement of the vacuum. The typical process temperature for DB is 50%-80% melting point of the base metals (or lower melting point if for dissimilar metals), which is higher than pressure welding and roll bonding[87]. In real DB applications, strain level is usually controlled at a lower level less than 10% to maintain the shape. Without sufficient deformation for oxide film break-up as in roll bonding, higher surface cleanliness and ultra-high vacuum environment

are critical for the DB process. Moreover, without sufficient material flow, the intimate contact of solid surfaces in DB is normally achieved through creep at a longer duration and the required duration for a sound bond depends on the material pairs, typically 5 min for steels [137] and 120 min for similar aluminium alloys [138]. In light of this, diffusion bonding is not an instant solid-state welding method.

Mechanisms

Due to the limited macroscopic strain applied in DB, plastic deformation only occurs in the local zone near asperities for actual contact. At a microscopic level, the voids formed from surface asperities are the barriers for the contact and unclosed voids are commonly observed in uncomplete diffuse bonded joints[86, 139-141]. The removal of voids and full contact of surfaces rely on the time-dependent material flow into the interfacial voids. Based on theories derived from pressure sintering studies, the mechanisms dominating the material flow and micro-void closure process include superplastic deformation, surface source diffusion, interface source diffusion[86, 142]. This void-closure process dominated by atom diffusion could be affected by the (1) surface roughness, which determines the initial dimension of interfacial voids[143, 144]; (2) yield stress and the diffusion flow rate, which are affected by the material nature together with the temperature[144]; (3) the load and the applied pressure providing the dynamic driving force for the atom diffusion process, thus higher pressure would benefit for closing the micro-voids[137, 145]; (4) the processing time which is decisive for the final joint performance since the diffusion is a time-dependent process[137]. As suggested from the diffusion bonded joints results, it normally presents an optimal time and pressure for certain materials[146]. When the voids are closed, a further increase in the duration and pressure would not help too much[137].

Apart from the micro-void closure mechanism, there are discussions on the process of recrystallization and atomistic diffusion during the solid-state bonding. DeCecco and Park[124] first proposed the recrystallization theory in the welding of aluminium in aircraft. Huang compared the diffusion bonding process of hot-rolled AA7075[147] with superplastic AA7075[138]. In the absence of oxide film after proper surface treatment, the elimination of the bond line during diffusion bonding is accompanied by the recrystallization in hot-rolled aluminium and grain growth in superplastic microstructure with small grains, which helped to achieve higher bond strengths.[148] observed the recrystallized fine-grain appearing along the interface for diffusion bonded TiAl alloys and believed that the recrystallization process was

caused by the dislocation accumulation blocked by the interface. Also, the grain boundary migration in diffusion bonding has been observed in nickel-based superalloy[149, 150]. Given the low deformation level, the grain migration over the bond line proceeds at a quite low rate.

Moreover, the atomistic diffusion process was observed in dissimilar materials bonding processes [137, 151, 152], and a complex intermetallic phase might appear in the transition zone which determines the joint performance. The investigation using Molecular Dynamics (MD) simulation[144] revealed the effect of increasing temperature on the diffused layer thickening. The diffusion of atoms only started when full contact was achieved. For both the grain boundary migration and atomic diffusion processes, the material transfer during bonding, in which the void elimination process is a prerequisite.

Model development

To present, due to the dominating role of void closure in achieving full contact, most diffusion bonding model studies regarded it as a rate-determining process. The void-closure rate is considered to be the diffusion bonding rate. According to the discussed void-closed mechanisms, the rate is multifactorial and determined by the rate of material flow to close the void. King and Owczarski [153] first stated the three void closure stages in their phenomenological model for diffusion bonding: (1) initial local plastic deformation at a large scale; (2) the removal of the majority of voids by interface migration; (3) the elimination of remaining micro-voids by volume diffusion.

Later, several extended studies had been done, mainly discussing mechanism operating [86, 154-156] and the void geometry consideration [86, 154-158]. Derby and Wallach [155] learned from pressure sintering in their theoretical model, and suggested the seven governing mechanisms, namely, (1) surface diffusion, (2) volume diffusion from surface source to neck, (3) interface diffusion and (4) volume diffusion from interface source to neck, (5) vapour deposition from interface to neck; (6) power-law creep and (7) yielding plastic deformation. In the subsequent research work, these material transfer mechanisms, which are shown in Figure 2-7f, were accepted and adopted. For each mechanism, the dynamic driving force for diffusion was analysed and the materials transfer rate was numerically calculated to estimate the diffusion bonding rate. And under different bonding conditions, different material transfer mechanisms may be considered according to [159].

In the numerical analysis, the assumption of void shape is critical, affecting which governing mechanism dominates the material flow process. Hill's model has adopted elliptical void as a geometrical assumption based on experimental observation to avoid the discontinuity for bonding speed prediction. Pilling's model[160] assumed the shape of the voids to be circular which can be maintained by surface diffusion. It mainly discussed the dominating creep deformation and predicted a larger rate of change in the fractional area of the non-bonded interface, which turns out to be in good agreement with experimental bonding results for fine-grained superplastic alloys. Also, some other typical void geometries adopted in different main diffusion models are shown in Figure 2-7 (a-e). In recent studies, with the aid of finite element analysis software, a three-dimensional model based on ablating spheroidal shaped void and four flow mechanisms were developed by [142], with which the void closure process in hot press bonding based on Ti–6Al–4V alloy was explained. And in another work by[161], a much more simplified model which assumed a square shape surface asperity shape was proposed and the effects of parameters including temperature, pressure and bonding time were presented in a more intuitive form.

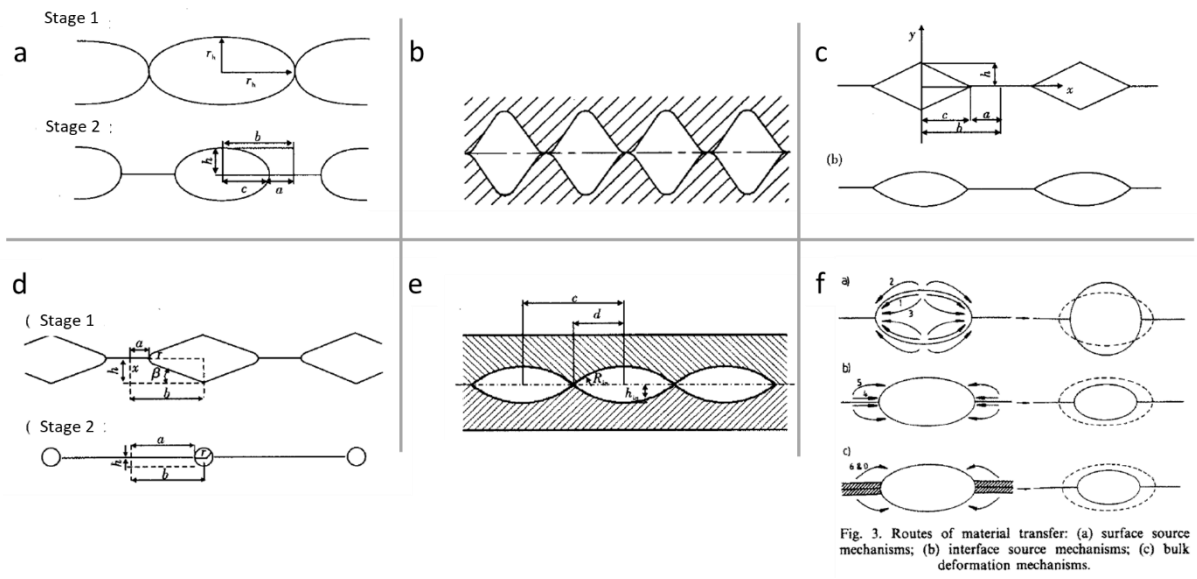


Figure 2-7 The different void geometric assumption in different models: (a) Hill's model[86]; (b) Orhan's model[158]; (c) [162]'s model; (d) Derby's model[143]; (e) Guo and Ridley's model[163]; (d) Routes of material transfer described in Hill's model[86].

2.2.3 Extrusion Bonding

In processes like hollow aluminum manufacturing[164-167], multi-layered plates[168], or the aluminum chips solid-state recycling [169] by hot extrusion, the solid-state bonding between similar or dissimilar materials is involved when two surfaces from different streams meet during the metal flow. The quality of the formed weld seam is of critical importance for load-bearing applications.

Similar to the aforementioned solid-state bonding processes, factors affecting the interface bond quality during extrusion include extrudate temperature, extrusion pressure and surface cleanliness, ram speed, etc. [167]. The metal flow in extrusion, which is related to the stress-strain state along the interface, is also a critical factor to be considered. The material flow in the extrusion process is more complicated than upsetting pressure welding and comprehensively determined by parameters like the extrusion die geometry[169, 170], reduction ratio, friction, etc.[169]. However, the development of Finite Element (FE) analysis made the metal flow predictable, and thus the bond interface can be tracked. Also, the stress state along the bond interface can be calculated from the simulation, which helps the understanding of the bonding mechanism.

Mechanisms

The observed bonding behaviour during extrusion is similar to that found in the cold pressure/roll bonding or diffusion bonding process as discussed in 2.2.1 and 2.2.2. Along the longitudinal weld interface in extrusion, the micro defects including remaining fractured oxide film, micro-voids [169, 171, 172] and recrystallization [165, 169, 173, 174] were observed. These similar bonding behaviours indicate that the previously discussed mechanisms and theories can be used to explain the bonding occurring in extrusion.

One or two different mechanisms could be simultaneously governing the bonding process. For example, as shown in Figure 2-8, due to the different stress states at different locations of the weld beam line, the bonding along the material flow was shown at different stages: at locations with lower local strain, the micro-void closure mechanism dominates, while with the increase of strain and closure of voids, the recrystallization turns to be dominating [172]. Moreover, the formation of a gas pocket, which is associated with the die structure design[171, 175], could also exert an effect on determining oxide film behaviour.

Given the complexity of bonding conditions along the weld line in extrusion, instead of using a single mechanism to describe the process, researchers found it much more accessible to wrap up the effects of different parameters and integrated them into a mathematical expression to evaluate and estimate the bond quality. And it can be physically explained as an energy barrier theory: an energy barrier, existing due to the mismatch of crystal lattices of bond pairs, needs to be overcome to achieve a metallurgical bond. This criterion has been proposed differently, considering different affecting factors: the pressure-time criterion (K criterion) by Plata[176], the pressure-time-flow criterion (Q criterion) by Donati[177] and the most recently developed criterion model (J criterion) by Yu et al.[172] that considers effects on stress-state on void closure and diffusion mechanism. By integrating them with the FE analysis results, the energy criterion method has been able to predict the weld quality in various extrusion bonding practices.

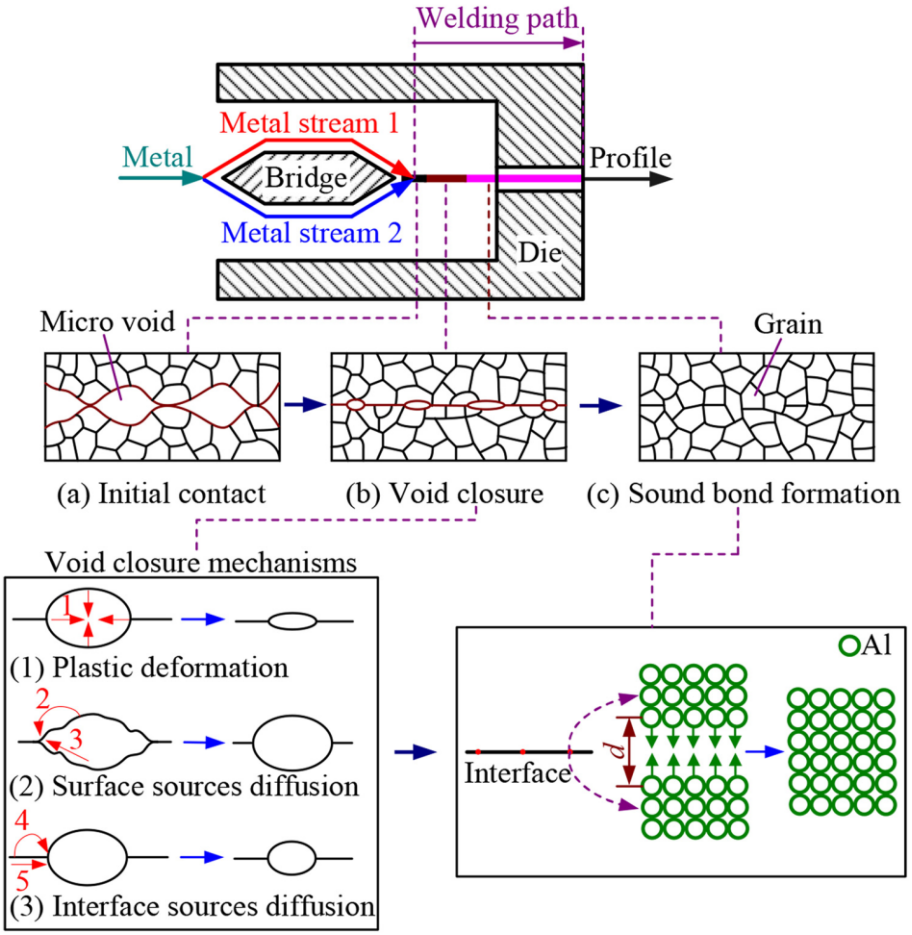


Figure 2-8 Schematic diagram of solid-state bonding mechanism in porthole die extrusion process.[172]

Model development

In extrusion, the complexity of the die makes it difficult to quantitatively describe the material flow path. Therefore, it is not easy to develop a physically-based model relating the seam quality directly to the extrusion parameters. To estimate the weld quality, different welding criteria have been proposed[169, 172, 176-178]. These welding criteria integrated the physical variables along the welding paths, based on the experimental results of the welding quality on extrusion parameters and the simulated stress/strain state.

In [178]'s study, it was believed that the bonding is dominated by the void-closure process, which was determined by the ratio of mean normal stress σ_m to effective stress $\bar{\sigma}$ and effective strain $\bar{\varepsilon}$ in the surrounding area, thus described the welding criterion G_m as:

$$G_m = \int_0^{\bar{\varepsilon}} \left(\frac{\sigma_m}{\bar{\sigma}}\right) d\bar{\varepsilon} \qquad \textit{Equation 2-3}$$

Later, based on the material transfer mechanisms discussed in diffusion bonding, a diffusion integration G_D was proposed by [179] as the welding criterion:

$$G_D = \int_0^t k_0 \, exp\left(\frac{RT}{Q_D}\right) dt \qquad \textit{Equation 2-4}$$

where, the t and T is the time (s) and absolute temperature (K), R is the universal gas constant, Q_D is the diffusion activation energy and k_0 is a coefficient related to material and the surface conditions of metal for bonding.

There are two widely accepted models for the bonding in the extrusion process: the pressure-time criterion (K criterion) proposed by Plata[176] and the pressure-time-flow criterion (Q criterion) by Donati[177] from the energy perspective. They calculated the integral of the ratio between normal pressure to yield stress on time or path and stated there is a critical value for this integrated value over which the bond is formed.

$$K_{ad} = \int_0^t \frac{p_{con}}{\bar{\sigma}} \nu dt \qquad \textit{Equation 2-5}$$

$$Q_{ad} = \int_0^t \frac{p_{con}}{\bar{\sigma}} dt \qquad \textit{Equation 2-6}$$

where, p_{con}, $\bar{\sigma}$ and ν represents the contact pressure, effective stress and metal flow velocity, respectively.

These criteria are proposed as the integral of the weld-quality related parameters based on the experimental observation. By comparing the calculated value with the characterized weld quality evaluation, the critical criterion is determined.

Instead of only considering the stress factor associated with the void-closure process, Yu et al.[172] considered the effect of stress state on the closure of micro-voids and atomic diffusion and incorporated these two mechanisms into a dimensionless integral (J criterion) based on the diffusion model by [179].

$$J = \int_0^t k_0 \frac{\sigma_m}{\bar{\sigma}} \dot{\varepsilon} exp\left(\frac{RT}{Q_D}\right) dt \qquad \textit{Equation 2-7}$$

Herein, the strain has been included as an integral of $\dot{\varepsilon}$ over time t due to the reported influential role that strain plays in the bonding process. The J criterion has presented a higher accuracy than the other classic models when comparing the integral values for the soundly bonded points at different locations along the interface. These discussed models assumed there is minimum energy needs to be overcome due to the mismatched crystal lattice near the bonding line. Since this energy barrier is difficult to be determined directly, the critical values are usually decided through interpreting the affecting factors into the energy integral and characterizing the bond quality of points along the interface. This calculated criterion is used as an indicator for the sound bonding of certain points.

2.2.4 Hot Compression Bonding

Although cold pressure welding and roll bonding methods have been widely involved, [87] pointed out its application has always been limited out of load-bearing components due to the inferior joint performance. Full strength and ductility comparable to the parent material were difficult to achieve. Diffusion bonding (DB) has successfully been applied in practice with parent level performance achieved, however, as shown in [83] and [150], only when the surface contamination barrier problem has been dealt with by proper surface treatment and strict oxygen-free environment control; moreover, the considerably long duration is needed for complete micro-voids closure in DB. Studies have shown that, compared to the time-dependent diffusion governing the bonding process, the bonding by plastic deformation is more efficient and shows potential in manufacturing large key components with high quality[5, 6].

The bonding-by-deforming methods normally require high temperature and plastic deformation. According to the specific hot working condition to achieve the bonding, it can be

referred to different names. For example, forging welding[180] is the oldest and simplest welding technique, which has been used in the production of pattern-welded blades[181] since ancient times. In forging welding, two pieces of metals are joined by being heated to a high temperature (typically 50 to 90 per cent of the melting temperature) and then hammered together. Hot roll bonding can also be classified into this category. [111] indicated that when the temperature was increased, a good quality bonding was achieved for the low-carbon steel cladding by 316 stainless steel. In the study of [182], the dependence of bond strength on the roll bonding temperature was presented. Also, the bonding under hot working conditions could occur in the void-healing process for casting ingot during subsequent hot forging or rolling [95, 183-187]. Recently, a new additive forging method, in which multi-layer plates were forged for a pre-form preparation for following the ring-rolling process, was proposed by [5]. The bonding behaviour under hot deformation conditions and effects of deformation parameters (temperature, strain and strain rate, surface condition and oxide film behaviour[188, 189]) have been studied in different materials, including copper[190], steel [191-194], nickel superalloy[195-197] and titanium[189].

Mechanisms

Similar to other solid-state bonding techniques, the formation of the metallurgical bond in the hot compression welding process depends on the close contact between atoms under pressure. Particularly, the hot temperature and high pressure, large deformation enables the high plasticity for the materials and high dynamic driving force for the void-closure and microstructure evolution, which facilitate the completion of the bonding.

In the hot compression bonding process, the oxide film problem can hardly be avoided, especially when active elements, e.g., chromium, manganese, iron, titanium or aluminium, are contained. [191] studied the oxidation of the steel during the hot compression boning process and found that, a thicker oxide film was formed under a lower vacuum and formed $FeCr_2O_4$ and $MnFe_2O_4$ turned into $MnCr_2O_4$ during the bonding process. In the bonding study of 316LN steel[192], with the prolonged holding time, it was observed that the oxide $MnCr_2O_4$ would be dissolved into the matrix, forming a particle precipitation zone (PPZ) with γ-Al_2O_3 nanoparticles. With the dissolution of the interfacial oxides, the joint was completely healed. This dissolution behaviour of interfacial oxide was also observed in earlier diffusion bonding research works[198-200]. Different from cold pressure welding/roll bonding, this oxide dissolution can only be happening in hot compression bonding and vacuum conditions.

When the oxidation is carefully controlled under a high vacuum, studies have shown that the interface grain microstructure evolution associated with the recrystallization under hot working conditions plays a dominating role in the resulting bond quality. The microstructure evolution that occurred along the interface was observed commonly in hot compression bonding processes. In the defect healing study for heavy forgings of 30Cr2Ni4MoV steel[201], new grain boundaries were found generated at the centre of the crack healing zone along the direction of the pre-crack and they became curved and turned into grain-boundary triple junctions, and several grains grew up across the original pre-crack gap with the increasing holding time. For hot compression bonding of copper-copper[190], the Rx process observed near the interface was found to be different from the discontinuous Rx in the matrix. The newly recrystallized grains appeared along the bonding interface when low-angle-grain-boundaries transformed into high-angle-grain-boundaries with the increase of the strain level. The interface grain boundary migration was believed to proceed with the recrystallization process and similar associations were found in the bonding process of other materials[193, 194, 196, 197]. For nickel-based superalloys, the effects of strain level, strain rate, temperature on the interface grain boundary migration process were investigated in [196, 197]. The joints presented higher bond quality with higher bonding temperature, higher strain and slower strain rate conditions, under which higher recrystallization fractions were demonstrated. Moreover, the tensile strength of the joints was evaluated and a positive correlation between the measure migrated interface grain boundary migration ratio and the resulting bonding strength was revealed. Although there is evidence showing the interface grain boundary migration over the initial bond line helps the recovery of the bond strength, the dynamic driving force of this migration has not been particularly discussed. And also, in [189]'s investigation of the surface roughness effect on the bonding behaviour of Ti-6Al-3Nb-2Zr-1Mo alloy, the recrystallization occurred to the interface with a higher roughness, however, the corresponding joints ended with lower elongation. Thus, it indicates that the recrystallization and the interface grain boundary migration could not be the only factor determining the final joint strength.

Even though there is more severe plastic deformation involved, the micro-voids caused by surface asperities still exist in hot compression bonding. For example, these voids were found in the healing process of carbon steel[183]. It was believed that under a lower temperature (≤900 ˚C), the closure of these voids dominated the healing, like that discussed in the DB process and the void-closure process is associated with bulk diffusion; but at a higher

temperature (> 900 ˚C), the healing process was more related to the microstructure evolution with recrystallization. In other voids/crack healing studies, the healing was in situ characterized with the TEM technique[202, 203] and the atom diffusion theory was proposed to be the governing mechanism. The atomistic diffusion simulation was also presented[202, 204, 205]. Similar to the material transfer mechanisms proposed for diffusion bonding, the main diffusion mechanism in the healing process also includes lattice, interface and surface diffusion modes[202]. This atom diffusion would also lead to the formation of the diffusion layers near the bonding line[144, 206].

To sum up, given the variety of the bonding conditions, it is difficult to agree that only one mechanism could explain the bonding behaviour during hot deformation. But generally, as the deformation and temperature are much higher, the driving force for void-closure and diffusion rate would be higher than other solid-state bonding methods discussed in 2.2.1-2.2.3. The interface grain boundary migration theory is a mainstream mechanism for hot compression bonding in today's research work.

Model development

As discussed, there are different mechanisms governing the hot compression bonding progress and it can be an integration of these mechanisms in one bonding process. To present, most models developed for hot compression bonding have been focused on a single mechanism. For example, in the defect healing process studies, models that simulated the atom diffusion behaviour have been developed with dynamic molecular methos[204, 205, 207, 208]. In [204], it was found that by computation, during the crack closure under compressive stress, the crack healing must overcome the surface energy (2γ) and the energy for dislocation generation and movement γ_p. On the other hand, the driving force included the elastic energy $\frac{\sigma^2\pi a(1-v^2)}{E}$ and energy provided by heating $\frac{\partial U_T}{\partial A}$. Therefore, the conditions for healing under compressive stress σ can be clarified as:

$$\frac{\sigma^2\pi a(1-v^2)}{E}+\frac{\partial U_T}{\partial A}\geq 2\gamma+\gamma_p \qquad \textit{Equation 2-8}$$

where a is the crack length, v and E are the Poisson's ratio and Young's modulus of the material, A is the Section area. [207] adopted Newtonian dynamics equations to calculate the motion velocity of thousands of atoms under certain temperature conditions. It was proved that

the temperature had a significant effect on the extent of microcrack healing. [208] simulated the healing of nano-cracks by disclination defects in nanostructured materials and demonstrated with the help of finite element analysis software. Although this atomistic simulation helped revealed the essence of the welding in solid-state, it has limitations in the simulation scale as well as the assumption in the ideal vacuum and full contact between solid surfaces.

From the perspective of the oxide film barrier on the surfaces, in the bonding process of 316LN steel, the thermodynamic stability of $MnCr_2O_4$ and decomposition mechanisms of interfacial oxides were studied by combining the first-principles calculations with the thermodynamics approach. However, these models cannot predict stable and non-decomposable oxide, like Al_2O_3. In the film theory for cold pressure welding/roll bonding, the oxide is considered to not contribute to the final bond strength[116]. However, with the increase of the bonding temperature, the dependence of the joint strength on the oxide might be working in a different way from cold welding. Moreover, at higher temperature and strain levels, the microstructure evolution is more severe, yet the advantageous effect of microstructure evolution has not been included in the classic film model. Thus, bond strength could be underestimated using the existing bonding model based on the film theory. Therefore, a new model, which incorporates the effect of remaining dispersed oxides and the microstructural change, is needed to predict the high strength bond achieved under hot deforming conditions.

The mechanism, either film theory or recrystallization theory, has been discussed separately in most studies. Existing modelling work, mainly based on the film theory, predicts inferior bond quality with the presence of remaining oxides. For the bonding based on hot plastic deformation, both theories need to be coupled to determine the final joint performance. To develop a comprehensive theory and model accounting for full-strength achievement, it is important to determine the role of each factor in this integrated bonding process.

2.2.5 Solid-State Bonding of IN718

In solid state, the metallurgical bond is achieved when two clean surfaces come into contact and atomic bond are formed. For IN718, one widely studied solid-state bonding technique is diffusion bonding, of which the typical conditions include moderate temperature, minor plastic deformation, long bonding time and a high requirement on the surface preparation and vacuum environment. Even under such strict bonding conditions, it is very difficult to get a joint of performance as good as base alloy 718. Zhang [209] evaluated the IN718 joint quality under

different bonding conditions with varying temperatures and bonding time, and a high-strength joint can be obtained when it is being bonded at a temperature of 1000 ˚C, under the pressure of 34 MPa for 30 min, in which case the ductility is merely 9%. The impaired ductility of the diffusion bond joint can be improved by increasing the time to 2h. According to the extensively accepted diffusion bonding mechanism, a long bonding time is a necessary condition as the elimination of the micro-voids along the interface depends on the atom diffusion rate and creep deformation rate, both of which are slow in superalloys. Especially for high-strength superalloys, high flow stress and low fluidity make the closure of micro-voids more difficult, and brazing or Transient Liquid Phase (TLP) diffusion bonding is more popular. By inserting a low-melting-point or composition-well-designed soft interlayer, a liquid phase zone would be formed between two surfaces and the diffusion of the element becomes more efficient in it. In this way, problems with the interfacial micro-voids can be addressed while the unexpecting issues with brazing or TLP are the phase transformation and precipitation in the diffusion affected zone (DAZ). Yu et al. proved that adding Hf into the nickel-based interlayer helped effectively avoid DAZ in the TLP bonding process of a single nickel crystal, and the time for isothermal solidification was reduced to half to 12h.

Compression bonding at high temperature and large strain is more effective to achieve atomic bonding in solid-state. The bonding behaviour of IN718 under hot compression was studied in [195-197, 210]. Under severe deformation, the interfacial micro-voids are closed within a shorter time and the interfacial microstructure was proved to evolve significantly during the bonding. The effects of various hot working conditions on the microstructural evolution were investigated, including different temperatures [195, 196], strain rate[197] and strain[195, 196]. It showed that at a lower temperature, or lower strain, the interfacial grain boundaries remained as a straight line. With the increase of the strain and temperature, interface grain boundaries (IGB) migrate over the bond line, and in the meantime, the bond quality was improved[195, 196]. At the same temperature and high strain level, higher ductility was reported for samples compressed at a lower strain rate, and Zhang et al. believed that it was due to the high extent of dynamic recrystallization (DRx) and well-developed fine DRx grains near the interface at lower strain rate[197]. The association of interface bonding with the migration of DRx grains is also observed in the hot compression bonding of copper[190] and steel[194]. Similar to diffusion bonding, the studies of hot compression were mostly conducted in a strict high

vacuum. The hindrance of surface contamination on the interface bonding was not discussed with the association with the DRx process.

The surface contaminating film is the other factor affecting the final bond quality. The bonding achieved under hot deformation conditions shows advantages in eliminating the effect of surface contaminate film. The film could be broken up under severe deformation, and dispersed fragments allow fresh materials to meet and bond, which is similar to the pressure bonding at room temperature[116]. Also, the elevated temperature was proved to facilitate the dissolution of oxides during bonding for certain materials[198], like steel [191, 192]. Moreover, the microstructure evolution with the DRx process could eliminate the effects of residual oxides. In the study of [211], the bonding behaviour of IN718 was investigated in a moderate vacuum condition, the residual oxide fragments were considered to do less harmful than in cold pressure welding, as with the occurrence of recrystallization these oxides were included inside grains. A high-quality joint comparable to the reference was obtained at a strain level of 50%, lower than the cold pressure welding[211].

2.3 The additive forming methods based on solid-state bonding

To avoid the large-size ingot preparation step, the bottom-up concept could be borrowed for large-size component manufacture. The extensively studied additive manufacturing (AM) technology typically belongs to this category[81]. However, most additive manufacturing technologies, either based on powder or wire, go through the melting and solidification processes. Thus, some casting defects are commonly seen, which leads to the unpredictable and inferior properties of printed parts[18]. Except for the fusion-based, there are other solid-state AM technologies, e.g., Cold Spray AM (CSAM), Binder Jetting (BJAM) based on powder sintering, Ultrasonic AM (UAM) and Addictive Friction Stir Deposition (AFSD) based on friction welding[212, 213]. With the limitations on the dimension of starting materials, the deposition rate of these solid-state AM technologies is the main limitation for applications in manufacturing large-scale components. For Friction-Welding-based FSAM, it uses metal sheets of 1.7 mm thickness while for UAM, the sheet thickness is much thinner (~0.1 mm)[212]. Recently, a new manufacturing method was proposed for large-scale stainless steel forgings by additive layering hot-compression bonding technology[5]. A similar construction method for a ring part was also seen in titanium by massive diffusion bonding[214]. Different from the solid-state AM aforementioned, these methods start with much thicker wrought sheets[6], thus with much higher efficiency.

Chapter 3 Methodology

3.1 Introduction

The proposed laminated forming process based on multi-layer solid-state bonding was investigated at different scales. To systematically study the effects of parameters, including strain, strain rate and temperature, small size bar samples were adopted and a series of compression bonding tests were designed and conducted, which will be presented in Section 3.2. In addition, a larger-scale test trial with three layers being piled was designed and bonded in a more real forging practice. The mechanical properties were evaluated and compared to industrial standards (in Section 3.3). Moreover, some bonding tests were designed to deepen the understanding of the bonding mechanism and indicate the effect of single factor on the final bond performance and the methodology will be given in Section 3.4).

3.2 The solid-state bonding of IN718 using Gleeble under different conditions

3.2.1 Materials – IN718 bar samples

The IN718 used in this study is as received from BIAM (Beijing Institute of Aeronautical Manufacturing, China) after open die forging on casting ingots. Its chemical composition is Ni 49.78%, Cr 18.85%, Fe 18.26%, Nb 5.51%, Mo 3.29%, Ti 0.93%, Al 0.43%. The original microstructure is shown in Figure 3-1a. Equiaxed grains with an average grain size of 20~25 μm are presented with needle-like δ phases distributed along grain boundaries. As a highly alloyed material, the addition of elements, including Nb, Ti, Al, form phases (e.g. γ'-Ni_3(Ti, Al) and γ''-Ni_3Nb), strengthening the γ matrix. For IN718, γ'' is the main strengthening phase and is separated in a plate shape with a coherent relationship to matrix γ at a nanoscale.

The as-received IN718 was machined to be cylinders with the dimension of 10 mm in diameter and 55 mm long with threaded ends, as shown in Figure 3-2c. The surface on the bold end is the one to be bonded and it was polished with P1200# abrasive paper to remove the contamination layer. After polishing, the samples were cleaned in an ultrasonic bath and protected in acetone.

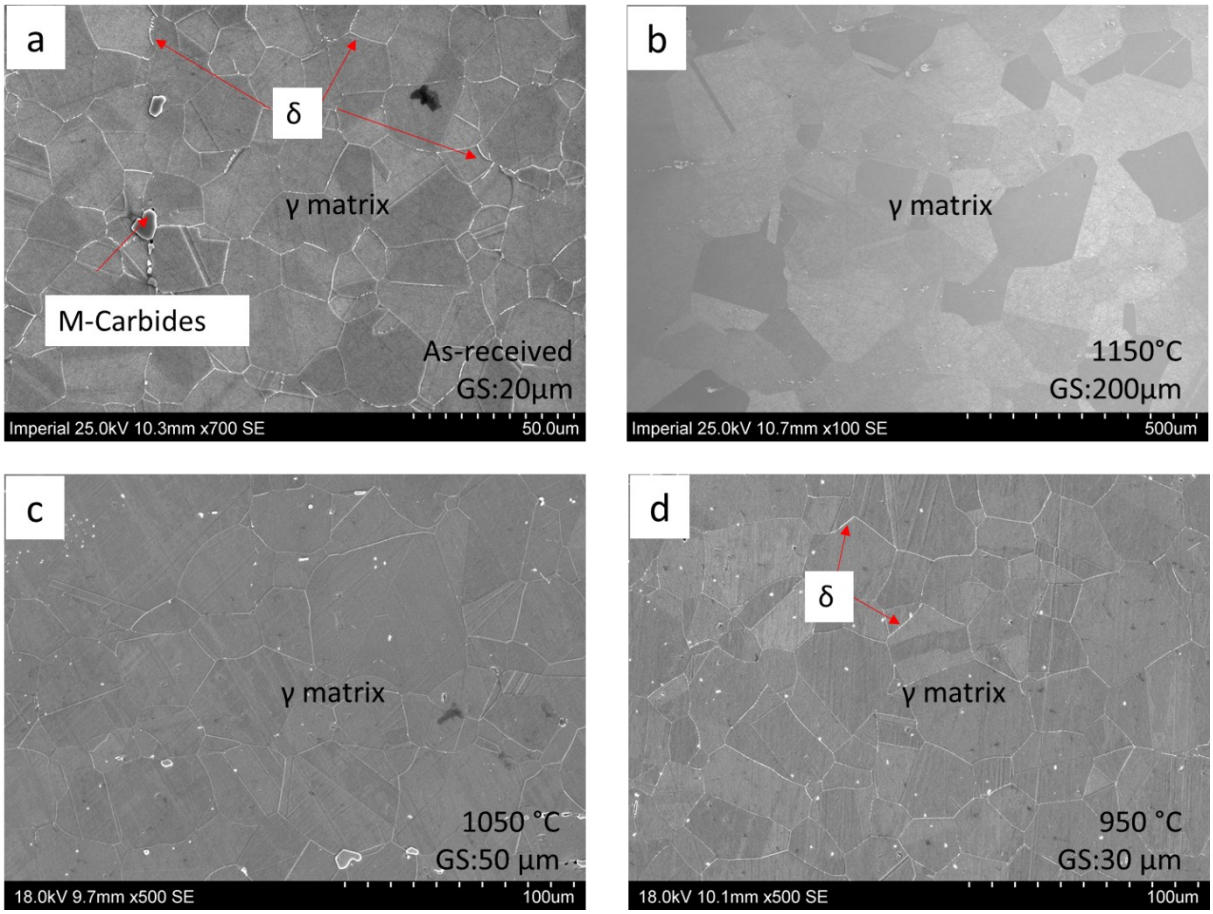


Figure 3-1 The microstructure of (a) as-received wrought IN718; and after being heated up and soaked for 3 min at the designated temperature of (b) 1150 ˚C; (c) 1050 ˚C; (d) 950 ˚C.

3.2.2 Gleeble bonding test with bar sample

The hot compression bonding tests were conducted using Gleeble 3800 thermo-simulator machine, which can precisely control and monitor the temperature, stroke and strain rate, and provide a rough 1.0 torr (~13.3 Pa) vacuum environment. Two cylindrical samples were fitted in copper grips with their axes kept concentrically aligned. The compression bonding setup in the Gleeble chamber is shown in Figure 3-2a. Before the hot compression, two ground surfaces were brought into contact under a pre-force of -0.5 kN and the sample was resistance heated to the designated temperature (1150 ˚C, 1050 ˚C, 950 ˚C) and soaked for 3 min before compression bonding to get a uniform temperature distribution. An interrupted sample was prepared after the heating and soaking process, right before the compression, as the original state and its microstructure are shown in Figure 3-1 (b-d). When IN718 was heated up to 1150 ˚C which is over the solvus temperature of δ phase, there is an obvious grain growth from ~20

μm to ~200 μm, and dissolution of gamma prime and delta phase after the pre-heating and soaking g process. only carbides (NbC/TiC) remained randomly distributed in the γ matrix. There would be no phase transformation occurring during the hot forging bonding process at 1150 ˚C. At 1050 ˚C, the grains grow to an average size of ~80 μm (Figure 3-1c). And at a lower temperature of 950 ˚C (lower than δ-solvus), δ phases are seen in Figure 3-1d. The original grains are relatively retained with a small size (~40 μm) as the δ phase at the grain boundaries inhibited the grain growth.

The whole heating scheme is given in Figure 3-2b. The compression proceeds under stroke-control mode: strain and strain rate were controlled by programming the relative movement of the grips and the speed of the stroke change. The two half cylinder bars were compressed to different strain levels, and the engineering strain (height reduction, HR) was set to be 0.05, 0.1, 0.3, 0.5, separately, based on the initial 20 mm length of the exposed central part. The bonded samples are shown in Figure 3-2d. Strain rate were set in a series of 0.001 s^{-1}, 0.01 s^{-1} to 0.1 s^{-1}. Besides, reference compressive tests on the wrought IN718 using a whole cylinder sample without an interface in the middle were conducted. The reference tests are to exclude the effect of microstructure near the bonding affected zone and separately discuss the completion of the interface bonding. Except for the existence of the interfaces, other compressive deformation parameters, e.g., the temperature, heating strategy, strain and strain rate, were controlled to be consistent with the corresponding bonding tests. And the bonding parameters are given in Table 3-1.

Table 3-1 The parameters for compression bonding tests of IN718 using Gleeble (B and R represent Bonding and Reference test, respectively)

Temp.	**SR 0.001 s^{-1}**					**SR 0.01 s^{-1}**				**SR 0.1 s^{-1}**			
Strain (Height reduction, HR)	**0**	**5%**	**10%**	**30%**	**50%**	**5%**	**10%**	**30%**	**50%**	**5%**	**10%**	**30%**	**50%**
1150 ℃	B		B&R	B&R	B&R		B&R	B&R	B&R	B&R	B&R	B&R	B&R
1050 ℃	B												B&R
950 ℃	B												B&R

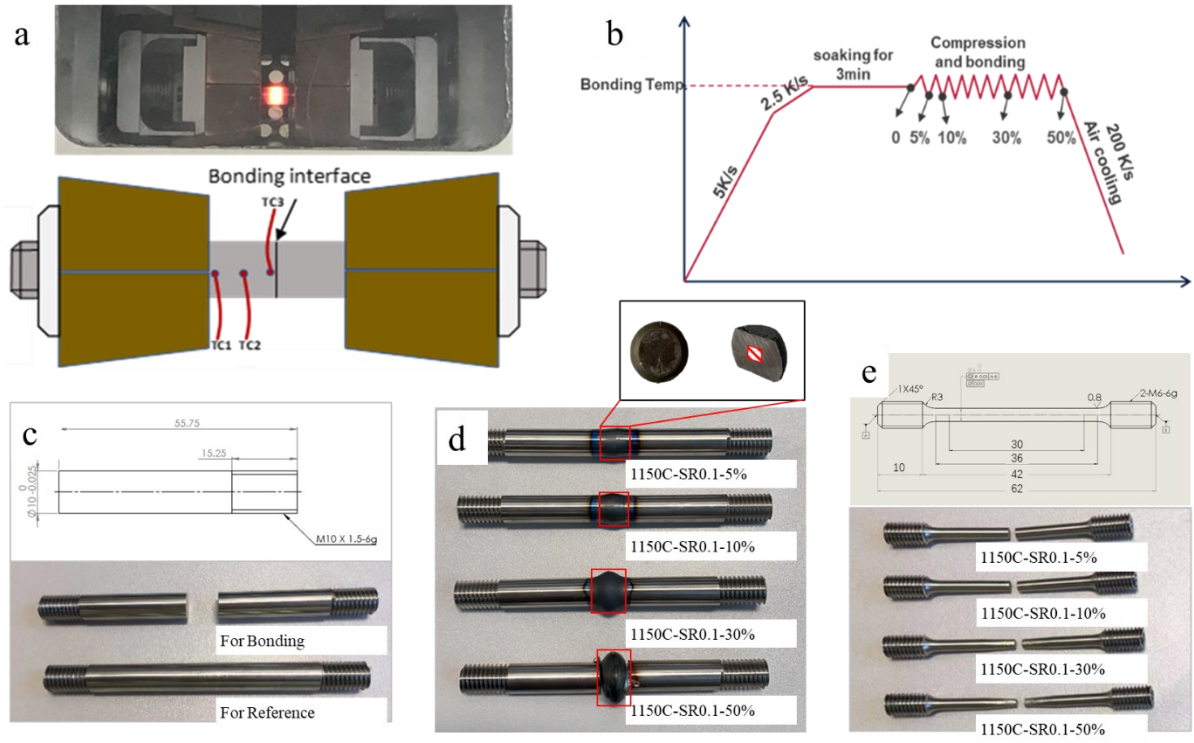


Figure 3-2 a) Compressive bonding set-up on Gleeble 3800; b) the heating scheme; c) half cylinder sample to be bonded and whole cylinder sample for reference test; d) bonded samples after compression (the reference samples are with the same shape, and the marked area taken for microstructure characterization); e) the dimension of tensile sample and fractured samples

Due to the non-uniform distribution of the temperature and constrain from the copper grips, the exposed central part has undergone non-uniform deformation. The temperature distribution over the exposed area measured with thermal couples is shown in Figure 3-3. The deformation condition for the tested central area and the stress state were obtained by conducting the Finite Element analysis with QForm 9.0.

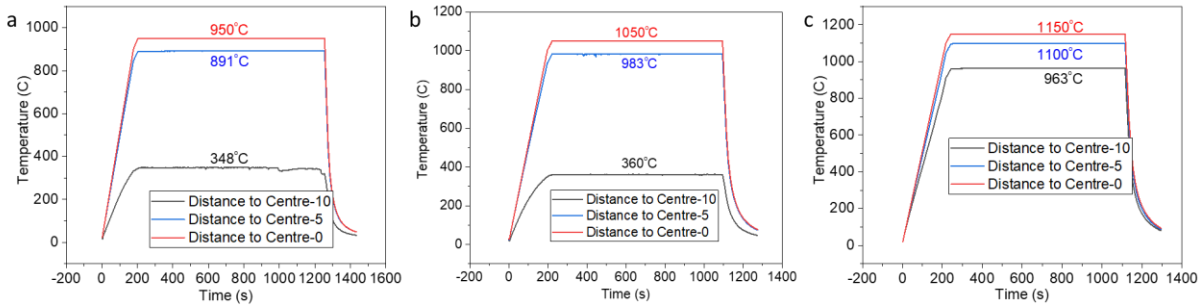


Figure 3-3 The temperature distribution of the bar samples in Gleeble after heating and soaking at different designated temperatures of a)950 ˚C; b)1050 ˚C; c)1150 ˚C; length unit, mm.

3.2.3 Bar sample tensile tests

The tensile samples were machined from the central bonded bar samples according to the configuration shown in Figure 3-2e, and also the fractured tensile samples are shown. The fracture surfaces were observed using the scanning electron microscope (SEM).

Tensile tests at room temperature were conducted with Instron to evaluate the properties of the joints, including the ultimate tensile strength (UTS), the yielding strength (YS) and elongation (EL, ductility). The tensile strain rate was constantly controlled at 0.45 mm/min before yielding and 5 mm/min afterwards. Ultimate tensile strength and yielding strength were determined using the recorded force-stroke data and the ductility was given based on the gauge length change.

3.2.4 Microstructure characterization

To understand the bonding behaviour of the interfaces and their microstructure evolution, compression bonding tests were repeated for microstructure characterization. The sample to be observed was cut from the central area of the bonding zone, where the tensile sample was taken from, and its machining position was shown in Figure 3-2d.

Metallographic samples were prepared according to standard procedures and etched with Adler's II solution. The microstructure was characterized using an optical microscope (OM, Zeiss), scanning electron microscope (SEM, Hitachi S-3400 N). Electron backscatter diffraction (EBSD) measurement was carried out in SEM with Bruker eSprit v2.1 software at an operating voltage of 20 kV, an aperture size of 120 μm, a working distance of 10 mm. The step sizes of 0.4 or 5 μm were used depending on the grain size being analysed. The EBSD Ni

sample was prepared using mechanical polishing with 1 μm OP-S (Oxide Polishing Suspensions) diluted with water to a ratio of 1:5 (OP-S: water) for 15min. Automated orientation analyses were performed with the MATLAB MTEX toolbox.

3.3 The multi-layer construction of IN718 plate in forging practice

3.3.1 Materials -IN718 plate samples

Wrought IN718 used in this forging study is identical to that was used in the Gleeble bonding test.

To imitate the proposed multilayer bonding-based forming method, instead of two layers with one interface using the bar samples in Gleeble, three layers (including two interfaces) were piled up to be forged. As-received IN718 was machined to a plate shape with 52 cm diameter, two different heights of 30 cm and 20 cm. Three plates with heights in sequences of 30 cm, 20 cm, 30 cm were piled up to a total height of 80 cm. The three-layered preform was encapsulated with 304 stainless steel. The configuration is shown in Figure 3-4. The design of the middle layer with a smaller thickness was to make sure the two bond interfaces are within the gauge range for the tensile sample. The four surfaces to be bonded were polished up to P1200# SiC paper and cleaned prior to the encapsulation. The sealed container was evacuated to a vacuum of 10^{-3} Pa.

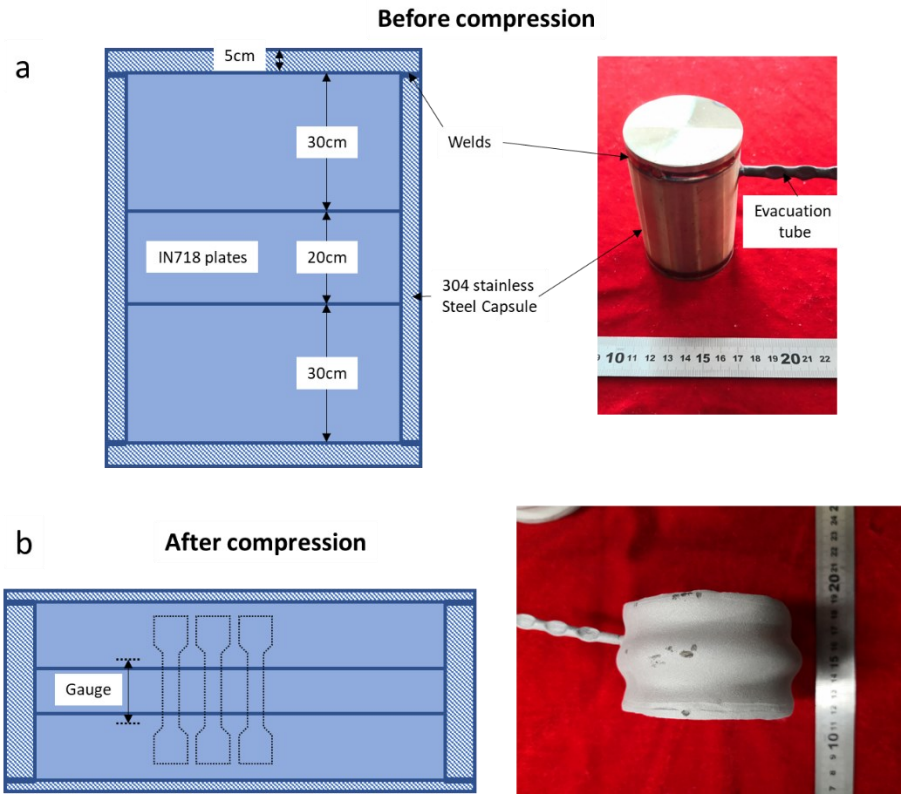


Figure 3-4 The configuration of the piled-up three-layered preform within the container, a) before compression and b) after compression.

3.3.2 Isothermal forging bonding process

The hot forging test was undertaken with Hydraulic Press HTB-2000. The conditions are listed in Table 3-2. The encapsulated piled-up plates were put into the pre-heated furnace at the designated temperature and soaked for 1.5 h to ensure temperature uniformity. After heated up, the plates were moved between the upsetting moulds. The moulds were pre-heated to the designated temperature as well. The strain rate was controlled by the forging speed, and the accuracy was controlled within the shown ranges. Under all conditions, the three-layered encapsulated set was compressed to 50% of the original total height (Noted: 50% height reduction was chosen according to the good bonding test results obtained at 50% with bar samples using Gleeble. Although the local strain along interfaces may not be as large as that of bar samples. It is expected that the higher vacuum adopted within the steel container will help to achieve high bond quality even with lower strain. Further investigation into the effect of strain could not be conducted due to the interruption by the pandemic). And the temperature is chosen according to the traditional hot forging process for IN718.

Table 3-2 The forging/compression conditions

Sample	Temperature, ℃	Velocity vs Strain rate		Strain, %
		Forging speed, $mm \cdot s^{-1}$	Strain rate range, s^{-1}	
1	950	10	0.1 → 0.2	50
2	1050	10	0.1 → 0.2	50
3-1	1150	0.1	0.001 → 0.002	50
3-2		1	0.01 → 0.02	50
3-3		10	0.1 → 0.2	50

3.3.3 Bonded plate microstructure and tensile test

For each forging condition, samples were taken from the forged plate for microstructure observation and mechanical tests. The Sectioned forged plates are shown in Figure 3-5a, and the sampling scheme is shown in Figure 3-5b. Each three-layered forging bonded sample was divided into two halves: one for investigating the quality in the as-forged state, the other one was undergone standard double ageing heat treatment ((950~980 ˚C) ± 10 ˚C × 1 h/AC → (720 ± 10) ˚C × 8 h → (620 ± 10) ˚C × 8 h/AC, AC as an abbreviation for air cooling) to evaluate the performance in the heat-treated (in-use) state. Two zones representing the centre zone (C) and edge zone (E) were defined and marked in deeper purple and lighter purple to examine the uniformity of the bonding quality. In each zone, samples were machined and two for each type of mechanical test for repeatability verification. Room-temperature tensile test (RT-T) tests were conducted. The sample geometry for tensile test is shown in Figure 3-6.

Considering the symmetry of the forging, a specimen was machined from the Section, marked as 0 in Figure 3-5b for microstructure observation to represent the whole plate. 0#-specimen was processively ground, polished and etched by standard procedures (same with stated in Section 3.2.4) to examine the interface. The overall microstructure near bond interfaces was characterized using OM (Zeiss). More detailed observation into the phases and oxide film was conducted with new TESCAN CLARA scanning electron microscopy (SEM).

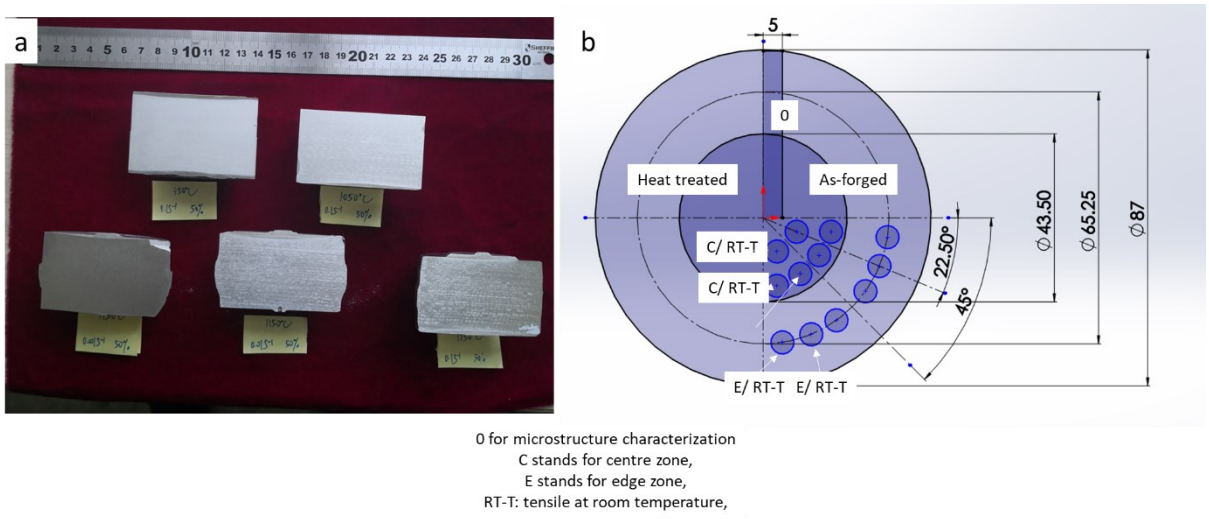


Figure 3-5 a) The forged samples at different conditions, b) The sampling scheme from the forged plate for microstructure characterization and mechanical tests.

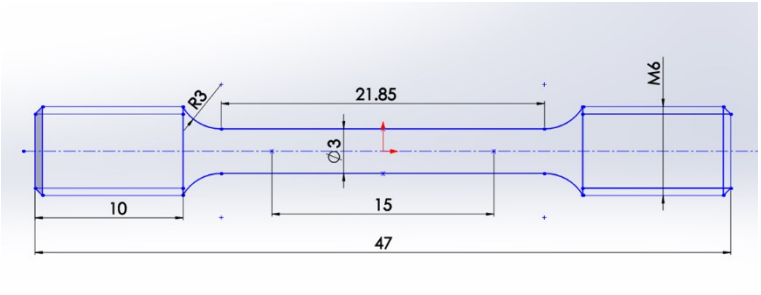


Figure 3-6 The geometry of samples for tensile test.

3.4 Bonding mechanism investigation with pure Ni and Al

3.4.1 Materials – Ni and Al small cylinder samples

In this study, two fcc-structured materials, pure aluminium and pure nickel were used. They were chosen to represent the property of the grain boundaries in typical fcc metal materials with different stacking fault energy (SFE) and herein, aluminium is typically with high SFE and nickel with low SFE.

For pure aluminium, samples were machined from a casting pure aluminium ingot (99.999% purity) at the marked locations in Figure 3-7. The aluminium ingot was provided by Shanghai Jiao Tong University. As shown, four samples are located within two adjacent grains (grain-A and grain-B) with curved grain boundaries and these two grains are with different orientations

A and B, separately. These four samples are composed of one orientation or two orientations: Al-1 with pure orientation-A; Al-2 with orientation-A and orientation-B separated by a horizontal grain boundary; Al-3 with orientation-A and orientation-B separated by a tilted grain boundary; Al-4 with pure orientation-B. The Al samples will be tested under tensile to investigate the property of the inherent grain boundary with different directions to the load.

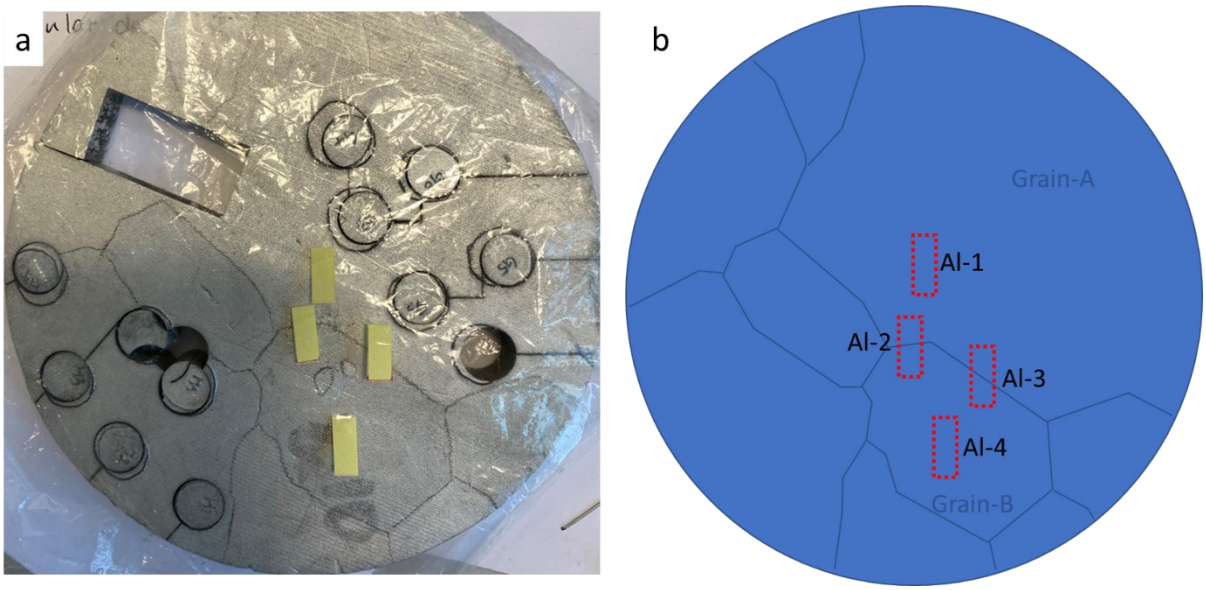


Figure 3-7 The pure aluminium samples from a casting ingot. (a) the ingot; (b) the schematic for sampling strategy.

NI007965 polycrystalline nickel rod with 99% purity from *Goodfellow* Ltd was used and machined to cylinders with a dimension of Φ10 mm × 10 mm for bonding. For the pure nickel, another reason for being chosen is that the oxide film on the bonding interface would be dissolved into a matrix under a certain vacuum environment at elevated temperature[198]. So that the effect of residual oxides on the interface can be neglected and the single effect of interface grain boundaries can be investigated. For both aluminium and pure nickel samples, the tensile tests were repeated three times to ensure repeatability.

3.4.2 Gleeble bonding with small cylinder samples

The pure nickel cylinders were bonded using Gleeble 3800 and the set-up is shown in Figure 3-8. The surfaces to be contacted were polished to P1200# and cleaned in an ultrasonic acetone bath prior to the bonding. Graphite foils were used between the cylinder sample and the anvil to reduce the friction.

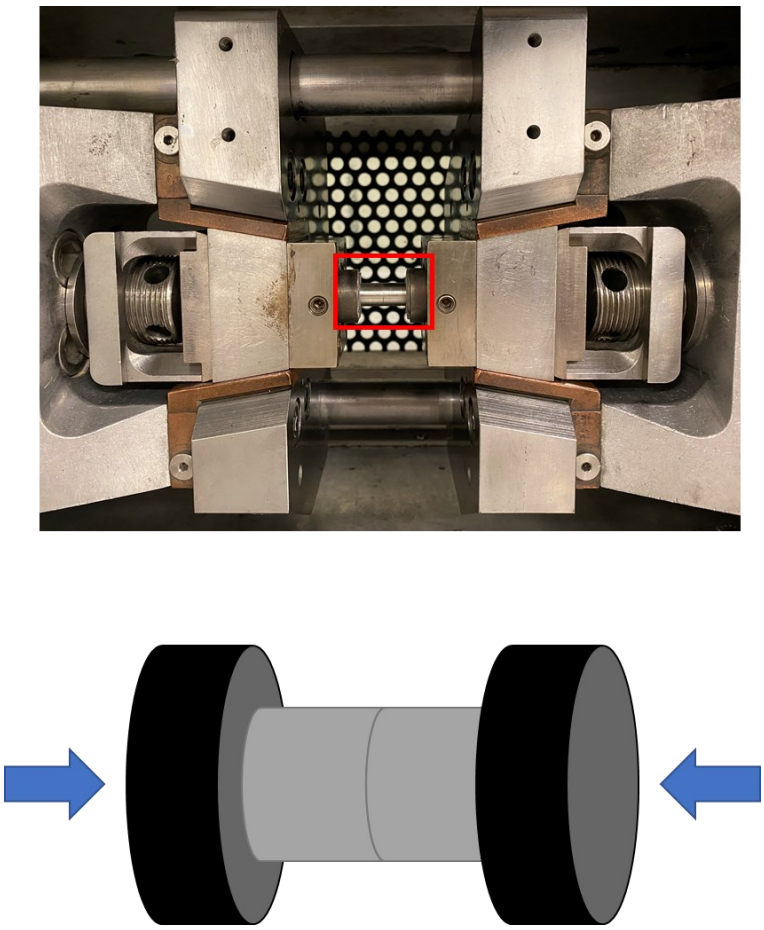


Figure 3-8 The Gleeble set-up for nickel bonding test

To study the effect of the interface grain boundary on the joint quality, two conditions typically for diffusion bonding and compression bonding were adopted to obtain joints without/with grain boundary migration. The two bonding conditions are listed in Table 3-3. For the diffusion bonding, short duration and low force were adopted as suggested in [137] with the aim to get a joint without grain boundary migration but interfaces fully contacted.

The obtained diffusion bonded joint is shown in Figure 3-9a with minor deformation, and the compression bonded joint with more obvious deformation is shown in Figure 3-9b. For each bonded joint, small tensile samples with two different orientations (parallel or vertical to the bonding interface) were machined. The samples machined with different orientations were supposed to have an identical microstructure and grain size, except that vertical samples are with bonding lines in the middle.

Table 3-3 The bonding conditions for pure nickel

	Bonding	Temperature	Strain	Vacuum	Force	Duration
Ni-1	Force control	1150 ˚C	~1%	0.1 torr	1 kN	5s
Ni-2					0.1 kN	120s
Ni-3	Stroke control	1150 ˚C	50%	0.1 torr	4~7 kN	~70s
Ni-4						

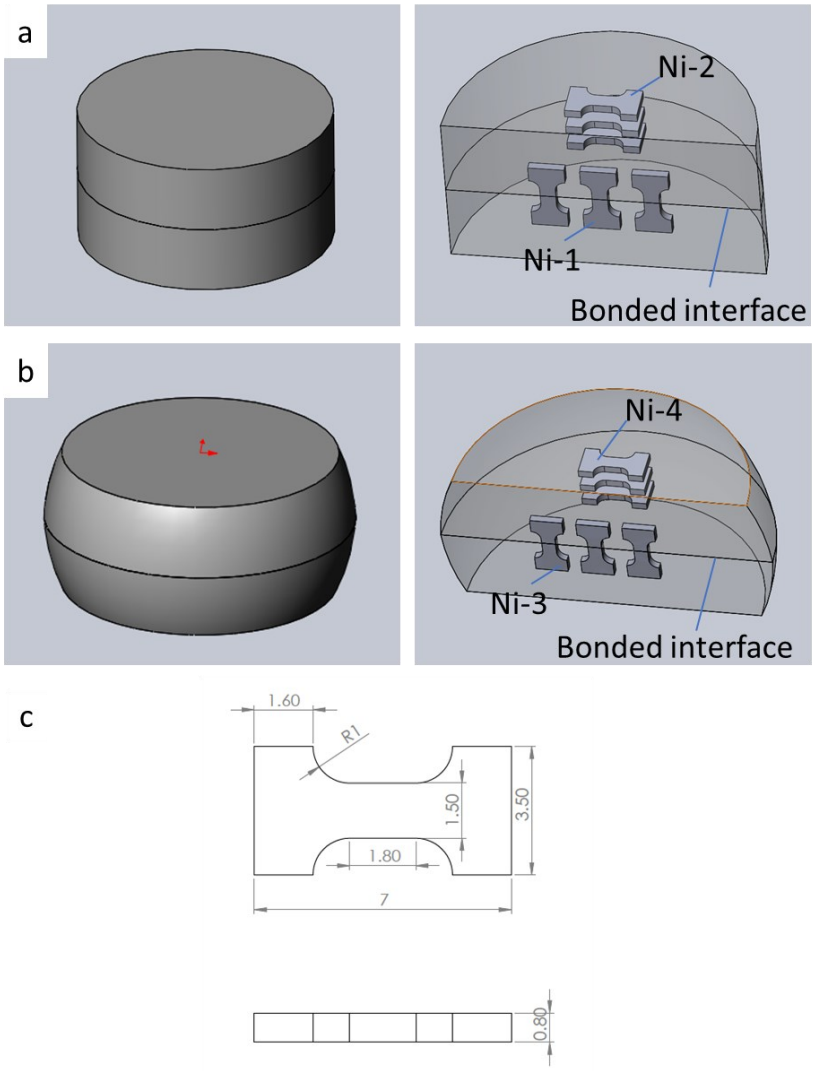


Figure 3-9 The (a) diffusion bonding test and (b) compression bonding test for pure nickel and sampling strategy for the micro tensile test; (c) the dimension for micro tensile sample.

3.4.3 Small sample tensile evaluation and in-situ observation

Tensile tests were carried out on Al and Ni bonded samples at room temperature with a speed of 0.1 mm/min. The specification of the sample for the micro-test is given in Figure 3-9c. 2 kN Deben micro-test machine (Figure 3-10a) was used with the Zeiss OM to in-situ observe the sample deformation during the tensile test, as shown in Figure 3-10b.

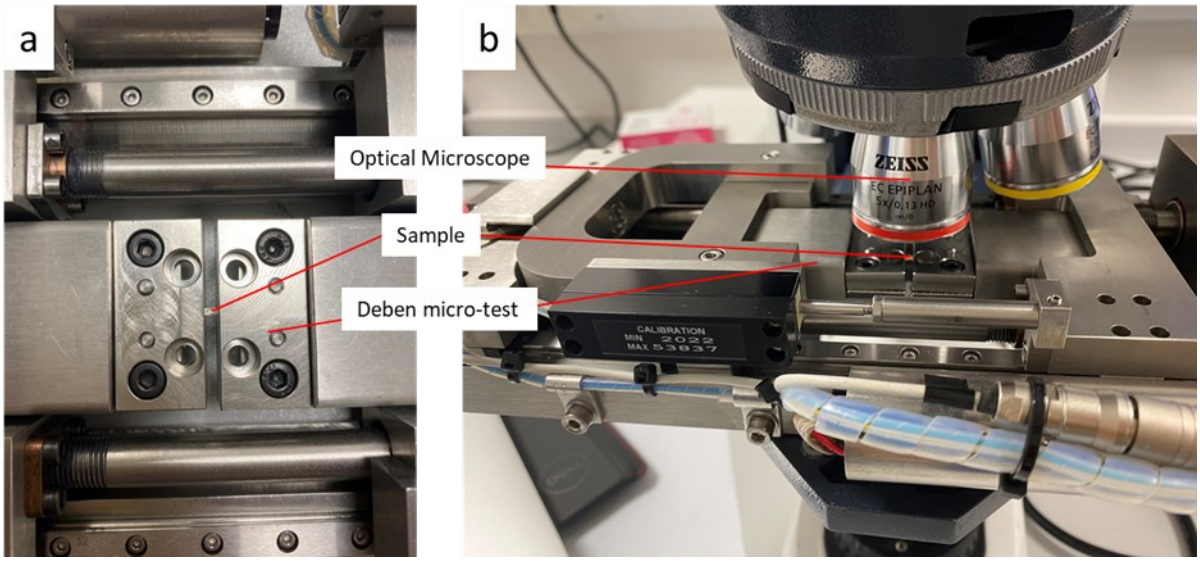


Figure 3-10 The (a) DEBEN micro-test machine and (b) set-up for in-situ observation using optical microscopy during tensile.

3.4.4 Small sample microstructure characterization

Zeiss OM, SEM and EBSD were adopted for microstructural characterization. EBSD was performed before and after tensile deformation in a TESCAN CLARA scanning electron microscopy (SEM) equipped with a CMOS EBSD detector and Oxford Instruments AZtec 5.1 EBSD system for data acquisition. EBSD maps were captured at an accelerating voltage of 20 kV and step size of 5 μm for nickel and 15 μm for pure aluminium, and the AZtecCrystal 2.1 software was used for EBSD data post-processing. Grains with misorientation larger than 15^{o} were recognised.

The samples for OM and SEM was same with introduced in Section 3.2.4. For EBSD, electro-polishing was used for pure Al and Ni. Samples were mechanically grounded using SiC paper up to 4000 grit and electropolished for 2 min in a solution of 9.5 vol. % perchloric acid in

ethanol at 19.5 V with a steady current density of around 1.5 A/cm^2. Ice was used to keep the temperature of the electrolyte under 15 ˚C for safety considerations.

Chapter 4 The solid-state bonding of IN718 using Gleeble under different conditions

4.1 Introduction

As reviewed in Chapter 2, for the widely-studied solid-state bonding methods, e.g. cold pressure welding/roll bonding, although their successful applications have been seen in copper wire welding or composite cladding plate manufacturing [87, 98], their applications have always been limited out of load-bearing components due to the inferior joint performance[87]. Full strength and ductility comparable to parent material are difficult to achieve in manufacturing practice.

By contrast, the solid-state bonding under hot deformation conditions is more prone to obtaining high quality. This is attributed to the combination of higher temperature (than cold pressure welding) and larger plastic deformation (than diffusion welding). More severe microstructure evolution and break-up of the oxide films occur, which facilitates the recovery of the joint performance.

This bonding method by hot deformation will be the basis of a newly proposed bonding-based additive manufacturing concept for the extra-large components. In the new manufacturing method, the quality of the bonded interface and its dependence on the hot deformation condition would be the key focus. To present, even though some studies on hot compression bonding has been done, most bonding tests were conducted with a strictly controlled high vacuum[189, 190, 193, 197]. The oxide film effect has been overlooked. Further investigation on the bonding under more practical conditions (under moderate vacuum condition) is needed.

In this work, a systematic study is conducted to investigate the effects of bonding parameters on the final bonding quality with existence of oxide film. The bonding-by-hot-deforming tests have been carried out on nickel-based IN718 bar samples using Gleeble under different temperature, strain and strain rate. Compared with the works reported in [189, 190, 193, 197], a more practical environment is used with a relatively lower vacuum. Detailed microstructure analysis regarding the interface grains and oxide films has been conducted. The focuses of this work include: to clarify how the Rx affects the bonding interface with the presence of oxide film, to describe the combined effects of multiple factors on the bonding mechanism, and to achieve better joint integrity with both improved strength and ductility.

Firstly, the influence of these factors on joint properties is shown by tensile test results, and the effects of bonding parameters on the interface bonding behaviour are discussed. Then, the evolution of the bond line, the oxide film and grain structure are investigated over the bonding process. Considering the microstructural change during bonding, reference tests are also designed to clarify the dependence of bond quality on the bonding condition, while excluding the microstructural effect. With the help of different microstructure characterization techniques and the correlation investigation between the microstructure and tested tensile properties, the solid-state bonding mechanism under a relatively more complex environment will be studied.

Structure of chapter: The bonding tests have been conducted using bar samples in Gleeble and the interface bond quality was evaluated with tensile tests. The interface microstructure evolution and tensile performance will be given for bonds formed at different strain levels (4.2), temperatures (4.3) and strain rates (4.4); the discussion on the bonding mechanism, as well as the effect of each variable (temperature and strain rate), will be presented in Discussion Section 4.5.

4.2 Strain effect results

4.2.1 The interface microstructure evolution during at different strain levels

As shown in Table 3-1, the Gleeble compression bonding tests were conducted under different conditions to investigate the effects of bonding parameters, including the strain, strain rate and temperatures. Here in this section, the effect of strain level is presented with the results of bonding formed at 1150 ˚C and strain rate of 0.1 s^{-1} to different strain levels (height reduction of 0%, 5%, 10%, 30% and 50%).

The bond line evolution of the joint zone

Optical observation in Figure 4-1 shows that the original straight bond line is disappearing with the increase of strain, and for the bonded sample 50% compressed in Figure 4-1e, the bond line can only be recognized when tracking from edges. According to the cold pressure welding mechanism stated in [89], the disappearance of bond line on large strain is related to the oxide film break-up and metal-to-metal contact; while in this case, the microstructure evolution has also exerted a great influence on eliminating the bond line. Since microstructure evolution is also a strain-driven process at hot working temperatures, more complete microstructure change is found at higher deformation. From Figure 4-1 (a-d), the straight clear bond line is also a co-

planar GB plane connected by the interface grains, and the common GB plane is vertical to the tensile direction. In Figure 4-1e, common grains shared by both sides appear where the bond line was originally located, and the co-planar interface grain boundaries are replaced by randomly misoriented grain boundaries; thus, the bond line becomes invisible. This interface grains randomization phenomenon has also been reported in hot compressive bonding of nickel by [196] and copper by [190] and in the diffusion bonding of aluminium by [138]. This elimination of the bond line, which is co-affected by both interface oxide film behaviour and microstructure evolution, has shown a direct influence on the final joint tensile properties.

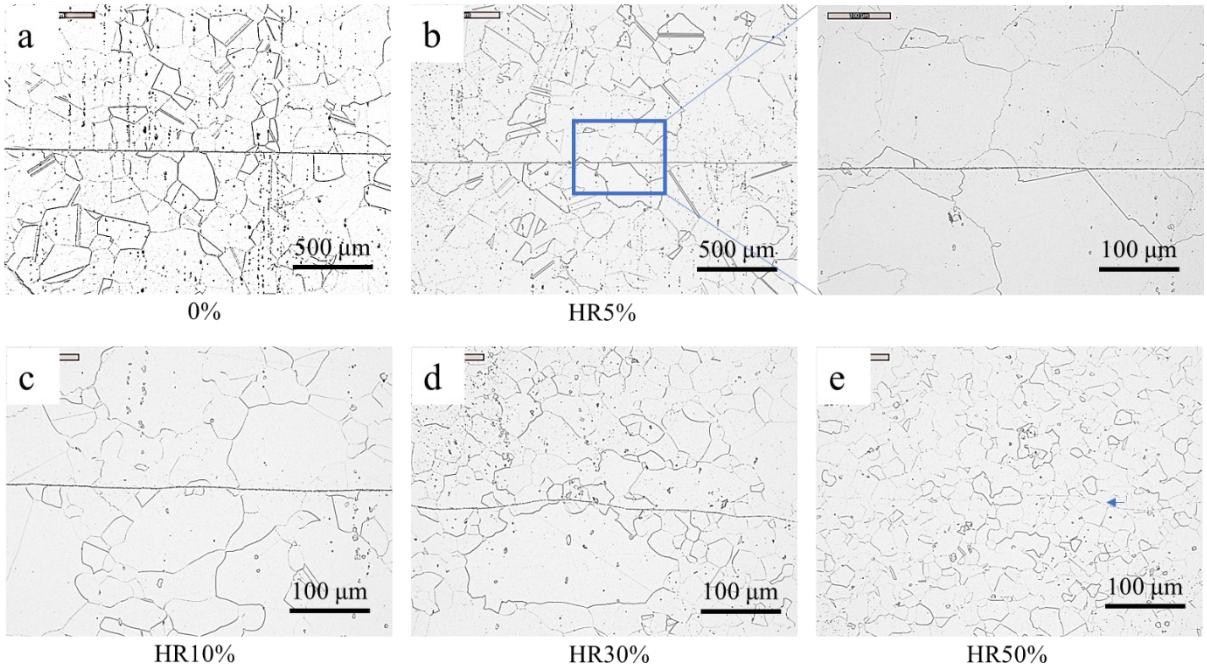


Figure 4-1 The bond line evolution of bonded samples at the height reduction of a) 0; b) 0.05; c) 0.1; d) 0.3; e) 0.5 at 1150 ˚C and strain rate of 0.1 s^{-1}.

The oxide film on bonding interfaces and the interface grains

Under a moderate vacuum condition of 1 torr, oxidation occurs during the hot deformation-bonding process. To give a clearer illustration of the oxide film behaviour, the microstructure is observed using SEM and the images are shown in Figure 4-2. From Figure 4-2a, micro-voids are seen to be effectively closed in the early stage of the compression bonding process, and the observed discontinuous bond line is oxide remaining on the interface. From the EDS elements analysis in Figure 4-2a, the oxide remaining along the interfaces are mainly alumina and

titanium oxide, despite their low content in IN718. For bonded samples compressed lower than 30%, the oxide films are straight and continuous; whereas in Figure 4-2d, when the height is 30% reduced, the surface is extended, and the oxide film is stretched into pieces with a gap equivalent to the fragment dimension. With the height being compressed to 50%, oxide segments are more scattered, allowing more metal-to-metal contact and spaces for atom diffusion.

Another important change is the relative location of the oxides. As shown in the OM observation in Figure 4-1e, common grains occupy where the bond line is. Combined with the SEM characterized oxide in a 50% compressed sample, the appearance of these interface grains has included the fracture oxide fragments within GBs (Figure 4-2e). While for samples with lower compression strain, continuous oxide film exists and separates grains on either side. Oxides remain on the coplanar GBs. In polycrystal materials, GBs are the main dislocation barriers for work hardening and also could be considered fragile defects due to the lattice misalignment, atomic gaps, and the aggregation of foreign atoms and other inevitable remaining contamination, e.g., the continuous oxide film in this case. When those coplanar GBs at the bonding interface are vertical to the tensile load and are weakened with the existence of the interface oxides, the maximum tensile stress is applied to pull GBs apart. Poor ductility of the bonded sample would be expected, and it was observed in [215] and from the fracture surfaces (Figure 4-7) in this study. However, with the oxide being included within the grains from intergranular, its negative effects on the bonding interface could be reduced.

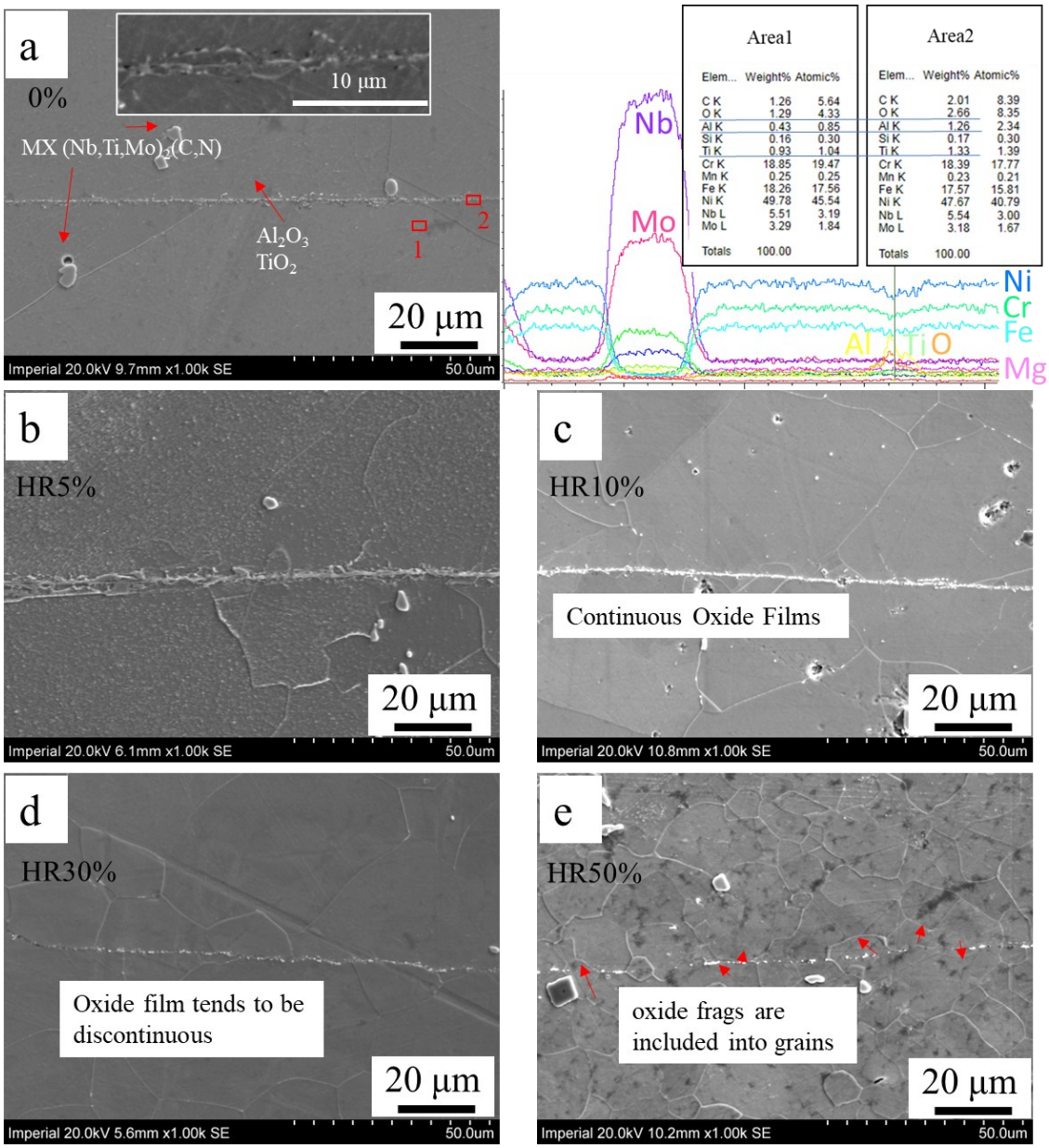


Figure 4-2 The microstructure of the bonding zone of IN718 samples compressed at strain of a) 0; b) 0.05; c) 0.1; d) 0.3 e) 0.5; (0, 5%, 10%, 30%, 50% height reduction, respectively) at 1150 °C and strain rate of 0.1 s^{-1}.

Recrystallization induced grain evolution

The EBSD grain orientation maps and Inverse Pole Figures (IPFs) in Figure 4-3 show the recrystallization at the bonding interface of the samples deformed to various strain levels. Driven by the increasing strain, the microstructure evolves with the proceeding of recrystallization, presenting a more uniform and finer microstructure. Similar to that shown in [34] and [216], Rx in hot deformed IN718 starts from the grain boundaries or triple junctions,

and eventually large original grains replaced by fine, equiaxed smaller ones. The necklace Rx grain structure is seen in Figure 4-3 (b-d). Over the whole observed region, recrystallized microstructure keeps in consistent for each sample, and no obvious difference is shown between the bonding interface zone and matrix. Thus, it is reasonable to neglect the effect of the interface imposed on the overall deformation behaviour of the joint.

However, locally along the interface, the coplanar GBs can also be seen in the EBSD maps in Figure 4-3 (a-d) and the randomization of the interface GBs in Figure 4-3e, which is in accordance with observation in Figure 4-1 and Figure 4-2. This randomization of the interface GB is related to the Rx process, and a higher Rx fraction leads to a complete interface GB randomization, shown in Figure 4-3 and Figure 4-4. A similar relation can be supported by [195], and it is proposed to be due to the nucleation, grain growth and GB migration during the Rx. The GB migration process, which turns the bond line to be less straight and with more bulges, occurs simultaneously with the Rx nucleation and grain growth. At lower strain, the under-developed dislocation accumulation provides no enough driving force for Rx, thus leaving the interface GBs straight. While under larger deformation, higher energy input promotes the movement of GBs and interface GBs migrate over the bond line, turning it to be randomized. When a complete GB migration occurs with a fully Rx, the original interface (also the common coplanar GBs) is conjoined by migrated recrystallized grains.

This randomization of interface GB benefits the joint performance: on the one hand, as discussed earlier in this section, the migrated interface GBs has surpassed the oxide fragments and turned the intergranular oxide contamination into inclusions inside grains, so the oxides enwrapped by metals would show a less impairing effect on joint properties; on the other hand, the GB migration turns the coplanar GBs into random-oriented, which helps resolve the load applied perpendicular to the weak coplanar GBs. Combined with the tensile results above, the disappearance of the straight bond line (coplanar GBs) implies the recovery of the ductility of the joint. This is especially the case for bonded samples with higher elongation, of which the Rx fully occurs, and GB migrates over the bond line. The complete transformation from the straight interface to random-oriented GBs could be the main reason for the high EL and UTS for the severely deformed bonding samples.

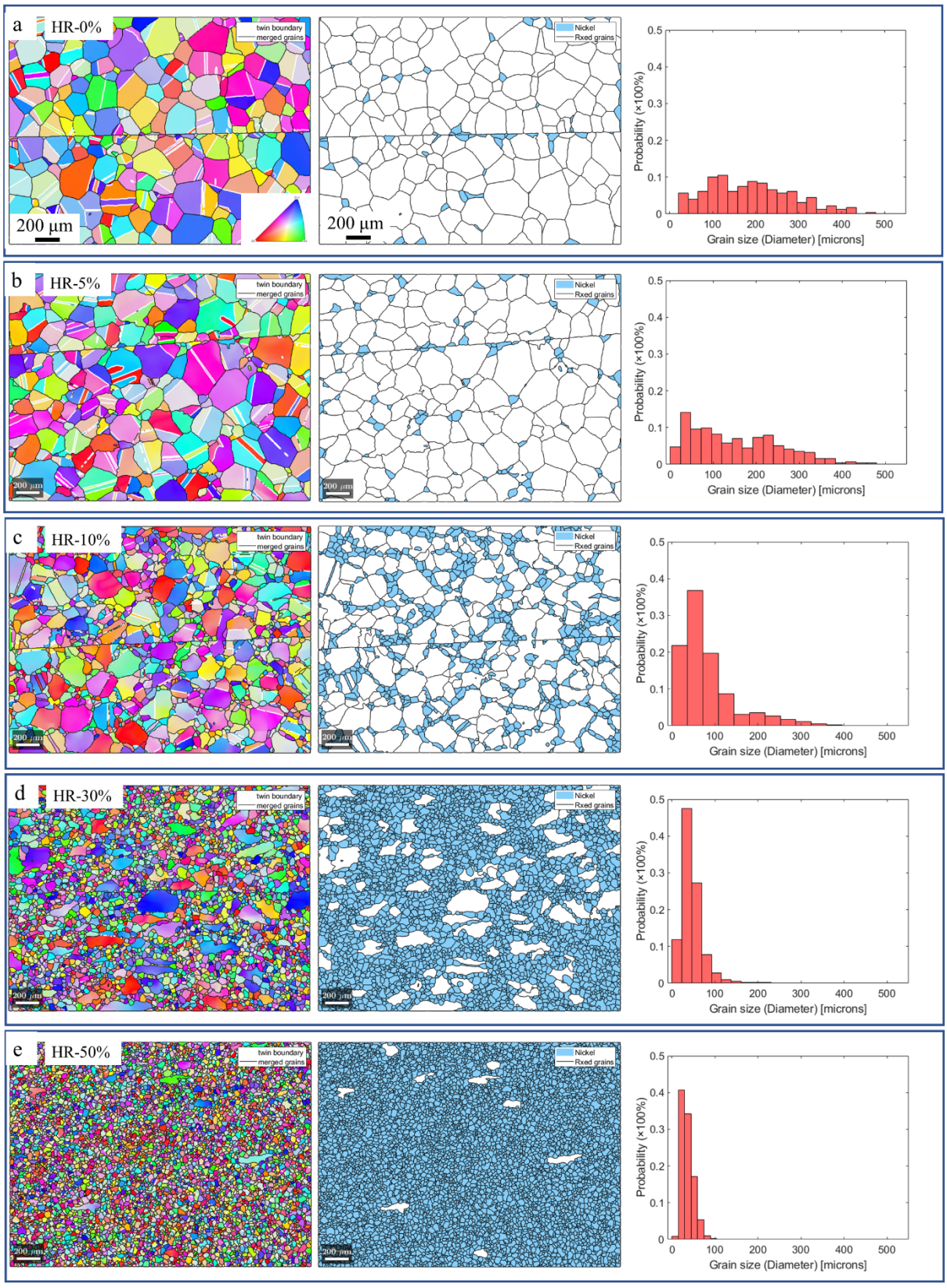


Figure 4-3 The EBSD orientation map, recrystallized grains and grain size distribution of the bonding zone of IN718 samples compressed at engineering strain of a) 0; b) 0.05; c) 0.1; d) 0.3 e) 0.5; (0, 5%, 10%, 30%, 50% height reduction, respectively) at 1150 ˚C and strain rate of 0.1 s^{-1}.

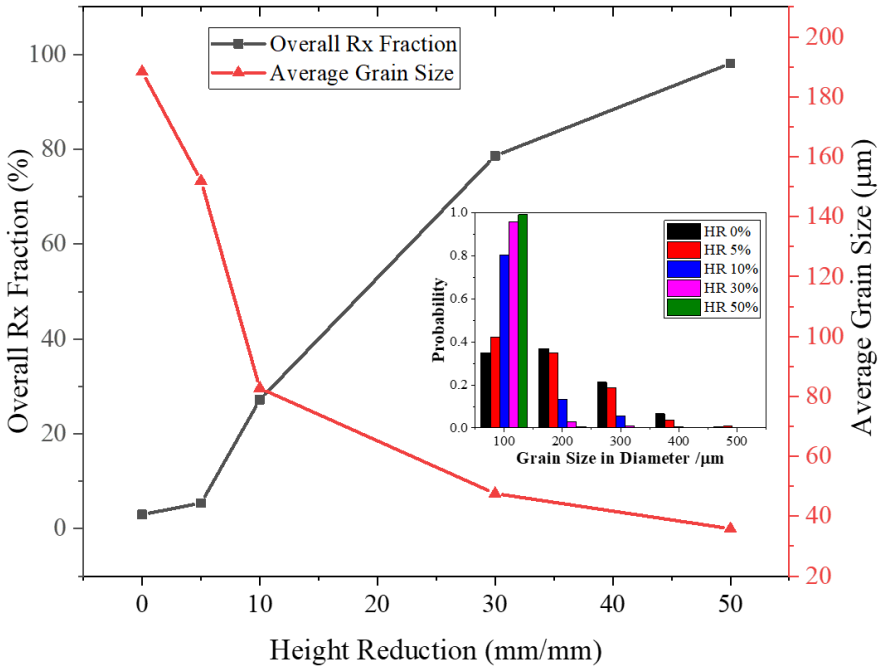


Figure 4-4 The Rx fraction and grain size distribution of the bonding zone of IN718 samples compressed at different strain levels: 0, 5%, 10%, 30%, 50% height reduction, respectively, at 1150 ˚C and strain rate of 0.1 s^{-1}.

The GB migration process over the bond line with the presence of oxides

For IN718, the nucleation and grain growth during Rx is achieved by GB migrating and closely related to the dislocation behaviour, which was shown in [196]; however, the existence of oxide in this bonding process has exerted an extra impeding effect on GB migration. Figure 4-5 presents the EBSD maps of bonded samples compressed to 10% and 30% at a larger magnification. Comparing the GBs migration near the interface in the EBSD map with the oxide distribution in SEM images, the Rx-ed grains migrate through the oxide gaps in the way of bulging. Compared with residual original larger grain, the boundaries of newly formed small recrystallized grains and these smaller grains, as suggested by [42], have higher boundary angle and interface energy, and bulges more easily. According to the energy theory in the recrystallization process, Rx initiates from the triple junctions, and it is the same case with the Rx near the interface: refined grains can be observed along the bond line. With the continuous oxide film in sample 10% compressed, the newly Rxed grains appear on sides of the bond line, composing the coplanar GBs. Further, when the sample is compressed to 30% and small gaps

have been formed as the oxide film is more stretched, GB migration and bulge occurs partially, as shown in Figure 4-5b. It is worth noting that recrystallization is a continuous process. More newly Rxed refined grains continue to appear near the interface and migrate more easily, forming a refined uniform structure without a co-planar interface in the end. It is difficult to distinguish the effects of oxide fragments and dislocations, for which lower strain leads to continuous oxide film and lower recrystallization fraction, both inhibiting the randomization of the coplanar GBs; and vice versa.

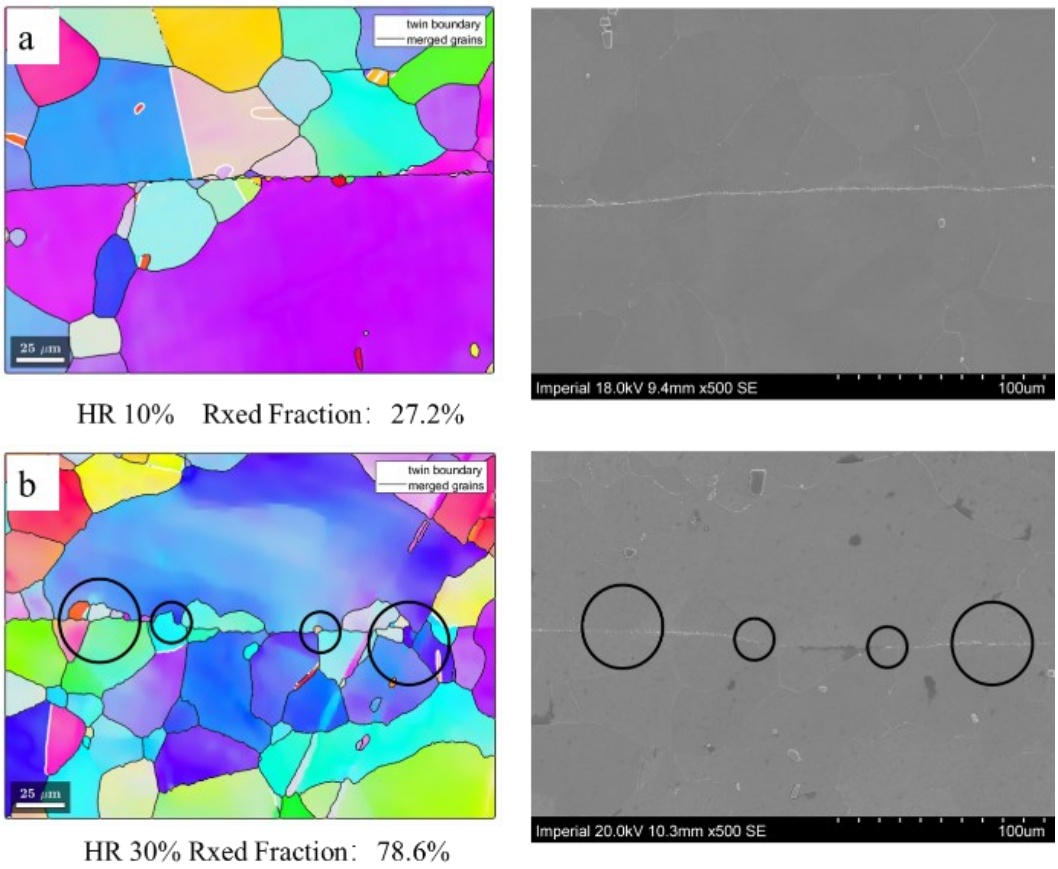


Figure 4-5 The EBSD maps and microscopic characterization of bonding zone of IN718 samples compressed at height reduction of a) 0.1, b) 0.3 at 1150 ˚C and strain rate of 0.1 s^{-1}.

4.2.2 The tensile results for samples bonded at different strain levels

Two half bar samples have been bonded under compression, and tensile properties have been tested at room temperature.

Tensile properties of the joints

The tensile results of samples bonded at different strain levels are shown in Figure 4-6. Their UTSs show an increasing trend for the joints bonded with an increasing imposed compressive strain (Figure 4-6a). This dependence of tensile strength on the applied compressive strain is similar to that of the tested shear strength in the previous roll bonding or pressure welding studies of [89] and [116]. It has been explained that the oxide film needs to be stretched under a larger strain to expose the clean metal and form the bond. More severe deformation parallel to the interface is induced at a higher height reduction, and the material flow helps the intimate contact of the surfaces to be bonded.

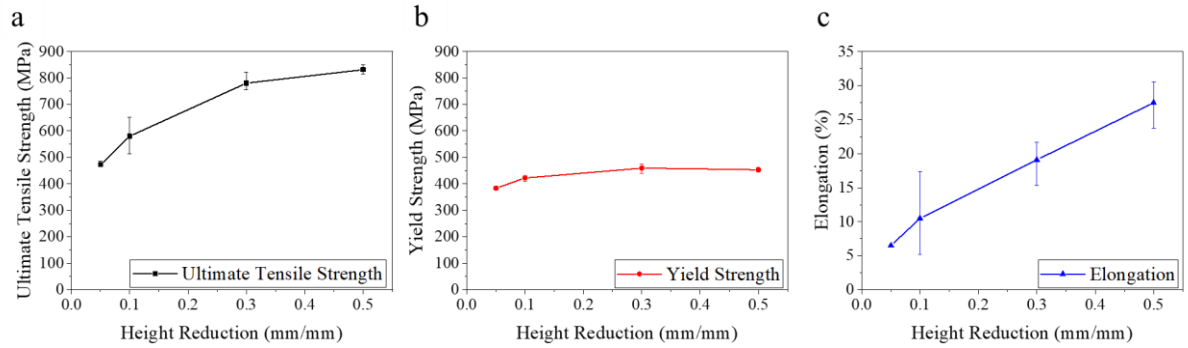


Figure 4-6 The tensile test results: a) ultimate tensile strength (UTS); b) yielding strength (YS); c) elongation (EL) of IN718 samples bonded at 1150 ˚C/0.1 s^{-1}.

Lower bonding strength is obtained when the sample is compressed at a reduction ratio of 0.05 as seen in Figure 4-6a. This compressive strain is much lower than the critical strain for initiating bonding in the cold roll bonding processes. For example, a typical value of the critical surface expansion for Al-Al contacting pairs is 0.3 in [89]. A critical value of 0.4 height reduction has been reported for the Al plates coated with Ni layer by [89]. As stated in the classic cold roll bond models by [118], later [90] and [121], this critical strain exists because the contamination and oxide film on the bonding interface stop the contact between clean surfaces at a lower strain level and makes no contribution to the bond. However, according to the studies of hot-pressed alumina-nickel by [217], a higher interface strength has been achieved under appropriate pressure and temperature. For the bond formed at a similar temperature and stress condition in this study, the cohesion between the existing oxide film with metal matrix could be the reason for the bond strength achieved at a lower strain level.

The elongation in Figure 4-6c results show a similar changing trend with UTS over the increasing compressive strain, however, the YS in Figure 4-6b has also increased very mildly over the compressive strain. The variation of UTS, YS and EL can also be seen from the tensile curves in Figure 4-7a: the elastic zone and yielding zone of four curves keep increasing similarly; while after yielding, they start to present different hardening effects and fracture strains. Joint formed under lower compressive strain shows lower hardening stress and fractures at the earlier stage. YS indicates the dislocation slip resistance from the grain boundaries or residual dislocation structure, and the YS difference gives a hint for the different grain sizes for these samples bonded at the different strains. Whereas the significant variations in UTS are more comprehensively affected by factors including microstructure, defects and interfaces. As UTS is based on both the YS and EL, combined with the hardening process, hence EL is considered to be more directly related to joint quality. The elongation of the joints increases with an almost constant rate as a function of applied compressive plastic bonding strain, which also implies the direct dependence of joint quality on elongation.

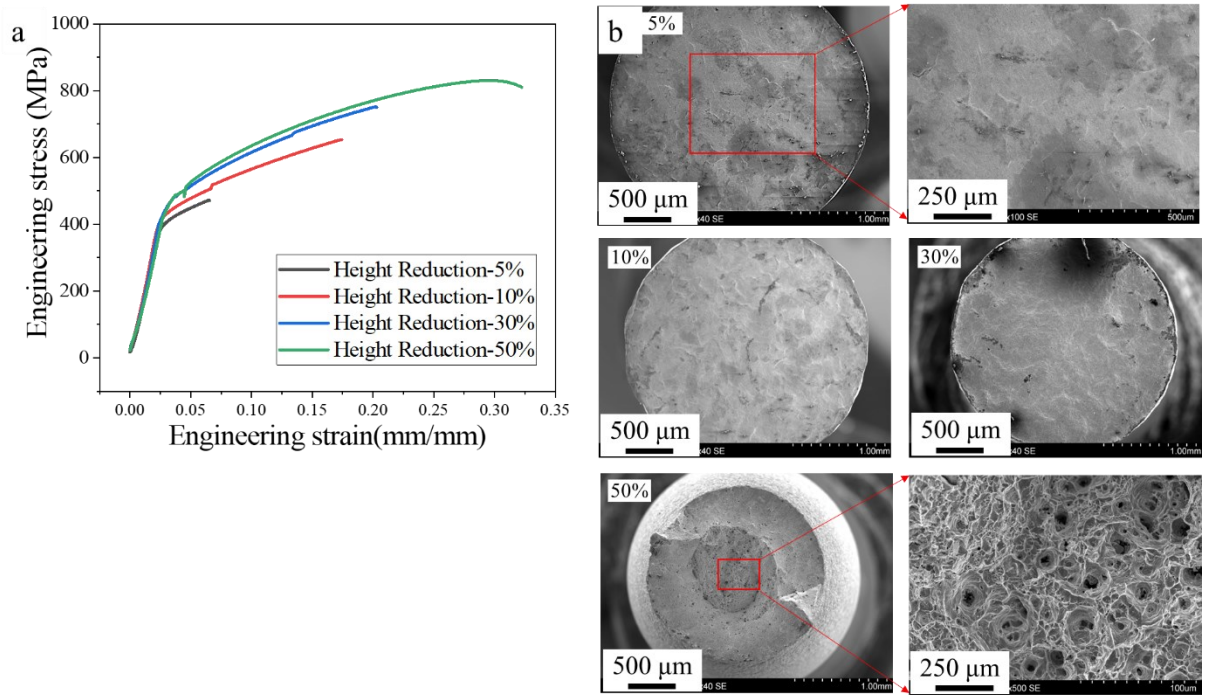


Figure 4-7 a) The tensile engineering stress-strain curves; b) the failure surfaces of IN718 samples bonded, bonded at 1150 ˚C/0.1 s^{-1}.

As shown in Figure 3-2e, all bonded samples fracture in the middle area. Figure 4-7b shows the fracture morphologies of bonded samples. Consistent with the inferior elongations of under-bonded samples at lower strain, their fracture surfaces are relatively flat and show an intergranular brittle feature. Some grain boundaries can be observed as straight edges on the fracture surfaces of samples compress bonded under 5% and 10% reduction. For the sample bonded at 50% reduction, some dimples can be seen, and the failure surface turns to be bumpier, which implies a more ductile fracture mode for the joint.

It is important to note that, the phenomenon that joints fracture near the middle is not evidencing that the joint interface is weaker. The fracture position near the middle could be a possible combined result of the bond interface and the non-uniform microstructure distribution along the whole deformed bar sample. The central exposed part of the whole sample has been subjected to heating without ageing, thus acting as a weaker point, while the other parts are held in the anvil connecting to the cooling system so to maintain the as-received higher strength. To separate this mixed effect of the microstructure and the interface, references without the presence of an interface in the middle have been deformed and tested under the same thermal-mechanical conditions. and they are supposed to have identical microstructures with their corresponding bonded sample, except the middle interface.

Relative tensile properties of joints to references

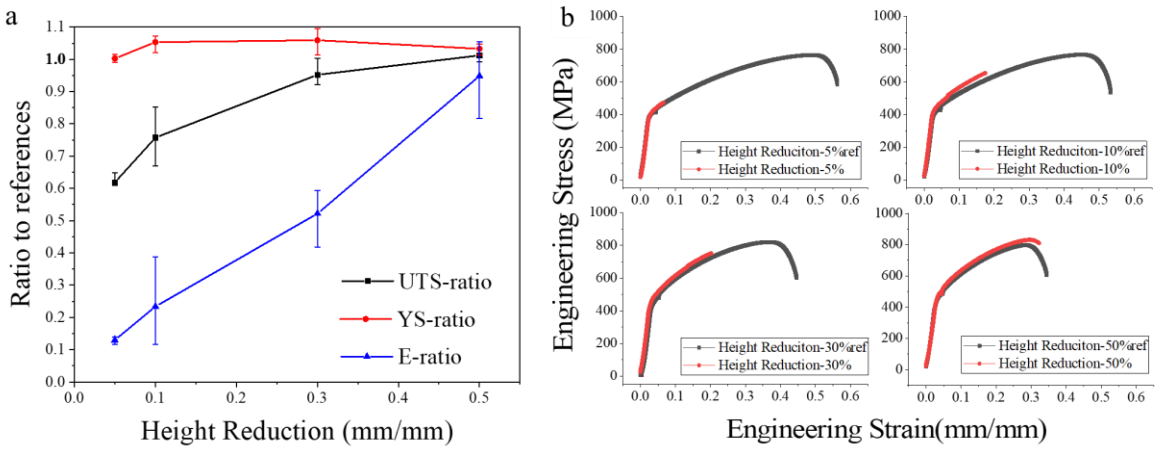


Figure 4-8 a) The tensile test results referred to the results of samples compressed at the same condition (reference test). b) The tensile engineering stress-strain curves referred to the results of samples compressed at the same condition (reference test) of 1150 ˚C/0.1 s^{-1} to different strains.

The comparison between the bonding strength of the bonded samples and the reference samples is shown in Figure 4-8. The strength ratio of the bonded sample to reference is considered here to reflect the joining interface behaviour, excluding the effect of microstructure on the joint properties. The UTS ratio and EL ratio are increasing with height reduction, and when the height is 50% compressed, the ratios of both UTS and EL approach 100%. For the YS, there is no such obvious change for different deformation strains, and the ratio keeps being stable at roughly 1.0, which is consistent with the results shown in Figure 4-7a. The achievement of tensile property ratios approaching 1.0 indicates full recovery of the joint integrity. Figure 4-8b shows the corresponding stress-strain curves, and the tensile stress of the bonded samples follows the references well in the elastic and initial plastic region, whereas, the bonded samples show brittle fracture before achieving UTS.

These interrupted stress-strain curves clearly show the variation in yielding, hardening, ultimate tensile stress and ductility of samples bonded at different stages of the thermal-mechanical tests. For samples bonded at lower strain, their inferior UTS is not only caused by microstructure but is also impaired by the incomplete joining of the interfaces. These under-bonded interfaces act as inner defects during the tensile test and determine the fracture of joints and their necking. With these interface defects being healed at large deformation (50%), the tensile stress tends to reach a plateau right before the failure and shows necking behaviour.

4.3 Strain rate effect results

The strain rate effect on the bonding was investigated within a range of 0.001 s^{-1}~0.1 s^{-1}. And to compare the bonding process under each strain rate, three strain levels were conducted (10%, 30% and 50%). The interface microstructure evolution is characterized, and tensile properties are evaluated.

4.3.1 Effect of strain rate on the interface bonding microstructure

As stated in Section 4.2, the oxide film and its interaction with Rx process play a critical role during the bonding. The oxide film behaviour vary with the surface expansion and local strain, which is changing with the deformation. Figure 4-9 compares the microstructure of the bonds formed under different strain rates at different strain levels. Similar to 0.1 s^{-1}, the oxide film of bond under 0.01 s^{-1} and 0.001 s^{-1} all show similar behaviour with the increasing of strain. While the strain rate somehow affects the dispersion of oxides at same strain.

In Figure 4-9(a-c), the oxide films are continuous when compressed at 10% for three strain rates and the gaps remain near zero. When compressed to 30%, in Figure 4-9 (d-e), the oxide films are stretched to fracture, and gaps start to increase from zero to ~4 μm for 0.001 s^{-1} and 0.01 s^{-1} and the gap remains very small for 0.1 s^{-1}; with the further increase of height reduction, as shown in Figure 4-9 (f-i), the oxide films are further stretched and oxide fragments are more dispersed with larger gaps: the gaps are ~10 μm for 0.001 s^{-1} and 0.01 s^{-1} and the gap for 0.1 s^{-1} is a bit smaller ~6 μm. At 50%, the widely dispersed oxides are included within the grain as the interface grain boundaries migration proceeds and the migrated grain boundaries are marked with red arrows. The oxide film and oxide fragments after fracture are marked with white arrows.

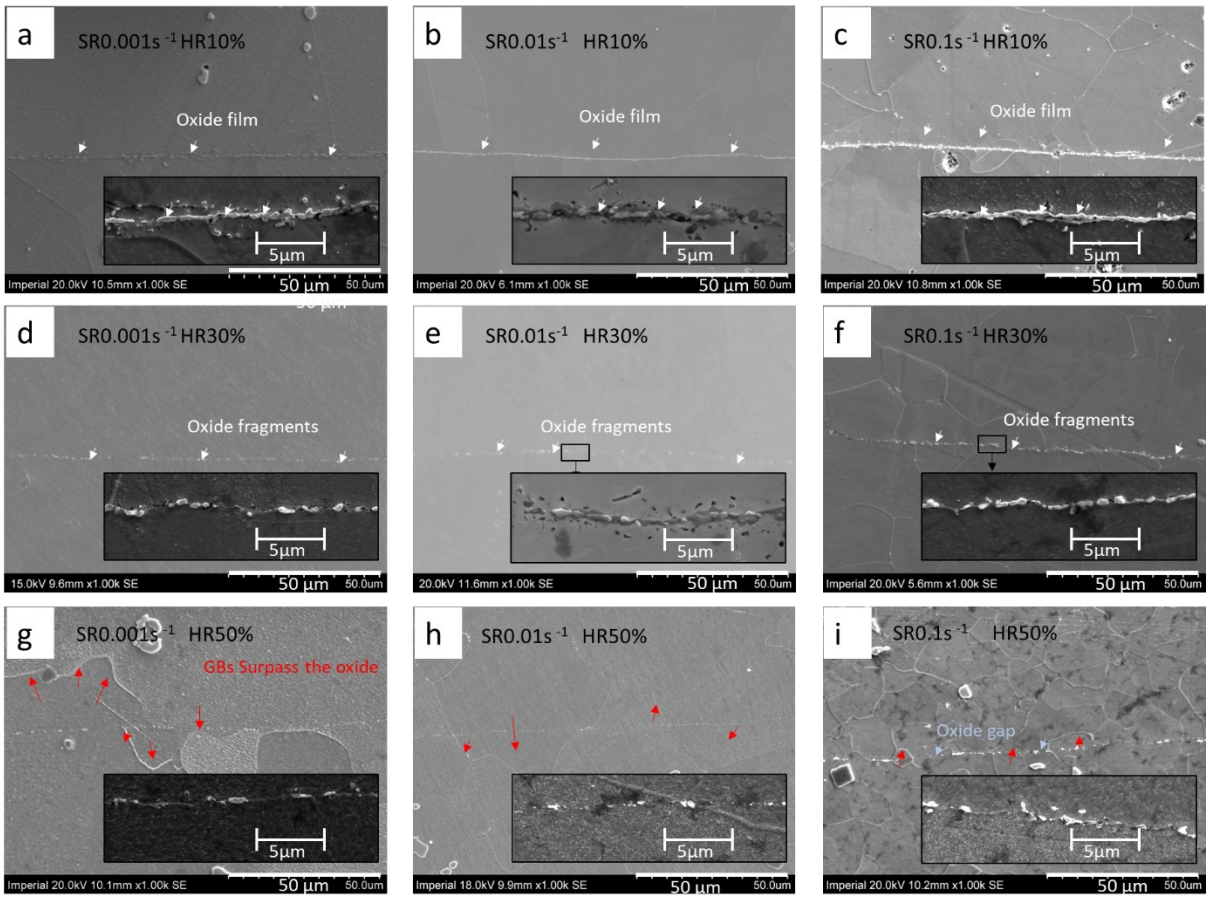


Figure 4-9 The microstructures and interfaces of IN718 samples bonded at 1150 ˚C under different conditions a) SR0.001 s^{-1}, HR 10%; b) SR0.01 s^{-1}, HR 10%; c) SR0.1 s^{-1}, HR 10%; d) SR0.001 s^{-1}, HR 30%; e) SR0.01 s^{-1}, HR 30%; f) SR0.1 s^{-1}, HR 30%; g) SR0.001 s^{-1}, HR 50%; h) SR0.01 s^{-1}, HR 50%; i) SR0.1 s^{-1}, HR 50%.

The microstructure evolution near the bond affects the overall bond strength and its interaction with the oxide film along the interface determines the bond quality, as concluded from Section 4.2. The grain microstructures of joints formed under different strain rates are given in Figure 4-10. Same with the hot forging of IN 718, typical discontinuous dynamic recrystallization (DDRx) necklace microstructure are seen in bonds at high strain rate of 0.1 s^{-1} [34]. Given a shorter deformation time, recrystallization occurs with high nucleation rate due to the high deformation energy while low grain growth rate. Thus, grains present equiaxed shape (Figure 4-10 c and f). And at lower strain rate of 0.001 s^{-1} and 0.01 s^{-1}, the recrystallized grains would be able to grow larger with an irregular shape (Figure 4-10 a, b and d, e). Under 0.001 s^{-1}, an uniform recrystallized microstructure is seen at an earlier stage of 30% reduction (Figure 4-10a compared to b and c). Under all three strain rates, the recrystallization would complete at 50% reduction (Figure 4-10 d, e and f). Much finer microstructure is obtained under 0.1 s^{-1}. EBSD maps show that the interface exerts no effect on the overall microstructure change as no difference is observed between the recrystallized microstructures of the interface zone and the matrix zone of the joint.

The strain rate make no obvious difference in when the original bond line is disappearing. The bond lines are seen under three strain rates at 30% reduction (Figure 4-10 a, b and c). The continuous oxide film observed in Figure 4-9 d-f stop the interface GB migration. At higher magnification, the Area-A, B and C from Figure 4-10a, b and c (compression to 30% at different strain rates) are also shown correspondingly underneath. For area-A under 0.001 s^{-1}, a clear strain line made of the co-planar GBs are shown, and grains present an irregular shape with a larger average size of around 300 μm. When the strain rate is increased to 0.01 s^{-1}, a mixed microstructure in seen in area-B. Some grains are presented crossing the bond line, which is marked. The grains marked with black circles are small, recrystallized grains appearing near triple junctions and migrating over the line; the grains marked with white circles are large, recrystallized grains irregularly bulging over the line. Similar to the large grains formed under a slow strain rate, the large grains in area-B are also grown as recrystallized grains. In area-C, also a microstructure mixed with large and small grains are shown. The difference is that larger grains present with a relatively regular shape, which is considered un-recrystallized deformed grains. Small equiaxed recrystallized grains appeared near GBs and triple junctions, and some were crossing the bond line. As the white circle marks, GB bulging is also observed. In comparison, the grain crossing the original line are mostly composed of

small equiaxed recrystallized grains. Although large grains could also bulge over the line, it might be more difficult. At 50% reduction, no bond line is seen under three strain rates.

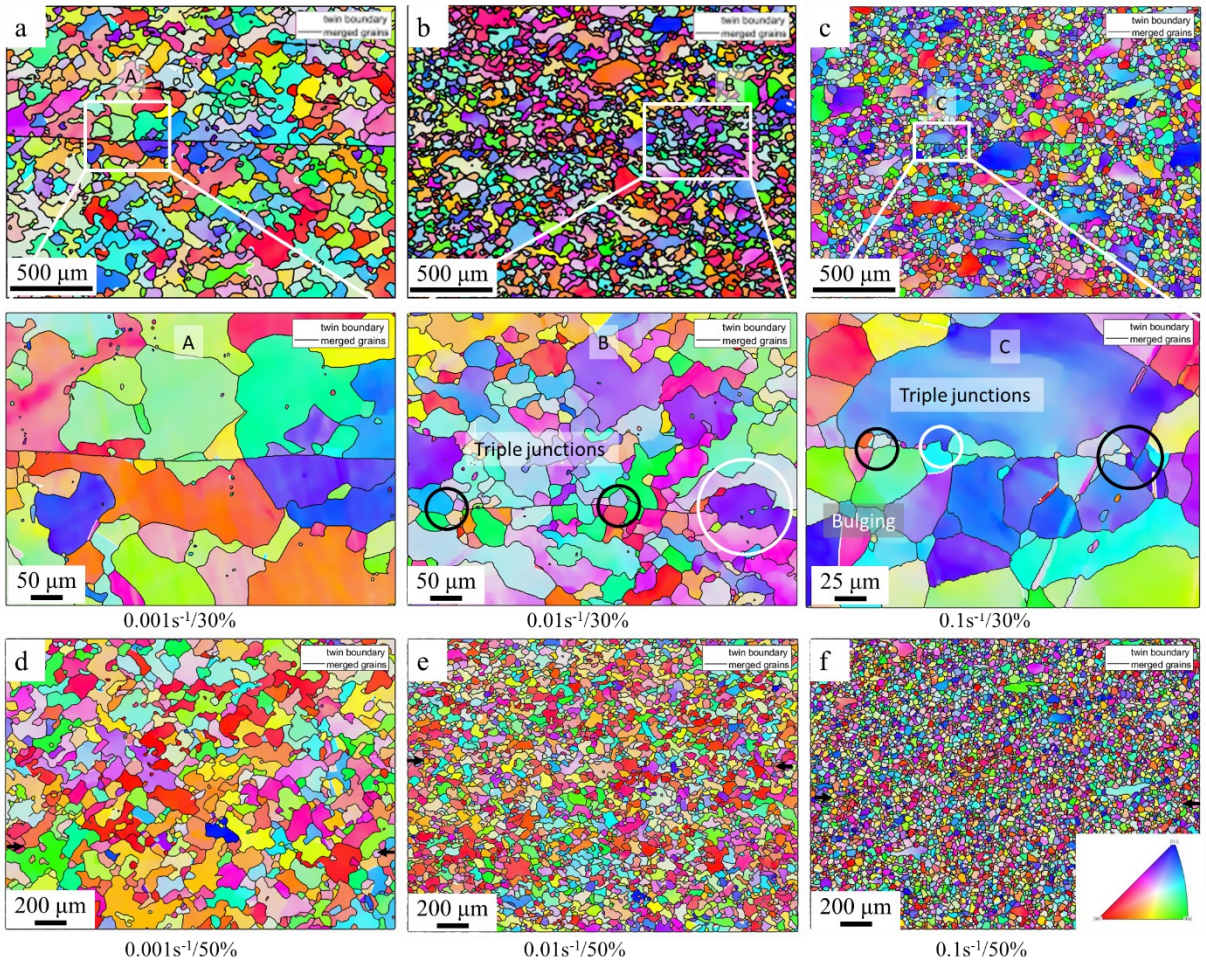


Figure 4-10 The IPF figures for samples bonded under different conditions at 1150 ˚C. 30% height reduction at a) 0.001 s^{-1}, b) 0.01 s^{-1}, c) 0.1 s^{-1}; 50% height reduction at d) 0.001 s^{-1}, e) 0.01 s^{-1}, f) 0.1 s^{-1}.

4.3.2 Effect of strain rate on tensile results

The tensile properties of samples compress bonded at different strain rates

Figure 4-11 presents the tensile test results of the joints formed under different strain rates at different reduction. The final tensile properties are compared in Figure 4-11 a and b. No obvious difference can be seen from the UTSs under different strain rates, both at 30% and 50% reduction. However, the YS under 0.1 s^{-1} is higher than lower strain rates.

Figure 4-11(c-e) provide the tensile curves of bonds formed under different strain rates, better explains the joint performance in Figure 4-11 a and b. It indicates the final tensile properties

are comprehensively affected by the microstructure and interface condition. 10% compressed samples show a similar yielding and hardening on the tensile curves. At the same time, the fracture at different strains presents various ELs, thus resulting in different UTSs. This similarity in yielding and hardening implies the similar grain microstructures obtained under different strain rates at 10%. The variation in UTS and ELs indicates the effect of interface on final bond performance. 30% compressed samples present similar elastic deformation behaviour but end with different yielding strengths and proceed with different hardening, which indicates different microstructure of the joints. Finer microstructure under 0.1 s^{-1} shows higher YS. And the variation in the ELs over the strain rate is reversed, and the sample compressed at 0.1 s^{-1} has the lowest EL yet the highest UTS. When the sample is further compressed, the differences in the yielding and hardening is more obvious, and a higher strain rate corresponds to a higher YS and hardening. It is due to the finer microstructure under fast deformation, as shown in Figure 4-10. At this stage, samples bonded at different strain rates tend to end with different ELs and all show a ductile fracture trend. At 50%, higher UTS and lower EL are presented with a high strain rate.

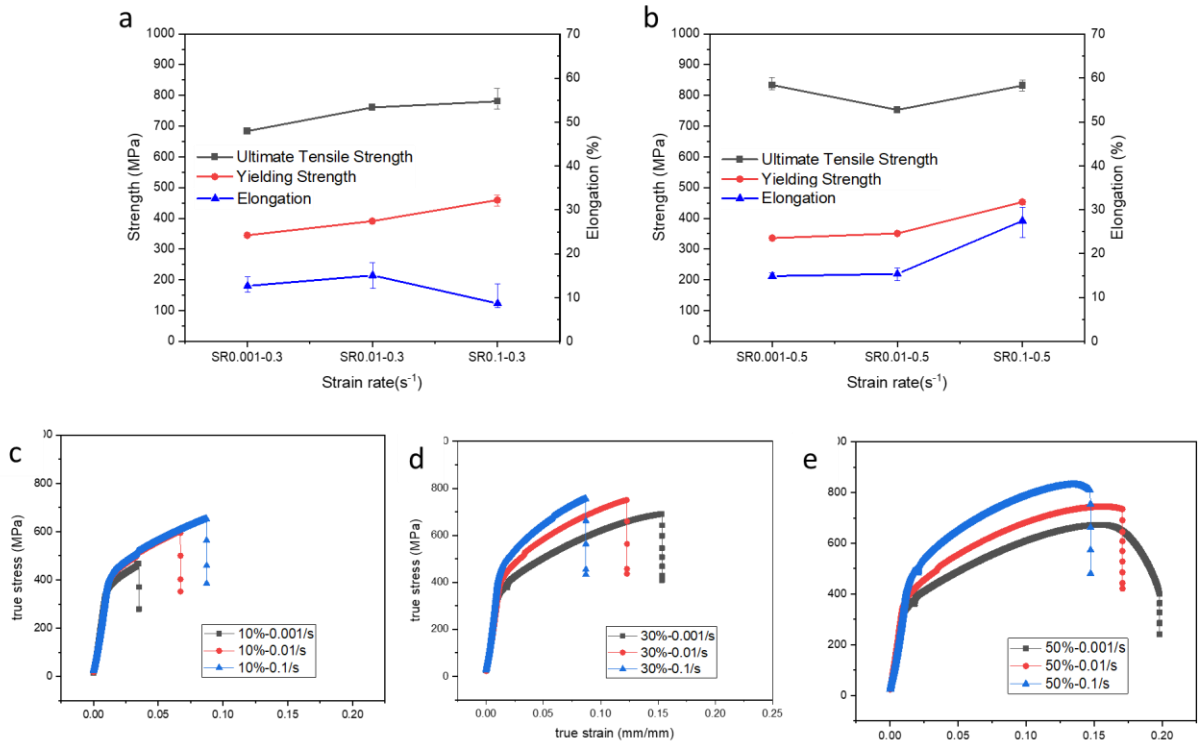


Figure 4-11 The tensile properties of bonds formed at different strain rates at 1150 ˚C a) 30% and b) 50%.The tensile curves of compress bonded samples at different conditions, c) 10%; d) 30%; e)50% height reduction.

The relative tensile property compared to references

As explain in 4.2.2, the microstructure effect in the bond tensile properties is decisive. Relative tensile properties can better indicate the bond quality and EL ratio is more intuitive compared to UTS ratio and YS ratio. Figure 4-12 a and b gives the tensile property ratios of the joints formed under different strain rates at 30% and 50% reduction, respectively. Difference is seen at 30% reduction: although similar UTS and YS are seen under different strain rates, lower EL ratio is seen under 0.1 s^{-1}. At all three strain rates, the tensile property ratios all achieved 1 at 50%, which means that the bonds all have good tensile properties comparable to the references.

For the 10% compressed samples, from the hint given from the tensile curves in Figure 4-11c, no obvious microstructure change occurs under low strain for different strain rates. Thus, their references are similar. However, as the microstructure evolution is obvious after 30%/50% compression, the comparison between the tensile curves of bonded sample and references are given. Figure 4-12 c-f compares the tensile curved of joints bonded under different strain rates with their references. Similar with the curve comparison in Section 4.2.2, for each condition, the curve of the bonded sample follows the reference quite well until the necking and fracture occur. Figure 4-12 c-d, together with Figure 4-8b (1150 ˚C/0.1 s^{-1}) show that when 30% compressed, the curves of bonded samples under different strain rates all present sudden fracture before getting to UTS (references). At higher strain rates (Figure 4-8b and Figure 4-12d), the fracture occurs at an earlier stage that lower strain rates (Figure 4-12c). This is in consistent with the results shown in Figure 4-12a. From Figure 4-12 e-f and Figure 4-8b, the tensile curve of bonded samples are almost identical to references and all present ductile fracture, which indicates the full recovery of the bond properties at 50% reduction under all three strain rates. This was also reflected with the results in Figure 4-12b. High integrity can be achieved at different strain rate levels.

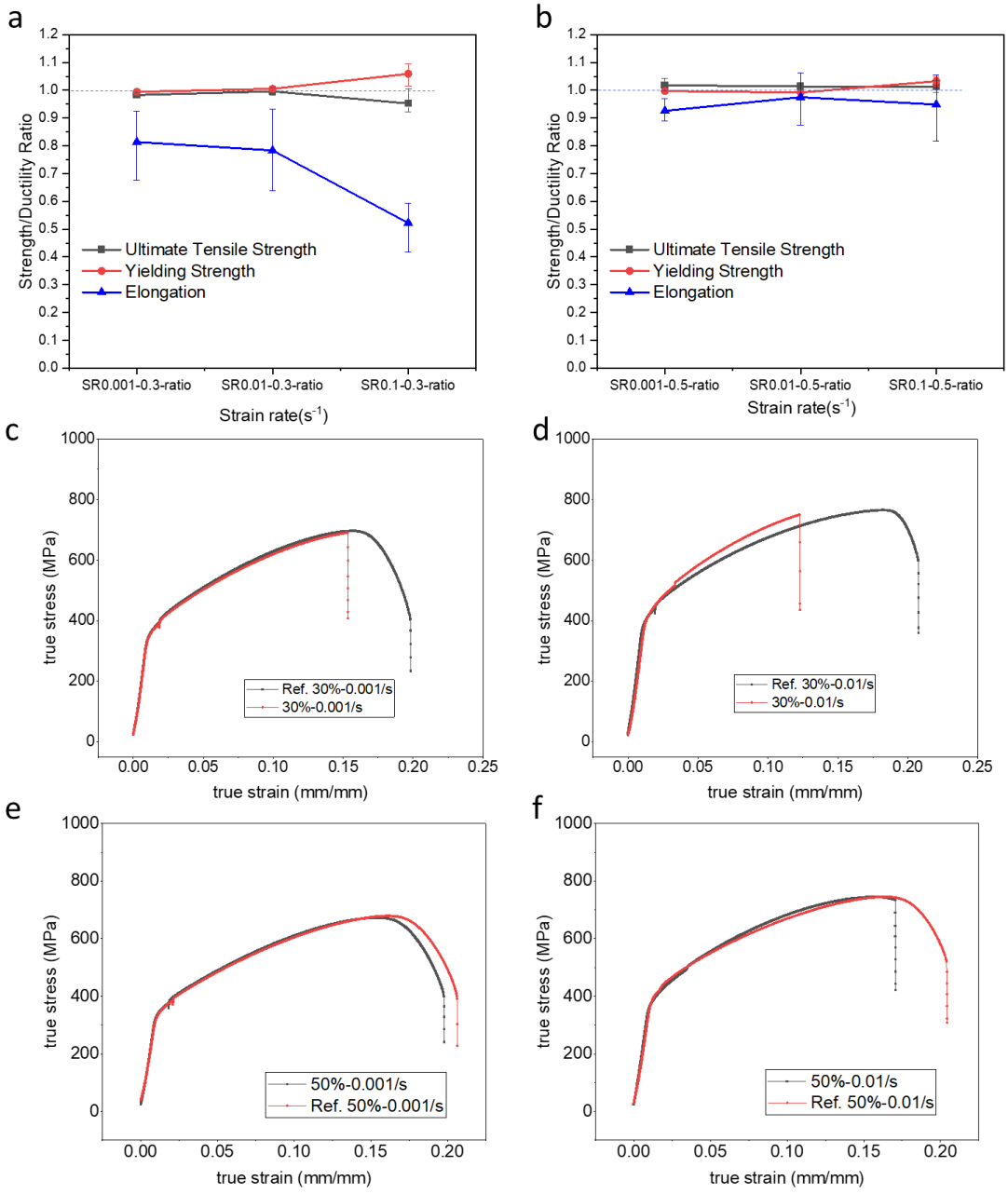


Figure 4-12 The relative tensile properties of bonds formed under different strain rates 1150 ˚C and a) 30% and b) 50%. Comparison of tensile curves of compress bonded sample and references at different strain rates to 30% height reduction, c) 0.001 s^{-1}; d) 0. 01 s^{-1}; 50% height reduction e) 0.001 s^{-1}; f) 0.01 s^{-1}.

Moreover, the fracture surface morphologies of bonded samples after tensile tests are shown in Figure 4-13. For samples bonded at 50%, they all present ductile fracture features with plastic deformed dimples. It is in agreement with the fracture feature that is shown with the tensile curves: when the bonded sample achieve the UTS followed by necking before fracture

(in Figure 4-12 e-f and Figure 4-8b), the joints have good bonding quality (Figure 4-13a_1-a_3); when the sample presents sudden fracture before getting to UTS, the bonding quality is not satisfactory (in Figure 4-12 c-d, together with Figure 4-8b), in which condition the fracture surface is relatively flat and small-size dimples are visible (Figure 4-13b_1-b_3).

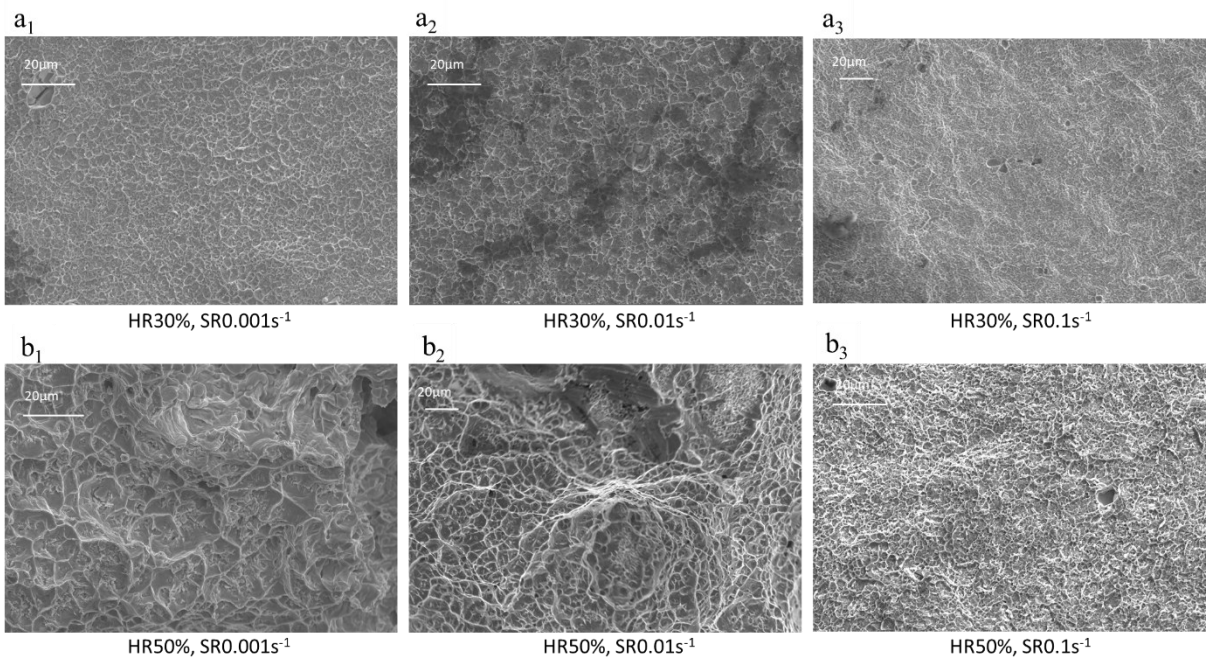


Figure 4-13 The fracture morphologies of samples bonded at HR 30% and a_1) 0.001 s^{-1}; a_2) 0. 01 s^{-1}; a_3) 0.1 s^{-1}; HR 50% and b_1) 0.001 s^{-1}; b_2) 0.01 s^{-1}; a_3) 0.1 s^{-1}.

4.4 Temperature effect results

The temperature effect is studied with a range of 950 ˚C to 1150 ˚C, at the strain rate of 0.1 s^{-1}. Different stages of the bonding at different temperatures is inferenced from 30%-50% height reduction. The interface microstructure is characterized and compared. Tensile properties will be presented with references.

4.4.1 Effect of temperature on the interface bonding microstructure

Figure 4-14 compares the interface microstructure of samples bonded at different deformation temperatures at different stages (30% and 50% reduction). At all three temperatures, continuous oxide films are observed along the bonding interface of samples deformed at a height reduction of 30%. With the height reduction increased to 50%, the oxide film for all three samples is broken into fragments, dispersing along the original interface. The OM images

in Figure 4-14 (d_2-f_2) help to identify the oxides fragments more clearly, and the original interfaces are marked. By comparison, the temperature makes no obvious difference in the interface oxide film behaviour.

In addition to the oxide film observed, the grain microstructure can also be seen from the images in Figure 4-14. In Figure 4-14 (a-c), due to the existence of the continuous oxide film, the grains are kept separate on both sides with no interface grain boundary migration. The bond lines seems at three temperatures at 30% reduction. With the break-down of the film at later stage of the bonding, fresh metal is extruded through the gaps and comes into contact, which paves the way for the interface grain growth and grain boundary migration. Thus, some common grains shared by both sides are seen crossing the interface. The residual oxide fragments are dispersed and included within the grains. Moreover, these images in Figure 4-14 also give a glimpse of the grain sizes for samples bonded under different conditions, which provides proof of the microstructural effect on the final joint performance. All recrystallized grains are shown with equiaxed shape, but high temperature results to a higher Rx fraction. At 1150 ˚C and 1050 ˚C, the Rx is completed at 30% strain, while at 950 ˚C, the Rx is not completed even at 50% strain. The EBSD IPF figures in Figure 4-14 (d_3-f_3) show the grain microstructure more clearly. Moreover, obviously with the increase of the temperature, the size of recrystallized grains is growing.

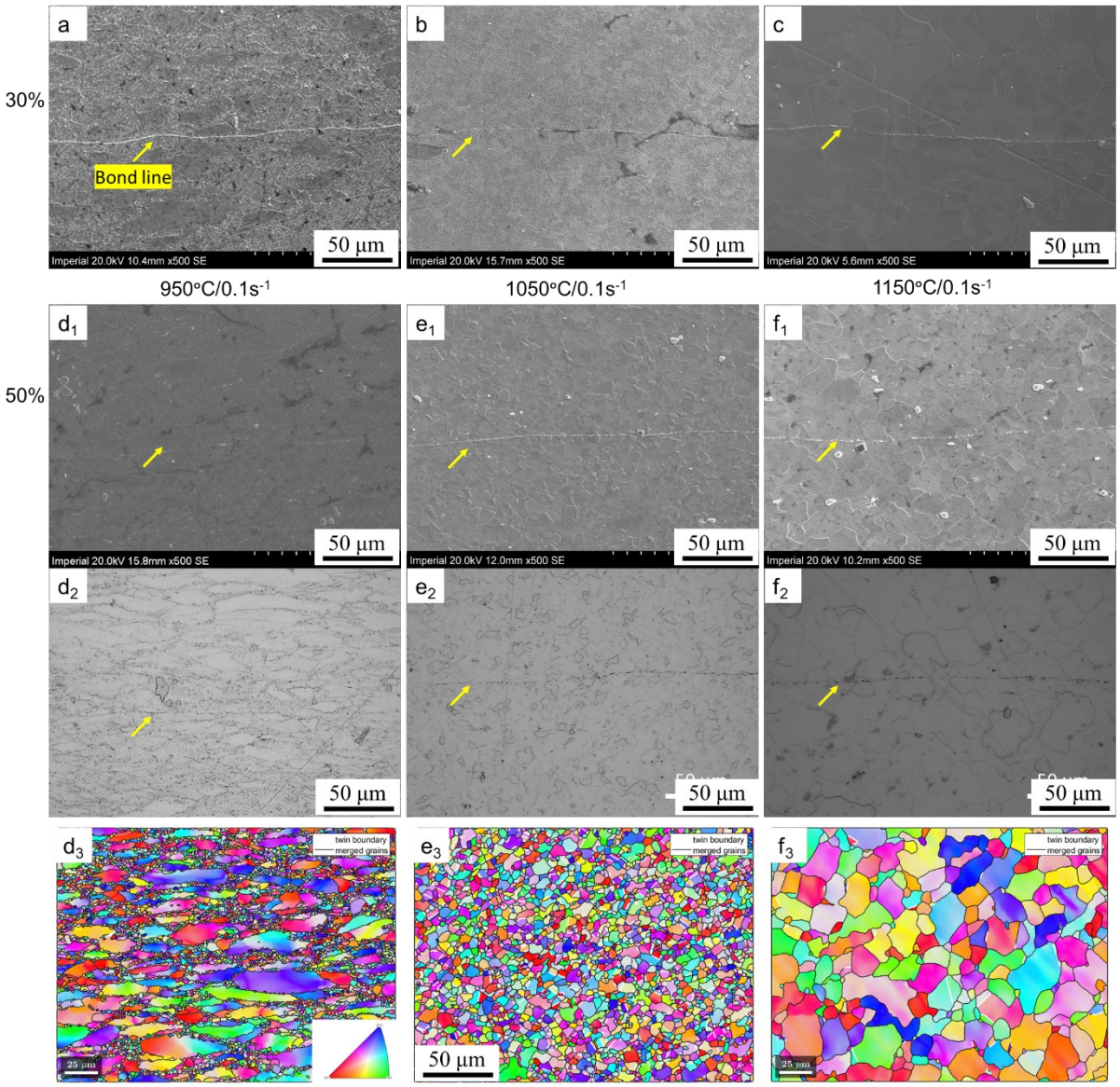


Figure 4-14 The microstructure of the interfaces bonded at different temperatures: 30% height reduction (a) 950 ˚C; (b) 1050 ˚C; (c) 1150 ˚C, 50% height reduction $d_{1\text{-}3}$) 1050 ˚C ($e_{1\text{-}3}$) 1050 ˚C; ($f_{1\text{-}3}$) 1150 ˚C.

As the recrystallized grains along the deformed large grains' boundaries of are much finer at 950 ˚C, to have a further temperature comparison and better illustration of the oxide interacting with the interface grain evolution, SEM images with the IPF figures at higher magnification are presented in Figure 4-15. At 950 ˚C and 1050 ˚C, interface GBs remains along the continuous interface oxide films Figure 4-15 a-b), no matter how small the recrystallized grains are. When the bonding is proceeding with increasing strain (at 50% reduction), although oxide films at all three temperatures are broken up and dispersed, larger dispersion is seen at higher temperature of 1150 ˚C (gap size around 8 µm in Figure 4-9i) and 1050 ˚C (6µm Figure 4-15d)

compared to 950 ˚C (3 μm Figure 4-15c). Thus, only part of interface GBs migrate, which are marked with black circles at 950 ˚C, while full interface GB migration occurs at 1150 ˚C and 1050 ˚C. As seen from the deformed shape of the bars bonded at 950 ˚C, gaps are seen near the edges, which may have more oxygen and caused server oxidation.

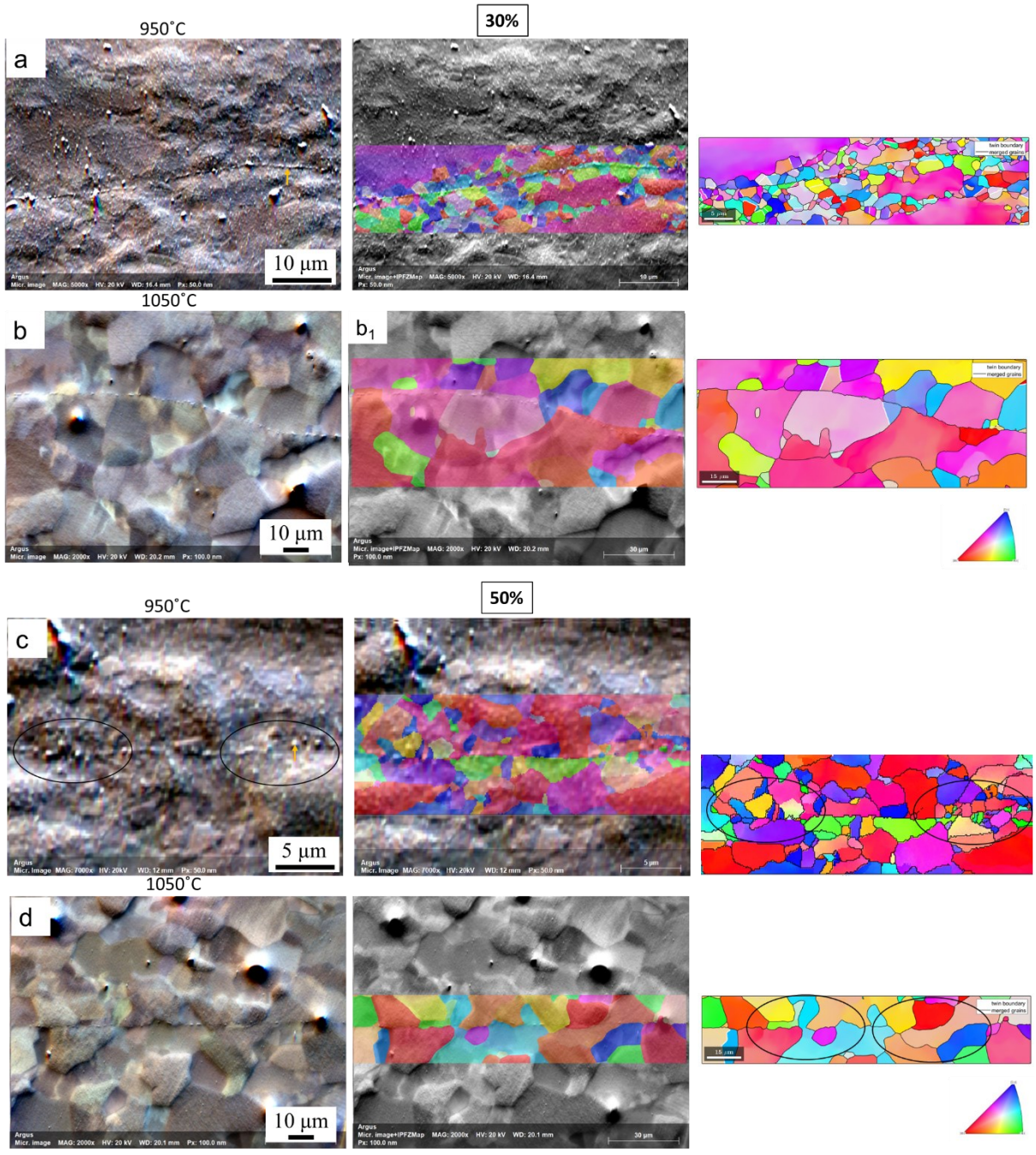


Figure 4-15 The microstructure of the interface bonded to 30% at (a) 950 ˚C and (b) 1050 ˚C; to 50% (c) 950 ˚C and (d) 1050 ˚C.

4.4.2 Effect of temperature on tensile results

The tensile results for the bonded bar samples are presented in Figure 4-16. From the ultimate tensile properties in Figure 4-16, higher EL, lower UTS and YS are seen with the increase of deformation temperature, both at 30% and 50% height reduction. According to the hall-patch effect of grain size on the strength, the larger grain size characterized in 4.4.1 at high temperature explains the obtained lower strength and higher ductility.

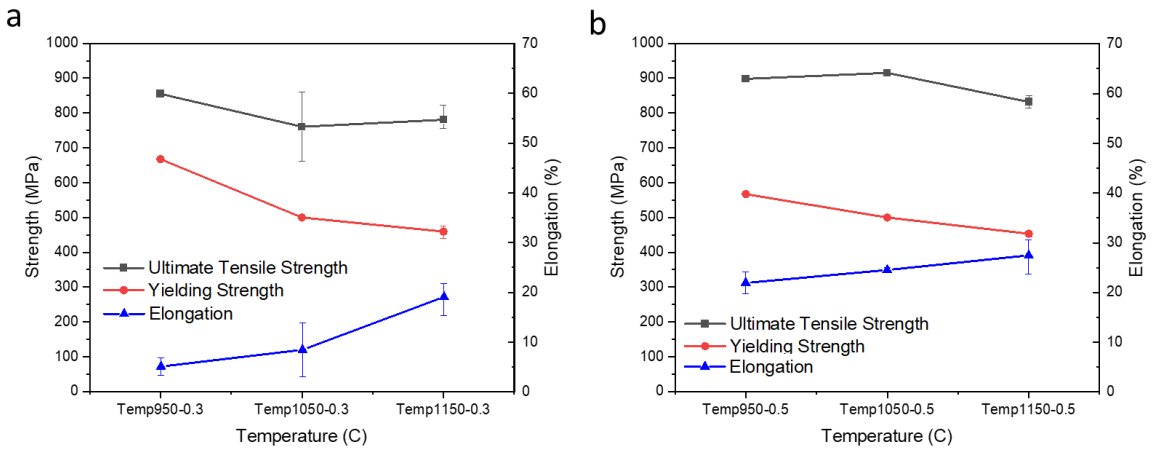


Figure 4-16 The tensile properties of the samples bonded at different temperatures. (a) 30% and (b) 50% height reduction.

Excluding the grain size effect, the nominal tensile properties are calculated with references and presented in Figure 4-17 (a and b). With the increase of temperature, the ratio of both strengths and ductility increase when bonded at 30% reduction. The magnitude of the increase in ductility is larger than the strengths. A slight difference is seen in the UTS/YS ratio obtained at different temperatures. When compared to the references, the UTS ratios are lower than 1 at three temperatures, however, the YS ratios are at around 1 at different temperatures. The ductility ratio is increasing with the temperature. When the bonding proceeds to a late stage, the tensile property ratios difference is decreased between different temperatures. Higher ratios around 1 are obtained in UTS, YS and EL, which indicates that good bond quality (strength and ductility equivalent to references) is achieved at different temperatures when the bar samples are 50% deformed.

To better compare the tensile performance of the bonded samples, the tensile curves of the bonded samples together with corresponding references are presented in Figure 4-17 (c-d) at

950 ˚C and 1050 ˚C. The comparison at 1150 ˚C can be found in Figure 4-8b. In all figures, the curve of the bonded sample follows the references in the elastic zone and initial plastic zone. At an earlier bonding stage, when the temperature is 950 ˚C, the bonded sample fractured at a low strain level of 6%, while the corresponding reference fractures at a strain of 22% (Figure 4-17c). When the temperature is increased to 1050 ˚C (Figure 4-17d) and 1150 ˚C (Figure 4-8b), the bonded sample also fails before the reference, however, its ductility performance is better than 950 ˚C. When bonding comes to late stage with large strains, at 950 ˚C (Figure 4-17b), 1050 ˚C (Figure 4-17d) and 1150 ˚C (Figure 4-8b), the curves of the bonded sample follow the reference till failure, although the minor difference is seen at 950 ˚C and 1050 ˚C. All the bonded samples show ductile failure features.

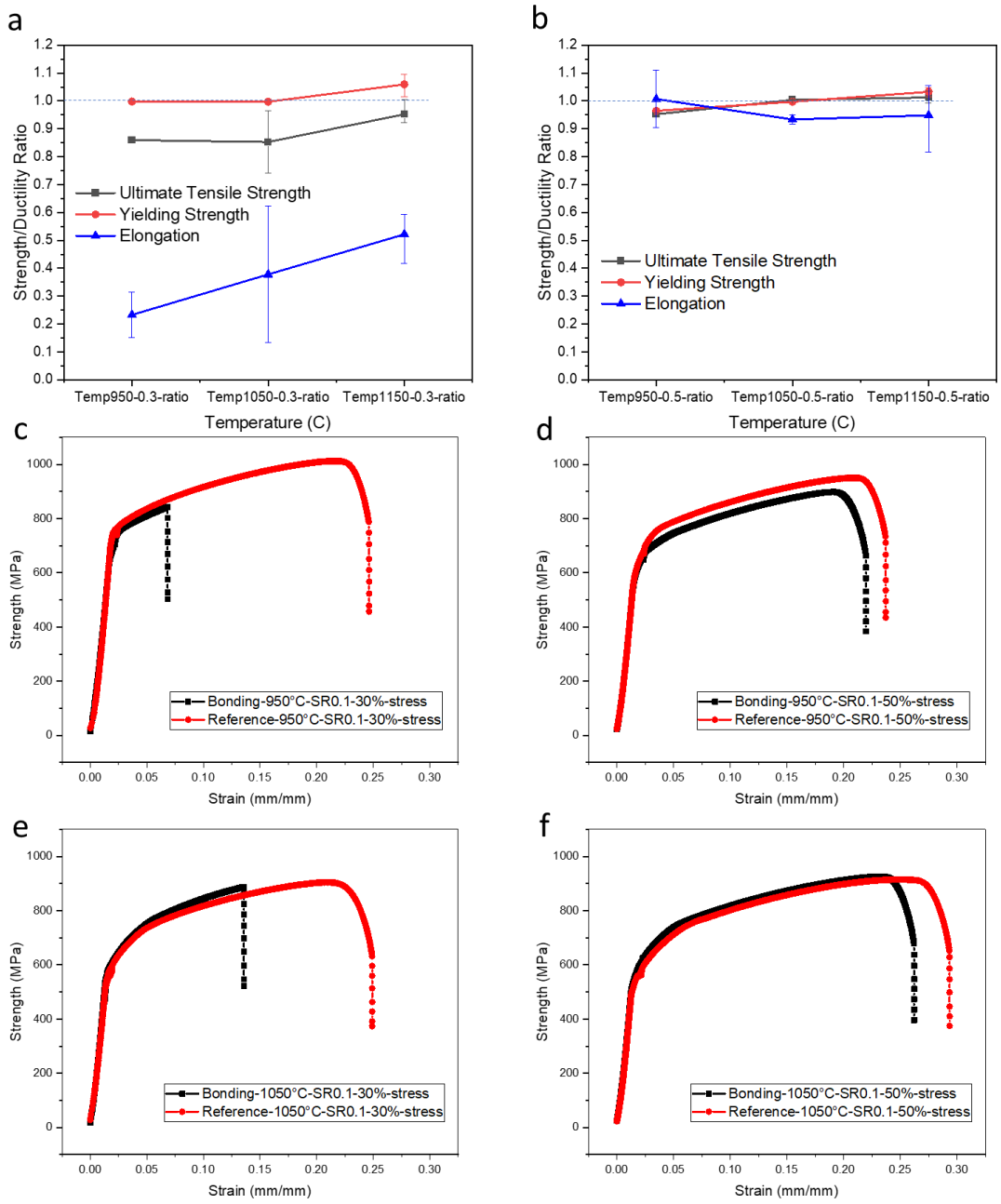


Figure 4-17 The relative tensile properties of the samples bonded at different temperatures. (a) 30% and (b) 50% height reduction. The tensile curves of samples bonded at different temperatures. (c-d) 950 ˚C; (e-f) 1050 ˚C.

4.5 Discussion

The bonding of IN718 is conducted under hot deformation conditions and full strength and ductility are achieved in a moderate vacuum of 1 torr. Oxidation problem exists during the bonding-by-deforming process, inhibiting the intimate contact of surfaces and interdiffusion.

The recovery of the joint performance depends on the disappearance of the straight bond line, that is the disruption of the continuous oxide film and coplanar GBs turning to be misoriented. This indicates the transformation from macro-interface into grain-level boundaries. In a hot working process with high temperature and large strain levels, the evolution of the bond lines and their effects on the bonding quality plays a coupled role with the microstructure.

4.5.1 The bonding mechanism - strain effect

With the existence of the interface oxides, the final joint performance is conjointly determined by the interface oxide behaviour and overall microstructure for the bond formed by hot plastic deformation. When excluding the microstructural effect, the elongation ratio is considered better to describe the relative quality of the bonded interface to reference due to its monotonical dependence on the bonded interface quality.

By comparing the interface microstructure characterization under the same temperature, strain rate, but increasing strain level, the evolution of the interface oxide film is clear. Although the surfaces to be bonded was degreased before bonding, the continuous oxide film can still be seen in the sample just after heating (0% height reduction in Figure 4-2a) and low strains (5%-Figure 4-2b, 10%-Figure 4-2c) and even at 30% (Figure 4-2d). The appearance of the oxide film comes from the residual pre-existed contamination, and also from the oxidation during the heating, soaking and bonding in a moderate vacuum environment in the Gleeble chamber. As discussed in classical cold bonding/roll bonding processes, the oxide film formed from the oxidation and would be extended during deformation[89, 90]. Similarly, the oxide film produced in the hot deformation bonding process will also be stretched when the bonding surface is expanded. As seen from the microstructure in Figure 4-2, the continuous oxide film is being broken up and gaps start to appear with the increase of the strain level.

Unlike the bond formed in cold rolling or pressure welding, the existence of the oxide film in hot deformation bonding may exert a different effect on the final joint performance. As it is seen at lower strains (0%-30%), even though the continuous oxide film is observed on the interface, higher joint quality is obtained than cold welding/roll bonding at equivalent strain levels. The reason could be that the cohesion between the oxide and oxide, or oxide and metal can be contributing at high deformation temperature. In the early stage of the deformation bonding process, when there is no gap or small gap between the oxides, even the contact is just made between the oxides, certain strength and ductility can be achieved.

Moreover, it is seen that the microstructure evolution occurs with the bonding process, proceeding with the recrystallization process. Although the microstructural effect can be excluded by comparing the bonded sample with reference, the effect of microstructure change on final the interface quality (ratio EL or ratio E) cannot be ignored. As reported in the hot deformation bonding of different materials[190, 193, 194, 196, 197], stated that the complete of the migration could promote the recovery of joint performances. Also, according to the results in this work, when the complete interface grain boundary migration is observed at a large strain of 50% height reduction (Figure 4-2e), full strength and ductility which is comparable to the reference are obtained (Figure 4-8b). However, different from the hot deformation bonding work in a high vacuum environment, where oxidation is not considered[196, 197], the effect of the interface oxide film on hindering the free movement of grain boundaries should be considered in this work.

Thus, the bonding mechanism of the hot deformation bonding process would involve the interface oxide film evolution, the grain microstructure evolution and the interaction between these two processes. At constant temperature and strain rate, when increasing the strain level, the continuous interface oxide film will be stretched. However, due to continuous oxidation during bonding, the oxide film remains continuous at a lower strain. At this early stage, the cohesion of oxide-oxide and oxide-metal contributes to the bond ratio. In the meanwhile, the recrystallization and grain growth are occurring, however, the movement of the interface grain boundaries is stopped by the covered oxide film; With the further increase of the strain, the oxidation stops at some point and gaps between broken oxides starts to appear. Then the fresh metal could be exposed and extruded through these gaps. When the extruded fresh metal meets, creating pathways for grain boundary motion, thus the interface grain boundary migration over the initial bond line would happen. At the late stage, the cohesion between metal-metal contact and the interface grain boundary migration would be dominating. Even there would be oxides remaining on the interface, the complete interface grain boundary could reduce the effect of these residual oxides.

4.5.2 The interaction between GB migration and oxide barrier during bonding

As is stated in the bonding mechanism in 4.5.1, the interaction between the microstructure evolution and interface oxide film behaviour is critical. From the characterization in 4.2-4.4, the recrystallization in the bonds, both near the interface or the base metal, shows no difference with the recrystallization in the traditional hot deformation of nickel IN718. Except that the

motion of the interface grain boundaries will be affected by the behaviour of the interface oxide film, as present in Figure 4-5 and Figure 4-15. Generally during hot deformation, the grain boundary migration could be dependent on various parameters, including the deformation condition (like temperature, strain, force)[218-220], the grain size[37, 221, 222], et al.. In this bonding by hot deformation process, except for the mentioned factors, the interface grain boundary migration would also be affected by the interface oxide film behaviours due to its pinning effect[223, 224].

Comparing the grain microstructures of the bonds obtained under different conditions (strains, strain rates and temperatures), the grain size varies. However, two typically different microstructures can be obtained: one is an uncompleted recrystallized microstructure with mixed large original grains and fine recrystallized grains near large grain boundaries, which is called necklace microstructure (Figure 4-3 a-d; Figure 4-10 c and f; Figure 4-14 a and d); the other is uniform fully recrystallized microstructures (Figure 4-3 e; Figure 4-10 a, d and Figure 4-14 b, c, e and f;). The recrystallized grains in the necklace microstructure are usually quite small and appear along the interface. By comparison, the grain size in uniform fully recrystallized microstructure are normally larger, yet also depends on the temperature and strain rate: lower strain rate and higher temperature facilitate the grain growth, resulting in larger grains.

Based on the interface oxide and microstructure observation in 4.2-4.4, the interaction between the oxide film barriers and the interface grain boundary migration in the two typical deformed microstructures is schematically shown in Figure 4-18. In a necklace structure, high-density dislocation is accumulated in a short time[34, 190] at a lower temperature or higher strain rate. These dislocation cells are preferentially stacked along boundaries and triple joints and transferred into small equiaxed grains. The nucleation and grain growth proceeds through GB migrating, driven by the stored energy, and retarded aside the continuous oxide film. As described in Figure 4-5 (a-b), GB migration can only occur at the oxide gap where the metal-metal contact is built for atom diffusion. The boundaries of Rxed grains, transformed from dislocation walls, bumps over the interface line with the free movement of dislocations through the connected aisle. With the strain increased and the film is further broken up into finer pieces, as shown in Figure 4-2c, the GBs migrate more easily passing the line, as on the one hand, more oxide-free spaces are exposed; on the other, the hindering effect of the oxide segments becomes weakened for the constantly refined recrystallized grains. Humphreys [225] has

elaborated on the relationship between the grain boundary movement velocity with the second phase particle features and initial grain size. The velocity is positively dependent on the overall migration driving pressure p, $v=Mp$, wherein $p=p_D-p_z=3\gamma_s/D-3F_v\gamma_b/d$, ($M$ is expected to be temperature-dependent; p_D is related to the stored energy, D is the average initial grain size, γ_s and γ_b represents for the boundary energy and high-angle boundary energy, respectively; p_z is the Zenger pinning pressure, F_v is the volume fraction of particles with a diameter of d). In a finer structure, in which the grain size is in a similar magnitude to the gaps, the pinning effect of the residual oxides is minimized.

Under a lower strain rate or higher temperature, the interface GB migration takes place in a similar way related to the dislocation accumulation. The difference is that given a longer time or higher diffusion rate at a higher temperature, the annihilation of the tangled dislocations and grain growth fully proceeds simultaneously. As a result, a microstructure with large and irregular grains is seen. As discussed, a higher migration driving pressure is needed for the larger grains with the same oxide dispersion condition. Thus, a lower GB migration ratio is found in Figure 4-10 a compared to Figure 4-10 (b and c), Figure 4-15 b compared to Figure 4-15 a.

However, when the grain size is small in fully recrystallized microstructure (e.g. Figure 4-10d and e, or Figure 4-14c) with a large strain level (50%), the oxide fragments are fully dispersed, even with a relatively larger grain size, full interface grain boundary migration can be completed, as shown in Figure 4-18 (c and e).

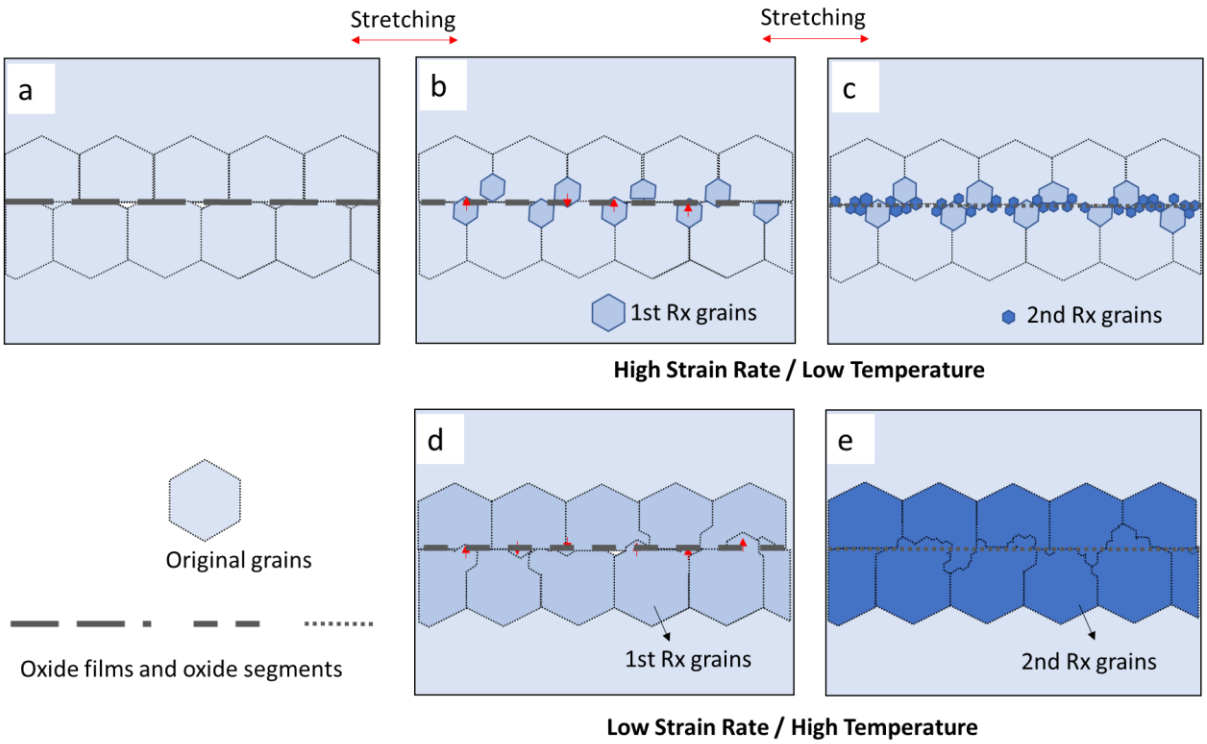


Figure 4-18 The mechanism of microstructure evolution and grain boundary migration near the bonding interface over the strain with the existence of oxide film, a-c) high strain rate/low temperature, d-e) low strain rate/ high temperature.

4.5.3 The effect of strain rate on the interface bonding behaviour

Considering the conjoint effect of the interface oxide film and microstructure evolution, the relative bond interface quality is highly dependent on the interaction between oxide behaviour and the recrystallization process. While this interaction, the oxide gap and interface grain boundary migration, is affected by the strain rate. Specifically, the strain rate affects the oxide gap by affecting the actual surface extension, while affecting the interface grain boundary migration by affecting the recrystallization. Moreover, the strain rate can also affect the cohesion between the different contact between oxide-oxide, oxide-metal.

Comparing the microstructures in 4.3.1 and the tensile results in 4.3.2 obtained at different strain rates, at a lower strain level when the samples are 10% compressed, the oxide film is hardly dispersed (Figure 4-9 b-d). At this early stage, the dominating mechanism for the interface bonding would be the cohesion between oxide/oxide or oxide/metals, for which the factors affecting the diffusion bonding can be considered. Among the factors, pressure is fairly

important. Herein, under different strain rates, the higher strain rate related to higher flow stress during compression can be a benefit for achieving a higher cohesion, as shown in the ratio-EL result in Figure 4-12.

When the oxide gaps appear and metal-metal starts to contact, the governing mechanism would change to cohesion between metal-metal and the recrystallization and grain growth process. Due to the different local surface expansion, the stage when the metal-metal contact starts may vary at different strain rates, but near 30% height reduction (Figure 4-9 e-g). Note that, at elevated temperature, once the freshly exposed metal is extruded and meets, the diffusion-dominating process, like the micro-void closure discussed in diffusion bonding[86] and grain boundary migration in [197], become the main bonding mechanism. Thus, when the bonding comes into the metal-metal contacting stage, to some extent, it turns to be time-dependent due to the metal diffusion processes. To achieve the same strain level, a longer time is needed with a lower strain rate, which stimulates the completion of the diffusion and leads to a better bond. In this work, the diffusion is considered equal to the grain boundary migration process.

When the strain is large at 50%, the oxides fully disperse and full interface grain boundary migration completes, the effect of the strain rate on the final bond quality can be minimized. The comparable tensile properties are achieved at all three strain rates, as presented in the results in Figure 4-12. In this way, it indicates that the complete interface grain boundary could minimize the effect of the residual oxides.

4.5.4 The effect of deformation temperature on the interface bonding behaviour

Similar to strain rate, the temperature would also affect the interface bonding quality by affecting the oxide film break-up and interface grain microstructure. At different temperatures, the surface extension would be different due to deformation, as well as the recrystallization and grain growth process would vary. Conjointly, the oxide film evolution, together with the grain microstructure, and the interaction between them would determine the final interface bond quality.

Based on the microstructure observation in 4.4.1, it can be seen that at the lower strain level, the oxide film remains continuously covered on the interface. As explained in the mechanism in 4.5.1, at this stage, the cohesion between the oxide-oxide, oxide-metal is supposed to dominate, in which the temperature would affect the cohesion with different flow stresses and different cohesion ratios. At a higher temperature, although the flow stress (normal pressure

applied on the bonding interface) is lower, the cohesion ratio would be higher. This is due to the larger contacting area ratio caused by the softness of the contacting pairs at a higher temperature. Moreover, during the cohesion between oxides, it can be regarded as a diffusion process, in which the temperature increase would cause a higher diffusion rate, thus leading to a higher cohesion ratio[217]. Combining with the tensile test results presented in Figure 4-16, at 30% height reduction, higher temperature resulted in higher bond quality (ratio of ductility), which indicates that at the oxide-film-fully-covered stage, at the strain rate of 0.1 s^{-1} with a temperature range of 950 ˚C~1150 ˚C, the cohesion ratio affected by temperature is over the stress effect.

At larger strain (50% height reduction in this work), as characterized in Figure 4-14 and Figure 4-15, oxides are largely dispersed and interface grain boundary migration is complete. At 950 ˚C, even though at a lower recrystallization fraction, the fine recrystallized grain preferably appears along the interface grain boundaries. These small grains usually have a larger grain boundary migration rate[226]. Thus whenever the gap between oxides appears, the grain boundaries along the bond line would migrate over the interface, including the oxide fragments into the grains. At 1050 ˚C and 1150 ˚C, higher temperature provides a higher driving force for grain boundary migration. Even though the grain size is a bit larger, the widely spread oxides at large strain and high migration rate work together to complete the interface grain boundary migration process, minimizing the effect of residual oxides and resulting in good bond quality.

4.6 Conclusions

At different strain levels, with a combination of different strain rates and temperatures, the bonding test was conducted using bar IN718 sample in Gleeble. With a mild vacuum (1 torr), the interface oxide film cannot be neglected. In the meantime, severe microstructure evolution occurs due to the dynamic recrystallization under hot working conditions. The combination of these two processes conjointly governs the bonding process.

1. By studying the bonding behaviour at different strain levels, a new mechanism taking the cohesion of different contacting pairs and microstructural effect into consideration is proposed. The new mechanism which explains the bond strength obtained at low strain and full strength obtained at the moderate strain level of 50%.
2. Excluding the microstructure grain size effect, the ratio of EL can more instinctively reflect the interface bond quality.

3. The interaction between the interface oxide film and grain microstructure evolution is found to be critical in determining the final bond performance. The breakage of interface oxide film provides space for the interface GBs to migrated during the Rx process. Large oxide gap and small grain size makes GB migration more easier.
4. Strain, stain rate and temperature affects the bond by changing the local interface strain-stress state and the Rx microstructure.

   Within a strain rate range of 0.001 s^{-1}~0.1 s^{-1}, and a temperature of 1150 ˚C, the impact of the strain rate is reflected: (1) in the normal stress in the early stage when the oxide film is continuously covered at low strain; (2) in the Rx diffusion and IGB migration in the late metal-metal contact stage when oxides are broken up. It results in a higher interface bond quality for a higher strain rate at lower strain, however, the bond quality tends to be similarly good at larger strain.

   Within a temperature range of 950 ˚C ~1150 ˚C, and a strain rate of 0.1 s^{-1}, the impact of the temperature is reflected: (1) in the normal stress and oxide cohesion ratio in the early stage when the oxide film is continuous at low strain; (2) in the Rx diffusion and IGB migration the late metal-metal contact stage when oxides are broken up. It results in a higher interface bond quality for the higher temperature at lower strain, however, the bond quality tends to be similarly good at larger strain.

Chapter 5 The simulation of the bonding process and model for bond quality prediction

5.1 Introduction

As introduced in Chapter 2, the bonding process in solid-state involves different mechanisms, including the interface oxide film fracture, the micro-void closure and interface microstructure evolution, etc. The models developed to predict solid-state bond quality discusses one dominating mechanism depending on the actual bonding conditions for different bonding processes. According to the observation and property results presented in Chapter 4, in the solid-state bonding process under hot deformation in combination with moderate vacuum, both the interface oxide and microstructure evolution over the bonding zone cannot be ignored.

The final mechanical properties of the bonded samples are determined by the bonding quality of the interface and the final microstructure of the base materials. However, the effects of microstructure changes at elevated temperatures on the mechanical properties of the base materials have rarely been isolated from the interfacial bonding quality investigation[89, 121, 135]. As the microstructure evolves in the bond zone and affects the final property of the joint, in this study, reference tests were performed and compared with the bonded samples to evaluate the interfacial bonding quality.

Therefore, a new physical-based model, which incorporates the effect of remaining dispersed oxides and the microstructural change, is needed to predict the high strength bond achieved under hot deforming conditions. By excluding the effects of grain size changes, a new bonding-by-hot-deforming mechanism and model are proposed and validated by the hot compression bonding test at different strain, strain rates and temperatures.

Structure of chapter: In order to obtain the stress-strain state of the investigated area of the bonded bar samples, the simulation of the hot compression will be conducted and the bonding model development will be presented in 5.2; and the model to describe the bonding mechanism will be explained in 5.3 and embedded into the FE model (5.4); with the calculated results, the bonding process under various conditions and the effects of strain, temperature and strain rate will be interpreted in 5.5.

5.2 The simulation of the bonding process with bar samples

Commercial finite element software QForm 9.0.8 was used in this study to simulate the compression on cylinder bar IN718 samples under various conditions. QForm shows good applicability in simulating large deformation with a short processing time.

A whole bar sample instead of two half IN718 parts are compressed in an electrical upsetting operation with QForm to simulate the compression bonding process using Gleeble, given that marginal effect has been imposed by the interface on the overall deformation. The 2D axisymmetric finite element model, as shown in Figure 5-1, comprises the deformable workpiece and rigid tools (Pusher, Current clamp, and Anvil). The tool material is copper and IN718 JMAK Huang[60] data was adopted for the workpiece to describe plastic deformation behaviour and the comparison between the library database from and collected by Gleeble hot compression tests is shown in Figure 5-2. For the electrical upsetting operation in QForm, the thermal process can be simulated, while only plastic deformation is available (the elastic part is ignored). Average radial strain and normal stress of the central area with a unit dimension of 3 mm×3 mm were exported, representing the deformation condition of the tested bonded area. Finite element mesh were generated using QShape. The adopted tetrahedral elements were refined in areas of intensive plastic deformation at each stage of deformation process and the remeshing during simulation are carried out automatically without any users' intervention.

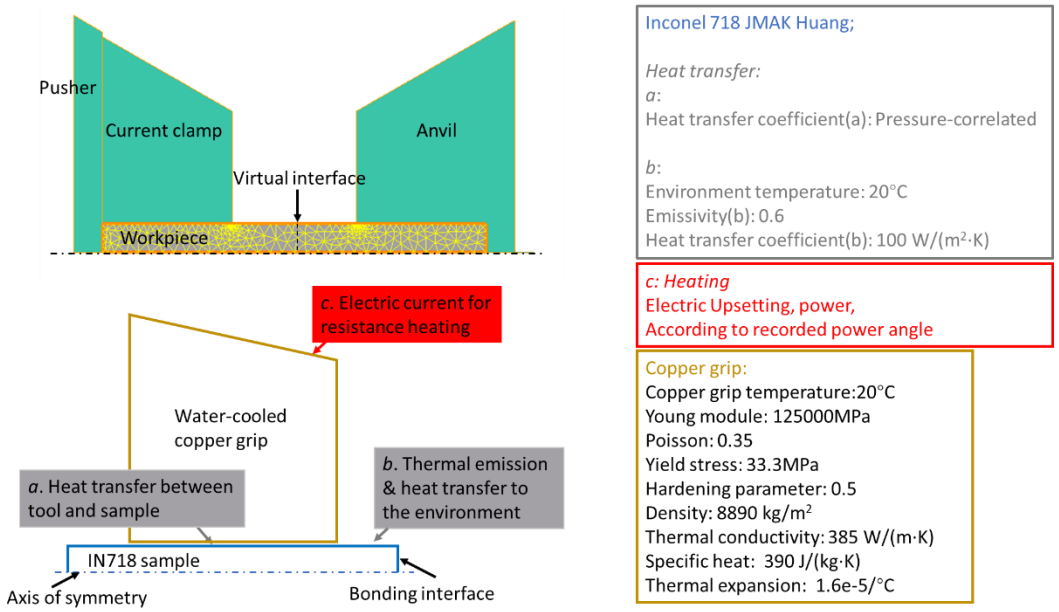


Figure 5-1 The electrical upsetting model for simulating the Gleeble hot compression bonding process with bar samples

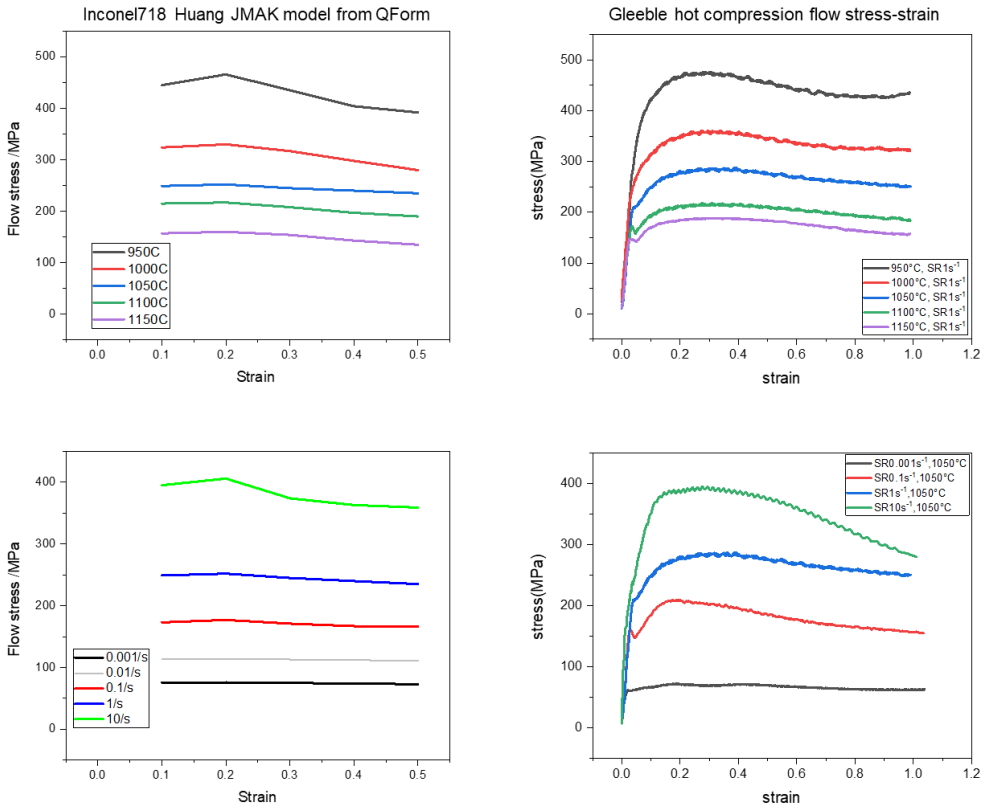


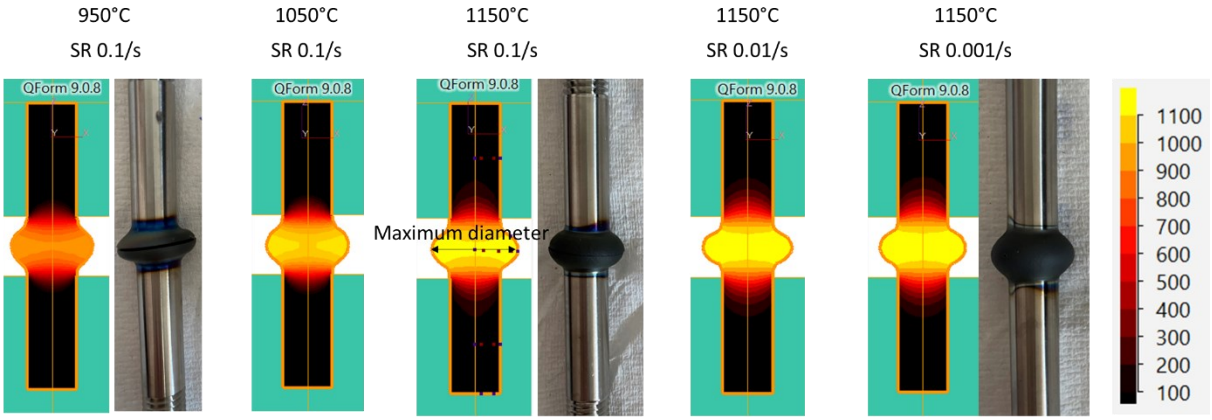
Figure 5-2 The flow stress-strain data comparison between Huang's JMAK model from the QForm library and Gleeble hot compression tests

In Gleeble, the two half bar samples are brought into contact under pre-load and heated by electrical current. The current is applied through the water-cooled copper grips (surface c in Figure 5-1). The temperature control on the workpiece is achieved by a closed-loop system, which compares the instant measured temperature and the prescribed temperature and returns the feedback to correct the power amplitude for the next step. A relative power angle is recorded by Gleeble and the current character is simulated in QForm based on the power data input. An adjustment has been made on the basis of the Gleeble record empirically for the best fit of the simulated temperature at bonding interface temperature to the recorded data.

In the meantime, heat transfer occurs on the contacting surface between copper grip and specimen via conduction (surface a in Figure 5-1) and the specimen's exposure in vacuum via conduction and convection (surface b in Figure 5-1). As the copper grips are connected to a circulant water-cooling system and the temperature is assumed to keep at 20 ˚C during the

upsetting. The heat transfer coefficient(a) is difficult to measure and is considered to be force-dependent since a more complete contact is achieved at high force. The heat transfer occurring at the specimen-vacuum interface is simulated via convection and conduction. The parameters are defined based on the vacuum furnace condition in the database, including emissivity (0.6) and the heat transfer coefficient (c) as 100 W/(m^{2}K). The environment temperature is set at 20 ˚C. For the bar samples, both the pre-heating and compression processes, and the initial temperature is set to 20 ˚C.

The heating and compression are simulated separately. For the first-step heating process, the electric upsetting power input was adjusted to obtain the measured temperature distribution shown in Figure 3-3 (T_1, T_2, T_3 representing the temperature of point at a distance of 10 mm, 5 mm, 0 mm). The heat transfer coefficient (b) is empirically determined as identical to be 30 W/(m^2·K) for the different processes and a lower Emissivity of interface-b at 0.06 was chosen to simulate the relatively lower heating loss rate in the high vacuum chamber in Gleeble. For friction factor and interface-a is zero as there is no relative movement.



Diameter of **(mm)**	Temperature 950˚C Strain rate 0.1s^{-1}	Temperature 1050˚C Strain rate 0.1s^{-1}	Temperature 1150˚C Strain rate 0.1s^{-1}	Temperature 1150˚C Strain rate 0.01s^{-1}	Temperature 1150˚C Strain rate 0.001s^{-1}
Gleeble bonded samples	17.3	16.9	16.0	15.2	15.0
simulated bonded samples	16.5	16.7	17.0	17.6	17.2
error	-4.6%	-0.8%	6.5%	15.7%	14.6%

Figure 5-3 The double-process simulated sample shape at different temperatures (1150 ˚C, 1050 ˚C, 950 ˚C) and different strain rates (0.001 s^{-1}, 0.01 s^{-1}, 0.1 s^{-1}) after compression deformation in comparison to the real samples.

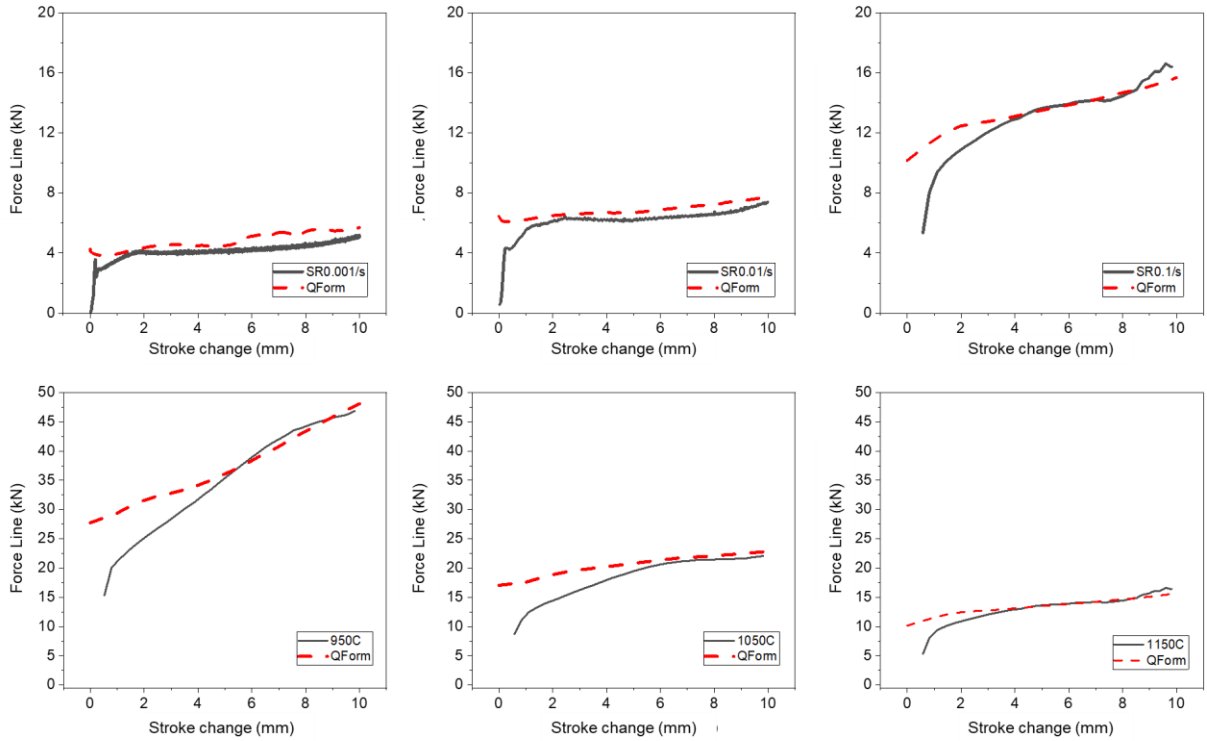


Figure 5-4 The comparison between the simulated and recorded force for the hot compression bonding process under different conditions using double-process simulation.

Error analysis: The comparison between the simulation results and bonded sample measurement are shown in Figure 5-3 and Figure 5-4. In Figure 5-3, the temperature distributions after first-step heating processes under different temperatures agree well with the measurement in Figure 3-3. After the compression, the simulated maximum diameters under different conditions show an identical trend with the measured results for the bonded bar samples using the thermal couples.

From Figure 5-4, errors between the recorded force and simulated results are shown at lower strain (small stroke change), especially under a higher strain rate of 0.1 s^{-1}. This could be due to the that elastic-plastic deformation is not available for electric upsetting operation, which causes the deviation in describing the low-strain elastic and the transition to viscoplastic deformation behaviour. Note that the error is reduced as the strain is increasing (larger than 25%). Given that the general simulated compressive loads are in agreement with the Gleeble

recorded load and can well reflect the tendency of different conditions, the double-process model will be used to simulate the Gleeble bonding process on bar samples.

5.3 Model description for bond quality

The new bonding-by-hot-deforming model is based on film theory but incorporates microstructural effects. The oxide film formed due to the trapped air, and it is stretched to fracture; the metal is extruded through the oxide gaps. Once the extruded fresh metal meets, the sound atomic bond can be established[119, 121]. Considering the high temperature, severe deformation, and microstructure changes, four assumptions are made and elaborated:

a. The cohesion between oxides and metal, oxides and oxides would be considered for the bonding at high temperatures;
b. The cohesion strength of metal-oxide and oxide-oxide shows a similar dependence on the actual area contact as a metal-metal pair;
c. Provided that enough GB crossing the bond line, when the oxide fragments are largely dispersed and wrapped by fully contacted metal, their adverse effect on the joint performance would be neglected;
d. The model predicts the relative bond ratio reflecting the interface quality and can be combined with the final microstructure to predict the final joint performance.

The oxidation and fracture of oxide films:

The initial contact is made between oxide and oxide under the deformation. The pre-existing oxide films on the interfaces could be formed during the heating and soaking before deformation. With the surface stretched, these oxides fracture brittlely. Due to the entrapped air at the interface, the oxidation reaction occurs in the early stage of the deformation with a lower strain. Nevertheless, as the surfaces are further stretched, the trapped oxygen would be consumed and depleted. New metal is exposed. At a critical strain η, the oxygen would be completely depleted and oxidation terminates. The typical η value in the cold roll bonding (surface roughness Ra = 5 μm, temperature T = 298 K) is determined as 0.35[121]. η is a fitting parameter. The range of parameter η is determined with the consideration of the applied vacuum and the deformation at different temperatures. At 1150 °C, as the bonding in this study was conducted under moderate vacuum condition, the trapped oxygen content would be considerably less and thus the parameter η can be less than the reported 0.35. However, the

critical strain value η can be temperature-dependent, since at a lower temperature, the compressed bar sample presented visible gaps from edges, which leads to a higher η consideration. The η values are given in Table 5-1. Due to the limited gap space, the oxides are newly formed between exposed clean metal surfaces from the entrapped air, and the contact is assumed to be built between metal and oxides.

Under surface strain ε, the area fractions of different contacting pairs are expressed as follows:

$$f_{o-o} = A_{o-o}/A_n = 1/(1+\varepsilon) \qquad \textit{Equation 5-1}$$

$$f_{o-m} = A_{o-m}/A_n = \begin{cases} \varepsilon/(1+\varepsilon), & \varepsilon \leq \eta \\ \eta/(1+\varepsilon), & \varepsilon > \eta \end{cases} \qquad \textit{Equation 5-2}$$

Where f_{o-o} and f_{o-m} is the area fraction of contacting oxide-oxide and oxide-metal pair, respectively. A_n is the nominal area, A_{o-o} is and A_{o-m} is the actual contact area of oxide-oxide and oxide-metal, respectively.

The metal extrusion and contact:

For simplicity, the oxide film is assumed to fracture and distribute equally with a constant gap. At a given strain, ε, parallel to the surface, the oxide gap, e, is derived as[121]:

$$e = K \cdot \lambda(\varepsilon - \eta)/(1+\eta) \qquad \textit{Equation 5-3}$$

Herein, the linear coefficient K is introduced and would be determined by fitting the oxide film observed. λ is the length of the oxide fragment and the typical value of λ for aluminide is 1000 nm, as characterized in Figure 4-9. Based on Hosfold and Caddel's discussion[227], in which rectangular slab shape and plain strain were assumed for the fractured oxide fragments, the extrusion pressure p_{ex} is calculated [121]:

$$p_{ex} = Y_m \cdot ln((\lambda + e)/e) + (Y_m t_c/e) \qquad \textit{Equation 5-4}$$

where t_c is the thickness of oxide film. The typical values of t_c for aluminide is 10 nm[121]. The yielding strength of metal Y_m is determined by the flow stress during the deformation.

After the oxide fractures, the fresh metal is exposed. The contacting metal-metal area fraction f_{m-m} at given strain ε is described as [121]:

$$f_{m-m} = A_{m-m}/A_n = \begin{cases} 0, & \varepsilon \leq \eta \\ (\varepsilon - \eta)/(1+\varepsilon), & \varepsilon > \eta, \end{cases} \quad \textit{Equation 5-5}$$

The cohesion established between different contacting pairs:

The bond formed between clean metal surfaces has been the most accepted mechanism for classical roll bonding models. Full strength was assumed to be achieved once intimate contact is formed between the clean metals. However, due to the surface asperities, complete intimate contact is practically difficult. The metal-metal cohesion is derived based on Conard and Rice's study in 1970[114], where the cohesion ratio of metal joining pairs were shown to be proportionally related to the actual metal-metal contact area fraction. Moreover, this dependence of the actual area of contact on the stress state was discussed in slip-line theories for the plastic deformation near surfaces with micro-asperities[228]. Therefore, referring to [121], the cohesion between metal-metal is derived as:

$$C_{m-m} = \alpha_{m-m} \cdot ((\sigma_n - p_{ex})/Y_{m-m}) \cdot (\sigma_{Ni}/\sigma_{Ni}) \quad \textit{Equation 5-6}$$

Where C_{m-m} is the achieved cohesion between contacting metal-metal pair, σ_n is the normal pressure applied on the interface, Y_{m-m} here is the yielding strength of metal and equal to the aforementioned Y_m. σ_{Ni} is the tensile strength of a full bonded Ni-Ni contacting pair. σ_n here is the applied normal pressure and $(\sigma_n - p_{ex})$ is the pressure applied on a contacted interface. The cohesion coefficient α_{m-m} for the relationship between contact area fraction and normal pressure is related to the stress state[24] and varies for different materials, e.g. the crystal structure[114]. The coefficient of 80% is selected in [121] as suggested in [114] for aluminium, and the coefficient for nickel can be selected as 80% as well since the cohesion coefficient for pure nickel was tested between 0.73-0.87 in [114].

Under hot deforming conditions at high temperatures, approximately 80% of the melting point, cohesion between oxides, oxides and metals occurs. Solid-state bonding between ceramic (like alumina) and metals, e.g. aluminium, nickel, copper and iron, were tested in the studies of ceramic hot-pressing [217, 229], brazing process[230], and interfaces in thermal barrier coating applications[231]. The bonding quality of the ceramic-metal interfaces is determined by the factors like diffusion time, pressure, temperature, purity, atmosphere, and chemical reactions. Metal-ceramic interface structure modelling was derived from the interface energy perspective[232, 233], e.g. the ab initio atomistic calculation and thermodynamic models or

empirical/semi-empirical atomistic calculation methods. However, no process model is available due to the complicated governing bonding mechanisms, both physically and chemically. In the studies of hot-pressed alumina-nickel[217], the bonding results showed that an appropriate pressure (15 MPa) and temperature (1100 ˚C) led to complete physical contact and a high interface strength; besides, no new phase formed until the temperature up to 1250 ˚C. The hot sintering of metal-oxides shows a similar dependence on the mass transfer and the diffusion process[234].

Compared to the sintering of metal with ceramics, the bonding between ceramics is more difficult due to their brittle nature and higher energy barrier to form the covalent bonds. According to the early studies of sintering and hot-pressing ceramics powders, the bulk density has been shown to be related to pressure and temperature. The densification rate was described in a linear relationship of pressure and inversely proportional to the viscosity[235]. In[234], the solid-state bond mechanism of ceramics was reviewed, and bonding conditions like temperature and pressure show a similar effect on the joint performance as in the metal joining pairs. Thus, similar to the cohesion between the metal-metal contact pairs, the bond quality between metal-oxide and oxide-oxide can be roughly but reasonably proposed as:

$$C_{o-o} = \alpha_{o-o} \cdot (\sigma_n / Y_{o-o}) \cdot (\sigma_{Al_2O_3} / \sigma_{Ni}) \qquad \textit{Equation 5-7}$$

$$C_{o-m} = \alpha_{o-m} \cdot (\sigma_n / Y_{o-m}) \cdot (\sigma_{Al_2O_3/Ni} / \sigma_{Ni}) \qquad \textit{Equation 5-8}$$

This relationship was proposed initially from the slip-line theory for metal-metal contacts. Since there is no strictly available slip plane in ceramics, the coefficient α_{o-o} and α_{o-m} describe the relationship between normal pressure and real area of contact for ceramics may vary from metals. Here for simplicity, ceramic alumina is approximated as a kind of metal with high yield strength and toughness, and the cohesion equation still applies. The reason for making this assumption lies in three aspects: one, the role of the normal force in bringing the atoms into contact is identical for both ceramics and metals and based on the similar relationship between bond energy and distance for metallic atoms and ceramic covalent-bonded atoms, the normal pressure could be reasonably assumed to be in a positive relationship with the cohesion[217]; secondly, although the dislocation slipping is rather difficult in ceramics, plastic deformation was observed in the friction motion studies of alumina [228]; thirdly, the contact cohesion can be reflected in the friction coefficient under dry wear conditions, and the

contact pairs with oxide film covered normally show a lower friction coefficient[236]. The compressive strength of oxide alumina, ~690 MPa[237], is used here as Y_{o-o}. For the metal-oxide, the real contact area under normal pressure mainly depends on the deformation of the softer metal, and the yield strength of the metal will be adopted ($Y_{o-m} = Y_m$) in the cohesion equation. The strength varies under different bonding condition, and its value are listed in Table 5-1. The discrepancy for the metal-oxide and oxide-oxide pairs in contact is supposed to be considered when determining the cohesion coefficient. Thus, in the equations for oxide-oxide, oxide-metal cohesion, the coefficient α_{o-o} and α_{o-m} would be temperature-dependent and be lower than the value of 0.8 for metal pairs taking the high stiffness and brittle nature of the oxide into consideration, as given in Table 5-1. $\sigma_{Al_2O_3}$ and $\sigma_{Al_2O_3/\mathrm{Ni}}$ is the tensile strength of fully bonded Al_2O_3/Al_2O_3 and Al_2O_3/Ni, respectively. The terms ($\sigma_{Al_2O_3}/\sigma_{Ni}$) and ($\sigma_{Al_2O_3/\mathrm{Ni}}/\sigma_{Ni}$) are to proportionally transfer the achieved cohesion of Al_2O_3/Al_2O_3, Al_2O_3/Ni equivalent to the strength of Ni, and ratios were adopted 30 and 1, respectively. Here for the metal-oxide pair, as the metal would be the weak part, the cohesion of Al_2O_3/Ni is equivalent to Ni/Ni.

The enwrapping of oxide fragments by metals:

In Bay's model[119], the oxide is discussed into two different types: the ductile thinner film and brittle thicker cover layer; In Cooper's work[121], it is simplified that the oxide film tends to fracture brittlely under tension and the oxide fragments on both interface sides are assumed to overlap, forming oxide-oxide contact. Both in Bay and Cooper's model, the cohesion between oxide and metal has not been considered. Thus, even the oxides fragments are dispersed with a large gap; they still impair the bond at a ratio of the area (or length). In solid state, the oxide is the barrier stopping the bond from being formed and these oxides fragments remaining in the joining zone affect the performance of the joint; However, the oxides in metal are not always harmful. Oxide Dispersed Strengthened (ODS) Alloy is an example of utilizing the uniformly dispersed fine oxide in the metal matrix to improve its strength and corrosion resistance, especially at high temperatures[238].

The effect of the remaining oxide debris depends on its dispersion. For friction welding processes, due to the severe plastic deformation induced by high shear stress, continuous oxide film could be intermingled, which benefits the recovery of the joint to full strength[93]. When the solid-state bond forms at a high temperature and the cohesion between oxide and metal is

considered, the impairing effect of the remaining oxides along the interface could be minimized the oxides are largely dispersed. Results from the study of IN718 bonding under hot forging conditions has shown that strength and ductility are comparable to the reference which underwent the same deformation[211]. The continuous oxide film fractures under a moderate strain and is separated with gaps, allowing the contact of the clean metal surfaces. As shown in Figure 5-5, these separated oxide pieces would be enwrapped with the bonded metal matrix. The oxide dispersion($e/(e+\lambda)$) depends on the strain level. At large strain, the dispersion level is large enough to consider these remaining oxide fragments to be oxide second phases. Moreover, the large gaps allow the fresh metal to meet and bond with a high cohesion ratio (C_{m-m}~1), and also provide spaces for the interface grain boundaries to migrate. The migration pushes the inferior grain boundaries away from the oxide fragments. These three factors together reduce the impairment of remaining oxides. Therefore, at large strain, these remaining oxides turn to be less weakening and affect the final bond quality at a ratio lower than their actual proportion.

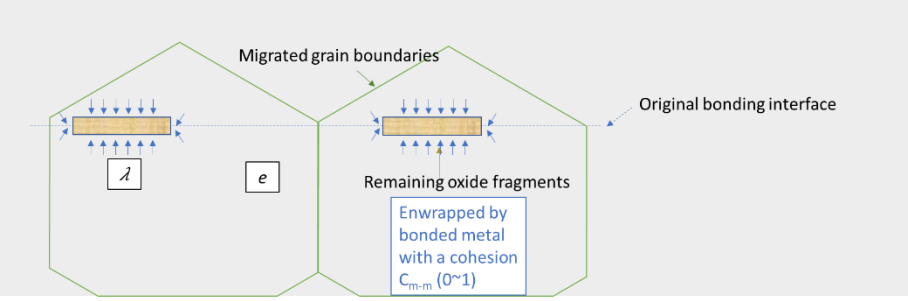


Figure 5-5 The schematic graph of the oxide fragments remaining on the original bonding interface at large strain

Thus, in the late stage, when the cracks are widened enough for the metal to contact, a factor, δ, is introduced in this model to describe the less weakening effect of the oxides, and the strategy is to magnify the strain according to the gap e. When the gap is small, δ approximately equals to 1 and the oxide is impairing the bond at its actual proportion; when the gap is large, δ approaches $1/(1-C_{m-m})$ and the oxide impairment is reduced. The reduction is related on the cohesion between metal-metal C_{m-m}: The high metal-metal cohesion, the larger-level of the reduction of the oxide impairment. At large strain, C_{m-m} goes to 1 and δ factor goes to infinity. The strain-amplifying factor δ is written as follows:

$$\delta = 1/(1 - C_{m-m} \cdot (e/(e+\lambda))) \qquad \textit{Equation 5-9}$$

In the presented equation, C_{m-m} is the metal contact condition through the oxide cracks (a full contact between extruded metals represents a good wrapping effect of the metal); the term $(e/(e+\lambda))$ reflects the dispersion of the oxide fragments, which is assumed to have a constant length λ, along the straight interface.

The introduction of the strain amplifying factor δ could also be used to explain the effect of the grain boundary migration on promoting plastic deformation bonding. In the studies of nickel alloy[196, 211], copper[190] and steel[194] bonding studies under hot deformation in a vacuum, the grain boundary migration occurs over the clean interface and improves the final joint strength. Without oxide film, a higher grain boundary migration ratio was obtained with a higher local strain and other deformation conditions, including temperature and strain rate, which have also been related[196, 197]. In the previous work[211], this grain migration was observed when the oxide film was widely dispersed with barrier-free space for the migration to happen. Combining the results from [197] and the observation in [211], in the premise of assuming the ideal full-strength bond for clean surface contact, the factor δ could amplify the effect of local strain on the bond quality. Its effect includes the metal-oxide cohesion of the enwrapped oxides, the improvement in grain migrating and the exposure of clean metal through larger cracks.

After considering the minimized effect of largely dispersed residual oxide fragments by introducing the strain amplifying factor, δ, the area fraction of different contact pairs should be rewritten as:

$$f_{o-o} = A_{o-o}/A_n = 1/(1+\varepsilon\cdot\delta) \qquad \textit{Equation 5-10}$$

$$f_{o-m} = A_{o-m}/A_n = \begin{cases} (\delta\cdot\varepsilon)/(1+\delta\cdot\varepsilon), & \varepsilon \le \eta \\ \eta/(1+\delta\cdot\varepsilon), & \varepsilon > \eta \end{cases} \qquad \textit{Equation 5-11}$$

$$f_{m-m} = A_{m-m}/A_n = \begin{cases} 0, & \varepsilon \le \eta \\ (\delta\cdot\varepsilon-\eta)/(1+\delta\cdot\varepsilon), & \varepsilon > \eta \end{cases} \qquad \textit{Equation 5-12}$$

Combining the contribution of different bonding pairs to the final joint performance, the nominal bond ratio is given as:

$$Ratio(B) = Ratio_{o-o} + Ratio_{o-m} + Ratio_{m-m} = \sum_{m-m,m-o,o-o} f\cdot C \qquad \textit{Equation 5-13}$$

The four stages over the bonding by deforming:

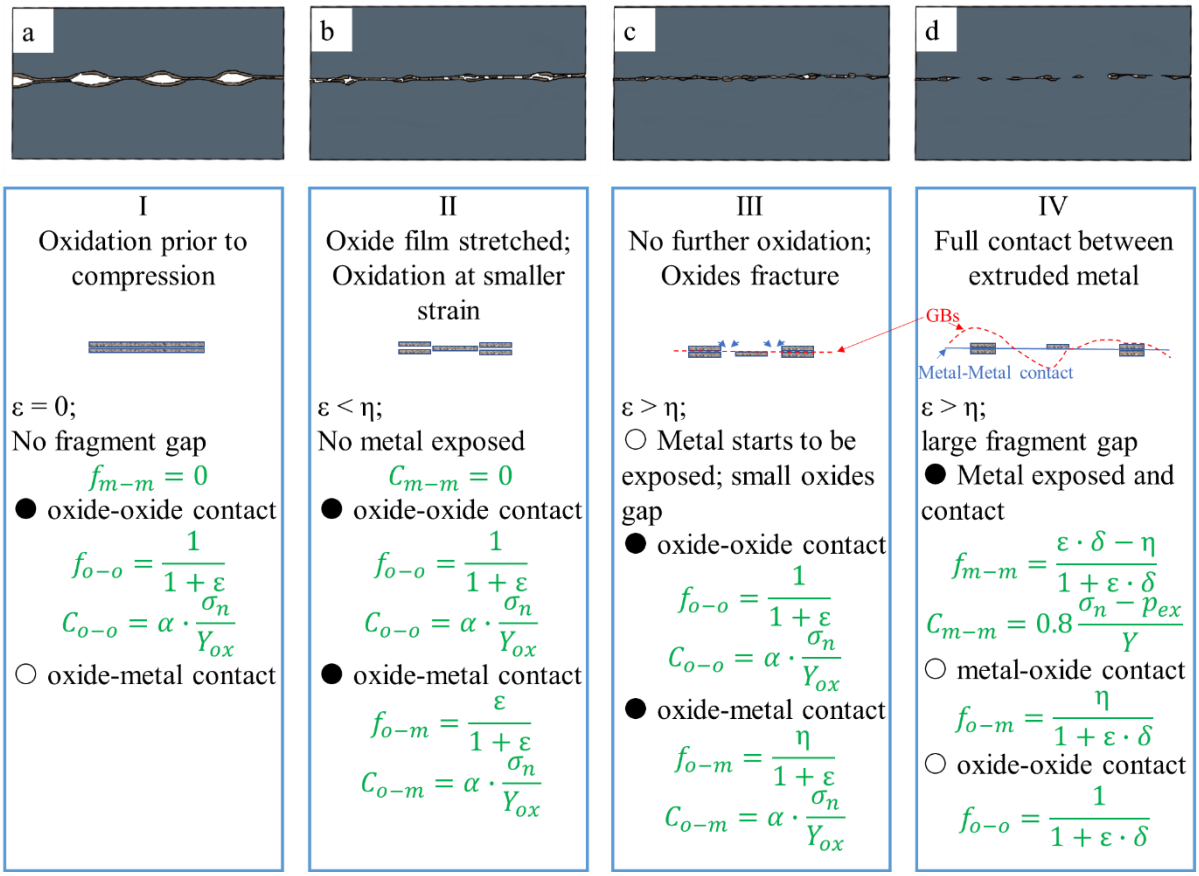


Figure 5-6 The interface behaviour and bonding mechanism at different stages.

According to the oxide film behaviour and the cohesion condition of different contacting pairs discussed above, the bonding mechanism can be divided into four stages as the Figure 5-6 shows below: Stage I, the initial contact is built between oxide and oxides pre-existed prior to compression ($\varepsilon = 0$); Stage II, at a lower surface strain range ($\varepsilon \leq \eta$), the oxide film is stretched to fracture and exposed metal is oxidized due to the trapped air, and the contact is formed between the metal and the newly formed oxide; Stage III, when the surface is further stretched ($\varepsilon > \eta$) and oxidation stops, clean metal begins to be exposed and extruded through small gaps, and extruded metal starts come into contact under pressure while the contact is mainly between the oxide-oxide and oxide-metal; Stage IV, the oxide is largely dispersed and metal-metal contact dominates, and in the meantime, with the occurrence of grain boundary (GB) migration and the oxide fragments being enwrapped, the impairing effect of the

remaining oxides is reduced. The role of each contacting pair in contributing to the joint performance is separately illustrated in Figure 5-6.

5.4 The implementation of the bonding model for bar sample bonding simulation

As explained in the bonding model in Section 5.3, the surface expansion and the normal stress are two key factors affecting the bond quality. Since the local stress-strain state of the central bonding area varies with locations under different bonding conditions, QForm was adopted to obtained the local stress-strain date of the central bonding area. As shown in the data flow diagram Figure 5-7, the stress/strain data were exported from QForm and substituted into the bond model equations in MATLAB scripts(see Appendix B). The oxide gap e, extrusion pressure p_{ex}, bond ratio of different contact pairs(oxide-oxide, oxide-metal and metal-metal) are separately calculated within the MATLAB code.

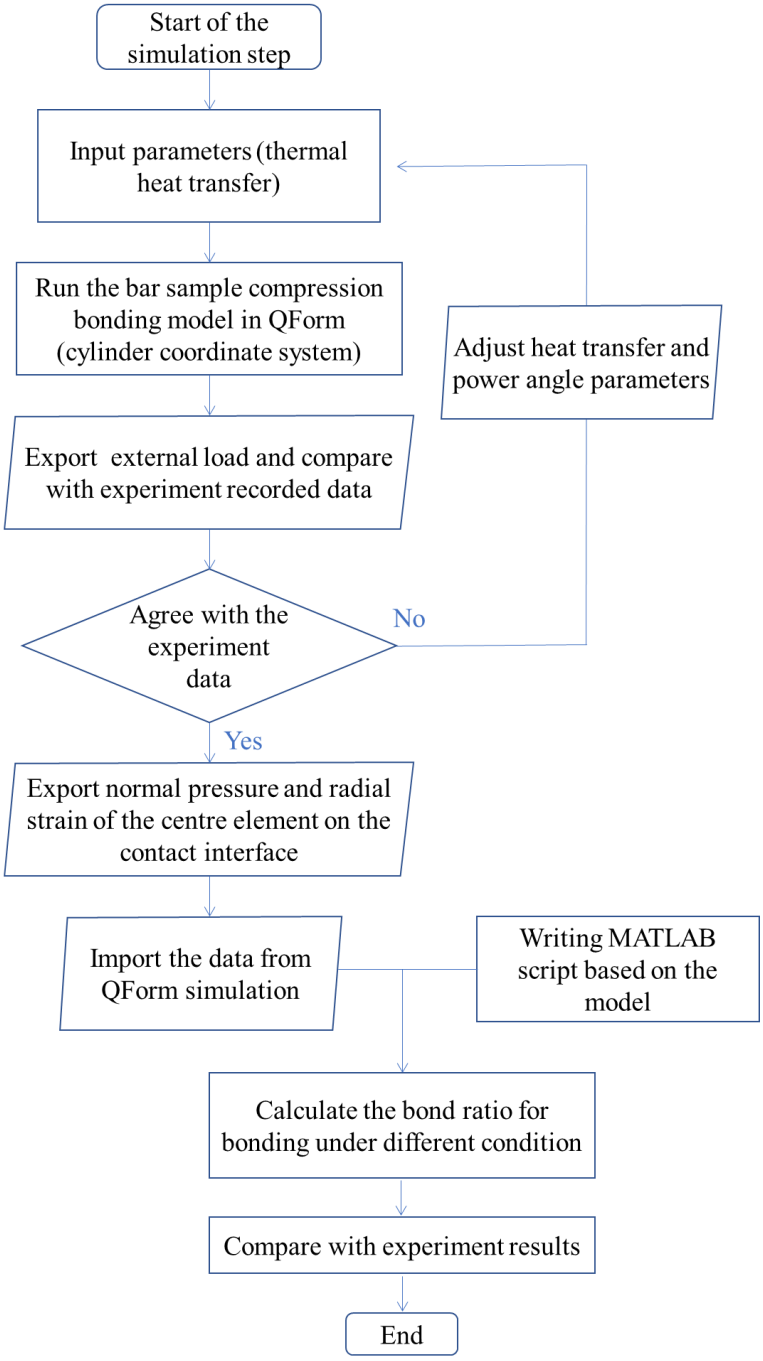


Figure 5-7 Flow chart of implementing the bond model with data from QForm simulation

The parameters used in the bonding model are listed in Table 5-1 and Table 5-2 and the parameters marked with * are fitting parameters. Therein, the oxide-related parameters η* and K* are fitted with the oxide film behaviour observed in Section 4.2. The cohesion of oxide-oxide α_{o-o} and oxide-metal is referred to the metal-metal α_{m-m} in [121], and fitted by final bond ratio. The yield

strength of metal is from the QForm material-IN718 library. Y_{o-o} is the compression strength of Al_2O_3[237]. Oxide fragment length is given based on the SEM observation in Section 4.2.

Table 5-1 The temperature/strain rate-dependent model parameters for simulating the Gleeble bonding process

Parameters	Y_{o-m}/Y_m	η*	α_{o-o}*	α_{o-m}*	α_{m-m}[121]
SR 0.001 s^{-1}	40 MPa	0.245	0.05	0.45	0.8
SR 0.01 s^{-1}	60 MPa				
SR 0.1 s^{-1}/T1150 °C	70 MPa				
SR 0.1 s^{-1}/T1050 °C	160 MPa	0.50	0.015	0.045	0.8
SR 0.1 s^{-1}/T950 °C	260 MPa	0.57	0.005	0.125	0.8

Table 5-2 The parameters relating to the oxide behaviour

Parameters	Y_{o-o}	K*	λ	t_c[121]
	690 MPa	18	1000 nm	10 nm

5.5 The implementation of the bonding model and predicted bond quality

5.5.1 The interpretation of bonding at different strains with calculated results

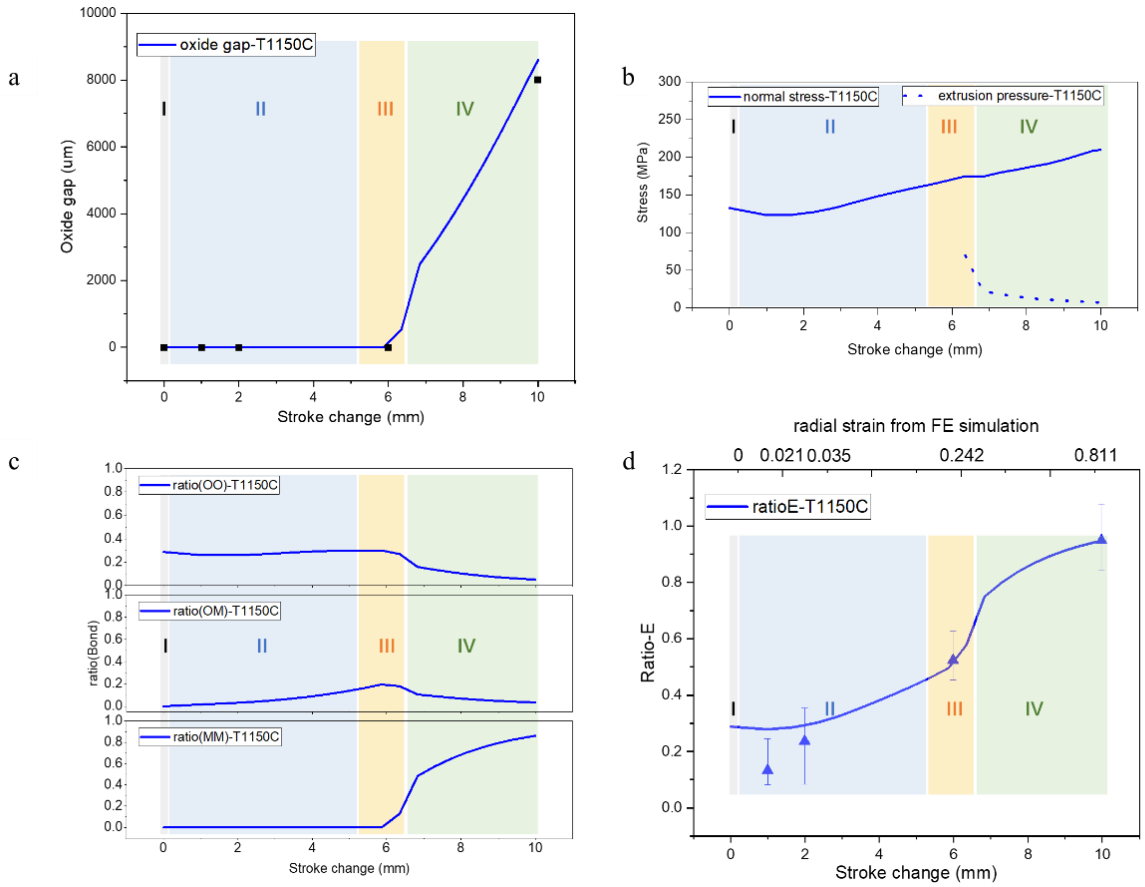


Figure 5-8 The FE simulation results of the hot compression tests and contribution of different contacting pairs on the final bonding quality: a) oxide fragment gap; b) the normal pressure applied, and pressure needed for extrusion; c) the contribution of different contacting pairs on final bond; d) the calculated total bonding ratio and tested elongation ratio of joints.

The simulated bonding quality results using the model described in 5.3 is shown in Figure 5-8. The simulated bonding process results shows a good coincidence with the four stages stated in the model: Before the oxide crack becomes large enough to allow the extrusion metal to meet (at stage I and II and early-stage III), it is the contact between oxide-oxide or oxide-metal that determines the joint tensile properties, as shown in Figure 5-8c. The oxide-oxide and oxide-metal are contributing at a percentage of the actual area fraction following Eqs. (5-1), (5-2) and (5-5). At these stages, the bonding quality is increasing slowly with the increased time and

strain, as the normal force applied is increasing relatively gently, moreover, the bond between oxide-oxide and oxide-metal is weak.

Starting from stage III, there is a clean metal surface exposed through oxide gaps. With the applied normal pressure increasing and the lower extrusion pressure decreasing through a larger gap, the metal comes into contact. The dispersed oxide frags become isolated and enwrapped by contacted nickel matrix, and in the meantime, GB migration occurs, turning the oxide frags within grains. At this time (stage IV), the introduced strain amplifying factor δ starts to play a role and weakens the impairing effect of remaining oxides. The bonding quality is increasing at a higher rate with strain/time because of metal-metal contact (Figure 5-8c and Figure 5-8d). It ends with a higher quality nearly equal to the reference level.

5.5.2 The calculated bond behaviour and quality at different strain rates

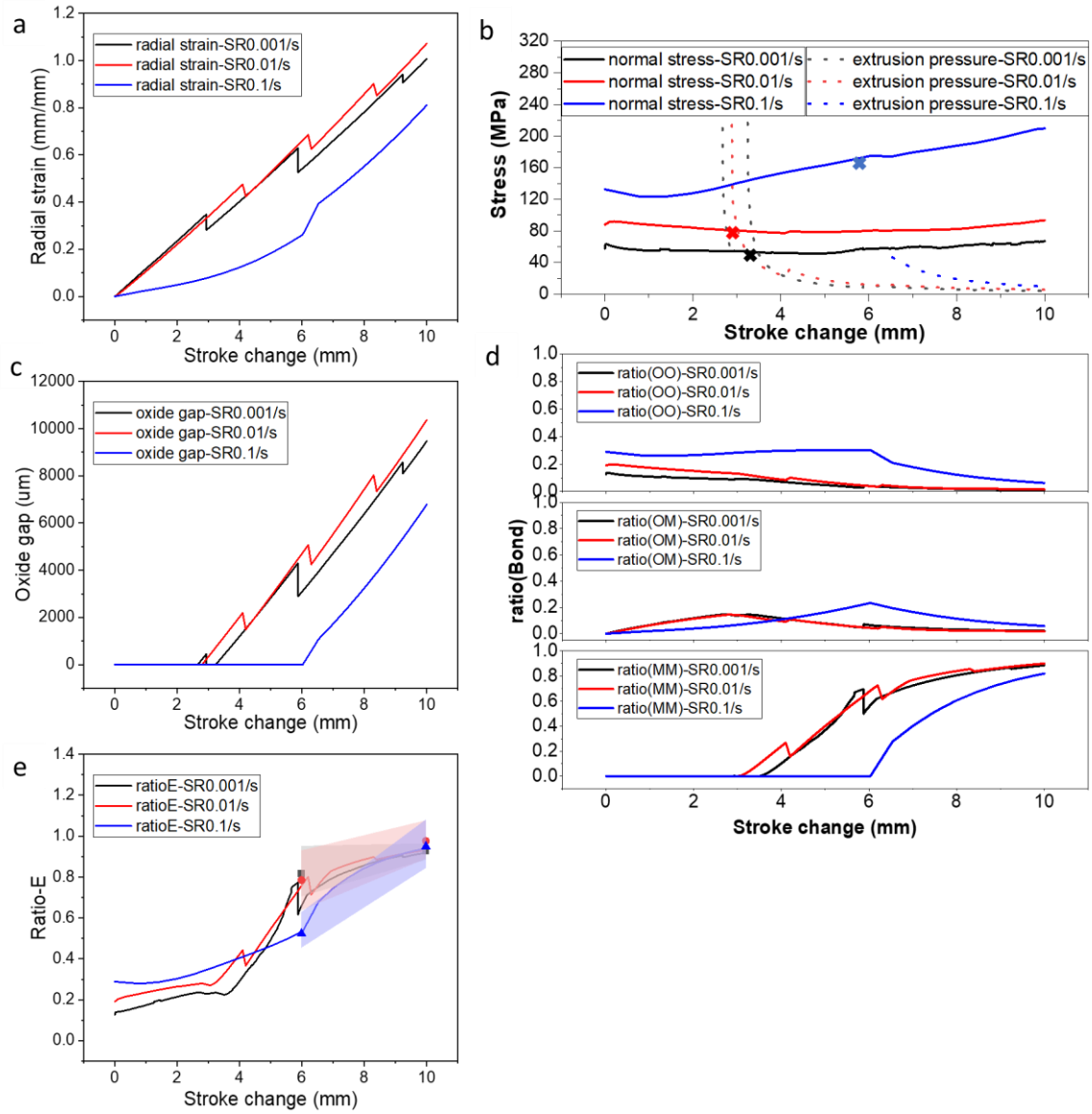


Figure 5-9 The calculated bond results for bonding at different strain rates, a) the radial strain; b) normal stress and extrusion stress; c) oxide gap; d) the contribution of different contacting pairs on bond ratio; e) the final bond ratio and obtained bond ratio.

Based on the proposed four-stage bonding model, the calculated results of the oxide dispersion, the cohesion of different contacting pairs over the compression at different strain rates are shown in Figure 5-9. As shown in Figure 5-9a, the radial strain measured locally from the central points is similar for 0.001 s^{-1} and 0.01 s^{-1}, higher than that for 0.1 s^{-1}. Besides, at a lower

strain level (stroke change smaller than 6 mm), the calculated radial strain is a little lower for 0.001 s^{-1} than 0.01 s^{-1} and changes reversely over 30% height reduction. According to Eq. (5-3), the oxide gap depends on the radial strain. At the earlier stage, when the imposed compression at lower strain (stage I and II, stroke change less than 3 mm for 0.001 s^{-1} and 0.01 s^{-1}, 6 mm for 0.1 s^{-1}), the oxide gap remains zero (Figure 5-9c) due to the continuous oxidation. The metal is covered with continuous oxide film with no gap for metal extrusion. Over the critical strain, the bonding comes into stage III, when oxidation stops, and gaps are exposed between oxides. The oxide gap presents a similar changing trend for different strain rates. In the oxide frag length Eq. (5-3), the parameter K is determined as 18 by measuring the actual gap between oxide frags from the microscopic observation (Figure 4-9). The calculated gap for 0.1 s^{-1} appears later and smaller than that for 0.001 s^{-1} and 0.01 s^{-1} and agrees with the observation in Figure 4-9. When the sample is 30% compressed, the gap shown in Figure 4-9d is smaller than Figure 4-9b and c. The oxides dispersion for 0.01 s^{-1} starts with a bit larger gap than 0.001 s^{-1}, and change reversely near the stroke change of 5 mm, similarly to the local strain change. At stage III, with gaps (Figure 5-9c) increasing, the extrusion pressure is calculated to decrease (Figure 5-9b). Metal starts to be extruded through the gaps when the extrusion pressure needed is lower than the applied normal pressure. The starting point at which the metal is extruded for different strain rates is marked (Figure 5-9b), which is consistent with the sequence that which oxide starts to be broken up in Figure 5-9c.

In stages I and II, no metal-metal cohesion occurs, and the cohesion of oxide-oxide and oxide-metal jointly make the main contribution to the final bond ratio. As the oxide-metal contact is built on exposed metal covered with the newly oxidized film, its area fraction increases with the surface strain (Figure 5-9d). The oxide-oxide formed only between the pre-existing oxide films fraction starts from 1 and decreases (Figure 5-9d). According to Eq. (5-7) and (5-8), the cohesion of both oxide-oxide and oxide-metal is dependent on the normal pressure and increase with compression (Figure 5-9d). However, due to the brittle nature of oxide and difficulties in ceramic bonding, the cohesion for oxide-oxide is much weaker than oxide-metal. The cohesion of metal-metal pairs starts to increase from zero as the extruded fresh metals come into contact. At stage IV, the cohesion of metal-metal reaches 1 with a fully intimate contact formed under pressure. As discussed in the model, at this stage, the oxide fragments are included within grains. The introduction of strain amplifying factor δ has effectively reduced the effect of

oxide-oxide and oxide-metal cohesion. The final bond ratio mainly depends on the metal-metal contact. The transformation from oxide-metal/oxide-oxide dominating mode to metal-metal dominating occurs at stage III. As the oxide thickness is smaller, metal extrusion is relatively easy to happen. This transformation occurs quickly, shown as the turning points on the OM-ratio and OO-ratio curves in Figure 5-9d.

Combining the contribution of different contacting pairs, the final bond ratio (ratio-EL) is calculated and shown in Figure 5-9e, and the relative elongation ratio for tested joint over 30% deformation is also shown for validation. For each condition, two identical samples were tested for repeatability study. A similar final bond ratio of 1 is achieved for three tested strain rates at the 50% height reduction deformation. Comparing the calculated results of bonding under different strain rates, similar oxide film behaviour and dependence of different contacting pairs in each stage are shown. However, due to the different local radial strains as calculated, the bonding could come into stages at different deformation levels. At a low deformation level, the larger strain from 0.001 s^{-1} and 0.01 s^{-1} results in a larger oxide gap and higher oxide-metal cohesion, which leads to a higher final bond ratio. As the tested bond ratio shows, the ratio for 0.1 s^{-1} is slightly lower. While at a high deformation level, when the gaps are widened enough, high oxide-metal cohesion from the high normal stress for 0.1 s^{-1} compensates for the difference by a lower strain. A little higher bond ratio is achieved, both as calculated and tested.

5.5.3 The calculated bond behaviour and quality at different deformation temperatures

The calculated bonding behaviour at different deformation temperatures is compared in Figure 5-10. As shown in Figure 5-10a, the sample compressed at 950 ˚C and 1050 ˚C reveals higher radial strain in the centre zone during the deformation compared to 1150 ˚C, which explains the larger diameter of the compressed bar sample obtained at lower deformation temperature (Figure 5-3). Although higher strain is obtained with lower temperature, as introduced in 5.2 and Figure 4-14, visible gaps are observed for the bar samples compressed at a lower temperature under a strain rate of 0.1 s^{-1}, therefore the oxidation during compression at 950 ˚C and 1050 ˚C is more serious. In Figure 4-14, the continuous oxide film is observed at 30%, and disrupted oxides are observed at 50%. After the points where the oxide gap begins to increase from zero in Figure 5-10c, the exposed metal starts to be extruded through oxide gaps when the normal stress is higher than the stress needed for extrusion. The comparison is given in Figure 5-10b. The marked points in Figure 5-10b represent the beginning of the metal-metal

contact. By comparison, the sample compressed at 1050 ˚C starts the metal-metal contact first, however, there is no remarkable difference between the three different temperatures. Before the metal-metal contact, it is the contact between oxide-oxide and oxide-metal are contributing. As explained in 5.2, the cohesion between oxide-oxide and oxide-metal are positively related to force and temperature. Here at different temperatures, the cohesion between oxide-oxide, oxide-metal are lower at lower temperatures. Thus, lower ratio(OO) and lower ratio(OM) is calculated at a lower temperature. After the oxide starts to be dispersed, the metal-metal contact starts to dominate. As observed in Figure 4-14, interface grain migration occurs at three all temperatures, the microstructural factor δ starts to work, a similar higher final bond ratio is calculated for three temperatures, as consistent with the tested joint performance (Figure 5-10e).

Overall, at the early stage of bonding, as there is continuous oxide film existing on the interface, it is the diffusion and cohesion that are dominating. Therefore, a higher temperature is favourable for higher joint quality; when the strain is high enough to break the oxides and metal-metal contact starts, as there is also interface grain boundary migration occurring with the recrystallization process during hot deformation, good joining quality can be obtained even at a lower temperature.

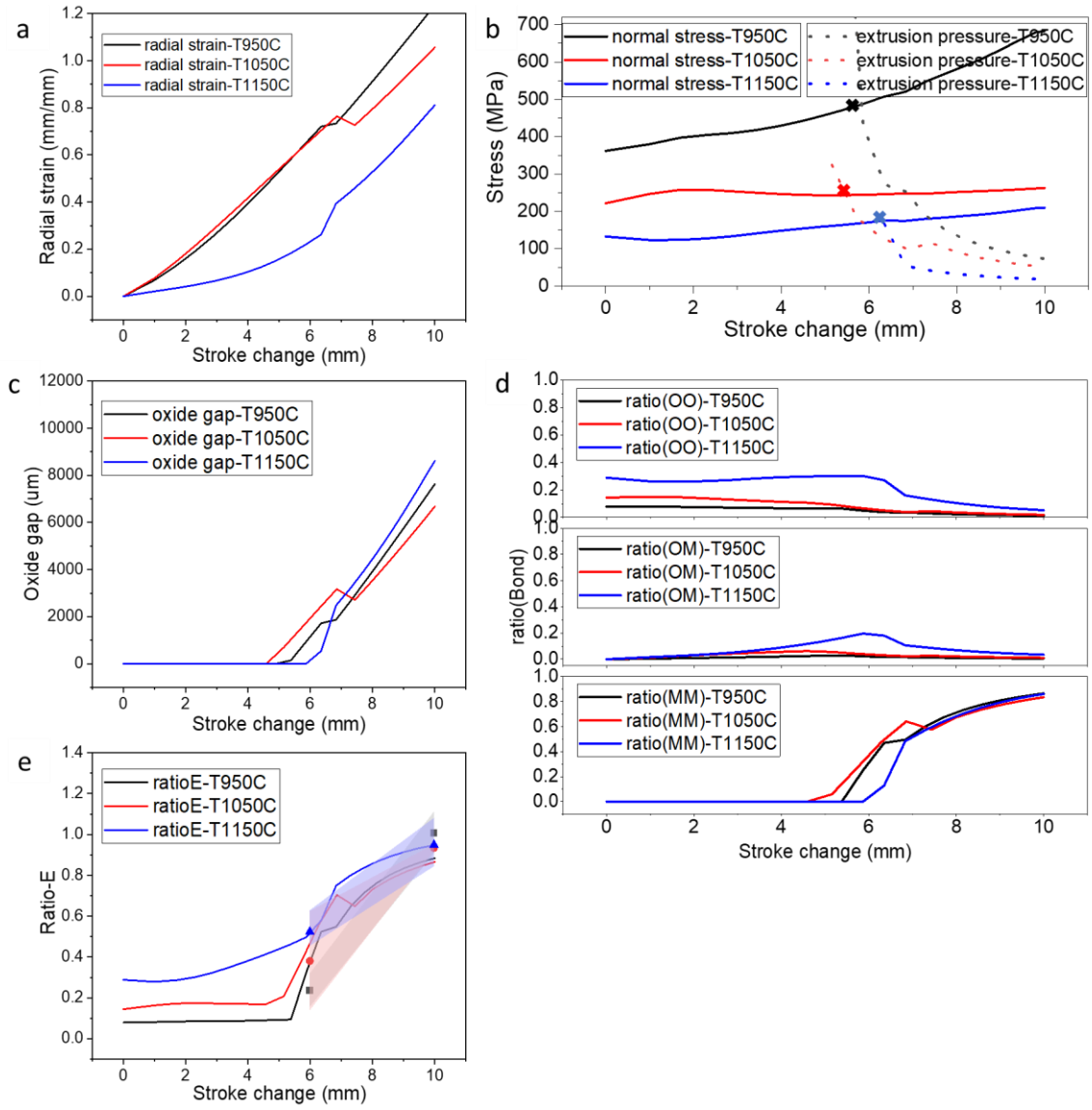


Figure 5-10 The calculated bond results for bonding at different strain rates, a) the radial strain; b) normal stress and extrusion stress; c) oxide gap; d) the contribution of different contacting pairs on bond ratio; e) the final bond ratio and obtained bond ratio.

5.6 The evaluation of the now bond model for bonding at hot deformation

Compared with the classic roll bond model developed by Bay and Cooper, this new model for bonding under hot deformation has incorporated the essential bond interface behaviour and critical microstructure related interfacial GB migration, and thus, predicts a high joint strength comparable to the parent level. From the simulated results, it is the interface cohesion between

oxide-oxide and oxide-metal, occurred at hot temperature and high stress, contributes to the joint quality at a lower strain level when the oxide films are rather continuous; while at a high strain and when the oxide films are fully broken into fragments and largely dispersed, the joint quality basically credits to the fully contacted metal-metal pairs. The role of different contacting pairs (oxide-oxide, oxide-metal and metal-metal) play can be clearly shown, and the behaviour of the bonding interface (basically the oxide film) is well described. Moreover, for a bond formed under hot deformation conditions, the reduced effect of remaining oxides from tensile property tests and observed microstructure evolution induced by the recrystallization process are both critical. As suggested in this work and studies on hot compressive bonded nickel by [196] or copper by [190], this microstructure evolution affects the joint performance: higher strain leads to a higher Rx fraction and higher GB migration ratio, which accounts for the ultimate bond quality. The introduction of the amplifying factor in this work has successfully described the reduced effect of remaining oxides and benefits of the interfacial GB migration at metal-metal fully contacting stage. Thus, the critical effect of Rx-induced microstructure change has been neglected previously yet considered and included properly for the first time in this model.

Despite its potential utility in predicting bond quality, the limitations of the theoretical bonding model in its current state must be reiterated. In this model, assumptions have been made regarding the cohesion between oxide and oxide or metals and the reduced effect of the broken oxide film, and the independence of the bonding on strain and stress is simplified with representative relationship or coefficients, e.g., the usage of radial strain, cohesion ratio coefficients for different contacted pairs. Hence, to further improve the proposed model, more direct experimental observation of the qualitative phenomena, regarding the factors influencing oxide-oxide or oxide-metal cohesion and the effects of the remaining oxides, are required. Also, the strengthening of the bond due to the movement of grain boundaries across the oxide debris at the bonding interface is currently less well-understood; its effects have been incorporated via the strain amplifying factor. Future work should therefore be undertaken to better understand this phenomenon and develop a more quantitatively and physically accurate mathematical form for the strain amplifying factor. Nevertheless, given the current dearth of existing models describing high-temperature solid-state compression bonding, the model proposed in the present work is a reasonable first step towards the development of a general

quantitative description of this phenomenon and the eventual use of such a model for the accurate simulation of joint quality.

With the full performance restored for the joining formed by hot deforming, the interface has been eliminated. This high bond integrity achievement would enable solid-state bonding to be applied in safety-critical components. With the help of forming process simulation, the developed model would achieve predictability of joining and enable the bonding-by-hot-forming to be transferred to a wider range of applications.

5.7 Conclusions

1. In accordance with the proposed bonding mechanism proposed in 4.5.1, a four-stage model is developed to describe the bonding process with the presence of oxide film and microstructural evolution. In earlier stages with a continuous oxide film, the cohesion of oxide-oxide and oxide-metal is assumed to be related to the force applied and make the main contributions to the bond ratio. In late stages with large strain, oxides are largely scattered, and interface migration occurs to include the oxide inside grains. The adverse effect of remaining oxides is minimized by introducing strain amplifying factors in the model.
2. Model validation is conducted with a bonding test by hot compression at different strain rates and temperatures. When excluding the microstructural effect by comparing with references, the EL ratio is considered to better indicate the interface bond quality.
3. The proposed model has successfully predicted the final interface bond ratio for three strain rates. According to the calculated bonding process, when samples are 30% compressed, the lower bond ratio for a slowly compressed sample is due to the lower normal stress applied. When samples are further 50% compressed, a near-full bond ratio is achieved for three strain rates due to amplification of the strain effect with oxides enwrapped.
4. The proposed model has successfully predicted the final interface bond ratio for three temperatures. According to the calculated bonding process, when samples are 30% compressed, the lower bond ratio for a slowly compressed sample is due to the lower cohesion between the oxides, or oxide-metal. When samples are further 50%

compressed, a near-full bond ratio is achieved for three strain rates due to amplification of the strain effect with oxides enwrapped.

5. The predicted interface bond ratio, combined with the microstructure, can be used to determine the final joint performance.

Chapter 6 The multi-layered forging of IN718

6.1 Introduction

For nickel-based superalloys, especially at practical hot forming, the forming temperature and strain level, phase transformation and grains behaviour are much more complicated, affecting the ending performance of the joint. In this chapter, instead of using a small demonstrating sample with a strictly controlled atmosphere, IN718 plates are bonded under actual hot forging conditions (as described in the Method Section 3.3.2), and the joint microstructure is characterized. The joint quality determined by the coupling effect of grain size, precipitation, the oxidation behaviour of the interface is evaluated by tensile tests. By varying the forge temperatures and deformation rates, the thermodynamics and kinetics bonding behaviour of the joint will be described. Another aim of this work is to quantitively examine the dependence of joint quality on actual forge welding parameters. Note that the work presented in this chapter is only the very first trial of industrial processing validation, other trials have been planned but unable to be completed due to the pandemic, more details will be presented in the discussion Section.

Structure of the chapter: The mechanical performance of the plates bonded under hot forging conditions within conventional forging windows will be presented and discussed. In the Result Section, an overview of the microstructure of interfaces and corresponding tensile test results at all forging conditions will be given with reference to the wrought standard; and a detailed correlation between the plate performance uniformity over edge and centre, as well as the phase evolution, will be discussed later in the Discussion Section 6.3.

6.2 Results

6.2.1 The microstructure near bonding interfaces

The forged plates were composed of three layers with two interfaces. Due to the nonuniform deformation condition, e.g., temperature, over the plate, the deformation behaviour along the bonding interface may differ. Herein, the microstructures near the two interfaces were examined in different zones (the positions C1 and C2 from the centre stand for interfaces 1 and 2, respectively, and E1 and E2 from the edge zone for interfaces 1 and 2, respectively).

Figure 6-1 show the optical morphologies for the bonded plates after forging and heat treatment. For the explored conditions, a small difference is seen except under the condition of Temp 950 ˚C/SR 10 mm·s^{-1}. At 950 ˚C, different microstructures are observed near the interface in both the centre and edge zone and the difference is more obvious in the centre zone. A more detailed discussion on the microstructural difference is presented in Section 6.2.3.

For the other four investigated conditions, the straight bond lines are visible and the grain microstructure is identical on both sides of the line. Equiaxed grains with an average size of 30 μm are presented for samples forged at 1050 ˚C/10 mm·s^{-1} (Figure 6-1b). At a higher temperature of 1150 ˚C with the same forging speed of 10 mm·s^{-1}, larger grains are shown in Figure 6-1e compared to 1050 ˚C. At a temperature of 1150 ˚C, when forged at lower strain rates, much larger equiaxed grains (~100 μm) are seen at 1 mm·s^{-1}, and microstructure mixed with large and small grains is shown in Figure 6-1c with further lowering the speed to 0.1 mm·s^{-1}. Even the grain microstructure at different conditions is different, the straight bond line can still be seen.

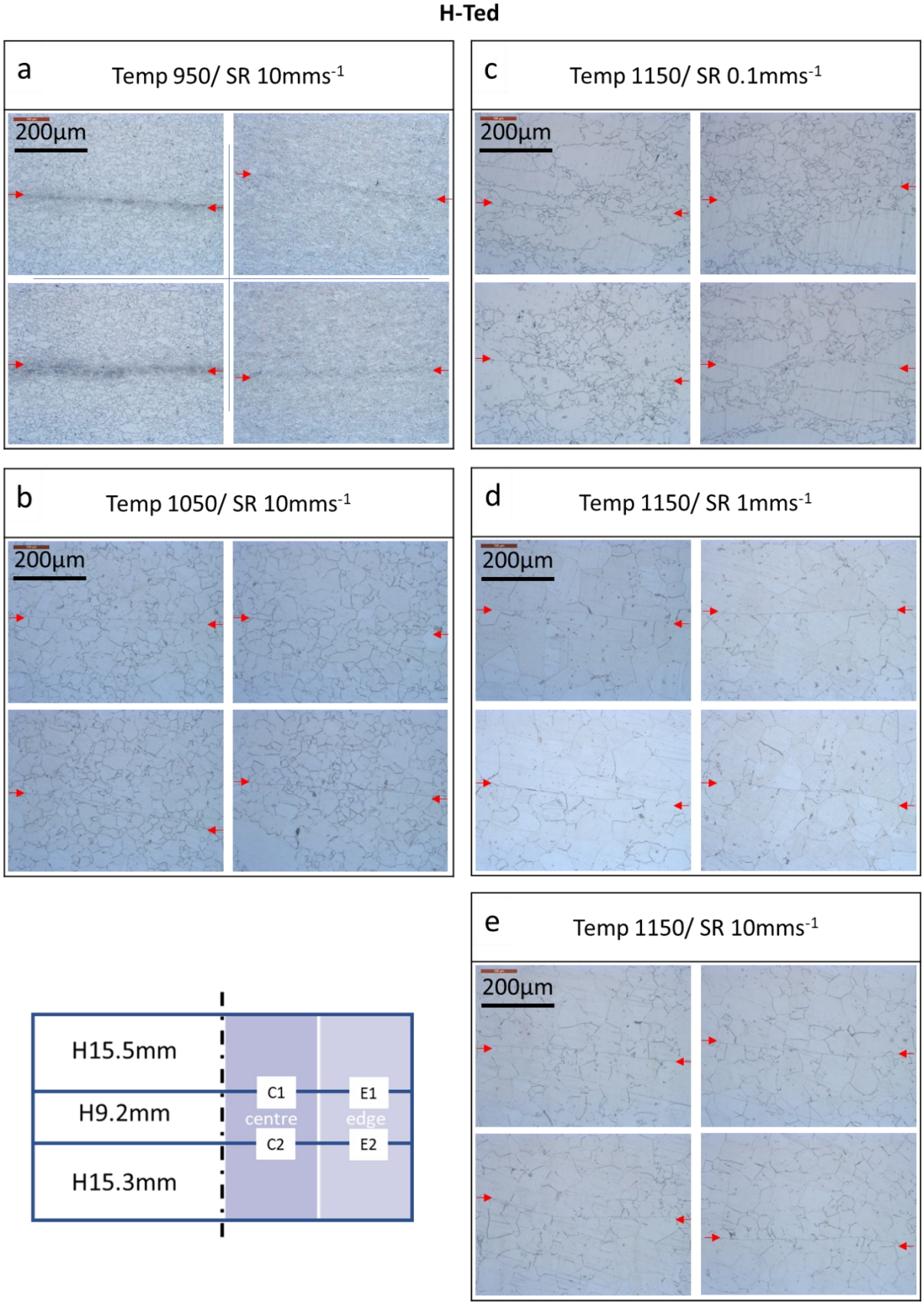

H-Ted
a
Temp 950/ SR 10mms-1
200µm
c
Temp 1150/ SR 0.1mms-1
200µm
b
Temp 1050/ SR 10mms-1
200µm
d
Temp 1150/ SR 1mms-1
200µm
e
Temp 1150/ SR 10mms-1
200µm
H15.5mm
H9.2mm
H15.3mm
C1
C2
centre
E1
E2
edge

Figure 6-1 Optical morphologies of the interfaces of deformed plates at different conditions after heat treatment. a) 950 ˚C /10 mm·s^{-1}, b) 1050 ˚C /10 mm·s^{-1}, c) 1150 ˚C /0.1 mm·s^{-1}, c) 1150 ˚C /1 mm·s^{-1}, c) 1150 ˚C /10 mm·s^{-1}.

6.2.2 The room-temperature tensile test

From the shape of forged parts in Figure 3-5, the deformation is uniform at a higher strain rate (10 mm·s^{-1}), and slightly drum-shape are seen for samples compressed with 1 mm·s^{-1} and 0.1 mm·s^{-1} at 1100 ˚C. Due to the temperature and stress differences, different microstructure and interface bond quality are shown in different zones. Figure 6-2 presents the room-temperature tensile results for an as-forged specimen which were taken from different zones of the three-layered piled-up plates bonded under different conditions. The zone in deeper purple represents the centre zone and lighter purple is the edge zone.

At a forging speed of 10 mm·s^{-1}, the samples forged at 950 ˚C presents a higher yielding and ultimate tensile strength than other conditions (Figure 6-2a), moreover, worthy to note that samples taken from the edge area show stronger strength and higher elongation than the centre area. Considering the microstructure effect on final tensile performance, high yielding is normally due to fine grain structure, which may lead to low elongation. The better performance of the sample from the edge zone indicates a better joining quality. The plates forged at 1050 ˚C (Figure 6-2b) and 1150 ˚C (Figure 6-2c) with a speed of 10 mm·s^{-1} shows better uniformity. The yielding and ultimate strength are similar in edge and centre zone, and elongation as well. Due to the grain growth at high temperatures, the strength at 1050 ˚C and 1150 ˚C has lower strength and higher elongation than that of 950 ˚C. At 1150 ˚C with slower forging speeds (1 mm·s^{-1} and 0.1 mm·s^{-1}), the yielding strength in the edge and centre zone is shown to be similar, which indicates a similar grain microstructure. However, together with the decrease of elongation, samples in the edge zone present lower ultimate strength. This inferior elongation and ultimate strength suggest the poor bond quality near the edge.

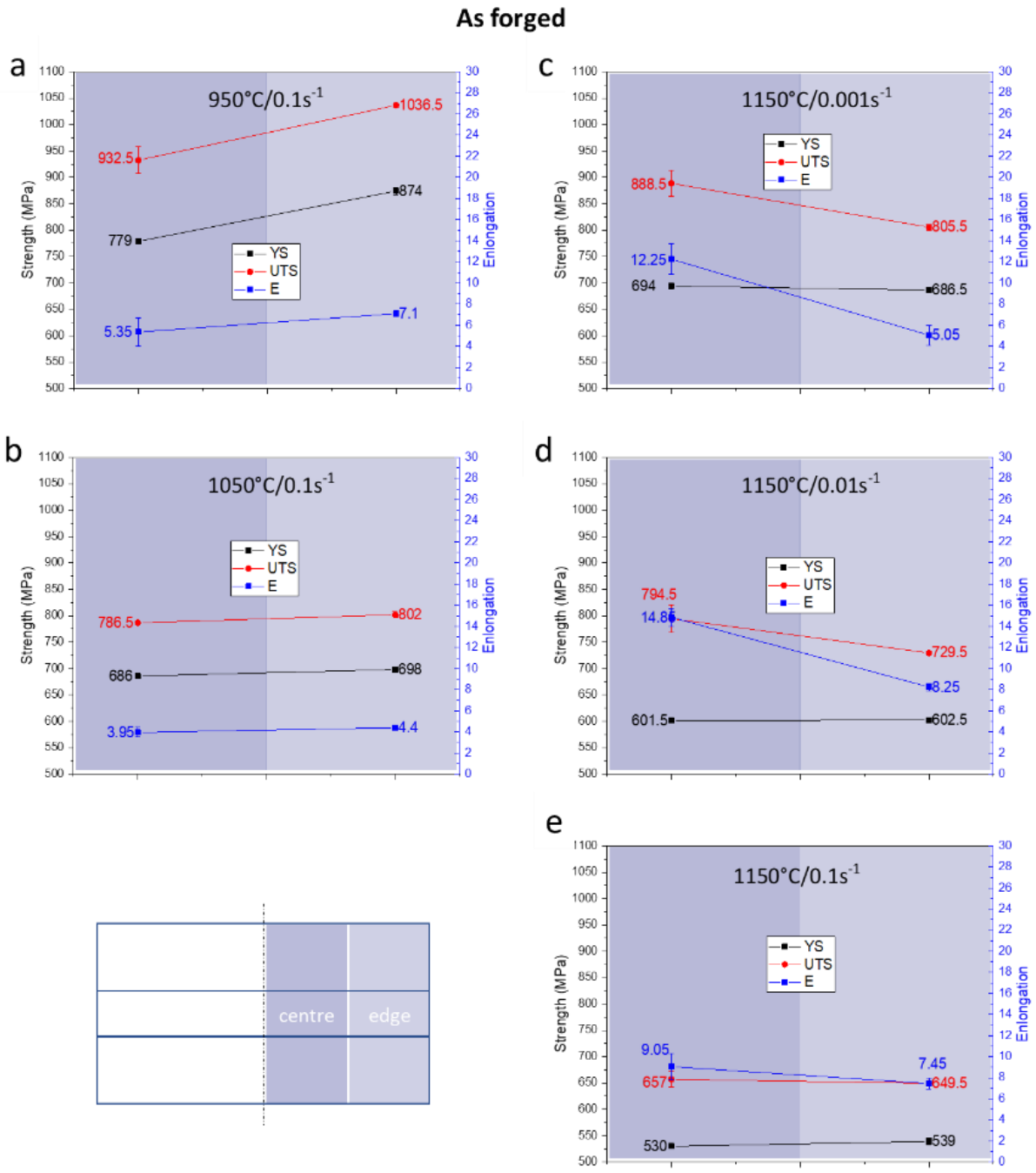


Figure 6-2 The room-temperature tensile test results, including UTS, YS, EL for three-layer piled-up samples bonded at different conditions. a-c), different temperatures with a forging speed of 10 mm·s^{-1}; c-e), different strain rates at the temperature of 1150 ˚C.

As the tensile test results in Figure 6-3 show, after the standard ageing heat treatment, the tensile test results show similar uniformity as in the forged state. The dashed lines in Figure

6-3a mark the standards for wrought IN718. Under all conditions, the samples taken from different positions of the plates present higher yielding strength than standards. However, due to the low elongation, the forged plates have hardly met the required ultimate strength as the wrought state. Under the condition of (1150 ˚C-10 $mm \cdot s^{-1}$, Figure 6-3c) and (1150 ˚C-0.1 $mm \cdot s^{-1}$, Figure 6-3e), the forged plates have comparable ultimate strength with standards and relatively better ductility. For the plate forged at (1050 ˚C-10 $mm \cdot s^{-1}$), the obtained ultimate strengths are higher than standard, yet ductility is much lower.

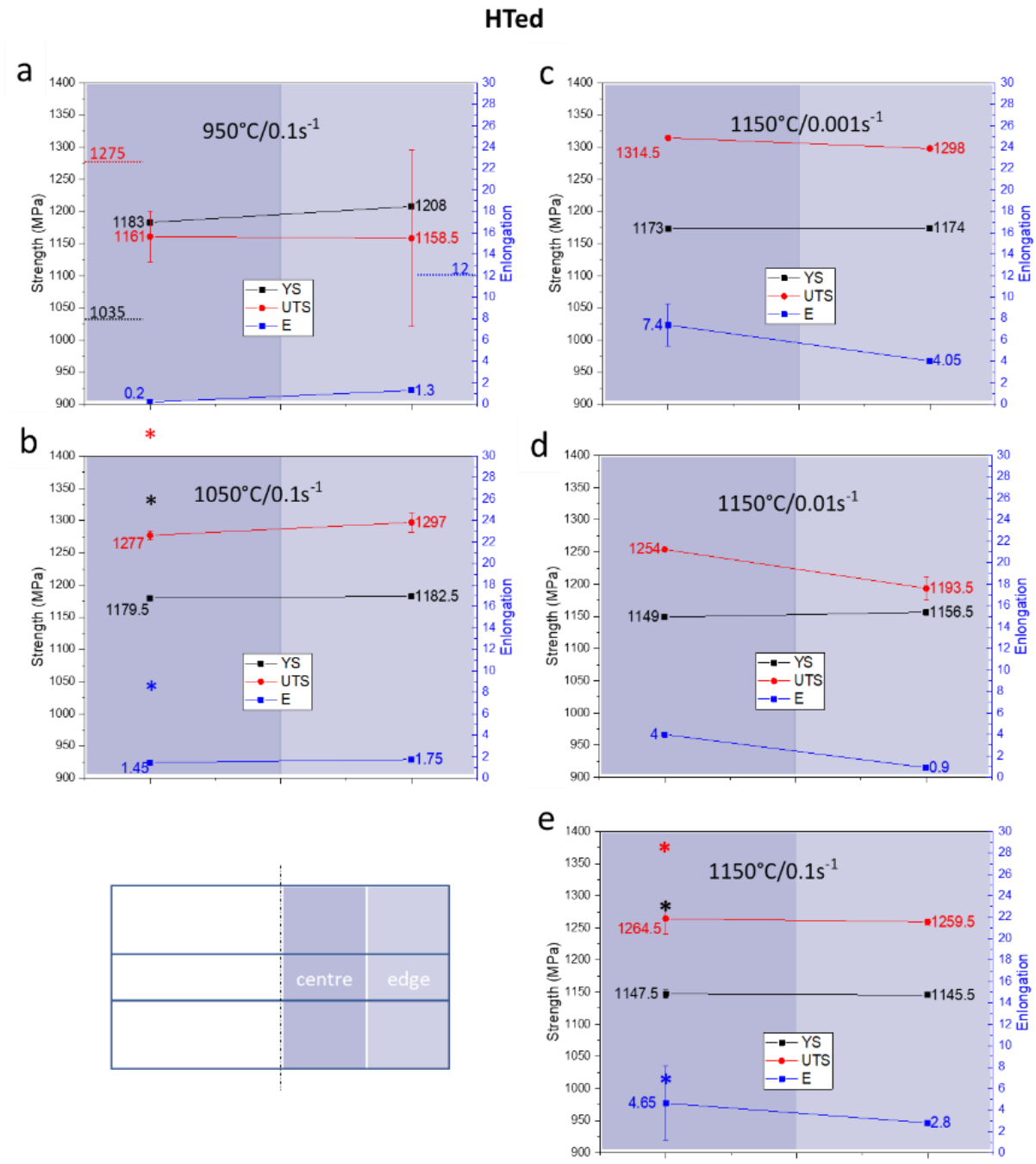


Figure 6-3 The room-temperature tensile test results, including UTS, YS, EL for three-layer piled-up s bonded at different conditions. a-c), different temperatures with a forging speed of 10 mm·s^{-1}; c-e), different strain rates at the temperature of 1150 ˚C after heat treatment.

6.2.3 The bond interface microstructure

Figure 6-4 shows the interface microstructure from different locations of the plates forging bonded at 950 ˚C/10 mm·s^{-1}. After hot forging, the interface area presents different microstructures from the base materials. From the SEM images in Figure 6-4, this difference is mainly caused by the presence of δ (orthorhombic Ni3Nb) phases. In the centre zone, short rod-like δ phases are distributed along part of grain boundaries (GBs) at a lower fraction in the base. And in contrast near the interface, more short-rod-like δ phases precipitate along GBs and also δ phases present long needle and plate shapes form inside grains, as shown in the magnified view in Figure 6-4a. The width of the high-density interface zone is about 50 μm. Particle δ phases precipitate continuously along the bond interface. Near the edge zone, no obvious difference is seen between the microstructure of the base and interface area, and both have high δ phase density. The δ phase precipitate with a needle shape, similar to the interface area in the centre zone.

After standard double ageing heat treatment, the corresponding microstructures are given in Figure 6-4(c-d). The difference between the base and interface still exists after heat treatment in the centre zone, which was also seen in the optical microscopic images in Figure 6-1. However, in the base, there are more short-rod-like δ phases continuously and uniformly appearing at GBs. Similar morphology of the δ phase with that before the heat treatment is shown near the bond interface, but its width is slightly narrowed down to approximately 30 μm. The microstructural difference is less obvious after heat treatment. In the edge zone, the overall microstructure is uniform with intragranular needle-like δ phase precipitating and intergranular short-rod-like δ phase. Compared with the interface in an as-forged state, the particle δ phases along the bond interface after heat treatment seem to dissolve and the bond lines are less obvious. The difference in the proportion of δ phases was quantitatively presented in Figure 6-5. Consistent with the microstructure characterization in Figure 6-1 and Figure 6-4, a higher δ phases content is seen near the interface, and the difference is more obvious in the centre zone than the edge area. After being ageing treated, more δ phases were precipitated and the difference between the interface and matrix is reduced, in both centre and edge zone.

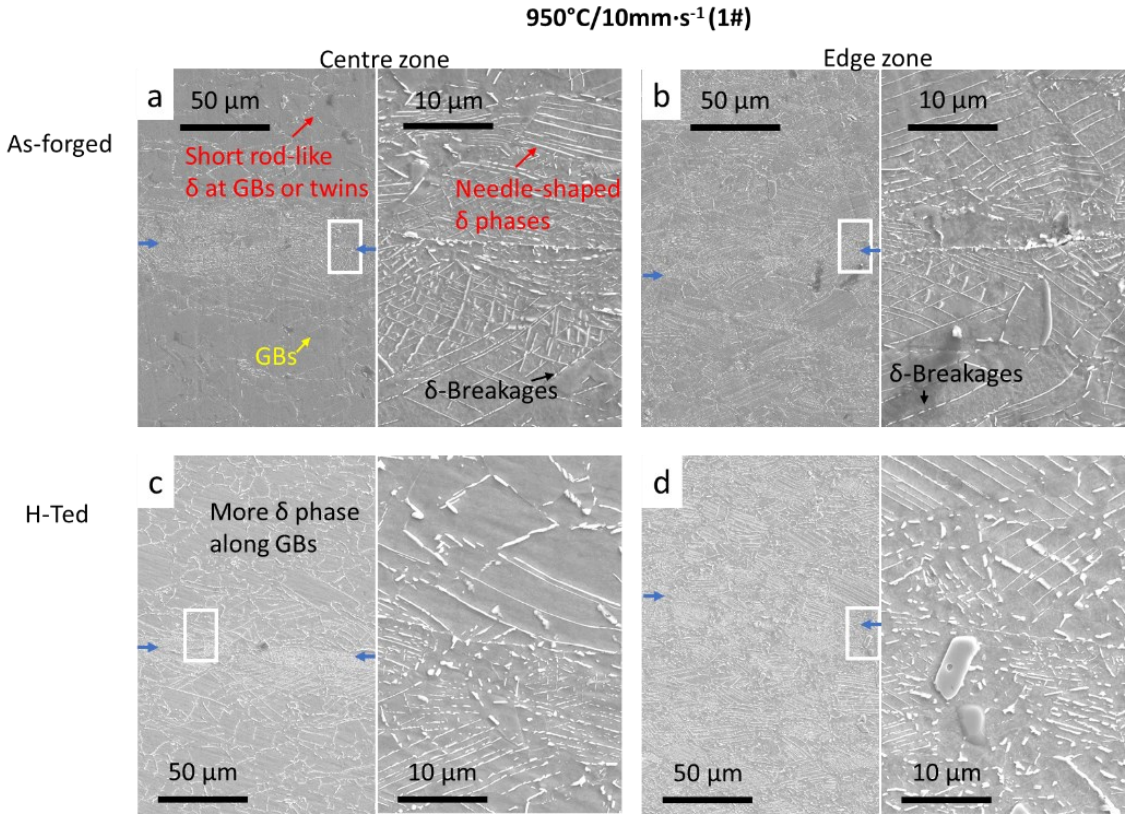


Figure 6-4 The interface microstructure at the centre and edge zone of the plate bonded at 950 ˚C/10 mm·s^{-1}. a-b) as forged, c-d) after heat treatment.

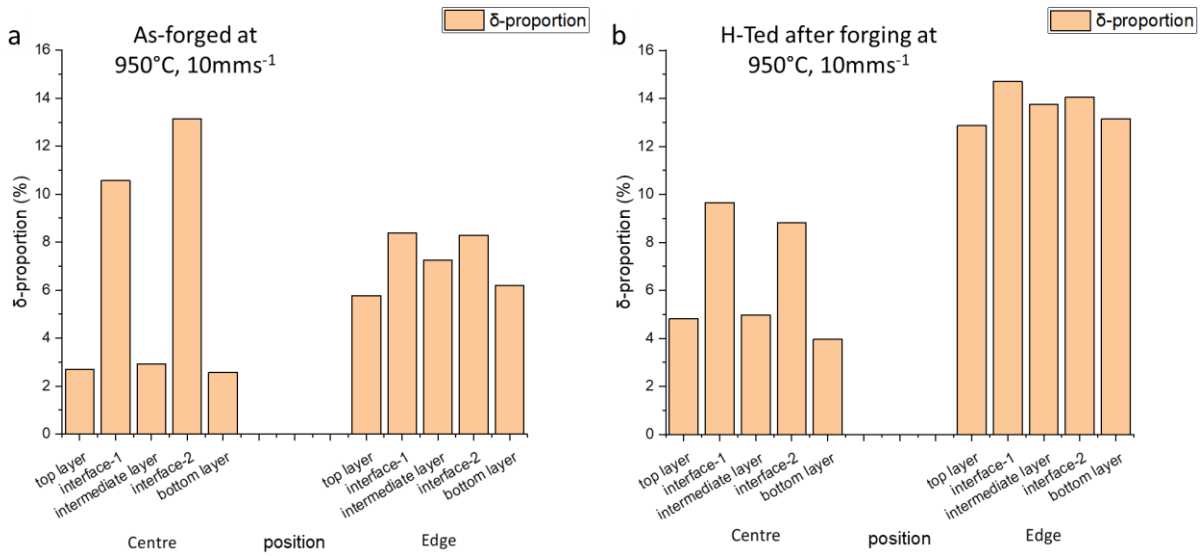


Figure 6-5 The quantitative analysis of the δ phase in different locations of the multi-layer-built plate at the forging condition of 950 ˚C, 10 mm·s^{-1}.

From the mechanical property results given in Section 6.2.2, the plate forged at 1150 ˚C/10 mm·s^{-1} and 1150 ˚C/0.1 mm·s^{-1} have much better performance in tensile test and stress rupture test. Figure 6-6 shows the interface microstructure from plate forging bonded at a higher speed of 10 mm·s^{-1} (3-3#). At a higher forging temperature, no δ phase appears after forging. The bond line is seen in both centre and edge zones of the plates. After heat treatment, this bond line retains, moreover, needle-like δ phases appear along grain boundaries and the interface bond line.

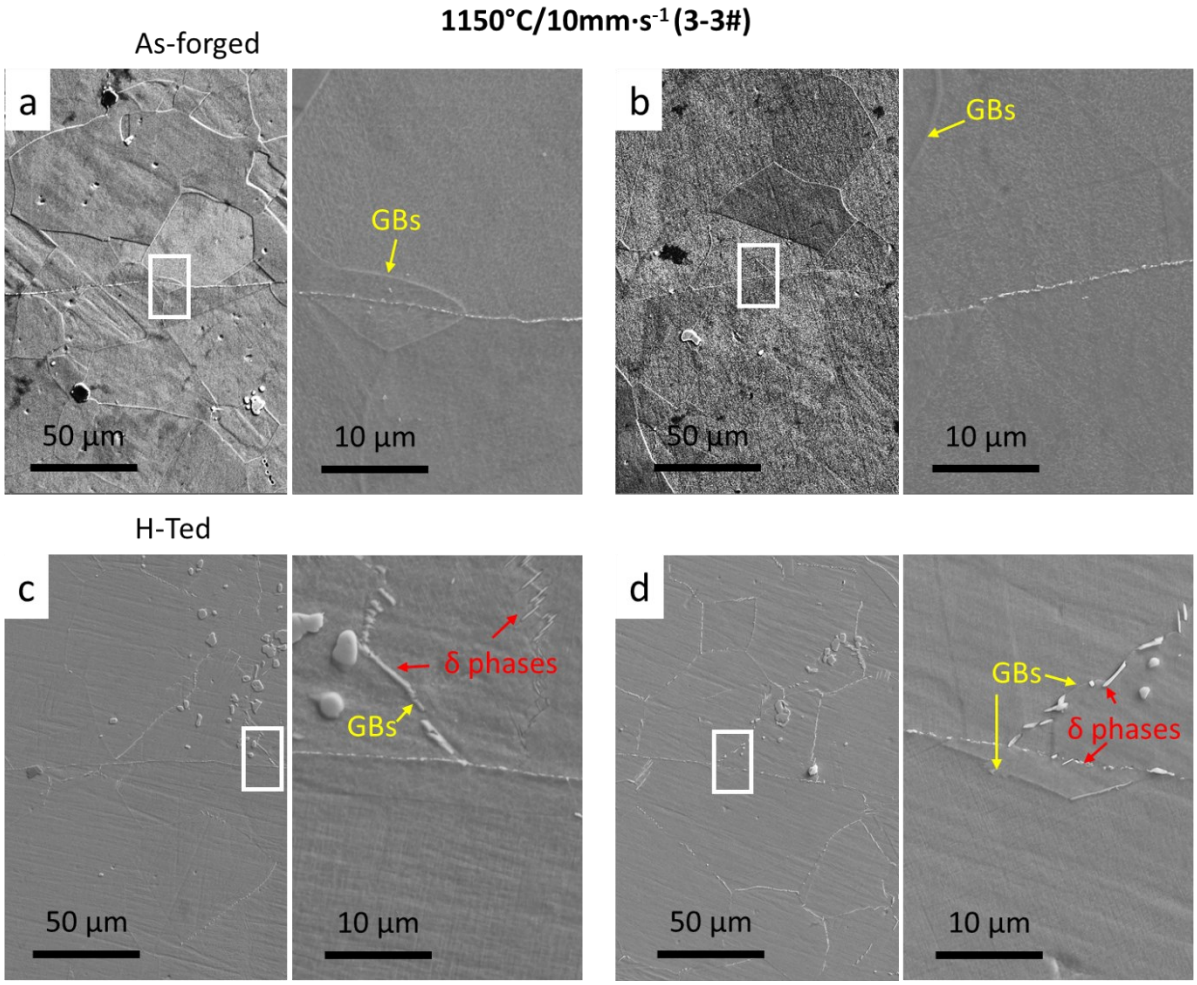


Figure 6-6 The interface microstructure at the centre and edge zone of the plate bonded at 1150 ˚C/10 mm·s^{-1}. a-b) as forged, c-d) after heat treatment.

At 1150 ˚C, similar interface microstructures are seen for the sample forged at a slower forging speed of 0.1 $mm \cdot s^{-1}$ (3-1#) and no δ phase is seen in the as-forged microstructure, except those larger grains are seen in Figure 6-7 (a-b) in the as-forged state. The grain grows given a lower strain rate. After heat treatment, the δ phase precipitates predominately at GBs, which is similar to its precipitation in the 3-3# plate. However, the grain's microstructure turns out to be mixed with large and small grains. No grain boundary migration is observed over the bond line. According to the EDS element analysis in Figure 6-8a, particles composed of M (Ti, Mo, Al)-oxides and carbides exist along the bond line. The oxides distribution uniformity in different areas (centre and edge) along the bond line shows no obvious difference. In the enlarged views in Figure 6-7 (a and b), compared with the centre zone, the oxide at the interface near the edge is more continuous.

After heat treatment, short rod-like δ phases precipitate at GBs. The δ phase size is smaller compared to 950 ˚C. As there is no grain boundary migration over the bond line, some δ phase can be seen on the bond line as well. Besides, some oxides exist on the bond interface. The EDS element analysis in Figure 6-8b indicates the precipitation of the δ phases (Ni3Nb) along the bond line in a short-rod shape (in framed area 3 and area 4). And these δ phases precipitated along the interface present no difference from that precipitated along grain boundaries.

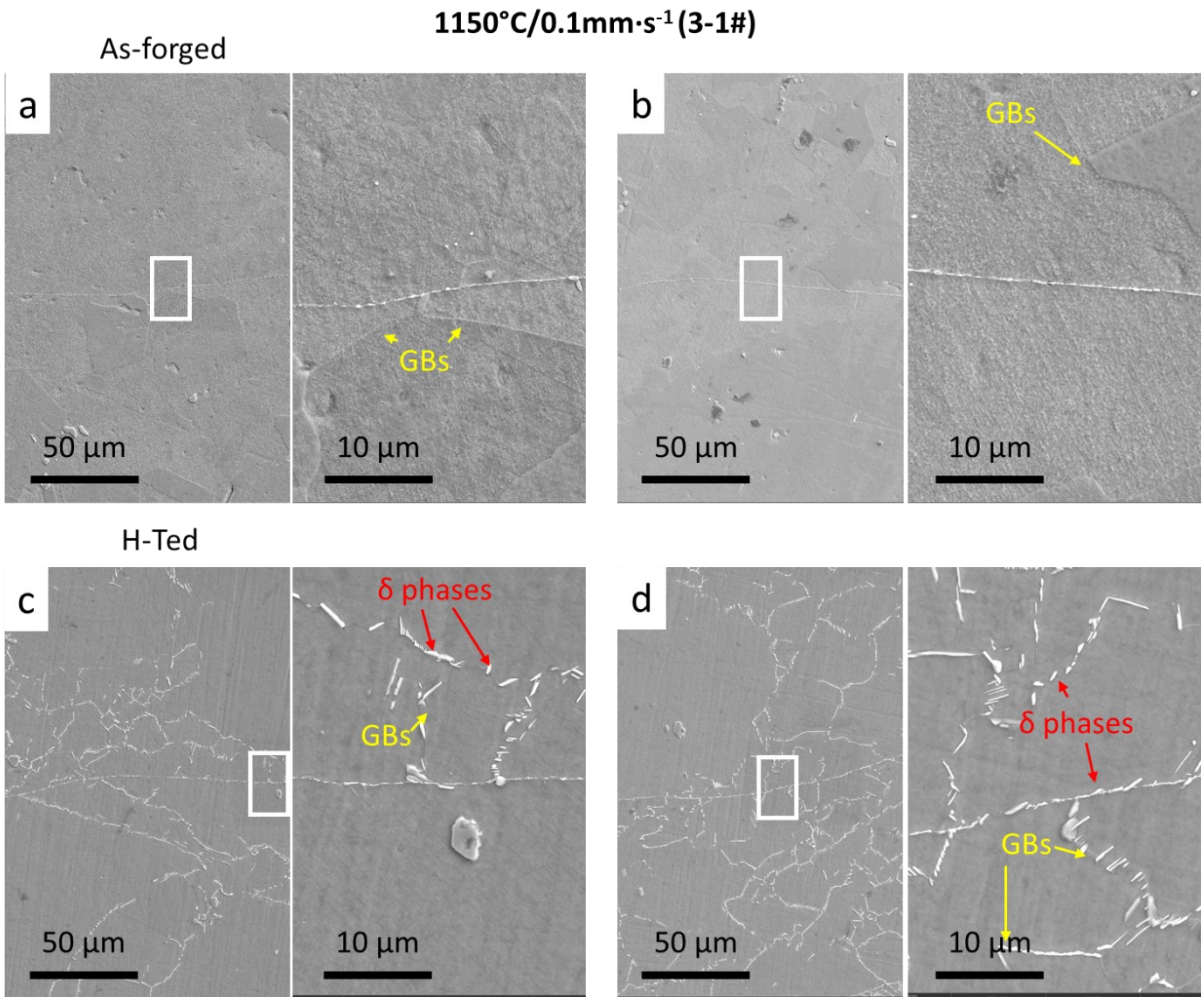


Figure 6-7 The interface microstructure at centre and edge zone of the plate bonded at 1150 ˚C/0.1 mm·s^{-1}. a-b) as forged, c-d) after heat treatment.

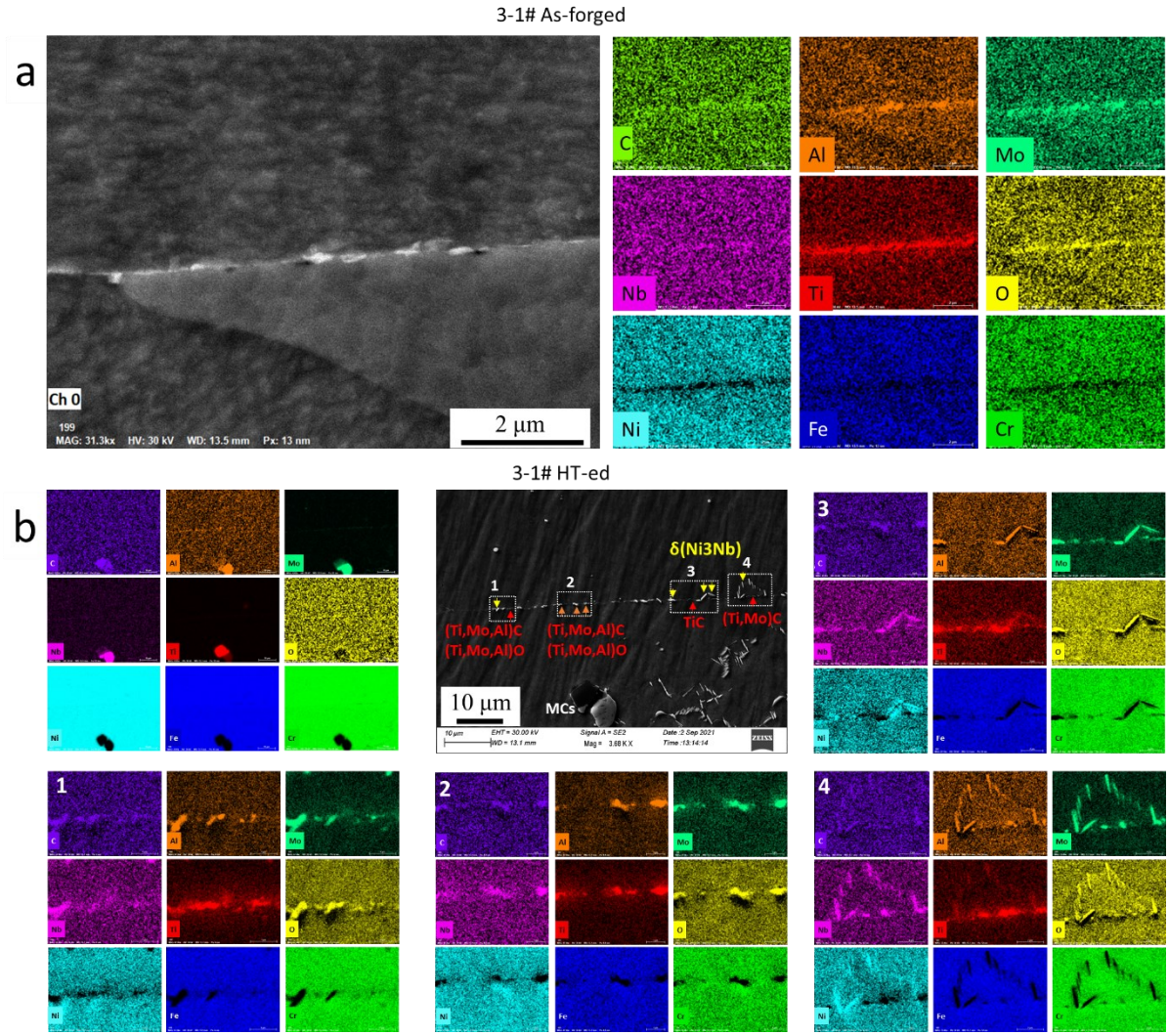


Figure 6-8 The interface microstructure and EDS mappings of the plate bonded at 1150 ˚C/0.1 mm·s^{-1} a) as forged, b) after heat treatment.

6.3 Discussion

6.3.1 The δ phase microstructure evolution at 950 ˚C

At a sub-δ-solvus temperature (950 ˚C), extensive δ phases stay after hot deformation, which is shown in Figure 6-1 and Figure 6-4. According to the Precipitation-Time-Temperature (PTT) diagram of different phases in IN718[239], long lath and acicular intragranular δ formed during heating and soaking, which was also seen in the as-received microstructure in [240] after soaking at 950 ˚C for 180 s and in other studies[241-243]. The δ phase precipitated in parallel clusters and intersected in different orientations in the interior of grains.

During the deformation at 950 ˚C, these long acicular δ phases disappear in the matrix and only remain near the interface in the centre zone. This is due to the adiabatic heating generated at fast deformation speed. The temperature rises over the δ-solvus temperature in the centre, the intragranular long acicular δ phases dissolve. As the phase interface energy between the δ phase and γ matrix is minimized at grain/sub-grain and twin boundaries, thereby, the δ phase tends to dissolve and present in a short rod shape. Near the interface, the dense network of long acicular δ phases within grains retain within the grains of the γ matrix and relatively short-length acicular δ precipitates at grain boundaries. As suggested in [244-246], the nucleation site for δ-precipitates is normally located where shows the high-density dislocation. From the enlarged view of the interface in Figure 6-6 and Figure 6-7, continuous precipitates exist along the interface, retarding the grain boundary migration and stopping the motion of dislocations. The hinder effect of the interface and accumulation of dislocation can also be observed in the study of [189, 195]. Dislocations accumulate and provide the energy needed for the transformation of δ from the γ matrix[247]. Thus, the intragranular acicular δ phase retains near the interface in the centre zone and the contrast due to the δ phase density between the interface and matrix can be seen. While near the edge, the local strain level is relatively low owing to the friction effect between the interaction of plates and dies. And in the meantime, surface heat loss inevitably occurs during the transfer from the furnace to the die and during forging due to the contact with the die, the temperature near the edge is lower and close to the temperature of maximum δ-precipitation (~950 ˚C) [239]. This is the expected reason for the globally high density of the δ phase in the edge zone. A less obvious contrast is seen between the interface and matrix due to the δ phase. After the deformation, breakage can be observed on the long lath and needle-shaped δ phase within grains. After the ageing treatment, more δ phases precipitate with a long acicular shape in the interior of grains and short rod-like continuously along the grain boundaries. The difference between the interface and matrix is globally reduced, as shown in Figure 6-1, which also follows the inspection of Figure 6-4.

Two types of δ-precipitate were found in the forged plate, which are intragranular long acicular and intergranular short rod-like. The stable δ phases precipitate incoherently from the matrix and the orthorhombic structure makes no significant contribution to strengthening[245]. However, as is studied in [248], the long acicular δ in parallel clusters in the matrix γ hardens the alloy and lows its ductility. In the as-forged plate, the specimen with a globally high density

of δ from the edge zone present both higher yield strength and ductility (in Figure 6-2 and Figure 6-3). While for the specimen from the centre, it presents a lower ductility even though with a lower δ phase fraction. This is due to the high density of intragranular acicular δ near the bonded interface causing stress-concentration at the interface. Since there is no interface grain boundary migration occurring, the bonded interface is still weak. The stress concentration on the inferior joint result in lower ductility in the centre zone. This also proves that the uniformity of the joint is critical to its integrity.

6.3.2 The bonding uniformity over forging bonded plates

The test results in 6.2.2 comprehensively present the tensile properties over the centre and edge zone of the forging joined plates. At each forging condition, the difference in the tensile strength in the centre (C-zone) and edge (E-zone) shows an identical trend with that in the elongation. Higher tensile strength corresponds to a higher elongation. Thus, the uniformity of the plates, which can be reflected by the difference either in strength or elongation, can be categorized into three types referred to as the forging conditions. a). The first one is shown under the condition of 950 ˚C/0.1 s^{-1}, for which the E-zone has higher elongation and strength than the C-zone. Based on the observation in 6.2.1, at the temperature near the δ-solvus point, the obtained microstructure is sensitive to the temperature drop during forging. The lower temperature in E-zone leads to a higher δ density and higher strength. As explained in 6.3.1, a higher δ density is shown near bonding interfaces. Therefore, the overall higher δ density at the interface and base make the microstructure near E-zone more uniform, and a higher elongation is shown for E-zone than C-zone. b). The second category is seen for conditions with high temperature and high forging speed (1050 ˚C/0.1 s^{-1} and 1150 ˚C/0.1 s^{-1}) and the tensile performance over the C-zone and E-zone are uniform. This is supported by the microstructure observation in 6.2.1. At a temperature higher than δ-solvus, the microstructure is not sensitive to temperature drop. Similar and uniform microstructures are seen over C-zone and E-zone. c). On the contrary, at higher temperatures with a lower forging speed (1150 ˚C/0.01 s^{-1} and 1150 ˚C/0.001 s^{-1}), although no obvious difference is seen between C-zone and E-zone, as presented in the picture of final forged plates in Figure 3-5, slight buckling was seen for the plates and there was relative sliding movement between the layers. A severer deformation was seen in the middle layer and this non-uniform deformation and relative sliding movement near E-zone would affect the uniformity of joints.

6.3.3 Comparison with Gleeble bonding and Optimization of properties

The results of the forge bonded specimen is compared with the Gleeble bonded bar samples at equivalent conditions. To exclude δ phase effect, the condition (1150 ˚C, 10 mm·s^{-1}) is chosen to be compared with the bar sample test results in Chapter 4 (1150 ˚C, 0.1 s^{-1}). In Figure 6-3, the tensile results of Gleeble bonded samples after same standard heat treatment are also shown with star markers. It is shown that at similar deformation conditions, the tensile properties of bar samples are higher than plate results.

To explain the difference, the forging process of the multi-layer plate is simulated using QForm with the developed bond-quality-predicting model implemented. The predicted relative bond quality ratio is shown in Figure 6-9, and low relative bond quality (bond ratio ~ 0.5) is seen along the interface at different investigated locations. Also, the simulated radial strain at the interface is shown as well. Comparing the simulated radial strain level at the interface of the multi-layer plate to the Gleeble compressed bar sample at the same temperature and strain rate (1150 ˚C, 10 mm·s^{-1}), the 50% compressed plate sample shows equivalent stress-strain condition with the bar sample compressed at 30%. At this strain level, the oxide film still remains continuous, which is consistent with the microstructural characterization in Section 4.2. According to the proposed four-stage bonding mechanism in the previous Chapter 4, the cohesion between the oxide and oxide, oxide and metal is the dominating bonding mechanism at this stage (stage-II).

According to the solid-state bonding mechanism and model discussed in previous chapters, a higher height reduction will be needed to achieve high bond quality. The grain boundary migration over the interface is necessary to eliminate the effect of the remaining contaminates and recover the full bond strength. Further investigation will be needed to verify the effect of strain on the final bond quality, however, in this thesis, due to the interruption caused by the COVID pandemic, it has not been conducted here. Nevertheless, the high accuracy of the developed bonding model has been confirmed and demonstrated in a practical forming bonding process.

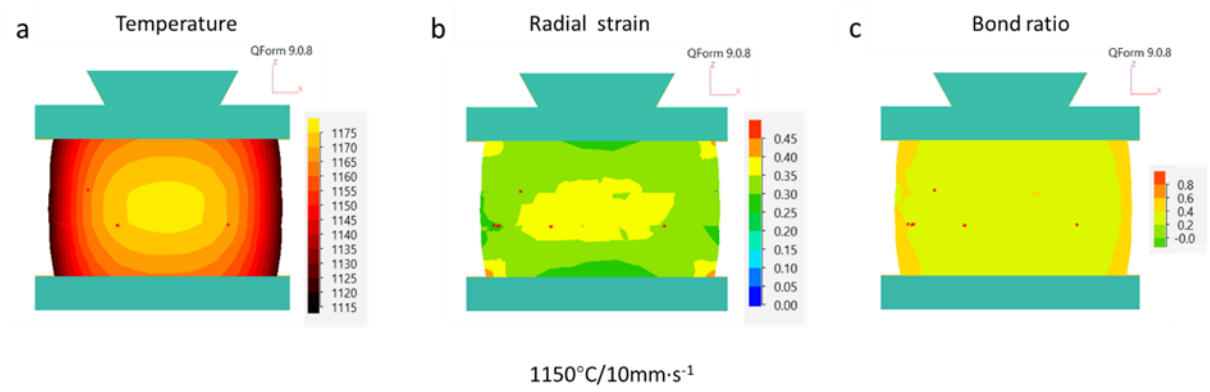


Figure 6-9 The simulated a) temperature, b) radial strain, c) bond ratio, results of the three-layer-built plate forged at 1150 ˚C, 10 mm·s^{-1}.

6.4 Conclusions

In this work, a new construction concept is proposed based on the forge bonding method. Three layers of IN718 plate were piled up and forged under practical forging conditions. The bonding interface behaviour and microstructure evolution from different locations of the plates were investigated. The thermal-mechanical properties of built plates were evaluated and compared with commercial standards for IN718.

1. Under the investigated conditions: a temperature range of 950-1150 ˚C, strain rate range of 0.001-0.1 s^{-1}, with an encapsulated atmosphere of 10^{-3} Pa, and is compressed to an overall height reduction of 50%, a straight bond line can be observed. After standard ageing treatment, the bond line remains and δ phases precipitate along grain boundaries and the interfaces.
2. At 950 ˚C with a high forging speed of 10 mm·s^{-1}, a higher density of long needle-like δ phases precipitates within grains due to the high density of dislocation blocked by the interface. And also, the uniform temperature distribution also imposes an effect on the microstructure at 950 ˚C: lower temperature near the edge leads to more δ phase precipitating in the matrix, thus presenting a relatively more uniform microstructure over the matrix and interface. A higher ductility is seen for the sample taken from the edge zone, which indicates the uniform joint microstructure is beneficial for achieving higher structural integrity.

3. Due to the mediate local strain level at an overall 50% compression and observed residual oxides and carbides, no interface boundary migration is observed at five investigated forging conditions. After standard heat treatment for IN718, the plates forged at 1150 ˚C (both at 10 $mm \cdot s^{-1}$ and 0.1 $mm \cdot s^{-1}$) show better tensile properties at room and high temperatures. Their yielding strength and ultimate tensile strength are comparable to wrought standards, while the ductility barely achieves a PM level.
4. Based on the bond mechanism proposed in the previous Chapter 4, a higher strain is needed in order to achieve a good bond quality. The effects of remaining interface oxides and carbides are to be eliminated by interface grain boundary migration.

Chapter 7 Role investigation of interface GB migration in the bonding with typical interfaces

7.1 Introduction

As reviewed in Chapter 2, in previous studies solid-state bonding, the importance of interface grain boundary migration and grain growth was stated in diffusion bonding[138, 147] and hot compression bonding[190, 193, 194, 196, 197].

The characterization evidence in diffusion bonded Al7075 clearly showed that local migration of interface boundaries led to the formation of triple point junctions between grains across the interface and the removal of the initial bond line, which guaranteed a high bond strength[138]. In hot compression under higher strain, the high temperature and plastic deformation provide higher stored energy, thus the interface grain boundary migration occurs more easily with the proceeding of dynamic recrystallization. This was observed in copper[190], nickel alloy[196, 197] and steels[193, 194]. The conducted tensile results also showed an increasing trend in the resulting tensile strength with the degree of interface grain boundary bulging and migration. For nickel superalloys, the complete migration occurred at a temperature of 1100 ˚C and a strain of 0.5, and when the temperature was increased to 1150 ˚C, the required strain level was reduced to 0.2 [196]. However, at the same strain level, the final tensile strength reduced slightly with the temperature increase, although the ductility of joints was improved, due to the overall grain growth at higher temperatures.

Also, based on the results presented in Chapter 4, with a complete interface grain boundary migration at 50% height reduction, full strength was obtained comparable to reference. As was explained in Chapter 4 and Chapter 5, it was believed that the interface grain boundary migration helped eliminate the original bond line and ensure good bond quality. However, both in the previously published work and in the work present here, the interface grain boundary migration occurred with other processes, oxide film fracture for example. The oxidation issue, although can be controlled, is quite tricky to be completely avoided on the bonded surface due to the existence of active elements, like aluminium, which can form stable oxides. Therefore, when evaluating the dominance of the interface grain boundary migration in determining the joint quality, the other factors, like oxide, micro-voids and microstructure change, should be carefully excluded.

Furthermore, although there is evidence confirming the positive correlation between the joint quality and the interface grain boundary migration ratio. The failure mechanism behind it has rarely been investigated. In this chapter, pure aluminium bi-crystal samples were used to study the effect of grain boundary inclination on tensile behaviour. In these bi-crystal samples, the incoherent pure grain boundaries existed with different angles to the tensile load and the tensile properties will be compared to their single-crystal counterparts. Moreover, polycrystalline nickel was also adopted to study the interface grain boundary migration effect in its tensile properties. Due to the dissolubility of nickel oxide at high temperatures in a vacuum, bond interfaces can be obtained free from oxides. By controlling the condition, typical interfaces with/without interface grain boundary migration were prepared and used to compare with references.

Structure of the chapter: Interface microstructure, as well as tensile tests with two types of interfaces (primary grain boundary, bonded interface grain boundaries), will be presented for Al bi-crystals and polycrystal Ni samples with references, separately in Result Section 7.2 and 7.3. The role of the grain boundaries in samples with a different number of grains will be elaborated on in the Discussion Section.

7.2 The tensile properties of Al samples

7.2.1 The grain structures

The EBSD IPF colouring maps of four Al samples were taken from different locations (shown in Figure 3-7) of the ingot. As shown in Figure 7-1, for Al-1 and Al-4, the samples are single crystals (G-1 for Al-1, G-2 for Al-4), while Al-2 and Al-3 are bi-crystals that are composed of these two single crystals of A1-1 and Al-4. And the grain boundaries are in different angles with the tensile direction: the grain boundary in Al-2 is roughly vertical to tensile load and the angle is around 45^{o} in Al-3. As shown in the IPF colouring and the corresponding orientation unit cell, Al-1 and the upper part of Al-2 and Al-3 have the same orientation (G-1), and Al-4 has the same orientation with the lower part of Al-2 and Al-3 (G-2).

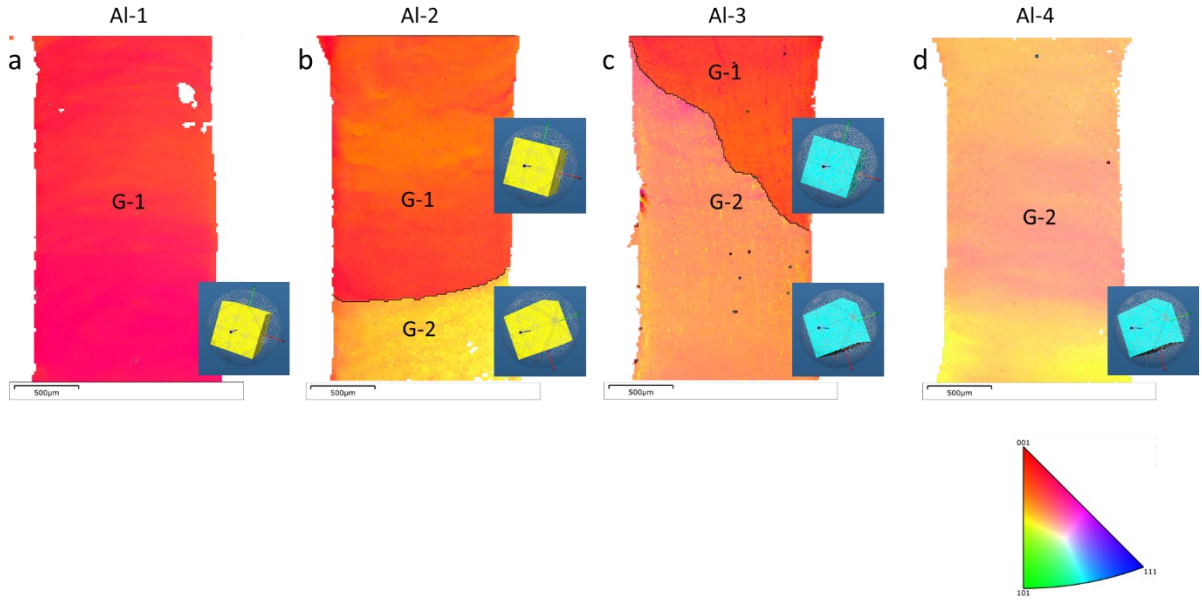


Figure 7-1 The EBSD IPF colouring maps showing the grain microstructure of pure aluminium samples, (a) Al-1, the single crystal sample with Grain G-1; (b) Al-2, the bi-crystal sample with vertical grain boundary; (c) Al-3, the bi-crystal sample with inclined grain boundary; (d) Al-4, the single crystal sample with Grain G-2.

7.2.2 The tensile results for Al samples

Correspondingly, the tensile stress-strain curves of the four Al samples are given in Figure 7-2, and the data from repeatability tests are shown in Table 7-1. The pure Al samples all present generally low tensile strength. In comparison, Al-1 has the lowest yielding strength and ultimate tensile strength, and its ductility is similar to the other single-crystal sample Al-4. The highest yielding strength and ultimate tensile strength are seen in bi-crystal sample Al-2, whilst presenting the lowest ductility, less than 1.0. Besides, the bi-crystal Al-3 sample with a tilted grain boundary shows a similar tensile performance to the single-crystal sample Al-4.

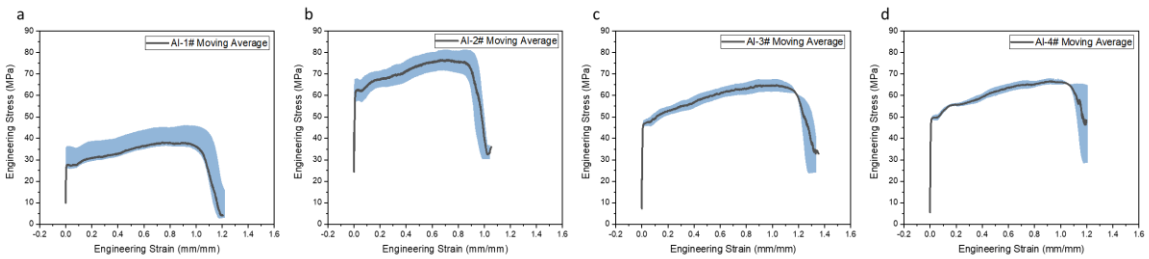


Figure 7-2 The tensile curves of pure aluminium samples: a) Al-1; b) Al-2; c) Al-3; d) Al-4.

Table 7-1 The tensile test results for pure aluminium samples

Sample	Yielding strength, MPa	Ultimate Tensile Strength, MPa	Ductility, mm/mm
Al-1	37, 27	45, 35	1.1, 1.05
Al-2	68, 58	81, 71	0.9, 0.85
Al-3	48, 46	68, 62	1.1, 1.2
Al-4	50, 48	68, 65	1.05, 1.2

The fractured Al samples are shown in Figure 7-3 and all of them present ductile fracture features with obvious necking prior to fracture. For single-crystal Al-1 and Al-4, the samples fracture at a random position in the gauge area and the fracture surface are relatively flat and perpendicular to the tensile loading direction. From the OM images, slip systems can be easily observed and they are indicated with orange lines. In grain G-1, only one main direction of slip systems is seen. Two slipping directions are observed from OM images of grain G-2, and the main direction is marked with a thicker orange line. These observed slipping systems are in accordance with the calculated results shown in Figure 7-3 (a_2-d_2), in which the blue lines indicate the trace of the slip plane and red arrows show the slip direction. According to the Schmid factor, it shows a higher Schmid factor in grain G-2 indicates a higher resolved shear stress, thus different directions of the slip system may be activated. The simultaneous activation of slip systems helps coordinate the deformation and improve the ductility, thus Al-4 shows a good ductility, as well as the Ni-3 sample containing grain G-2. While the good ductility of sample Al-1 can also be due to there being no grain boundary inhibiting the dislocation movement during plastic deformation.

For Al-1 and Al-4, the fracture surface intersects with the slipping direction. As for the bi-crystal samples, neither of the fractures occurs along the grain boundary and no crack is seen along either GBs. For Al-2 and Al-3, the fracture points are both located in grain G-2. However, the fracture position in Al-2 is near the grain boundary, while the fracture position in Al-3 is far away from the inclined grain boundary.

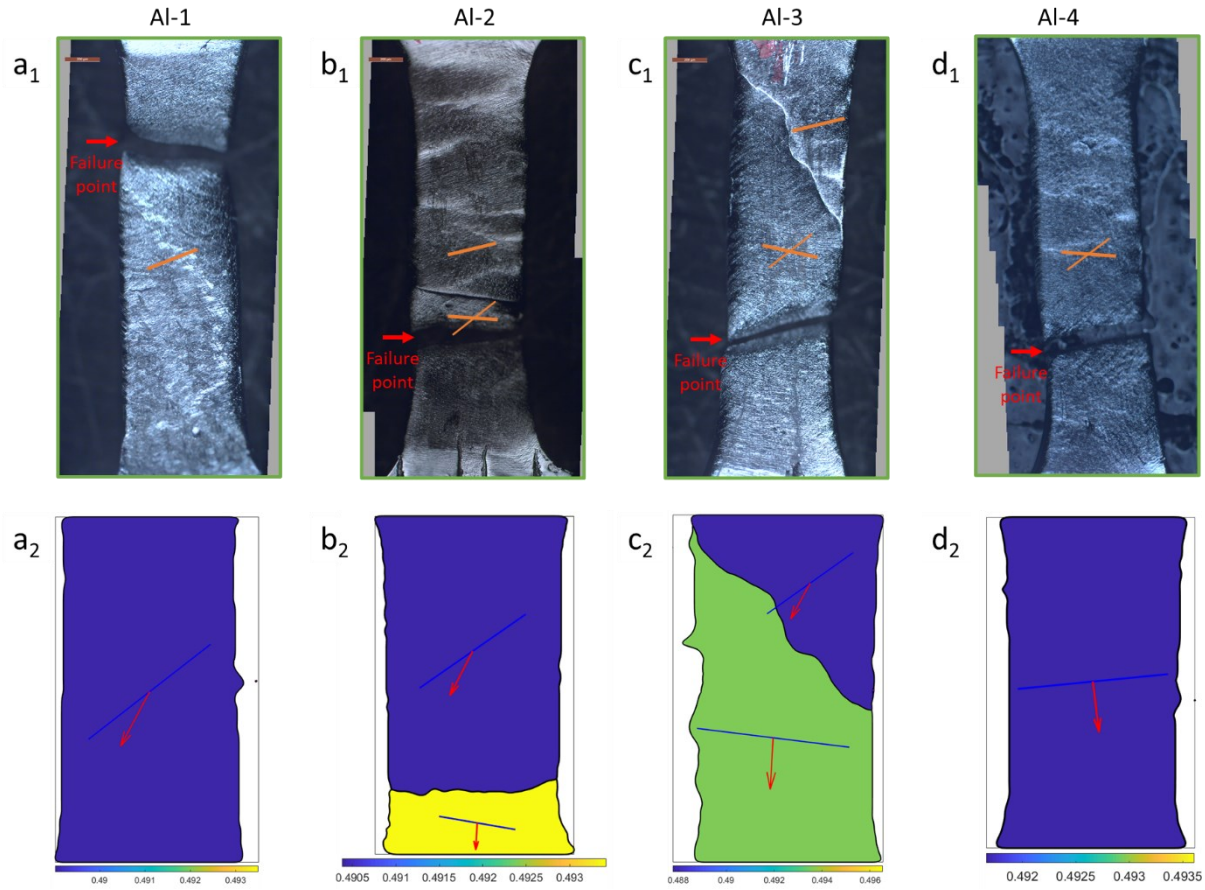


Figure 7-3 (a_1-d_1) The fracture aluminium samples and (a_2-d_2) the corresponding Schmid Factor calculation. (a) Al-1; (b) Al-2; (c) Al-3; (d) Al-4, note: blue line shows the slip plane and red arrow line in (a_2-d_2) indicates the sliding direction.

For each Al sample, they were being stretched to the same mild strain (28%) and the OM and enlarged SEM images of selected areas are also shown in Figure 7-4. The slipping systems are identical correspondingly to that observed in the fractured samples. At a lower strain, only the main slip system was activated in grain G-2. In order to study the plastic deformation behaviour in grains with different grain boundary inclinations, the dislocation density was measured with the EBSD method and visualized as GND maps in Figure 7-4 (a_3-d_3). According to Figure 7-4 (a_3 and d_3), it presents quite low GND in the single-crystal sample (Al-1 and Al-4), and in bi-crystal samples of Al-2 and Al-3, the GND near the grain boundary is shown to be higher than inner grains. And in comparison, the GND near grain boundary in Al-2 is similarly higher with Al-3 with a tilted grain boundary. The accumulation of dislocation near the grain boundary may explain the failure in Al-2 near the grain boundary. While in Al-3, the accumulated dislocation is aligned in angle with the tensile stress and the resolved stress along the vertical

direction to the grain boundary is less than the stress applied, thus presenting better ductility but lower yield strength.

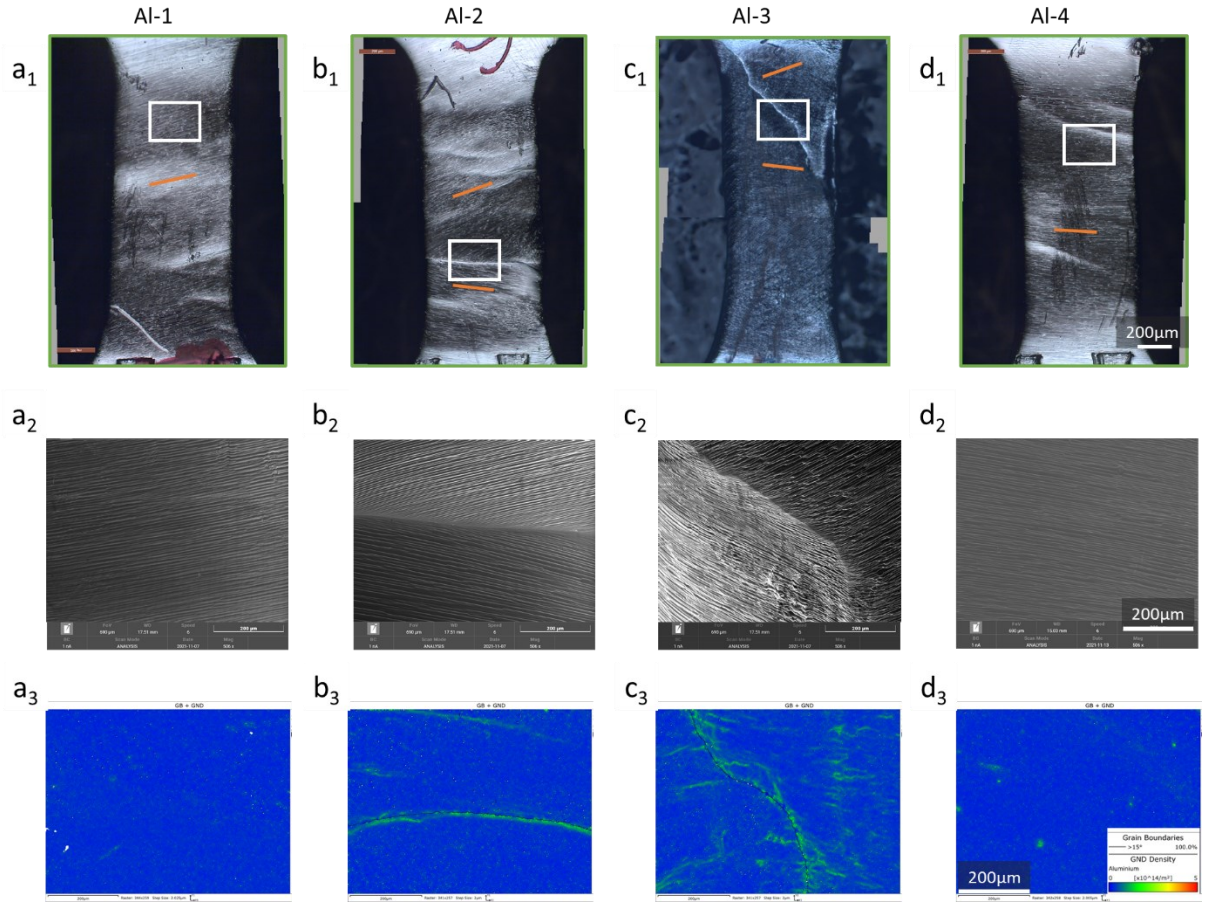


Figure 7-4 (a_1-d_1) The interrupted tensile pure aluminium samples, (a_2-d_2) SEM morphology images near the grain boundary and (a_3-d_3) corresponding GND maps from EBSD measurement.

7.3 The tensile properties of bonded polycrystalline pure nickel joints

7.3.1 The microstructure of nickel joints

Figure 7-5 gives the EBSD inverse pole figure mapping of the gauge area of pure nickel samples joined under diffusion bonding conditions. For Ni-1 (Figure 7-5a), a straight line can be seen in the near middle of the gauge, given a low force and short duration applied for bonding. This bonding line is composed of unmigrated interface grain boundaries, which are presented in co-planar. As a reference, the grain microstructure of Ni-2 is shown in Figure 7-5b, which contains no bonding interface. Both samples show similar microstructure with equiaxed grains, and their grain size distribution is shown in Figure 7-5c. Ni-1 and Ni-2 are with a similar

average grain size of 67.1 and 63.4 μm, respectively. The corresponding pole figures indicate grains are randomly oriented and no strong texture exist in the joint. Therefore, since Ni-2 has a very similar microstructure to Ni-1 except for the straight bond line, it is reasonable to use Ni-2 as a reference to investigate the unmigrated interface grain boundary migration in the bond quality.

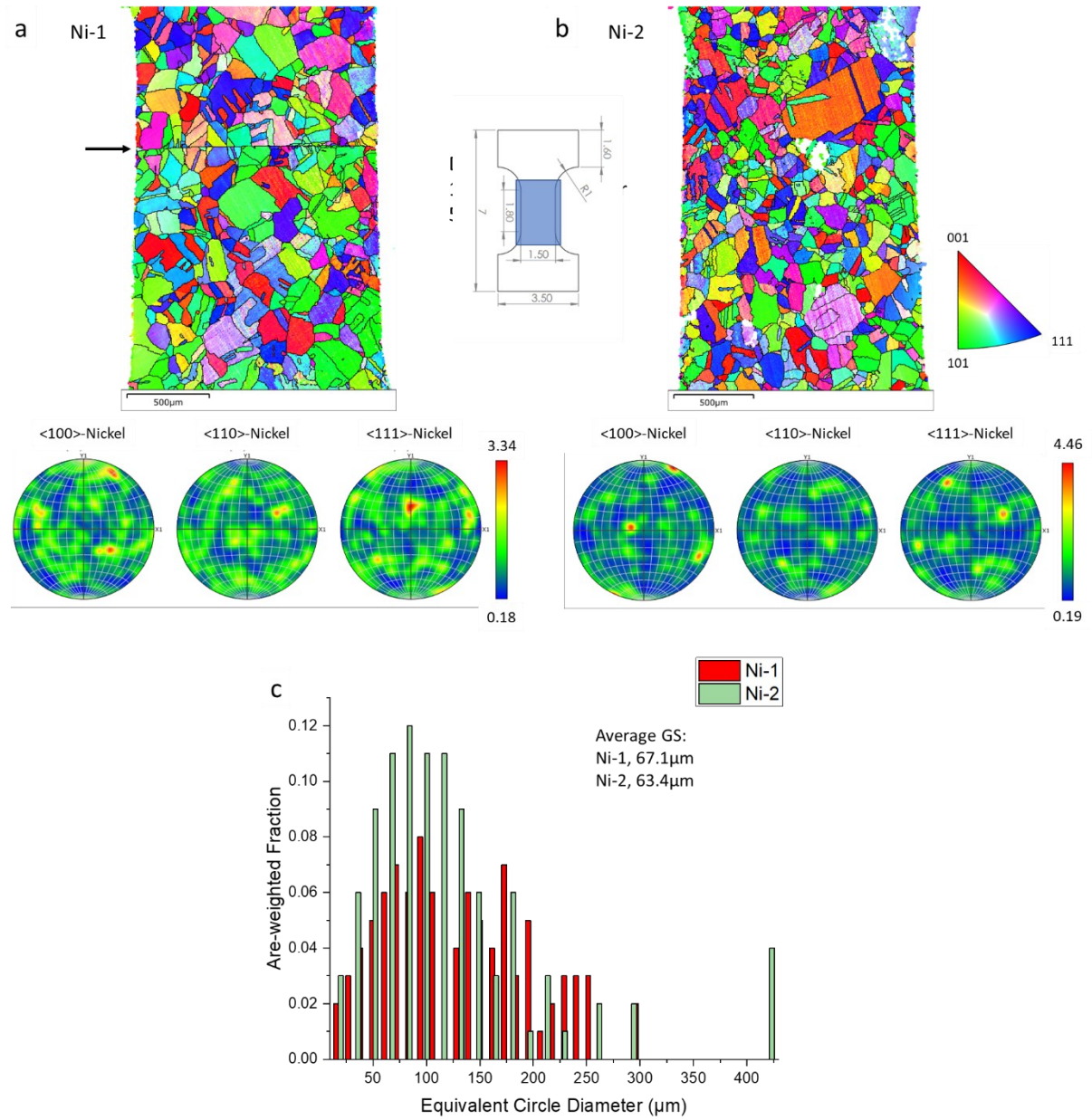


Figure 7-5 The IPF colouring maps of polycrystalline pure nickel samples, (a) Ni-1, (b) Ni-2; and (c)the grain size distribution of Ni-1 and Ni-2.

An enlarged view of the straight bond line is shown in Figure 7-6. Along the interface, most of the grain boundaries remain coplanar, as the enlarged EBSD orientation colouring map shown in Figure 7-5b. In some certain triple joints, some small grains appear. In an enlarged view of the area near the right edge, more fine grains are observed along the interface at triple-joints in Figure 7-5c. Since at diffusion bonding condition with minor strain, the deformation over the joint is uniform, which can also seem from the deformed shape of the joint. Variation in the strains along the interface is negligible. The appearance of these fine grains may be related to the misorientation of the adjacent grains over the bond line. Considering the size of these newly formed grains are much smaller, the over interface grain boundaries remain straight and unmigrated, vertical to the tensile direction.

In Figure 7-5d, the SEM images of the diffusion bonded interface are provided. The interface area is marked with white narrow and dash lines. Along the interface, no oxide film or oxide fragments can be seen, except for several micro-pores observed nearby. Interface micro-voids are typical defects for uncomplete diffusion bonded joints, as the closure of these voids requires a long duration for atom diffusion and creep deformation[142, 159]. In this investigation, diffusion bonded pure-Ni sample joint, these micro-voids with a dimension less than 1 μm and a small amount can be neglected compared to that observed in [209]. Without oxide film and continuous large voids along the interface, the diffusion bonded joint is regarded composed of a group of in-coplanar unmigrated grain boundaries, and these interface grain boundaries formed from the bonded surface are identical to inherent grain boundaries.

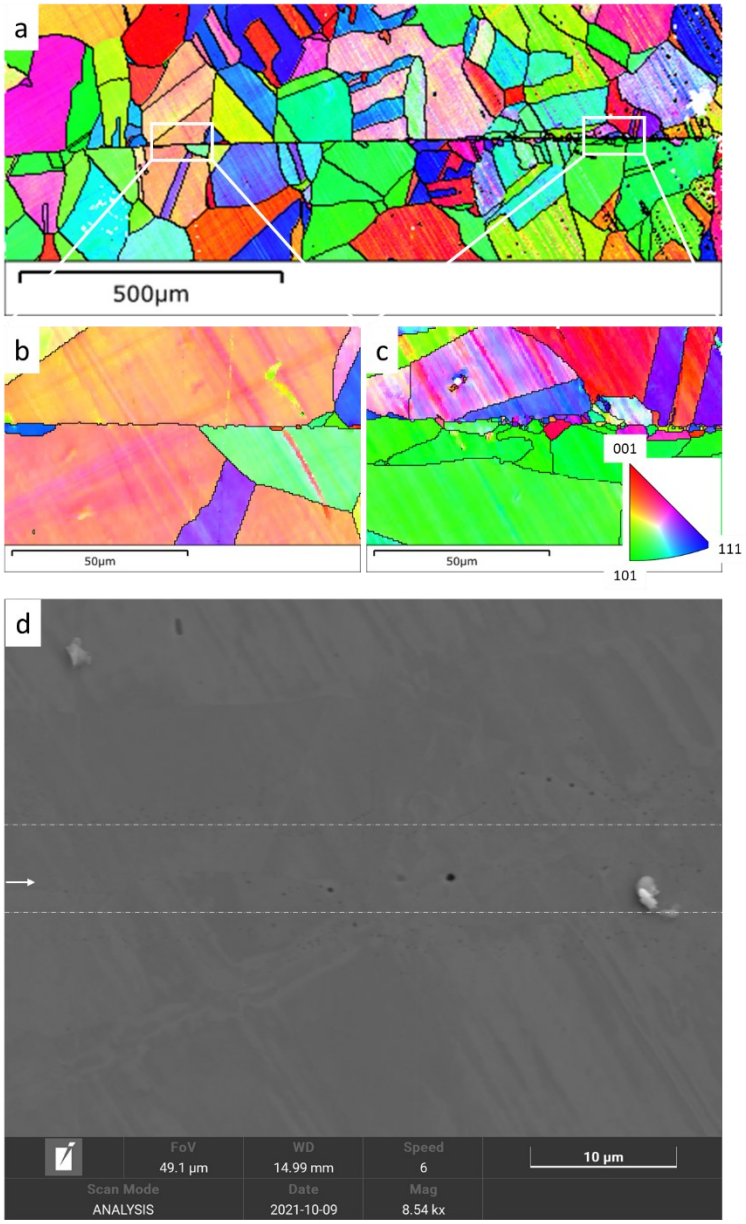


Figure 7-6 (a-c) Enlarged view of the grain microstructure near the diffusion bonded interface in Ni-1 sample and (d) the SEM image.

The EBSD orientation maps of hot compress bonded pure nickel joint in the gauge area are shown in Figure 7-7. Ni-3 sample was taken vertically to the bond interface and the Ni-4 sample was taken parallel as reference. They both show similar microstructure with random-oriented equiaxed grains, and the average grain size is 74.1 μm for Ni-3 and 74.8 μm for Ni-4. Their grain sizes follow the identical distribution. Under higher-strain (50%) compression, interface grain boundary migration proceeds completely over the initial bonding interface, which was

also present in the hot compression bonding studies of other materials[190, 194, 196]. Thus, no straight bond line is seen in Ni-3.

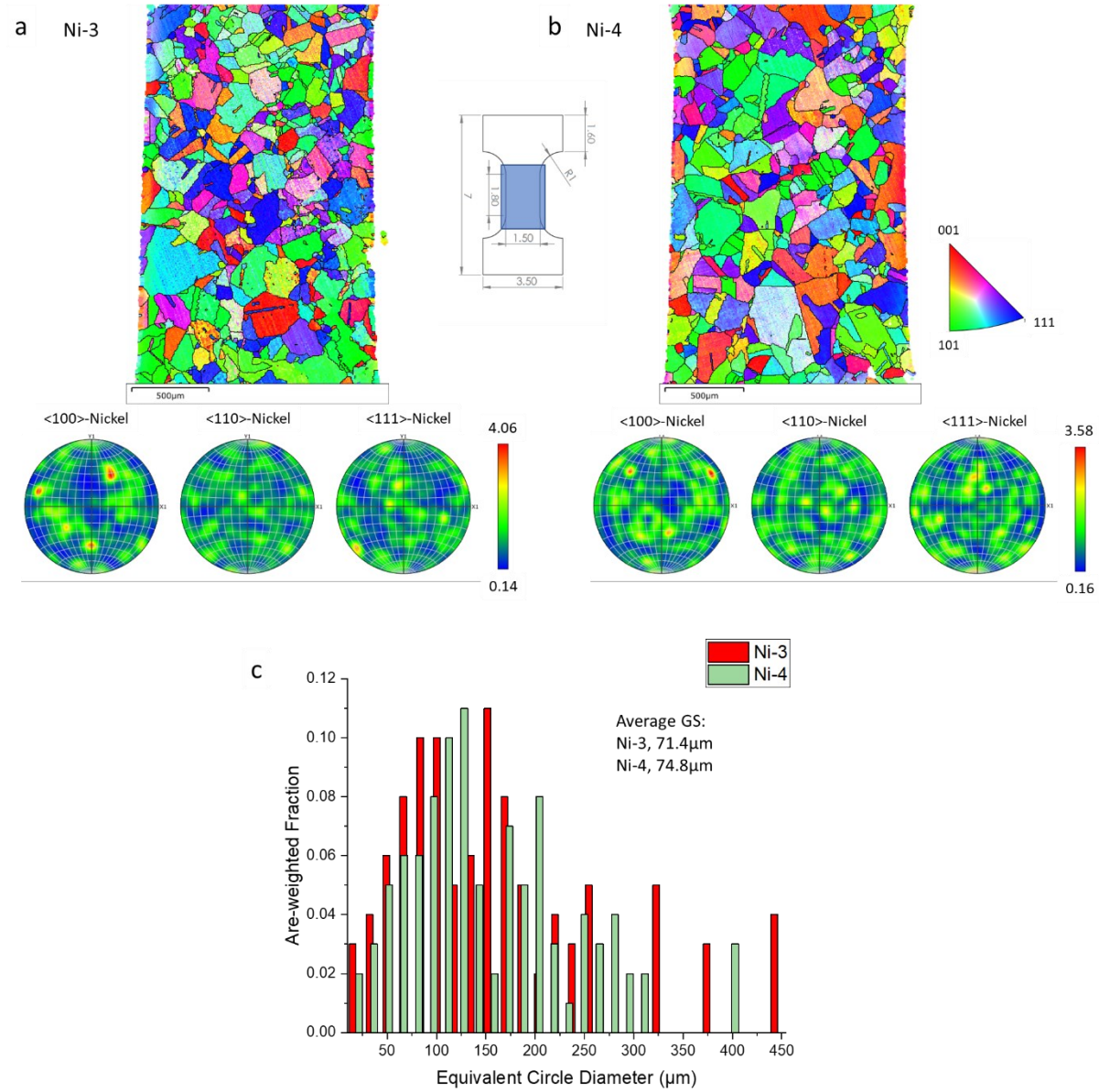


Figure 7-7 The IPF colouring maps of polycrystalline pure nickel samples, (a) Ni-3, (b) Ni-4; and (c)the grain size distribution of Ni-3 and Ni-4.

The SEM images in Figure 7-8 presents the interface zone of the compress bonded joint from Ni-3. Neither oxide nor continuous/semi-continuous micro voids are observed near the interface.

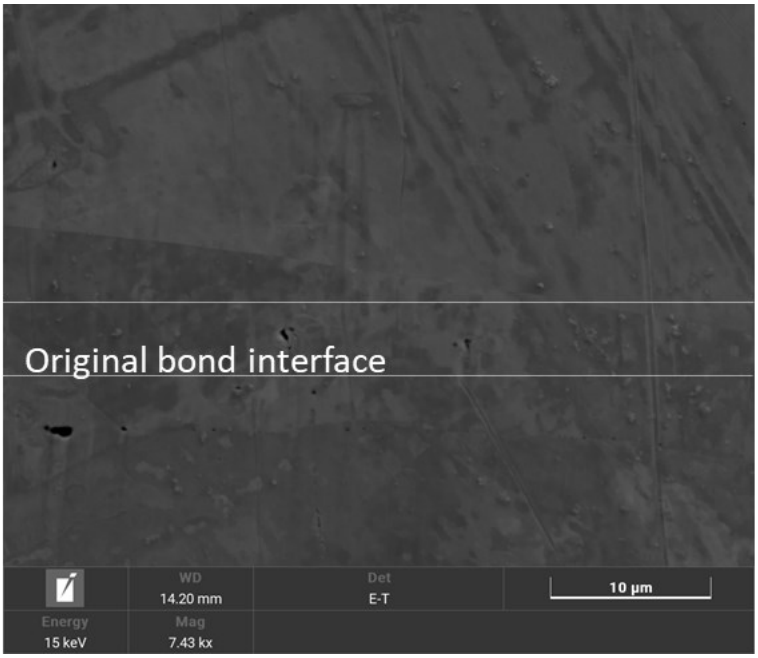


Figure 7-8 The SEM image of Ni-4 near the bonded interface.

7.3.2 The tensile test results for nickel joints

The tensile stress-strain curves for pure nickel joints bonded under different conditions and the references without bonding interface are present in Figure 7-9. For the diffusion bonded joint, Ni-1 reveals a similar stress response under tensile with the reference Ni-2, as shown in Figure 7-9a. Both show a yield strength of ~100 MPa , 100% ductility and ultimate tensile strength of 420 MPa . The identical yielding behaviour confirms the identical microstructure for Ni-1 and Ni-2. The similarity in the tensile properties for Ni-1 and Ni-2 indicates that, although the bond line remains straight with unmigrated interface grain boundaries in coplanar under short-time diffusion bonding, the joint still could present high ductility and high tensile strength. The role of the interface grain boundary migration might be less determining than that shown in the solid-state bonding of IN718 in Chapter 4.

For the compress bonded joint, Ni-3, as shown in Figure 7-7, the interface grain migration fully occurs and no straight bond line can be seen. From the tensile stress-strain curves in Figure 7-9b, similar tensile properties are observed for the bonded samples, Ni-3, and the reference sample, Ni-4. As the microstructure of both is of no obvious difference, they present identical yielding strength (~100 MPa), similar ductility (100%) and ultimate tensile strength (400 MPa). Since the grain size of the compress bonded sample (~70 μm) is slightly larger than that

bonded under diffusion condition (~65 μm), there is no difference in their tensile properties. Under compression, the complete interface grain boundary migration over the bond line ensures the bond quality is as good as the reference.

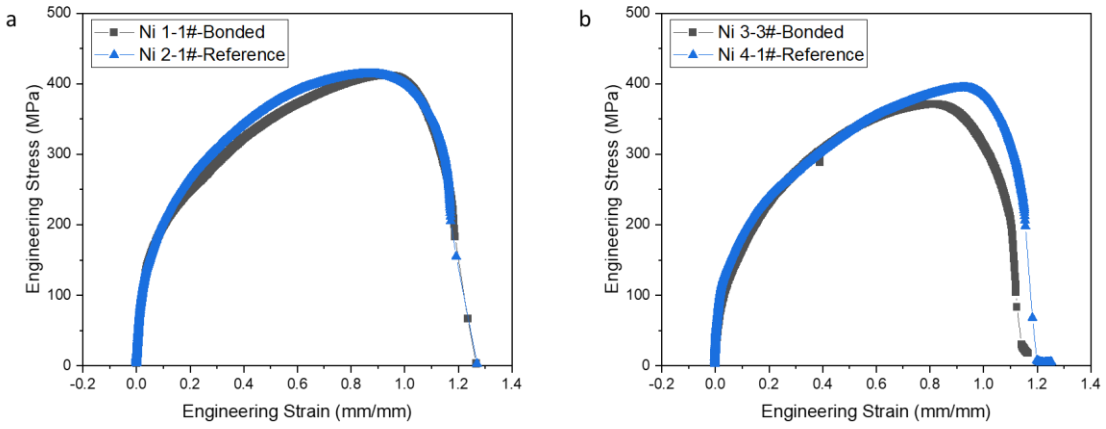


Figure 7-9 The tensile curves of polycrystalline pure nickel samples, a) diffusion bonded Ni, b) compress bonded Ni.

In Figure 7-10, the SEM images of the micro-test tensile samples gauge area are given in Figure 7-10 (a_1-d_1), the straight bond line in Ni-1 can be seen as the white arrow marks. No bond interface or bond line is observed in three other samples. The OM images of the four fractured samples are shown in Figure 7-10 (a_2-d_2), respectively below the SEM images. All four pure nickel samples present ductile fracture features with elongated gauges and wavy fracture surface curves. Necking occurs to all, and the necking points are randomly located within the gauge length. In Figure 7-10a_2, the deformed area, where marked as the original straight bond line, is framed. The bond line is away from the necking and fracture position, which indicates that the bonded interface with no grain boundary migrating over is not a weak point for the joint. The interface which is composed of coplanar grain boundaries is as strong as other inherent grain boundaries.

The enlarged view characterized by OM of the original straight bond line and after deformation is provided in Figure 7-10 (a_3 and a_4). This is the same sample that was characterized using EBSD in Figure 7-6, which also is shown in Figure 7-10a_4. For comparison, a representative grain was marked in strips in the EBSD map, G-o, and the identical same grain after deformation is highlighted in green, G-d. Comparing the same grain before and after

deformation, the original grain boundary of G-o along the straight bond line is turning curved in G-d after deformation, as the red arrows mark. This straight grain boundary turning curved is also observed. After deformation, the original straight bond line remains relatively straight, except for these bulging areas where red arrows point. The results of the coplanar grain boundaries doing no particular harm to the joint performance could be due to the bulging evolution of the original straight grain boundaries.

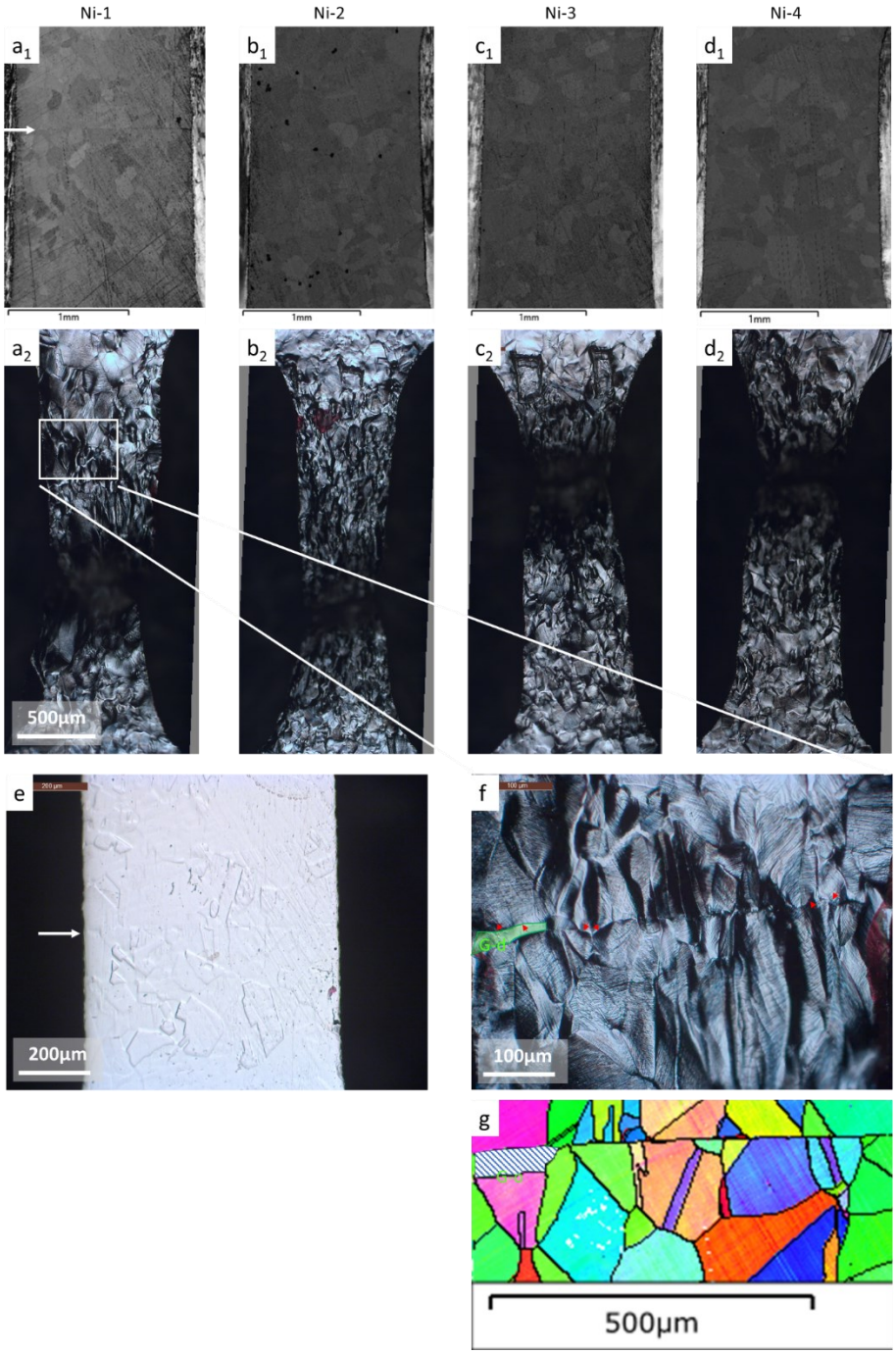


Figure 7-10 (a_1-d_1) The SEM images of Ni samples before the tensile test; (a_2-d_2) the OM images of fractured Ni samples after tensile test; (e) the OM image of diffusion bonded Ni sample, Ni-1, white narrow marks the interface; (f) the OM image of the interface area of Ni-1 after tensile test and its corresponding EBSD IPF colouring map.

In order to observe the interface evolution, the tensile test on a new Ni-1 specimen (with a straight bonding line) was conducted under OM. Pictures were taken at an interval of 0.25 mm

stroke change and are presented in Figure 7-11. The original straight bond line is marked. With the increase of the tensile strain, slip lines are getting clearer within each grain. For grains with different orientations, slip systems with different directions are activated at different stages of deformation, which depends on the Schmid factor. When the sample is stretched to 3.25 mm, severe deformation is seen in a big grain (red arrow). Besides, coordination deformation occurs among adjacent grains and the shape of each grain may change (for example, a deformed twining grain marked in a green frame). The grains along the interface deform in the same behaviour as other grains in the matrix, as the grains circled in yellow. With the coordination deformation, the grain boundaries which were originally along the interface may be deformed to change their shape and orientation. Finally, the necking occurs where the large grain with severe deformation is located. No crack initiation is seen along the unmigrated interface grain boundaries.

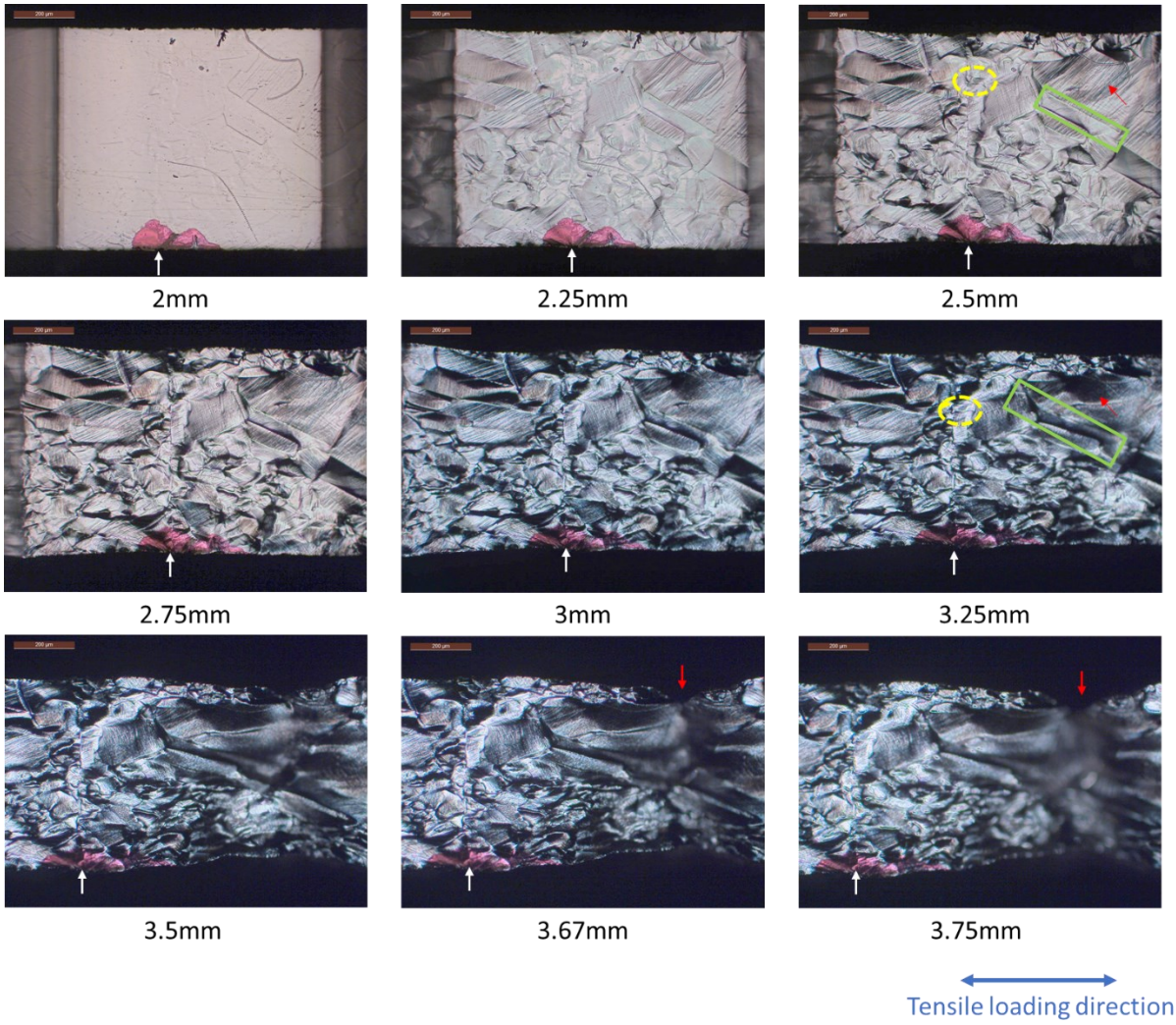


Figure 7-11 The in-situ observation (OM images) of the Ni-1 sample during the tensile test.

In Figure 7-12, the pure nickel samples from interrupted tensile tests are presented at a strain of 28%. It can be seen that slip systems in different directions are activated in different grains. It shows no difference in the diffusion bonded and hot compression bonded samples and their references from the surface morphologies. The GND of the selected areas in samples Ni-1 and Ni-3 were measured and shown in Figure 7-12 (e and f), and both areas are selected near the bonded interface from different bonding methods. In sample Ni-1 (Figure 7-12e) with the unmigrated interface grain boundary, the average GND is slightly higher than Ni-3 (Figure 7-12f) with complete migrated interface grain boundaries during the tensile. At a small scale in Ni-1, there is not much difference in the GND distribution near the normal grain boundaries and interface grain boundaries. As it is shown in (Figure 7-12e_1), the GND along the two marked boundaries with white arrows show similar density distribution in the inserted graphs. This similarity between the unmigrated interface grain boundary from bonding and inherent grain boundary is more clearly shown at a larger magnification in Figure 7-12 (e_2 and f_2).

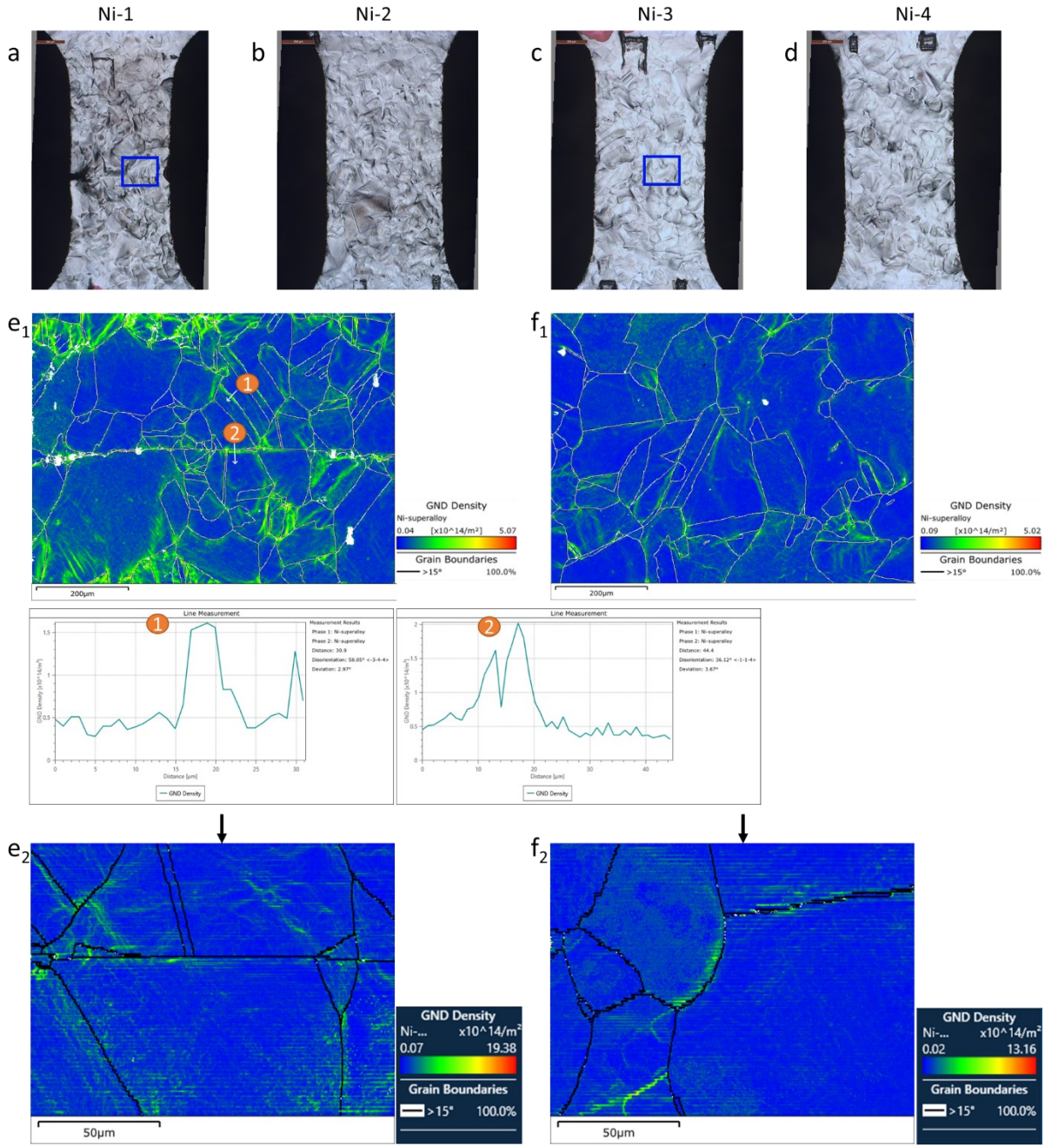


Figure 7-12 The OM images of interrupt Ni samples during the tensile test, (a) Ni-1; (b) Ni-2; (c) Ni-3 and (d) Ni-4; and the GNP maps for (e) the framed area in Ni-1 (a); (f) the framed area in Ni-3 (c).

7.4 Discussion

7.4.1 The role of interface grain boundary migration

In most solid-state bonding studies, the importance of interface grain boundary migration has been demonstrated with a mechanical property evaluation. For example, in the diffusion

bonding process of aluminium alloy, the recrystallization process was initiated, and recrystallized grains extended across the interface with the increase of the duration, leading to high bond strength[138]. Moreover, the dependence of final joint performance on the interface grain boundary migration was further verified in the hot compression bonding of various materials[190, 194, 196].

However, the results in this work tend to question this global picture concerning the interface grain boundary formed during solid-state bonding. This chapter presents, with the comparison between the bonded sample and reference, how the migrated or unmigrated interface grain boundaries affect the final tensile performance. For the FCC bi-crystalline Al samples and polycrystalline Ni samples, their tensile mechanical response to the grain boundary inclination and migration reveals a dependence on the number of grains. In the Al bi-crystals, the sample with grain boundary vertical to the tensile loading shows a higher hardening and flow strength than their counterpart single crystals, while the Al bi-crystalline with inclined grain boundary presents no obvious difference with the single crystalline samples, as compared in Figure 7-2. As suggested in previous literature [249, 250], high angle grain boundary (HAGB) stops the movement of the dislocations as obstacles and the phenomenon that was simulated using dislocation dynamics methods. In Figure 7-4, higher GND is observed along the grain boundary in the bi-crystalline Al samples when stretched to a mild strain of 28% as proof of the pile-up of dislocations. Besides, by comparison, the difference in GND intensity between Al-2 and Al-3 (with different grain boundary inclination angles) is negligible. However, as the piled-up dislocation walls make the slip transmission more difficult, for which the hardening effect becomes more evident, the inclination of the hardening zone, which is composed of the GB and dislocation accumulation, affects the mechanical response as the tensile loading would be decomposed along the GB direction and vertical, as shown in Figure 7-13a. The decomposed stress parallel to the grain boundary can still facilitate the slip moving along the grain boundary, even when the slip transmission would be stopped. Therefore, the hardening effect of inclined grain boundary is weakened, thus presenting lower strength and better ductility.

However, as revealed from the tensile test result of the poly-crystalline Ni samples, the diffusion bonded sample with unmigrated interface grain boundaries presents, in Figure 7-9, a similar mechanical response to tensile deformation compared with references. This phenomenon indicates that the unmigrated interface grain boundaries may deform as normal inherent random grain boundaries in polycrystalline. According to the in-situ observation of

the bonded sample being stretched in Figure 7-11 and the interrupted tensile sample shown in Figure 7-10, the shape of interface grains would be changed under deformation, resulting in the unmigrated interface grain boundary deviating from the original straight line. Figure 7-12 presents that, higher GND is found near certain grain boundaries, and shows no preferences for interface grain boundaries or normal grain boundaries. As suggested in [249] and [251], the grain boundary may act as a dislocation sink or obstacle, depending on the grain boundary characteristics, e.g., misorientation, which explains that not all grain boundaries are similarly stopping the slip transmission and shows with higher GND. Different from bi-crystallites, plastic deformation simultaneously happened to multiple neighbouring grains, together with the uneven high GND distribution within one grain, the grain sliding or rotation, and elongation could occur. As shown in Figure 7-13b, a different grain deformation mode turns the interface grain boundaries into random orientation, more similar to the inherent grain boundaries. Therefore, the original straight unmigrated interface grain boundaries exert no obvious effect on its deformation behaviour.

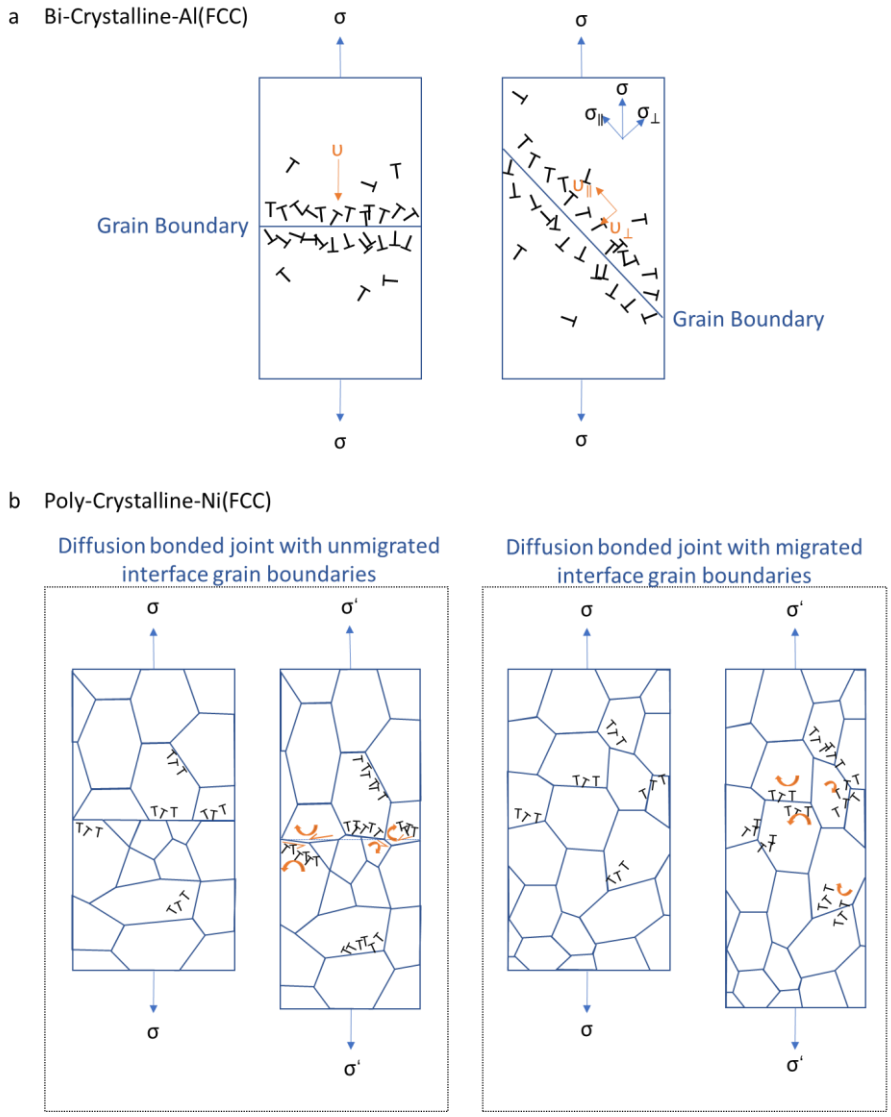


Figure 7-13 The deformation mechanism of a) the bi-crystalline Al samples and b) bonded poly-crystalline Ni samples during tensile tests.

7.5 Conclusions

In this chapter, the importance of the interface grain boundary migration is examined with bi-crystallites with single grain boundaries differently aligned and joints with unmigrated/migrated interface grain boundaries that are bonded under different conditions. Their tensile properties are tested and compared to the references with very similar grain microstructure, and in-situ observation of the deformation is conducted. From their mechanical response during the tensile deformation, the following conclusions could be drawn:

1. The bi-crystalline Al samples with different grain boundary inclinations present different hardening and flow strengths during tensile tests. The sample with the grain boundary vertical to the tensile loading shows higher strength and lower ductility; while the sample with an inclined aligned grain boundary has a similar mechanical response to the tensile load with its corresponding single crystal counterpart; For both bi-crystal Al samples, the failure point is away from GB.
2. According to the dislocation density measurement of the interrupted tensile bi-crystalline Al sample, the GND in the sample with different grain boundary inclination shows no obvious difference in its intensity. Their different tensile performance could be due to that: when the grain boundary is inclined with a certain angle, although the grain boundary would stop the slip transmission and motion, the slips would be able to slide parallel to the grain boundary, which endows some plasticity and reduce the hardening effect caused by grain boundary;
3. Both the polycrystalline Ni joints with/without complete interface grain boundary migration shows similar tensile properties with their corresponding references, which indicates that the interface grain boundary migration makes no obvious difference in their final tensile performance when the interface purification can be guaranteed. The interface grain boundary migration is not an essential condition to achieve sound bond strength;
4. The reason for the similar mechanical response to the tensile loading in Ni no-interface-grain-boundary-migration joints with references could be that the coordination in deformation between neighbouring grains in poly-crystallite can turn the original straight grain boundaries into random distribution, close to the normal inherent grain boundaries during plastic deformation.

Chapter 8 Summary and Future Work

8.1 Summary

The work presented in this thesis investigates the bonding behaviour of nickel-based superalloy IN718 under hot deformation conditions. It provides preliminary evidence for the feasibility of a new proposed laminated manufacturing method based on the multi-layer solid-state bonding process.

The bonding trials were conducted at different scales, each aiming to explore the bonding process from a different perspective: small bar samples were bonded under compression using Gleeble in the lab to investigate the bonding mechanism and study the effect of bonding condition on the final bond quality; a four-stage model based on the bonding mechanism was developed in order to predict bond quality and to describe the bonding process numerically. The validity of the model was examined using the results from bar samples under various conditions together with results from three-layer plate bonding tests. Tests on typical bonded interfaces with specified pure nickel and bi-crystal aluminium samples were used to reveal the failure mechanism of the bonded joints and the role interface grain boundary migration plays in the bond quality. A summary of the main findings from this PhD project is presented in this chapter.

At a small scale, the bonding tests with bar samples were conducted using Gleeble in a mild vacuum. The dimension design of the bar sample makes it possible to evaluate the tensile properties of the solid-state bonded joints. And the microstructure of the bonding interface is characterized. The bonding mechanism is studied based on the microstructure observation and its tensile properties.

- The bond quality (reflected by a ratio of ductility) increases with the strain level. Compared to cold welding, a relatively higher strength is obtained at lower strain and good bond quality is achieved at 50% height reduction.
- The bonding mechanism involves oxide film break-up, and metal extrusion, interacting with recrystallization-induced interface grain boundary migration. These three processes determine the final joint performance. In addition, this work indicates that cohesion between the oxide films should also be considered for the bond tensile properties, and that complete interface grain boundary migration during the later stages

of bonding could incorporate the residual oxide fragment into grains, thus minimizing the adverse effect of oxide film on joint performance.

- According to the newly proposed mechanism, the tensile results from bonding at different strain rates (0.001 s^{-1}~0.1 s^{-1}) and temperatures (950 ˚C~1150 ˚C) are explained. Generally, at the early stage with lower strain, the cohesion between oxide-oxide, or oxide-metal mechanism dominates, which is related to the normal pressure and "cohesion ratio". Higher normal pressure at a higher strain rate and higher cohesion ratio at higher temperature led to a higher interface bond ratio. However, at the late stage of bonding, height reduction, with the widespread breakup of oxides and completion of interface grain boundary migration, the effect of the strain rate and temperature is minimized, and interfaces with a 100% bond ratio are obtained at all conditions.

According to the proposed mechanism, a four-stage model is developed, which discusses the different processes and the interaction between them. Using the model, and with the help of FE simulation to calculate the stress-strain state, each single process can be analysed and presented to show their separate contribution in determining final joint performance.

- In the new model, assumptions are made mainly regarding (a) the cohesion between oxide-oxide, and oxide-metal, and (b) consideration of the role interface grain microstructure plays in minimizing the effect of the residual oxides by introducing a strain-related factor-δ.
- By introducing parameters corresponding to the cohesion between oxide-oxide, oxide-metal related to the normal pressure, and cohesion ratio, the effects of the strain rate and temperature on the resulting interface bond quality can be well explained and predicted.

After gaining a general understanding of the bonding process through using small samples, a bonding trial with a larger three-layer-built plate was conducted under forging conditions. This scale-up trial was designed to demonstrate the new laminated constructing concept through a preliminarily test under more practical industrial conditions. The multi-layer plate was forged under various conditions and given a standard heat treatment.

- By examining the microstructure at different locations along the bonded interfaces, the uniformity over the whole plate was checked. The plates forged at 1050 ˚C and 1150

˚C revealed better microstructural uniformity, both between the interface zone and base zone and between the centre and the edge zone of the plate. However, for the plate forged at 950 ˚C, the interface zone shows a different microstructure with the base zone and edge zones both showing higher δ phase density than the centre zone. This could be explained by the slightly higher dislocation density near the bonding interface or a lower temperature near the edge promoting δ phase precipitation. At all interfaces, oxides were observed, and no complete interface grain boundary migration was seen.

- After standard heat treatment, the plates forged at 1150 ˚C, with forging speed of 10 $mm \cdot s^{-1}$ or 0.1 $mm \cdot s^{-1}$, presented the best tensile properties. However, although the tensile strength is comparable to wrought standards, the ductility is less than satisfactory.
- For 950 ˚C-forged plates, although the strength results are not satisfied, from the uniformity examination in both microstructure and mechanical performance, the edge zone has less difference in the δ phase concentration and shows better integrity. This indicates the importance of uniformity over the interface and base in determining the joint integrity.
- The multi-layer plate forging process was simulated using QForm and the developed model was implemented in the simulation. Around 40% bond quality was predicted for 1150 ˚C-forged plates. Deformation with a higher strain level is suggested to achieve better properties for the plate forging.

The bonding mechanism study in Chapter 1 shows at late stage, with the interface grain boundary migration the remaining oxide fragments would be included within grains, thus minimizing their adverse effects. The positive effect of interface grain boundary migration has also been reported elsewhere, however, no direct evidence has been given considering the hybridity of the different mechanisms and is not referenced. To investigate this, a study with some typical solid-state bonded interfaces was conducted to investigate the independent effect of interface grain boundary migration on the failure behaviour of the joints.

- Bi-crystal pure aluminium samples were utilized to study the effect of the inclination of the grain boundary during the tensile test. The sample in which the grain boundary is vertical to loading direction has higher tensile strength but lower ductility compared both to sample with inclined grain boundary or its counterpart single crystalline samples.
- Using pure nickel samples , typical solid-state bonded interfaces with no or complete interface grain boundary migration were prepared under diffusion and hot compression

bonding conditions, respectively. No oxides were observed in the bonded interfaces, due to the dissolubility at high temperature in vacuum. Sample with both interfaces presented similar tensile performance to reference values, indicating that the interface grain boundary migration makes no obvious difference to the bond when the interface is pure.

- Combining the bonding test results with those of IN718, where the interface oxide film should be considered, it is inferred that interface grain boundary migration could help minimize the adverse effects of oxide remaining on the interface, however, the effect of the interface grain boundary migration would be less obvious without the existence of oxides.

This work has shown that fully recovered joints (comparable to references) can be instantly achieved in solid-state under hot deformation with a proper condition, which indicates the feasibility of the new proposed multi-layer bonding manufacturing method and its potential in constructing large components. The proposed mechanism provides a more comprehensive understanding of the bonding process and integrates different theories. In the meanwhile, the model developed based on the mechanism we interprets the bonding behaviour under different conditions well, make attempts to predict the bond quality in practical cases, and provides guidance in the future bonding process design. Moreover, investigation of the failure of the joints with typical interfaces offers a hint for the study of single interface grain boundary migration mechanisms during bonding alongside the other mechanisms operating.

8.2 Suggestions for further research work

The overall aim of the project is to develop a new laminated manufacturing concept for constructing large components, based on solid-state bonding methods. The research in this PhD thesis has been presented as a preliminary study, aiming to gain an understanding of the bonding mechanism under hot compression conditions and how the process parameters can affect the bonded interface properties. Another aim has been to propose a model that can be used to describe the bonding process and predict the resulting bond quality, thus giving guidance in the design of the process for future application. The following section offers some recommendations for future work that would build on the results of the current work. This discussion focuses on three aspects: bonding mechanism, model development modification, and manufacturing optimisation.

8.2.1 Distinguish the role of a single process in the complex bonding mechanism

As reviewed in Chapter 2, different theories have been proposed to explain the correlation between the solid-state bonding parameters and joint performance. According to the different conditions applied, the dominating mechanism/process can vary. For example, the most accepted oxide film theory (involving the oxide film break-up process) can explain roll-bonding/cold welding, and the micro-void closure process has been adopted to understand the dependence of the joint property on the duration of the diffusion bonding.

However, with the requirement to achieve the bonding in a more realistic industrial application, e.g., a shorter time lower vacuum environment, with the use of higher temperatures and large strain, a single theory cannot explain the complex bonding process as mechanisms can be mixed. In this work, a bonding mechanism that integrates different processes is proposed and these different processes are each considered to dominate at different stages during the bonding. Moreover, some new assumptions are made, including the cohesion between the oxide-oxide, or oxide-metal to explain the strength obtained with continuous oxide film cover, and the oxide minimizing effect of the interface grain boundary migration of residual oxides on the joint performance to explain the 100% bond ratio (4.5.1).

Although assumptions have been made based on related studies on hot pressing of ceramics, diffusion bonding and other hot compression bonding results (as explained in the model description 5.3), besides, some evidence has also been provided in this study, for example, the bonding results obtained from different strain rates and temperatures (4.5.3 and 4.5.4, 5.5.2 and 5.5.3), and also the bonding trial with multi-layer plates (6.3.3), providing more direct evidence. Isolating the effect of a single process on the bonding quality is suggested as a future topic for investigation. For example, the single effect of interface grain boundary migration on the bonding quality has been studied with some typical solid-state bonded interfaces and specific materials, excluding the oxide film factor (Chapter 7). ***Suggestion 1-*** Other processes that could occur during the bonding, such as cohesion between oxides, oxide and metals, and the factors affecting the cohesion are recommended for further studies with more direct evidence. Ceramic coating deposited onto a surface[252, 253], followed by subsequent bonding tests under various conditions could be a suggestion for this study. ***Suggestion 2-*** In terms of the interface grain microstructure evolution process, the interface grain migration process, including the influence factors like grain size, stress-strain state, dislocation behaviour, et al., and its interaction with the oxides, can be further studied.

8.2.2 Model further modification with more detailed research

In Chapter 5, a model is developed to describe and explain the bonding results. This new model integrates different mechanisms and theories and can give a good prediction of the interface bond ratio. However, in considering the availability of this model in industrial applications, the effect of the different processes on the bonding quality has been simplified. This model could be modified further with a detailed discussion of the effects of each parameter on each process.

For instance, the effect of the interface microstructure evolution on improving joint performance is considered by introducing a strain-related factor δ. The δ factor simplifies the dependence of the microstructure evolution degree on strain level, which help explain the good bond quality obtained with the existence of residual oxides and complete interface grain boundary migration (Chapter 4 and Chapter 5). However, in this work, no detailed effect of the migration progress is discussed. ***Suggestion 3-*** Further investigation of the factors affecting the grain boundary migration rate with the presence of interface oxides, the simulation of this migration process and its effect on the final bond quality will be the focus of future work.

The new model proposed in this work is based on the bonding mechanism study using IN718 under a mild vacuum, in which oxides and oxidation are considered. However, the mechanism for different materials (for example pure nickel, in which the oxidation problem can be ignored) might be different. Therefore, ***Suggestion 4-*** the application of this model to other situations where oxidation could be neglected would need adequate modification.

8.2.3 Suggestions for the practical manufacturing application

The aim of the presented solid-state bonding study in this thesis is to propose a new laminated construction method for large size components. Although it has been shown in this thesis that 100% interface bond quality can be achieved at the height reduction of 50%, In real applications, the achievement of good quality with less strict conditions would be highly desirable, for example, with even lower strain or a lower vacuum environment.

Even though, as assumed in this work, the cohesion should be considered between oxides, oxide and metals under hot pressing conditions, the cohesion ratio is much lower than metal-metal contact. The existence of interface oxides is still not ideal, especially at lower strain. Therefore, ***Suggestion 5-*** the surface pre-treatment, e.g. protective interlayer[254] or coating layer[255-257], which aims to reduce the interface oxide or prohibit the oxidation, could be conducted in future work.

References

1. Erve, M., et al., *State of the art in the manufacture of heavy forgings for reactor components in the Federal Republic of Germany.* Nuclear engineering and design, 1988. **108**(3): p. 485-495.
2. Tanaka, Y. and I. Sato, *Development of high purity large forgings for nuclear power plants.* Journal of nuclear materials, 2011. **417**(1-3): p. 854-859.
3. Debarbadillo, J.J. and S.K. Mannan, *Alloy 718 for oilfield applications.* JOM, 2012. **64**(2): p. 265-270.
4. Kadau, K., P.W. Gravett, and C. Amann, *Probabilistic Fracture Mechanics for Heavy-Duty Gas Turbine Rotor Forgings.* Journal of Engineering for Gas Turbines and Power, 2018. **140**(6).
5. Sun, M., et al., *Leading manufacture of the large-scale weldless stainless steel forging ring: Innovative approach by the multilayer hot-compression bonding technology.* Journal of Materials Science & Technology, 2021. **71**: p. 84-86.
6. Sun, M., et al., *Research advances on homogenization manufacturing of heavy components by metal additive forging.* Chinese Science Bulletin, 2020. **65**(27): p. 3043-3058.
7. Maidorn, C. and D. Blind, *Solidification and segregation in heavy forging ingots.* Nuclear engineering and design, 1985. **84**(2): p. 285-296.
8. Wang, J., et al., *Shrinkage porosity criteria and optimized design of a 100-ton 30Cr2Ni4MoV forging ingot.* Materials & Design, 2012. **35**: p. 446-456.
9. 蔺永诚 and 陈明松, *高性能大锻件控形控性理论及应用*. 2013, 北京: 科学出版社.
10. Thamboo, S., Schwant, R., Yang, L., Jackman, L., Bond, B., Kennedy, R., *LARGE DIAMETER 718 INGOTS FOR LAND-BASED GAS TURBINES.* Superalloys, 2001.
11. Pollock, T.M. and S. Tin, *Nickel-Based Superalloys for Advanced Turbine Engines: Chemistry, Microstructure and Properties.* Journal of Propulsion and Power, 2006. **22**(2): p. 361-374.
12. Schafrik, R.E., D.D. Ward, and J.R. Groh, *Application of alloy 718 in GE aircraft engines: past, present and next five years.* Superalloys, 2001. **718**(625): p. 1-11.
13. Hardy, M.C., et al., *Solving Recent Challenges for Wrought Ni-Base Superalloys.* Metallurgical and Materials Transactions A, 2020. **51**(6): p. 2626-2650.
14. Uginet, J. and J. Jackson, *Alloy 718 forging development for large land-based gas turbines.* Superalloys, 2006. **718**: p. 625-706.

15. Taminger, K.M. and C.S. Domack, *Challenges in Metal Additive Manufacturing for Large-Scale Aerospace Applications*, in *Women in Aerospace Materials: Advancements and Perspectives of Emerging Technologies*, M.E. Kinsella, Editor. 2020, Springer International Publishing: Cham. p. 105-124.

16. Henderson, M., et al., *Nickel based superalloy welding practices for industrial gas turbine applications.* Science and technology of welding and joining, 2004. **9**(1): p. 13-21.

17. Dhinakaran, V., et al., *Wire Arc Additive Manufacturing (WAAM) process of nickel based superalloys – A review.* Materials Today: Proceedings, 2020. **21**: p. 920-925.

18. SATAIR. *Five challenges additive manufacturing*. 2018; Available from: https://blog.satair.com/five-challenges-additive-manufacturing.

19. *Why Choosing Inconel 718 for Aerospace Additive Manufacturing? .* 2020.

20. LIU, Y., et al., *Recent progress on evolution of precipitates in inconel 718 superalloy.* Acta Metall Sin, 2016. **52**(10): p. 1259-1266.

21. Lewandowski, M., et al., *High temperature deformation of Inconel 718 castings.* Superalloys, 1993. **718**: p. 625-706.

22. Atkinson, H. and S. Davies, *Fundamental aspects of hot isostatic pressing: an overview.* Metallurgical and Materials Transactions A, 2000. **31**(12): p. 2981-3000.

23. Kuo, Y.-L. and K. Kakehi, *Influence of Powder Surface Contamination in the Ni-Based Superalloy Alloy718 Fabricated by Selective Laser Melting and Hot Isostatic Pressing.* Metals, 2017. **7**(9).

24. Rao, G.A., M. Srinivas, and D.S. Sarma, *Effect of oxygen content of powder on microstructure and mechanical properties of hot isostatically pressed superalloy Inconel 718.* Materials Science and Engineering: A, 2006. **435-436**: p. 84-99.

25. Chang, L., et al., *Microstructure, Tensile Properties, and Hot-Working Characteristics of a Hot Isostatic-Pressed Powder Metallurgy Superalloy.* Metallurgical and Materials Transactions A, 2017. **48**(3): p. 1273-1287.

26. Bai, Q., et al., *A study of direct forging process for powder superalloys.* Materials Science and Engineering: A, 2015. **621**: p. 68-75.

27. Qin, C.-H., et al., *Grain size effect on multi-scale fatigue crack growth mechanism of Nickel-based alloy GH4169.* Engineering Fracture Mechanics, 2015. **142**: p. 140-153.

28. Liu, G., et al., *The effects of grain size, dendritic structure and crystallographic orientation on fatigue crack propagation in IN713C nickel-based superalloy.* International Journal of Plasticity, 2020. **125**: p. 150-168.

29. Trosch, T., et al., *Microstructure and mechanical properties of selective laser melted Inconel 718 compared to forging and casting.* Materials Letters, 2016. 164: p. 428-431.

30. Zhang, S., et al., *Processing and microstructural evolution of superalloy Inconel 718 during hot tube extrusion.* Journal of Materials Sciences and Technology, 2009. 21(02): p. 175-178.

31. Sui, F.-L., et al., *Processing map for hot working of Inconel 718 alloy.* Journal of Materials Processing Technology, 2011. 211(3): p. 433-440.

32. Douglas, J. and T. Altan, *Flow stress determination for metals at forging rates and temperatures.* Journal of Engineering for Industry, 1975. 97(1): p. 66-76.

33. Lars Renhof, C.K., Ewald Werner, Martin Stockinger, *Analysis of microstructural properties of IN 718 after high speed forging.* The Minerals, Metals & Materials Society, 2005.

34. Azarbarmas, M., et al., *Dynamic recrystallization mechanisms and twining evolution during hot deformation of Inconel 718.* Materials Science and Engineering: A, 2016. 678: p. 137-152.

35. Xie, B., et al., *DDRX and CDRX of an as-cast nickel-based superalloy during hot compression at γ′ sub-/super-solvus temperatures.* Journal of Alloys and Compounds, 2019. 803: p. 16-29.

36. Gourdet, S. and F. Montheillet, *A model of continuous dynamic recrystallization.* Acta Materialia, 2003. 51(9): p. 2685-2699.

37. Momeni, A., et al., *Microstructure evolution at the onset of discontinuous dynamic recrystallization: A physics-based model of subgrain critical size.* Journal of Alloys and Compounds, 2014. 587: p. 199-210.

38. Huang, K. and R.E. Logé, *A review of dynamic recrystallization phenomena in metallic materials.* Materials & Design, 2016. 111: p. 548-574.

39. Lin, Y.C. and X.-M. Chen, *A critical review of experimental results and constitutive descriptions for metals and alloys in hot working.* Materials & Design, 2011. 32(4): p. 1733-1759.

40. Gujrati, R., et al., *Understanding activation energy of dynamic recrystallization in Inconel 718.* Materials Science and Engineering: A, 2019. 744: p. 638-651.

41. Huber, D., et al., *Microstructure Modeling of the Dynamic Recrystallization Kinetics during Turbine Disc Forging of the Nickel Based Superalloy Allvac 718 Plus*, in *Superalloys 2008 (Eleventh International Symposium)*. 2008. p. 855-861.

42. Wang, J., et al., *Effect of Grain Size Distribution on Processing Maps for Isothermal Compression of Inconel 718 Superalloy.* Journal of Materials Engineering and Performance, 2016. 25(2): p. 677-686.

43. Sakai, T., et al., *Dynamic and post-dynamic recrystallization under hot, cold and severe plastic deformation conditions.* Progress in Materials Science, 2014. 60: p. 130-207.

44. Lin, Y.C., et al., *EBSD study of a hot deformed nickel-based superalloy.* Journal of Alloys and Compounds, 2015. 640: p. 101-113.

45. Thomas, J.-P., et al., *EBSD investigation and modeling of the microstructural evolutions of superalloy 718 during hot deformation.* Proceedings of superalloys, 2004: p. 959-968.

46. Candioto, K.C.G., et al., *Characterization of the Superalloy Inconel 718 After Double Aging Heat Treatment*, in *Mechanical and Materials Engineering of Modern Structure and Component Design*. 2015. p. 293-300.

47. Krueger, D., *The development of direct age 718 for gas turbine engine disk applications.* Superalloy 718: Metallurgy and Applications, 1989: p. 279-296.

48. Zhang, S.-H., H.-Y. Zhang, and M. Cheng, *Tensile deformation and fracture characteristics of delta-processed Inconel 718 alloy at elevated temperature.* Materials Science and Engineering: A, 2011. 528(19-20): p. 6253-6258.

49. Páramo-Kañetas, P., et al., *High-temperature deformation of delta-processed Inconel 718.* Journal of Materials Processing Technology, 2018. 255: p. 204-211.

50. Azarbarmas, M., et al., *Microstructural evolution and constitutive equations of Inconel 718 alloy under quasi-static and quasi-dynamic conditions.* Materials & Design, 2016. 94: p. 28-38.

51. Liu, Y., et al., *Effect of deformation temperature and strain rate on dynamic recrystallized grain size of a powder metallurgical nickel-based superalloy.* Journal of Alloys and Compounds, 2017. 691: p. 554-563.

52. Sellars, C.M. and W. McTegart, *On the mechanism of hot deformation.* Acta Metallurgica, 1966. 14(9): p. 1136-1138.

53. Ponge, D. and G. Gottstein, *Necklace formation during dynamic recrystallization: mechanisms and impact on flow behavior.* Acta Materialia, 1998. 46(1): p. 69-80.

54. Reshetov, A., et al., *An approach to microstructure modelling in nickel based superalloys.* Superalloys 2016, 2016: p. 531-538.

55. Lin, Y.C., et al., *New constitutive model for high-temperature deformation behavior of inconel 718 superalloy.* Materials & Design, 2015. 74: p. 108-118.

56. Shen, G., J. Rollins, and D. Furrer, *Microstructure modeling of forged waspaloy discs.* 1996.

57. Lin, J. and T.A. Dean, *Modelling of microstructure evolution in hot forming using unified constitutive equations.* Journal of Materials Processing Technology, 2005. 167(2-3): p. 354-362.

58. Tang, X.-F., et al., *Modeling of microstructural evolution and flow behavior of superalloy IN718 using physically based internal state variables.* Rare Metals, 2015.

59. Zouari, M., N. Bozzolo, and R.E. Loge, *Mean field modelling of dynamic and post-dynamic recrystallization during hot deformation of Inconel 718 in the absence of δ phase particles.* Materials Science and Engineering: A, 2016. **655**: p. 408-424.

60. Stefani, N., et al., *On the applicability of JMAK-type models in predicting IN718 microstructural evolution.* Computer Methods in Materials Science, 2017. **17**(1): p. 59-68.

61. Gebisa, A.W. and H.G. Lemu. *Additive manufacturing for the manufacture of gas turbine engine components: literature review and future perspectives*. in *Turbo Expo: Power for Land, Sea, and Air*. 2018. American Society of Mechanical Engineers.

62. Gibson, I., D.W. Rosen, and B. Stucker, *Additive manufacturing technologies*. Vol. 17. 2014: Springer.

63. Wang, X., X. Gong, and K. Chou, *Review on powder-bed laser additive manufacturing of Inconel 718 parts.* Proceedings of the Institution of Mechanical Engineers, Part B: Journal of Engineering Manufacture, 2016. **231**(11): p. 1890-1903.

64. Jia, Q. and D. Gu, *Selective laser melting additive manufacturing of Inconel 718 superalloy parts: Densification, microstructure and properties.* Journal of Alloys and Compounds, 2014. **585**: p. 713-721.

65. Chlebus, E., et al., *Effect of heat treatment on the microstructure and mechanical properties of Inconel 718 processed by selective laser melting.* Materials Science and Engineering: A, 2015. **639**: p. 647-655.

66. Mostafa, A., et al., *Structure, Texture and Phases in 3D Printed IN718 Alloy Subjected to Homogenization and HIP Treatments.* Metals, 2017. **7**(6).

67. Mostafa, A., et al., *Hot compression behavior and microstructure of selectively laser-melted IN718 alloy.* The International Journal of Advanced Manufacturing Technology, 2018.

68. Zhao, X., et al., *Study on microstructure and mechanical properties of laser rapid forming Inconel 718.* Materials Science and Engineering: A, 2008. **478**(1-2): p. 119-124.

69. Qi, H., M. Azer, and A. Ritter, *Studies of Standard Heat Treatment Effects on Microstructure and Mechanical Properties of Laser Net Shape Manufactured INCONEL 718.* Metallurgical and Materials Transactions A, 2009. **40**(10): p. 2410-2422.

70. Bambach, M., et al., *Hot workability and microstructure evolution of the nickel-based superalloy Inconel 718 produced by laser metal deposition.* Journal of Alloys and Compounds, 2018. 740: p. 278-287.

71. Sanz, C. and V. García Navas, *Structural integrity of direct metal laser sintered parts subjected to thermal and finishing treatments.* Journal of Materials Processing Technology, 2013. 213(12): p. 2126-2136.

72. L.M. SOCHALSKI-KOLBUS, E.A.P., P.A. CORNWELL, T.R. WATKINS, S.S. BABU, R.R. DEHOFF, M. LORENZ, O. OVCHINNIKOVA, and C. DUTY, *Comparison of Residual Stresses in Inconel 718 Simple Parts Made by Electron Beam Melting and Direct Laser Metal Sintering.* 2015. 46A.

73. Hosseini, E. and V.A. Popovich, *A review of mechanical properties of additively manufactured Inconel 718.* Additive Manufacturing, 2019. 30.

74. Zhang, Y.-N., et al., *Tensile properties of laser additive manufactured Inconel 718 using filler wire.* Journal of Materials Research, 2014. 29(17): p. 2006-2020.

75. Dutton, B., et al., *Metal additive manufacturing defect formation and nondestructive evaluation detectability.* Structural Integrity of Additive Manufactured Parts, 2020: p. 1-50.

76. Pröbstle, M., et al., *Superior creep strength of a nickel-based superalloy produced by selective laser melting.* Materials Science and Engineering: A, 2016. 674: p. 299-307.

77. Lewandowski, J.J. and M. Seifi, *Metal Additive Manufacturing: A Review of Mechanical Properties.* Annual Review of Materials Research, 2016. 46(1): p. 151-186.

78. Tammas-Williams, S., *XCT analysis of the defect distribution and its effect on the static and dynamic mechanical properties in Ti-6Al-4V components manufactured by electron beam additive manufacture*. 2016, University of Manchester.

79. Di Serio, E.T., et al., *Method for the production of parts made from metal or metal matrix composite and resulting from additive manufacturing followed by an operation involving the forging of said parts*. 2017, Google Patents.

80. Jiang, J., et al., *An integrated method for net-shape manufacturing components combining 3D additive manufacturing and compressive forming processes.* Procedia engineering, 2017. 207: p. 1182-1187.

81. Babu, S.S., et al., *Additive manufacturing of materials: Opportunities and challenges.* MRS Bulletin, 2015. 40(12): p. 1154-1161.

82. Salih, O.S., et al., *A review of friction stir welding of aluminium matrix composites.* Materials & Design, 2015. 86: p. 61-71.

83. Shirzadi, A.A., H. Assadi, and E.R. Wallach, *Interface evolution and bond strength when diffusion bonding materials with stable oxide films.* Surface and Interface Analysis, 2001. **31**(7): p. 609-618.

84. Groche, P., et al., *Joining by forming—A review on joint mechanisms, applications and future trends.* Journal of Materials Processing Technology, 2014. **214**(10): p. 1972-1994.

85. Mori, K.-i., et al., *Joining by plastic deformation.* CIRP Annals, 2013. **62**(2): p. 673-694.

86. A.Hill and E.R.Wallach, *Modelling solid-state diffusion bonding.* Acta Materialia, 1989. **37**(9).

87. Bralla, J.G., *Handbook of manufacturing processes*. 2006: Industrial Press.

88. Bay, N., *Cold pressure welding—the mechanisms governing bonding.* 1979.

89. Bay, N., et al., *Bond Strength in Cold Roll Bonding.* CIRP Annals, 1985. **34**(1): p. 221-224.

90. Le, H.R., et al., *Surface oxide fracture in cold aluminium rolling.* Acta Materialia, 2004. **52**(4): p. 911-920.

91. Li, L., K. Nagai, and F. Yin, *Progress in cold roll bonding of metals.* Sci Technol Adv Mater, 2008. **9**(2): p. 023001.

92. Vaidyanath, L., M. Nicholas, and D. Milner, *Pressure welding by rolling.* British Welding Jour, 1959. **6**: p. 13-28.

93. Chamanfar, A., M. Jahazi, and J. Cormier, *A Review on Inertia and Linear Friction Welding of Ni-Based Superalloys.* Metallurgical and Materials Transactions A, 2015. **46**(4): p. 1639-1669.

94. Chamanfar, A., et al., *Maximizing the integrity of linear friction welded Waspaloy.* Materials Science and Engineering: A, 2012. **555**: p. 117-130.

95. Lee, Y.S., et al., *Internal void closure during the forging of large cast ingots using a simulation approach.* Journal of Materials Processing Technology, 2011. **211**(6): p. 1136-1145.

96. C.Y.Park and D.Y.Yang, *A study of void crushing in large forgings I : Bonding mechanism and estimation model for bonding efficiency.* Journal of Materials Processing Technology, 1996. **57**(1-2).

97. Afshan, S., et al., *A new experimental method for identifying the conditions necessary for diffusion bonding in free cutting steels.* Materials Science and Engineering: A, 2013. **586**: p. 25-30.

98. Vyas, K. *Cold Welding: Joining Metals Without Heat*. 2019; Available from: https://interestingengineering.com/cold-welding-joining-metals-without-heat.

99. Ridley, N., *Metals for superplastic forming*, in *Superplastic Forming of Advanced Metallic Materials*. 2011, Elsevier. p. 3-33.

100. Beausir, B., et al., *Plastic anisotropy of ultrafine grained aluminium alloys produced by accumulative roll bonding.* Materials Science and Engineering: A, 2010. **527**(13-14): p. 3271-3278.

101. Chekhonin, P., et al., *Confined recrystallization of high-purity aluminium during accumulative roll bonding of aluminium laminates.* Acta Materialia, 2012. **60**(11): p. 4661-4671.

102. Lee, S., et al., *Role of shear strain in ultragrain refinement by accumulative roll-bonding (ARB) process.* Scripta Materialia, 2002. **46**(4): p. 281-285.

103. Zhang, Y.B., et al., *Microstructure and mechanical properties of nickel processed by accumulative roll bonding.* Materials Science and Engineering: A, 2013. **576**: p. 160-166.

104. Zhang, Y.B. and O.V. Mishin, *Stored energy and recrystallized microstructures in nickel processed by accumulative roll bonding to different strains.* Materials Characterization, 2017. **129**: p. 323-328.

105. Nunes, L.G.d.S. and M.L.P. Machado, *Simulation of the Accumulative Roll-Bonding process through warm torsion test.* Journal of Materials Research and Technology, 2018. **7**(3): p. 326-330.

106. Prakash, A., et al., *A multiscale simulation framework of the accumulative roll bonding process accounting for texture evolution.* Materials Science and Engineering: A, 2015. **631**: p. 104-119.

107. Jamaati, R. and M.R. Toroghinejad, *Investigation of the parameters of the cold roll bonding (CRB) process.* Materials Science and Engineering: A, 2010. **527**(9): p. 2320-2326.

108. Eizadjou, M., H. Danesh Manesh, and K. Janghorban, *Mechanism of warm and cold roll bonding of aluminum alloy strips.* Materials & Design, 2009. **30**(10): p. 4156-4161.

109. Jamaati, R. and M.R. Toroghinejad, *Effect of friction, annealing conditions and hardness on the bond strength of Al/Al strips produced by cold roll bonding process.* Materials & Design, 2010. **31**(9): p. 4508-4513.

110. N. Tsuji, Y.S., H. Utsunomiya and S. Tanigawa, *Ultra-fine grained bulk steel produced by accumulative roll-bonding (ARB) process.* Scripta Materialia, 1999. **40**(7): p. 795-800.

111. Dhib, Z., et al., *Cladding of low-carbon steel to austenitic stainless steel by hot-roll bonding: Microstructure and mechanical properties before and after welding.* Materials Science and Engineering: A, 2016. **656**: p. 130-141.

112. Nezhad, M.S.A. and A.H. Ardakani, *A study of joint quality of aluminum and low carbon steel strips by warm rolling.* Materials & Design, 2009. **30**(4): p. 1103-1109.

113. Johnson, K.I. and D.V. Keller, *Effect of Contamination on the Adhesion of Metallic Couples in Ultra-High Vacuum.* Journal of Applied Physics, 1967. **38**(4): p. 1896-1904.

114. Conrad, H. and L. Rice, *The cohesion of previously fractured Fcc metals in ultrahigh vacuum.* Metallurgical Transactions, 1970. **1**(11).

115. Milner, D. and L. Vaidyanath, *Significance of surface preparation in cold pressure welding.* Met Constr Br Weld J, 1960. **7**: p. 1-6.

116. Mohamed, H.A. and J. Washburn, *Mechanism of solid state pressure welding.* Welding Journal, 1975. **54**.

117. Vorm, T., N. Bay, and T. Wanheim, *Influence of the hydrostatic stress component on critical surface expansion in forging compound products∗.* International Journal of Production Research, 1974. **12**(1): p. 77-87.

118. Bay, N., *Cold Pressure Welding—The Mechanisms Governing Bonding1.* 1979.

119. Bay, N., *Mechanisms producing metallic bonds in cold welding.* Welding Research Suppliment, 1983. **S**.

120. Danesh Manesh, H. and A. Karimi Taheri, *Study of mechanisms of cold roll welding of aluminium alloy to steel strip.* Materials Science and Technology, 2013. **20**(8): p. 1064-1068.

121. Cooper, D.R. and J.M. Allwood, *The influence of deformation conditions in solid-state aluminium welding processes on the resulting weld strength.* Journal of Materials Processing Technology, 2014. **214**(11): p. 2576-2592.

122. Khaledi, K., et al., *A microscale finite element model for joining of metals by large plastic deformations.* Comptes Rendus Mécanique, 2018. **346**(8): p. 743-755.

123. Wang, Y., et al., *Research status on interface bonding mechanisms and strength of cold pressure welding.* Journal of Materials Engineering, 2016. **44**(4): p. 119-130.

124. DeCecco, N.A., J.M. Parks, and C. Wright Air Development, *Recrystallization welding of aluminum aircraft alloys*. 1953, Wright-Patterson Air Force Base, Ohio: Wright Air Development Center, Air Research and Development Command, United States Air Force.

125. Parks, J.M., *Recrystallization welding.* Welding journal, 1953: p. 209-222.

126. Iordachescu, M., et al., *Material flow and hardening at butt cold welding of aluminium.* Journal of Materials Processing Technology, 2009. **209**(9): p. 4255-4263.

127. Wu, H.-Y., S. Lee, and J.-Y. Wang, *Solid-state bonding of iron-based alloys, steel–brass, and aluminum alloys.* Journal of Materials Processing Technology, 1998. **75**(1-3): p. 173-179.

128. Li, Y., Z. Du, and J. Yang, *Study on Interfacial Bonding State of Ag-Cu in Cold Pressure Welding.* Transactions of Tianjin University, 2003. **9**(3): p. 219-222.

129. Cai, W., et al., *A State-of-the-Art Review on Solid-State Metal Joining.* Journal of Manufacturing Science and Engineering, 2019. **141**(3).

130. Semenov, A., *The phenomenon of seizure and its investigation.* Wear, 1961. **4**(1): p. 1-9.

131. Müller, E. and O. Nishikawa, *Adhesion or cold welding of materials in space environment.* ASTM Special Publ, 1968. **431**: p. 67.

132. Zhang, W. and N. Bay. *State of the art in cold welding*. in *Invited paper, JOM-/, 7th Int. Conf. on the Joining of Materials, Elsinore*. 1995.

133. Veritasium, *Why metals spontaneously fuse together in space?* 2016.

134. Lu, Y., et al., *Cold welding of ultrathin gold nanowires.* Nature nanotechnology, 2010. **5**(3): p. 218-224.

135. Zhang, W. and N. Bay, *A Numerical Model for Cold Welding of Metals.* CIRP Annals, 1996. **45**(1): p. 215-220.

136. Bambach, M., et al., *A finite element framework for the evolution of bond strength in joining-by-forming processes.* Journal of Materials Processing Technology, 2014. **214**(10): p. 2156-2168.

137. Kazakov, N.F., *Diffusion bonding of materials*. 2013: Elsevier.

138. Y. Huang, et al., *Diffusion bonding of superplastic 7075 aluminium alloy.* Materials Science and Engineering: A, 1999. **266**(1-2).

139. Spence, P.J., F.R. Hall, and N. Emekwuru, *Preliminary study of improving the speed and cost of diffusion bonding of metal sheets.* Proceedings of the Institution of Mechanical Engineers, Part B: Journal of Engineering Manufacture, 2013. **228**(1): p. 95-110.

140. Li, H., M.Q. Li, and P.J. Kang, *Void shrinking process and mechanisms of the diffusion bonded Ti–6Al–4V alloy with different surface roughness.* Applied Physics A, 2015. **122**(1).

141. Sharma, G. and D.K. Dwivedi, *Impulse pressure-assisted diffusion bonding of ferritic stainless steel.* The International Journal of Advanced Manufacturing Technology, 2018. **95**(9-12): p. 4293-4305.

142. Zhang, C., H. Li, and M.Q. Li, *Modeling of Solid-State Hot Press Bonding and Its Application to the Fabrication of Titanium Alloy Joints.* Journal of Manufacturing Science and Engineering, 2018. **140**(8).

143. DerbyE., B. and R. Wallach, *Diffusion Bonds In Copper.* Journal of Materials Science, 1984. **19**(10).

144. Chen, S., et al., *Atomistic investigation of the effects of temperature and surface roughness on diffusion bonding between Cu and Al.* Acta Materialia, 2007. **55**(9): p. 3169-3175.

145. Yeh, M. and T. Chuang, *Effects of applied pressure on the brazing of superplastic INCONEL 718 superalloy.* Metallurgical and Materials Transactions A, 1997. **28**(6): p. 1367-1376.

146. LI, Z., et al., *Vacuum diffusion bonding of GH4169 superalloy.* Transactions of the China Welding Institution, 2013(6): p. 7.

147. Huang, Y., et al., *Diffusion bonding of hot rolled 7075 aluminium alloy.* Materials Science and Technology, 1998. **14**(5): p. 405-410.

148. Tang, B., et al., *Recrystallization Behavior at Diffusion Bonding Interface of High Nb Containing TiAl Alloy* Advanced Engineering Materials, 2016. **18**(4): p. 657-664.

149. Kim, S.H., C. Kim, and C. Jang. *Diffusion Bonding of a Cold-Worked Ni-Base Superalloy*. in *ASME 2018 Symposium on Elevated Temperature Application of Materials for Fossil, Nuclear, and Petrochemical Industries*. 2018. American Society of Mechanical Engineers.

150. Sah, I., et al., *The recovery of tensile ductility in diffusion-bonded Ni-base alloys by post-bond heat treatments.* Materials & Design, 2013. **47**: p. 581-589.

151. Li, Y., et al., *XRD and SEM analysis near the diffusion bonding interface of Mg/Al dissimilar materials.* Vacuum, 2007. **82**(1): p. 15-19.

152. Ghosh, M., et al., *Diffusion bonding of titanium to 304 stainless steel.* Journal of Nuclear Materials, 2003. **322**(2-3): p. 235-241.

153. King, W.H. and W.A. Owczarski, Welding J., Supplement, 1967: p. 289-298.

154. Hamilton, C.H., *Pressure requirements for diffusion bonding titanium.* Titanium Science and Technology, 1973. **1**: p. 625-648.

155. Derby, B. and E.R. Wallach, *Theoretical model for diffusion bonding.* Metal Science, 1982. **16**(1): p. 49-56.

156. Derby, B. and E.R. Wallach, *Diffusion bonding: Development of theoretical model.* Metal Science, 1984. **18**(9): p. 427-431.

157. Garmong, G., N.E. Paton, and A.S. Argon, *Attainment of full interfacial contact during diffusion bonding.* Metallurgical Transactions A, 1975. **6**(6): p. 1269-1279.

158. N. Orhana, M. Aksoyb, and M. Eroglub, *A new model for diffusion bonding and its application to duplex alloys.* Materials Science and Engineering: A, 1999. **271**(1-2).

159. Ma, R., et al., *Modeling of void closure in diffusion bonding process based on dynamic conditions.* Science China Technological Sciences, 2012. **55**(9): p. 2420-2431.

160. Pilling, J., et al., *Solid state bonding in superplastic Ti-6Al-4V.* Metal Science, 1984. **18**(3): p. 117-122.

161. Chen, G., et al., *Analytical approach for describing the collapse of surface asperities under compressive stress during rapid solid state bonding.* Scripta Materialia, 2017. **128**: p. 41-44.

162. Takahashi, Y. and K. Inoue, *Recent void shrinkage models and their applicability to diffusion bonding.* Materials science and technology, 1992. **8**(11): p. 953-964.

163. Guo, Z.X. and N. Ridley, *Modelling of diffusion bonding of metals.* Materials Science and Technology, 1987. **3**(11): p. 945-953.

164. Edwards, S.P., et al., *Physical Simulation of Longitudinal Weld Seam Formation During Extrusion to Produce Hollow Aluminum Profiles.* Materials and Manufacturing Processes, 2009. **24**(4): p. 409-421.

165. Yu, J., G. Zhao, and L. Chen, *Investigation of interface evolution, microstructure and mechanical properties of solid-state bonding seams in hot extrusion process of aluminum alloy profiles.* Journal of Materials Processing Technology, 2016. **230**: p. 153-166.

166. Yu, J., et al., *Evaluating the welding quality of longitudinal welds in a hollow profile manufactured by porthole die extrusion: Experiments and simulation.* Journal of Manufacturing Processes, 2019. **38**: p. 502-515.

167. Liu, G., J. Zhou, and J. Duszczyk, *FE analysis of metal flow and weld seam formation in a porthole die during the extrusion of a magnesium alloy into a square tube and the effect of ram speed on weld strength.* Journal of Materials Processing Technology, 2008. **200**(1-3): p. 185-198.

168. Xin, Y., et al., *Fabrication of Mg/AL multilayer plates using an accumulative extrusion bonding process.* Materials Science and Engineering: A, 2015. **640**: p. 210-216.

169. Güley, V., et al., *Effect of die design on the welding quality during solid state recycling of AA6060 chips by hot extrusion.* Materials Science and Engineering: A, 2013. **574**: p. 163-175.

170. Kim, K., C. Lee, and D.-Y. Yang, *Investigation into the improvement of welding strength in three-dimensional extrusion of tubes using porthole dies.* Journal of Materials Processing Technology, 2002. **130**: p. 426-431.

171. Yu, J. and G. Zhao, *Interfacial structure and bonding mechanism of weld seams during porthole die extrusion of aluminum alloy profiles.* Materials Characterization, 2018. **138**: p. 56-66.

172. Yu, J., G. Zhao, and L. Chen, *Analysis of longitudinal weld seam defects and investigation of solid-state bonding criteria in porthole die extrusion process of aluminum alloy profiles.* Journal of Materials Processing Technology, 2016. **237**: p. 31-47.

173. Chen, G., et al., *Microstructure analysis of an Al-Zn-Mg alloy during porthole die extrusion based on modeling of constitutive equation and dynamic recrystallization.* Journal of Alloys and Compounds, 2017. **710**: p. 80-91.

174. Yu, J., et al., *A comparative study on hot deformation and solid-state bonding behavior of aluminum alloys for the integration of solid-state joining and forming processes.* The International Journal of Advanced Manufacturing Technology, 2019. **104**(9-12): p. 3849-3866.

175. Valberg, H. *Extrusion welding in porthole die extrusion*. in *PROCEEDINGS OF INTERNATIONAL ALUMINIUM EXTRUSION TECHNOLOGY SEMINAR*. 1996. ALUMINIUM ASSOCIATION INC, & ALUMINIUM EXTRUDERS COUNCIL.

176. Plata, M. and J. Piwnik. *Theoretical and experimental analysis of seam weld formation in hot extrusion of aluminum alloys*. in *Proceedings of International Aluminum Extrusion Technology Seminar*. 2000.

177. Donati, L. and L. Tomesani, *The prediction of seam welds quality in aluminum extrusion.* Journal of Materials Processing Technology, 2004. **153**: p. 366-373.

178. Nakasaki, M., I. Takasu, and H. Utsunomiya, *Application of hydrostatic integration parameter for free-forging and rolling.* Journal of Materials Processing Technology, 2006. **177**(1-3): p. 521-524.

179. Cooper, D.R. and J.M. Allwood, *Influence of Diffusion Mechanisms in Aluminium Solid-state Welding Processes.* Procedia Engineering, 2014. **81**: p. 2147-2152.

180. Wikipedia. *Forge welding*. 2021; Available from: https://en.wikipedia.org/wiki/Forge_welding.

181. Wikipedia. *Pattern welding*. 2021.

182. Zhang, X.P., et al., *Proposal of bond criterion for hot roll bonding and its application.* Materials & Design, 2011. **32**(4): p. 2239-2245.

183. Xin, R., Q. Ma, and W. Li, *Microstructure and mechanical properties of internal crack healing in a low carbon steel.* Materials Science and Engineering: A, 2016. **662**: p. 65-71.

184. Xin, R., et al., *Restoration of impact properties of internal crack healing in a low carbon steel.* Materials Science and Engineering: A, 2017. **682**: p. 433-440.

185. Yang, C.L., et al., *Recovery of tensile properties of twinning-induced plasticity steel via electropulsing induced void healing.* Scripta Materialia, 2018. **147**: p. 88-92.

186. A.Wang, P.F.Thomson, and P.D.Hodgson, *A study of pore closure and welding in hot rolling process.* Journal of Materials Processing Technology, 1996. 60(1-4).

187. Zhang, X., et al., *A criterion for void closure in large ingots during hot forging.* Journal of Materials Processing Technology, 2009. 209(4): p. 1950-1959.

188. Zhao, Y., et al., *Effect of Surface Cleaning on Interface Bonding Performance for 316H Stainless Steel Joints Manufactured by Additive Forging.* Materials & Design, 2021.

189. Xie, B., et al., *Effects of surface roughness on interfacial dynamic recrystallization and mechanical properties of Ti-6Al-3Nb-2Zr-1Mo alloy joints produced by hot-compression bonding.* Journal of Materials Science & Technology, 2022. 96: p. 199-211.

190. Zhang, J.Y., et al., *Evolution of the interfacial microstructure during the plastic deformation bonding of copper.* Materials Science and Engineering: A, 2019. 746: p. 1-10.

191. Xie, B., et al., *Oxidation of stainless steel in vacuum and evolution of surface oxide scales during hot-compression bonding.* Corrosion Science, 2019. 147: p. 41-52.

192. Xie, B., et al., *Dissolution and evolution of interfacial oxides improving the mechanical properties of solid state bonding joints.* Materials & Design, 2018. 157: p. 437-446.

193. Zhou, L., et al., *Interfacial microstructure evolution and bonding mechanisms of 14YWT alloys produced by hot compression bonding.* Journal of Materials Science & Technology, 2019. 35(8): p. 1671-1680.

194. Zhou, L., et al., *Dynamic recrystallization behavior and interfacial bonding mechanism of 14Cr ferrite steel during hot deformation bonding.* Journal of Materials Science & Technology, 2020. 43: p. 92-103.

195. Zhang, J.Y., et al., *Interfacial Microstructural Evolution and Metallurgical Bonding Mechanisms for IN718 Superalloy Joint Produced by Hot Compressive Bonding.* Metallurgical and Materials Transactions B, 2018. 49(5): p. 2152-2162.

196. Zhang, J.Y., et al., *Microstructure evolutions and interfacial bonding behavior of Ni-based superalloys during solid state plastic deformation bonding.* Journal of Materials Science & Technology, 2020. 46: p. 1-11.

197. Zhang, J.Y., et al., *Effect of strain rate on plastic deformation bonding behavior of Ni-based superalloys.* Journal of Materials Science & Technology, 2020. 40: p. 54-63.

198. Takahashi, Y., T. Nakamura, and K. Nishiguchi, *Dissolution process of surface oxide film during diffusion bonding of metals.* Journal of materials science, 1992. 27(2): p. 485-498.

199. 大橋修, 田沼欣司, and 木村隆, *拡散溶接部の密着部での酸化皮膜の挙動: 拡散溶接部での表面皮膜に関する研究 (第 3 報)(昭和 61 年度春季全国大会論文発表講演討論記録).* 溶接学会論文集: quarterly journal of the Japan Welding Society, 1986. **4**(3): p. 62.

200. 益本功, et al., *拡散接合の最近の進歩.* 日本金属学会会報, 1970. **9**(10): p. 653-665.

201. Xin, R., J. Luo, and Q. Ma, *Effect of Parameters on Internal Crack Healing in 30Cr2Ni4MoV Steel for 600-Ton Ultra-Super Ingots.* Metals, 2017. **7**(4).

202. Song, M., et al., *In situ electron microscopy investigation of void healing in an Al–Mg–Er alloy at a low temperature.* Acta Materialia, 2014. **69**: p. 236-245.

203. Gao, K., L. Qiao, and W. Chu, *In situ TEM observation of crack healing in α-Fe.* Scripta materialia, 2001. **44**(7): p. 1055-1059.

204. Zhou, G., et al., *Atomistic simulation of microcrack healing in aluminium.* Modelling and Simulation in Materials Science and Engineering, 2000. **8**(4): p. 603.

205. Li, J., et al., *Mechanism of crack healing at room temperature revealed by atomistic simulations.* Acta Materialia, 2015. **95**: p. 291-301.

206. Sun, C.Y., et al., *Element diffusion model of bimetallic hot deformation in metallurgical bonding process.* Materials & Design, 2016. **94**: p. 433-443.

207. Wei, D., et al., *Simulation of crack healing in BCC Fe.* Scripta Materialia, 2004. **51**(6): p. 583-587.

208. Xu, G.Q. and M.J. Demkowicz, *Healing of nanocracks by disclinations.* Phys Rev Lett, 2013. **111**(14): p. 145501.

209. Zhang, G., R. Chandel, and H. Seow, *Solid state diffusion bonding of Inconel 718.* Science and technology of welding and joining, 2001. **6**(4): p. 235-239.

210. Yang, X., et al., *Physical simulation of interfacial microstructure evolution for hot compression bonding behavior in linear friction welded joints of GH4169 superalloy.* Materials & Design, 2016. **104**: p. 436-452.

211. Wang, Y., et al., *A study of solid-state bonding-by-hot-deforming mechanism in Inconel 718.* Journal of Materials Processing Technology, 2021. **295**.

212. Vaezi, M., P. Drescher, and H. Seitz, *Beamless Metal Additive Manufacturing.* Materials (Basel), 2020. **13**(4).

213. Tuncer, N. and A. Bose, *Solid-State Metal Additive Manufacturing: A Review.* Jom, 2020.

214. Lee, H.-S., J.-H. Yoon, and Y.-M. Yi, *Fabrication of titanium parts by massive diffusion bonding.* Journal of Materials Processing Technology, 2008. 201(1-3): p. 280-284.

215. Alabort, E., et al., *Grain boundary properties of a nickel-based superalloy: characterisation and modelling.* Acta Materialia, 2018. 151: p. 377-394.

216. Nicolaÿ, A., et al., *Influence of strain rate on subsolvus dynamic and post-dynamic recrystallization kinetics of Inconel 718.* Acta Materialia, 2019. 174: p. 406-417.

217. Lourdin, P., D. Juvé, and D. Tréheux, *Nickel-alumina bonds: mechanical properties related to interfacial chemistry.* Journal of the European Ceramic Society, 1996. 16(7): p. 745-752.

218. Farkas, D., S. Mohanty, and J. Monk, *Strain-driven grain boundary motion in nanocrystalline materials.* Materials Science and Engineering: A, 2008. 493(1-2): p. 33-40.

219. Ulomek, F. and V. Mohles, *Separating grain boundary migration mechanisms in molecular dynamics simulations.* Acta Materialia, 2016. 103: p. 424-432.

220. Shvindlerman, D.A.M.J.S.G.G.W.L.L.S., *Effect of pressure on grain boundary migration in Aluminum bicrystals.* Acta Materialia, 1994. 42(10).

221. Zhang, H., *Grain Boundary Migration in Metals: Molecular Dynamics Simulations.* 2005.

222. Lagos, M. and C. Retamal, *Grain dynamics and plastic properties of highly refined materials.* Physica Scripta, 2010. 82(6).

223. Song, K. and M. Aindow, *Grain growth and particle pinning in a model Ni-based superalloy.* Materials Science and Engineering: A, 2008. 479(1-2): p. 365-372.

224. Gladman, T., *On the theory of the effect of precipitate particles on grain growth in metals.* Proceedings of the Royal Society of London. Series A. Mathematical and Physical Sciences, 1966. 294(1438): p. 298-309.

225. Humphreys, F. and M. Ardakani, *Grain boundary migration and Zener pinning in particle-containing copper crystals.* Acta materialia, 1996. 44(7): p. 2717-2727.

226. Zhou, X., X. Li, and K. Lu, *Size Dependence of Grain Boundary Migration in Metals under Mechanical Loading.* Phys Rev Lett, 2019. 122(12): p. 126101.

227. Hosford, W.F. and R.M. Caddell, *Metal forming: mechanics and metallurgy*. 2011: Cambridge university press.

228. Wanheim, T., N. Bay, and A. Petersen, *A theoretically determined model for friction in metal working processes.* Wear, 1974. 28(2): p. 251-258.

229. Esposito, L., et al., *Solid state bonding of Al2O3 with Cu, Ni and Fe: characteristics and properties.* Journal of materials science, 1998. 33(7): p. 1827-1836.

230. Hattali, M.L., et al., *Effect of thermal residual stresses on the strength for both alumina/Ni/alumina and alumina/Ni/nickel alloy bimaterials.* Journal of Materials Science, 2009. **44**(12): p. 3198-3210.

231. Utsumi, J. and R. Takigawa, *Surface activated bonding of aluminum oxide films at room temperature.* Scripta Materialia, 2021. **191**: p. 215-218.

232. Sinnott, S.B. and E.C. Dickey, *Ceramic/metal interface structures and their relationship to atomic- and meso-scale properties.* Materials Science and Engineering: R: Reports, 2003. **43**(1-2): p. 1-59.

233. Zhang, H., et al. *Ab Initio Molecular Dynamics Study on the Dissolution of Interfacial Iron Oxides in Hot Compressive Bonding Combined with Experiments*. in *TMS 2019 148th Annual Meeting & Exhibition Supplemental Proceedings*. 2019. Springer.

234. Akselsen, O., *Diffusion bonding of ceramics.* Journal of materials science, 1992. **27**(3): p. 569-579.

235. Felten, E., *Hot-Pressing of Alumina Powders at Low Temperatures.* Journal of the American Ceramic Society, 1961. **44**(8): p. 381-385.

236. Buckley, D.H. and K. Miyoshi, *Friction and wear of ceramics.* Wear, 1984. **100**(1-3): p. 333-353.

237. Marsen, C. *Alumina - Aluminium Oxide - Al2O3 - A Refractory Ceramic Oxide*. 2001; Available from: https://www.azom.com/properties.aspx?ArticleID=52.

238. Benjamin, J.S., *Dispersion strengthened superalloys by mechanical alloying.* Metallurgical transactions, 1970. **1**(10): p. 2943-2951.

239. Thomas, A., et al., *High temperature deformation of Inconel 718.* Journal of Materials Processing Technology, 2006. **177**(1-3): p. 469-472.

240. Zhang, H.Y., et al., *Deformation characteristics of δ phase in the delta-processed Inconel 718 alloy.* Materials Characterization, 2010. **61**(1): p. 49-53.

241. Lalvani, H.M. and J.W. Brooks, *Hot Forging of IN718 with Solution-Treated and Delta-Containing Initial Microstructures.* Metallography, Microstructure, and Analysis, 2016. **5**(5): p. 392-401.

242. Mignanelli, P.M., et al., *Microstructural evolution of a delta containing nickel-base superalloy during heat treatment and isothermal forging.* Materials Science and Engineering: A, 2015. **621**: p. 265-271.

243. Kañetas, P.J.P., et al., *Influence of the Delta Phase in the Microstructure of the Inconel 718 subjected to "Delta-processing" Heat Treatment and Hot Deformed.* Procedia Materials Science, 2015. **8**: p. 1160-1165.

244. Wei, X.-p., et al., *Strain-induced precipitation behavior of δ phase in Inconel 718 alloy.* Journal of Iron and Steel Research International, 2014. **21**(3): p. 375-381.

245. Calvo, J., M. Penalva, and J.M. Cabrera, *Characterization of Strain-Induced Precipitation in Inconel 718 Superalloy.* Journal of Materials Engineering and Performance, 2016. **25**(8): p. 3409-3417.

246. Páramo-Kañetas, P.J., et al., *Analysis of strain-induced precipitates by delta-processing in Inconel 718 superalloy.* Materials Characterization, 2021. **173**.

247. Zhang, H., et al., *Delta precipitation in wrought Inconel 718 alloy; the role of dynamic recrystallization.* Materials Characterization, 2017. **133**: p. 138-145.

248. Anderson, M., et al., *δ Phase precipitation in Inconel 718 and associated mechanical properties.* Materials Science and Engineering: A, 2017. **679**: p. 48-55.

249. Aragon, N.K., J.D. Gravell, and I. Ryu, *Dislocation interactions at the grain boundary in FCC bicrystals: An atomistically-informed dislocation dynamics study.* Acta Materialia, 2022. **223**.

250. Imrich, P.J., et al., *Differences in deformation behavior of bicrystalline Cu micropillars containing a twin boundary or a large-angle grain boundary.* Acta Materialia, 2014. **73**: p. 240-250.

251. Kunz, A., S. Pathak, and J.R. Greer, *Size effects in Al nanopillars: Single crystalline vs. bicrystalline.* Acta Materialia, 2011. **59**(11): p. 4416-4424.

252. Rehman, H.u., et al., *Study on the deformation mechanics of hard brittle coatings on ductile substrates using in-situ tensile testing and cohesive zone FEM modeling.* Surface and Coatings Technology, 2012. **207**: p. 163-169.

253. Guo, T., et al., *Brittle film-induced cracking of ductile substrates.* Acta Materialia, 2015. **99**: p. 273-280.

254. Xiong, J., et al., *Diffusion bonding of nickel-based superalloy GH4099 with pure nickel interlayer.* Journal of Materials Science, 2019. **54**(8): p. 6552-6564.

255. Reuven, R., et al., *Ni Interlayer to Improve Low-Pressure Diffusion Bonding of 316L SS Press Fit Tube-to-Tubesheet Joints for Coiled Tube Gas Heaters.* Journal of Nuclear Engineering and Radiation Science, 2017. **3**(3).

256. Habisch, S., et al., *The Effect of Interlayer Materials on the Joint Properties of Diffusion-Bonded Aluminium and Magnesium.* Metals, 2018. **8**(2).

257. Genova, V., et al., *Pure thick nickel coating obtained by electroless plating: Surface characterization and wetting properties.* Surface and Coatings Technology, 2019. **357**: p. 595-603.

Appendices

Appendix A

Different heating scheme to simulate the hot compression of bar samples in QForm

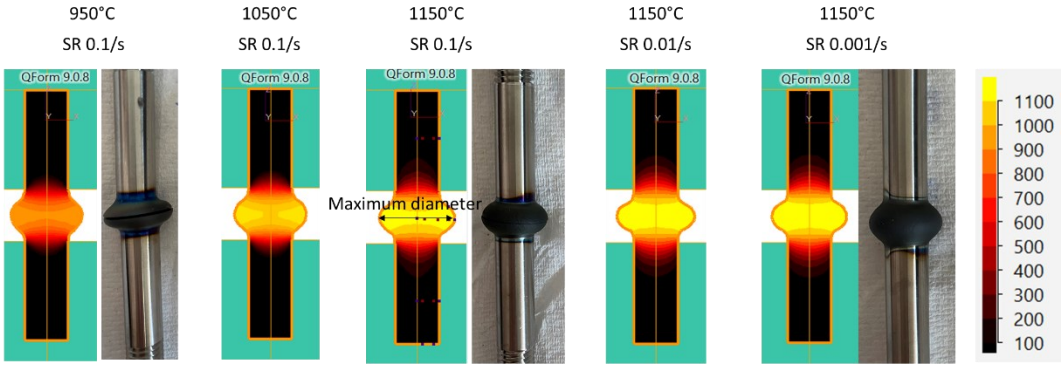
For the initial temperature setting of the workpiece, another schemes have been undertaken and compared. That is to simulate the single compression process and set the initial temperature uniformly as the designated bonding temperature.

The heat transfer coefficient (a) is force correlated and the coefficients for different hot compression conditions are listed below in Table A-1. The selected coefficients are based on the QForm library data for Cu alloy under no lubricant condition (45000-50000 W/(m^2·K)), and for Ni alloy under graphite + water condition (22500 W/(m^2·K)). The friction factor was set at 0.8 considering the unlubricated condition. The electric current (in Power) was adjusted according to recorded power angle data during the compression.

Table A-1 The heat transfer coefficients (a) is force correlated and the coefficients for different hot compression conditions

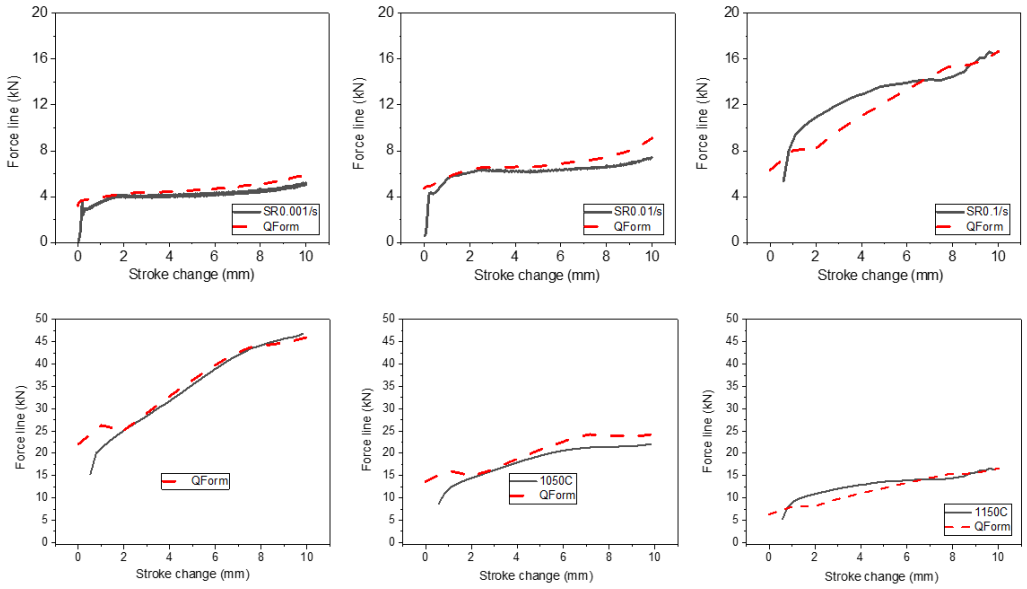
	1150 ˚C, 0.001 s^{-1}	**1150 ˚C, 0.01 s^{-1}**	**1150 ˚C, 0.1 s^{-1}**	**1050 ˚C, 0.1 s^{-1}**	**950 ˚C, 0.1 s^{-1}**
Heat transfer coefficient(a), W/(m^2·K)	8500	10000	40000	5e4	1e5

The simulated sample shape at different temperatures (1150 ˚C, 1050 ˚C, 950 ˚C) and different strain rates (0.001 s^{-1}, 0.01 s^{-1}, 0.1 s^{-1}) after compression deformation in comparison to the real samples (the diameter of the deformed shape) are shown in Figure A-1. Moreover, the simulated and recorded force is shown in Figure A-2.



Diameter of **(mm)**	Temperature 950˚C Strain rate 0.1s^{-1}	Temperature 1050˚C Strain rate 0.1s^{-1}	Temperature 1150˚C Strain rate 0.1s^{-1}	Temperature 1150˚C Strain rate 0.01s^{-1}	Temperature 1150˚C Strain rate 0.001s^{-1}
Gleeble bonded samples	17.3	16.9	16.0	15.2	15.0
simulated bonded samples	16.5027	16.7007	17.0408	17.5918	17.1948
error	-4.6%	-0.8%	6.5%	15.7%	14.6%

Figure A-1 The single-process simulated sample shape at different temperatures (1150 ˚C, 1050 ˚C, 950 ˚C) and different strain rates (0.001 s^{-1}, 0.01 s^{-1}, 0.1 s^{-1}) after compression deformation in comparison to the real samples.



FigureA-2 The comparison between the simulated and recorded force for the hot compression bonding process under different conditions using single-process simulation.

Error analysis: According to recorded Gleeble power angle data, the power for electric upsetting power was adjusted to better copy the loading data and temperature evolution. As

shown in Figure A-2, the compressive load can be obtained with acceptable deviation, and the simulation can well reflect the loading in actual compression under different conditions. As the initial temperature of the workpiece was set as the designated temperature, neglecting the temperature distribution along the length, the error in the initial load simulation is higher, yet does not affect the general loading trend between different deformation conditions. However, the comparison in the maximum diameter between the deformed bar samples and simulation results reveals that the simulation can better reflect the diameter change trending for samples compressed bonded under different strain rates, but not the sample bonded under different temperatures.

Appendix B

```
% constants for the oxide
frag_length = 1000; %nm
frag_thickness = 10; %nm
oxide_ratio = 0.35*0.7; %dependent on the oxidation
%oxide-oxide
a_OO = 0.05; %stress coefficient for oxide-oxide
compressive_strength_OO = 690; %compressive yielding strength,MPa
P_OO = 30; %ratio of oxide-oxide cohesion to metal
%oxide-metal
a_OM = 0.45; %stress coefficient for oxide-metal
compressive_strength_OM = 70; %compressive yielding strength,MPa
P_OM = 1; %ratio of oxide-oxide cohesion to metal
%metal-metal
flow_stress = 70; %yielding strength of metal, as constant for the moment
migration_ratio = 1; %GB migration ratio, dependent on temp,GS,frag_gap...

%% SR0.001
% data import from FE results
data001 = xlsread('C:\Users\yw18\OneDrive - Imperial College London\IC
Yaping Wang\Experiments
Folder\Matlab\SelfLearning\ElectricDoubleAdjustment-SR0001-T1150.xls');

normal_stress001 = data001(:,3); % stress_zz
radial_strain001 = data001(:,2); % strain_xx
time001 = data001(:,1);
pressure_ex001 = zeros();
compressive_strength_OM = 40; %compressive yielding strength,MPa
flow_stress = 40; %yielding strength of metal, as constant for the moment

L001 = length(normal_stress001);
%
for i = 1:L001

    % extrusion pressure calculation
    frag_gap001(i) = 18*frag_length*(radial_strain001(i)-
oxide_ratio)/(1+oxide_ratio);%nm

        if frag_gap001(i) < 0
           frag_gap001(i) = 0;
        end

    pressure_ex001(i) =
1*flow_stress*(log((frag_length+frag_gap001(i))/frag_gap001(i))+frag_thickn
ess/frag_gap001(i));


     % metal-metal contact

    f_MM001(i) = (radial_strain001(i)-oxide_ratio)/(radial_strain001(i));

    if f_MM001(i) < 0
        f_MM001(i) = 0;
    end
```

```
    if frag_gap001(i) == 0
        C_MM001(i) = 0;
    else
        C_MM001(i) = 0.85*(normal_stress001(i)-
pressure_ex001(i))/flow_stress;
    end



    if C_MM001(i) > 1
        C_MM001(i) = 1;
    elseif C_MM001(i) < 0
        C_MM001(i) = 0;
    end


    delta001(i) = 1*(1-
C_MM001(i).*(1.0*frag_gap001(i)./(frag_length+frag_gap001(i))));%effect
factor of oxide scattering
    f_MM001(i) = (radial_strain001(i)./delta001(i)-
oxide_ratio)/(1+radial_strain001(i)./delta001(i));

    ratio_MM001(i) = f_MM001(i)*C_MM001(i)*migration_ratio;


    % oxide-oxide contact
    f_OO001(i) = 1/(1+radial_strain001(i)./delta001(i));
    C_OO001(i) = a_OO*(normal_stress001(i)/compressive_strength_OO)*P_OO;
    ratio_OO001(i) = f_OO001(i)*C_OO001(i);

    % oxide-metal contact
    if radial_strain001(i) < oxide_ratio
        f_OM001(i) =
(radial_strain001(i)./delta001(i))/(1+radial_strain001(i)./delta001(i));
    else
        f_OM001(i) = oxide_ratio/(1+radial_strain001(i)./delta001(i));
    end

    C_OM001(i) = a_OM*(normal_stress001(i)/compressive_strength_OM)*P_OM;
    ratio_OM001(i) = f_OM001(i)*C_OM001(i);




    % bonding ratio
    if radial_strain001(i) == 0
        ratio_E001(i) = ratio_OO001(i);
    else
        ratio_E001(i) = ratio_MM001(i)+ratio_OO001(i)+ratio_OM001(i);
    end

end
```

```
%% SR0.01
% data import from FE results
data01 = xlsread('C:\Users\yw18\OneDrive - Imperial College London\IC
Yaping Wang\Experiments
Folder\Matlab\SelfLearning\ElectricDoubleAdjustment-SR001-T1150.xls');

normal_stress01 = data01(:,3); % stress_zz
radial_strain01 = data01(:,2); % strain_xx
time01 = data01(:,1);
pressure_ex01 = zeros();
compressive_strength_OM = 60; %compressive yielding strength,MPa
flow_stress = 60; %yielding strength of metal, as constant for the moment

L01 = length(normal_stress01);
%
for i = 1:L01

    % extrusion pressure calculation
    frag_gap01(i) = 18*frag_length*(radial_strain01(i)-
oxide_ratio)/(1+oxide_ratio);%nm

        if frag_gap01(i) < 0
           frag_gap01(i) = 0;
        end

    pressure_ex01(i) =
flow_stress*(log((frag_length+frag_gap01(i))/frag_gap01(i))+frag_thickness/
frag_gap01(i));


     % metal-metal contact

    f_MM01(i) = (radial_strain01(i)-oxide_ratio)/(radial_strain01(i));

    if f_MM01(i) < 0
        f_MM01(i) = 0;
    end


    if frag_gap01(i) == 0
        C_MM01(i) = 0;
    else
        C_MM01(i) = 0.85*(normal_stress01(i)-pressure_ex01(i))/flow_stress;
    end



    if C_MM01(i) > 1
        C_MM01(i) = 1;
    elseif C_MM01(i) < 0
        C_MM01(i) = 0;
    end
```

```
    delta01(i) = 1*(1-
C_MM01(i).*(frag_gap01(i)./(frag_length+frag_gap01(i))));%effect factor of
oxide scattering
    f_MM01(i) = (radial_strain01(i)./delta01(i)-
oxide_ratio)/(1+radial_strain01(i)./delta01(i));

    ratio_MM01(i) = f_MM01(i)*C_MM01(i)*migration_ratio;


    % oxide-oxide contact
    f_OO01(i) = 1/(1+radial_strain01(i)./delta01(i));
    C_OO01(i) = a_OO*(normal_stress01(i)/compressive_strength_OO)*P_OO;
    ratio_OO01(i) = f_OO01(i)*C_OO01(i);

    % oxide-metal contact
    if radial_strain01(i) < oxide_ratio
        f_OM01(i) =
(radial_strain01(i)./delta01(i))/(1+radial_strain01(i)./delta01(i));
    else
        f_OM01(i) = oxide_ratio/(1+radial_strain01(i)./delta01(i));
    end

    C_OM01(i) = a_OM*(normal_stress01(i)/compressive_strength_OM)*P_OM;
    ratio_OM01(i) = f_OM01(i)*C_OM01(i);


      % bonding ratio
    if radial_strain01(i) == 0
        ratio_E01(i) = ratio_OO01(i);
    else
        ratio_E01(i) = ratio_MM01(i)+ratio_OO01(i)+ratio_OM01(i);
    end

end


%% SR0.1
% data import from FE results
data1 = xlsread('C:\Users\yw18\OneDrive - Imperial College London\IC Yaping
Wang\Experiments Folder\Matlab\SelfLearning\ElectricDoubleAdjustment-SR01-
T1150.xls');

normal_stress1 = data1(:,3); % stress_zz
radial_strain1 = data1(:,2); % strain_xx
time1 = data1(:,1);
pressure_ex1 = zeros();
compressive_strength_OM = 70; %compressive yielding strength,MPa
flow_stress = 70; %yielding strength of metal, as constant for the moment

L1 = length(normal_stress1);
%
for i = 1:L1

    % extrusion pressure calculation
    frag_gap1(i) = 18*frag_length*(radial_strain1(i)-
oxide_ratio)/(1+oxide_ratio);%nm
```

```
        if frag_gap1(i) < 0
           frag_gap1(i) = 0;
        end

    pressure_ex1(i) =
flow_stress*(log((frag_length+frag_gap1(i))/frag_gap1(i))+frag_thickness/fr
ag_gap1(i));


     % metal-metal contact

    f_MM1(i) = (radial_strain1(i)-oxide_ratio)/(radial_strain1(i));

    if f_MM1(i) < 0
        f_MM1(i) = 0;
    end


    if frag_gap1(i) == 0
        C_MM1(i) = 0;
    else
        C_MM1(i) = 0.85*(normal_stress1(i)-pressure_ex1(i))/flow_stress;
    end



    if C_MM1(i) > 1
        C_MM1(i) = 1;
    elseif C_MM1(i) < 0
        C_MM1(i) = 0;
    end


    delta1(i) = 1*(1-
C_MM1(i).*(frag_gap1(i)./(frag_length+frag_gap1(i))));%effect factor of
oxide scattering
    f_MM1(i) = (radial_strain1(i)./delta1(i)-
oxide_ratio)/(1+radial_strain1(i)./delta1(i));

    ratio_MM1(i) = f_MM1(i)*C_MM1(i)*migration_ratio;


    % oxide-oxide contact
    f_OO1(i) = 1/(1+radial_strain1(i)./delta1(i));
    C_OO1(i) = a_OO*(normal_stress1(i)/compressive_strength_OO)*P_OO;
    ratio_OO1(i) = f_OO1(i)*C_OO1(i);

    % oxide-metal contact
    %
    if radial_strain1(i) < oxide_ratio
        f_OM1(i) =
(radial_strain1(i)./delta1(i))/(1+radial_strain1(i)./delta1(i));
    else
        f_OM1(i) = oxide_ratio/(1+radial_strain1(i)./delta1(i));
    end
```

```
    C_OM1(i) = a_OM*(normal_stress1(i)/compressive_strength_OM)*P_OM;
    ratio_OM1(i) = f_OM1(i)*C_OM1(i);




    % bonding ratio
    if radial_strain1(i) == 0
        ratio_E1(i) = ratio_OO1(i);
    else
        ratio_E1(i) = ratio_MM1(i)+ratio_OO1(i)+ratio_OM1(i);
    end

end

figure
subplot(4,3,1)
plot(10*time1,frag_gap1);
hold on
plot(time01,frag_gap01);
hold on
plot(0.1*time001,frag_gap001);
set(gca,'fontname','times new roman');
xlabel('height reduction /%','fontname','times new roman');
ylabel('/um','fontname','times new roman');
title('frag gap','fontname','times new roman');

subplot(4,3,2)
% yyaxis left
plot(10*time1,pressure_ex1);
hold on
plot(time01,pressure_ex01);
hold on
plot(0.1*time001,pressure_ex001);
set(gca,'fontname','times new roman');
hold on
% yyaxis right
plot(10*time1,normal_stress1);
hold on
plot(time01,normal_stress01);
hold on
plot(0.1*time001,normal_stress001);
xlabel('height reduction /%','fontname','times new roman');
ylabel('/MPa','fontname','times new roman');
legend({'extrusion pressure-0.1','extrusion pressure-0.01','extrusion
pressure-0.001','normal stress-0.1','normal stress-0.01','normal stress-
0.001','fontname','times new roman'},'Location','northwest');
legend('boxoff');
title('pressure_e_x vs normal stress','fontname','times new roman');

subplot(4,3,3)
plot(10*time1,ratio_E1);
hold on
plot(time01,ratio_E01);
hold on
plot(0.1*time001,ratio_E001);
set(gca,'fontname','times new roman');
xlabel('height reduction /%','fontname','times new roman');
```

```
title('total bonding ratio','fontname','times new roman');

subplot(4,3,4)
plot(10*time1,f_MM1);
hold on
plot(time01,f_MM01);
hold on
plot(0.1*time001,f_MM001);
set(gca,'fontname','times new roman');
xlabel('height reduction /%','fontname','times new roman');
title('f-MM Plot','fontname','times new roman');

subplot(4,3,5)
plot(10*time1,C_MM1);
hold on
plot(time01,C_MM01);
hold on
plot(0.1*time001,C_MM001);
set(gca,'fontname','times new roman');
xlabel('height reduction /%','fontname','times new roman');
title('C-MM Plot','fontname','times new roman');

subplot(4,3,6)
plot(10*time1,ratio_MM1);
hold on
plot(time01,ratio_MM01);
hold on
plot(0.1*time001,ratio_MM001);
set(gca,'fontname','times new roman');
xlabel('height reduction /%','fontname','times new roman');
title('metal-metal contact','fontname','times new roman');

subplot(4,3,7)
plot(10*time1,f_OO1);
hold on
plot(time01,f_OO01);
hold on
plot(0.1*time001,f_OO001);
set(gca,'fontname','times new roman');
xlabel('height reduction /%','fontname','times new roman');
title('f-OO Plot','fontname','times new roman');

subplot(4,3,8)
plot(10*time1,C_OO1);
hold on
plot(time01,C_OO01);
hold on
plot(0.1*time001,C_OO001);
set(gca,'fontname','times new roman');
xlabel('height reduction /%','fontname','times new roman');
title('C-OO Plot','fontname','times new roman');

subplot(4,3,9)
plot(10*time1,ratio_OO1);
hold on
plot(time01,ratio_OO01);
hold on
plot(0.1*time001,ratio_OO001);
```

```
set(gca,'fontname','times new roman');
xlabel('height reduction /%','fontname','times new roman');
title('oxide-oxide contact','fontname','times new roman');

subplot(4,3,10)
plot(10*time1,f_OM1);
hold on
plot(time01,f_OM01);
hold on
plot(0.1*time001,f_OM001);
set(gca,'fontname','times new roman');
xlabel('height reduction /%','fontname','times new roman');
title('f-OM Plot','fontname','times new roman');

subplot(4,3,11)
plot(10*time1,C_OM1);
hold on
plot(time01,C_OM01);
hold on
plot(0.1*time001,C_OM001);
set(gca,'fontname','times new roman');
xlabel('height reduction /%','fontname','times new roman');
title('C-OM plot','fontname','times new roman');

subplot(4,3,12)
plot(10*time1,ratio_OM1);
hold on
plot(time01,ratio_OM01);
hold on
plot(0.1*time001,ratio_OM001);
set(gca,'fontname','times new roman');
xlabel('height reduction /%','fontname','times new roman');
title('oxide-metal contact','fontname','times new roman');
```

Appendix C

The evaluation of high-temperature mechanical properties of the multi-layer forging bonded plate in Chapter 6

After standard ageing heat treatment, the high-temperature tensile properties of forging bonded plates were tested at 650 ˚C to give a preliminary indication of the performance of the joints under real service conditions. The results are shown in Table B-1, of which the trend is in agreement with the room-temperature tensile results, and for each position, the average value was taken and presented in the table. For yielding, all plates have stronger strength than standards, while for ultimate strength, the plates bonded at (1150 ˚C-10mm·s^{-1}) and (1150 ˚C-0.1mm·s^{-1}) show comparable high-temperature strength to wrought standard. The high ultimate strength obtained in these two conditions is due to the achieved relatively higher ductility,

compared with other conditions. The best ductility achieved at 3-1#(1150 ˚C-10mm·s^{-1}) and 3-3#(1150 ˚C-0.1mm·s^{-1}) are below wrought standards by over 50%. The high-temperature tensile properties of powder metallurgically manufactured IN718 part is also listed in the Table. For powers hot isostatically pressed with an oxygen content of 275 ppm and a vacuum of 6.5×10^{-4} Pa, clear Prior Particle Boundaries (PPB) network were shown. These continuous networks composed of carbides and oxides led to low ductility[24], with which the bonding formed plates shows a similar ductility level.

For plates presenting better high-temperature tensile properties (3-1# and 3-3#), samples taken from different position show a slight difference, and samples that were taken from the edge area has relatively lower tensile strength and ductility.

Table B-1 The 650 ˚C tensile properties of heat-treated samples from multi-layered plates bonded under different conditions and comparison with standard specification, C stands for centre andELfor edge zone.

Sample	Ultimate Tensile Strength (UTS), MPa	Yielding Strength (YS), MPa	Elongation (EL), %	Area Reduction (AR), %
1#	902(C) / 795(E)	864(C) / 738(E)	0.7(C) / 0.5(E)	1.7(C) / 2.3(E)
2#	924(C) / 1004(E)	884(C) / 989(E)	0.6(C) / 1.3(E)	1.7(C) / 2.3(E)
3-1#	1061(C) / 1027(E)	982(C) / 998(E)	3.6 (C) / 2.2(E)	5.9(C) / 3.6(E)
3-2#	980(C) / 912(E)	930(C) / -(E)	3.5 (C) / 2.0(E)	4.0(C) / 2.6(E)
3-3#	1030(C) / 991(E)	955(C) / -(E)	4.6 (C) / 3.0(E)	5.0(C) / 2.7(E)
PM-IN718 [24]	1140	1018	3.0	7.7
AMS 5662J	1000	860	12.0	15.0

Appendix D

Publications during Ph. D.

Part of the work presented in this thesis (results in Chapter 4 and Chapter 5) has been published in the following literature:

Wang Y, Jiang J*, et al. 2021. A study of solid-state bonding-by-hot-deforming mechanism in Inconel 718. *Journal of Materials Processing Tech.,* 295, 117191. DOI: 10.1016/j.jmatprotec.2021.117191

Wang Y, Jiang J*, et al. 2021. Develop a new physical model for solid-state pressure bonding and predicted effect of strain rate on the bond quality. *Materials & Design*, 215 (2022) 110436 DOI.org/10.1016/j.matdes.2022.110436

Other published work is listed as follows:

Lan B, **Wang Y***, et al. 2021. The microstructural anisotropy effect of wire arc additive manufactured (WAAM) Inconel718 on the subsequent hot deformation. *Materials Science and Engineering: A,* 823, 141733. DOI: 10.1016/j.msea.2021.141733.